



HAL
open science

Multiscale modeling of multiferroic nanocomposites

Sergei Prokhorenko

► **To cite this version:**

Sergei Prokhorenko. Multiscale modeling of multiferroic nanocomposites. Engineering Sciences [physics]. Ecole Centrale Paris, 2014. English. NNT : 2014ECAP0045 . tel-01127181

HAL Id: tel-01127181

<https://theses.hal.science/tel-01127181>

Submitted on 7 Mar 2015

HAL is a multi-disciplinary open access archive for the deposit and dissemination of scientific research documents, whether they are published or not. The documents may come from teaching and research institutions in France or abroad, or from public or private research centers.

L'archive ouverte pluridisciplinaire **HAL**, est destinée au dépôt et à la diffusion de documents scientifiques de niveau recherche, publiés ou non, émanant des établissements d'enseignement et de recherche français ou étrangers, des laboratoires publics ou privés.

ÉCOLE CENTRALE PARIS

DOCTORAL THESIS

Multiscale Modeling of Multiferroic nanocomposites

Author:
Sergei PROKHORENKO

Supervisor:
Dr. Igor KORNEV

<i>Defense Committee President:</i>	LAURENT BELLAICHE
<i>Referees:</i>	ALEXANDER TAGANTSEV
	ERIC BOUSQUET
<i>Committee Members:</i>	IGOR KORNEV
	GREGORY GENESTE
	BRAHIM DKHIL

*A thesis submitted in fulfilment of the requirements
for the degree of Doctor of Philosophy*

in the

Laboratoire Structures, Propriétés et
Modélisation des Solides
École Centrale Paris

8 September 2014

Contents

Contents	i
List of Figures	iii
Introduction	1
1 Muliferroic Nanocomposites	4
1.1 Ferroelectric and Magnetic materials	4
1.2 Magnetoelectric effect	8
1.2.1 Single-phase multiferroics	9
1.2.2 Magnetoelectric composites	14
1.3 Geometrical characteristics of binary mixtures	15
1.3.1 Composite connectivity	17
1.3.2 Fractal dimension	19
1.3.3 Euler-Poincaré characteristic	21
1.4 Finite-Temperature properties of model materials	26
1.4.1 BaTiO ₃	27
1.4.2 BiFeO ₃	30
1.4.3 (BaTiO ₃)/(BiFeO ₃) heterostructures	33
1.4.4 (BaTiO ₃) _x (BiFeO ₃) _{1-x} solid solutions	35
2 Theoretical background	39
2.1 Introduction	39
2.2 First principles approaches	40
2.2.1 Density Functional Theory	40
2.3 Lattice models	45
2.3.1 Effects of structural disorder	46
2.4 Second principles models: Effective Hamiltonian approach	52
2.4.1 Perovskite compounds	52
2.4.2 Monte Carlo simulations	59
2.4.3 Temperature dependent ME effect	62
3 Effective Hamiltonian approach for heterogeneous systems	64
3.1 Model: methodology and assessment	65
3.1.1 Introductory background	65
3.1.2 Methodology	66

3.1.3	Assessment of the model	74
3.2	Room-temperature phase diagram of (BiFeO ₃) _x (BaTiO ₃) _{1-x} solid solutions	76
3.3	Finite-temperature properties of (BiFeO ₃)(BaTiO ₃) bicrystals	84
3.3.1	Lattice geometry with (0,0) connectivity	85
3.3.2	Lattice geometry with (1,1) connectivity	86
3.3.3	Lattice geometry with (2,2) connectivity	88
3.3.4	Lattice geometry with (3,3) connectivity	89
3.3.5	Compositionally asymmetric structures: (3,2) and (2,3)	91
3.3.6	Summary of the obtained results	98
3.4	Example of structure-property relations: fractal (Ba,Sr) ₂ TiO ₃ structures	99
4	Nonlinear thermodynamic theory of piezoelectric/piezomagnetic heterostructures	107
4.1	Introduction	107
4.2	Nonlinear thermodynamic model	109
4.3	Polarization states and physical properties of ferroelectric nanolayers	113
4.4	Direct magnetoelectric effect displayed by ferroelectric-ferromagnetic mul- tilayers	117
4.4.1	Magnetoelectric polarization coefficients and output charge signal	119
4.4.2	Magnetoelectric voltage coefficients and output voltage signal	122
4.5	Conclusions	123
	Conclusion	125
	Bibliography	130

List of Figures

1.1	Schematic illustration of the collective polar displacements of the ions. On the left image, the ions of the unit cell of perovskite BaTiO_3 compounds are situated in high symmetry cubic positions. On the right: displacement of the ions leads to the appearance of a nonzero polarization component P_z . This situation corresponds to the room-temperature tetragonal phase of BaTiO_3	5
1.2	Schematic illustration of the nonequilibrium free energy describing thermal fluctuations of the order parameter ξ at different temperatures. (1) At low temperature the \mathbb{Z}_2 symmetry is broken. The symmetric double-well shape of the thermodynamic potential indicates the existence of two equivalent equilibrium states, related to each other via the inversion operation I . (2) At the phase transition temperature, the quadratic coefficient becomes equal to zero, whereas above T_c (3) $\alpha > 0$ and $\xi_0 = 0$	6
1.3	On the left: Experimentally observed ferroelectric hysteresis loop $P(\mathcal{E})$ exhibited by the samples of single-crystal BaTiO_3 (after [7]). On the right: Dependence of equilibrium order parameter magnitude $\xi(\mathcal{E})$ on the value of the external field with the model (eq. (1.1)). Different colors correspond to different temperatures, in accordance with those used in Fig. 1.2	6
1.4	(a) Schematic representation of mixed perovskite structure. Gray arrows represent local dipole moments, while black arrows correspond to magnetic moments. Multiferroicity is achieved by combining transition metal ions with empty and partially filled d shells in a single structure. (b) Schematic representation of polarization appearing due to ordering of lone pairs associated with $6s$ outer electrons of Bi^{3+} cations. (After D. I. Khomskii [10])	8
1.5	Schematic representation of the relationship between multiferroic and magnetoelectric materials, indicating their noncomplete overlap. Ferromagnets (ferroelectrics) form a subset of magnetically (electrically) polarizable materials such as paramagnets and antiferromagnets (paraelectrics and antiferroelectrics). The intersection (gray hatching) represents materials that are multiferroic. Magnetoelectric coupling (green) is an independent phenomenon that can, but need not, arise in any of the materials that are both magnetically and electrically polarizable. In practice, it is likely to arise in all such materials, either directly or via strain. (Adapted from D. I. Khomskii [10])	9

1.6	On the left: Temperature dependence of parallel and transverse magnetoelectric susceptibilities (α_{\parallel} and α_{\perp} respectively) of Cr_2O_3 estimated from phenomenological theory of G. T. Rado [18, 19]. Temperature dependence is described as a product of magnetic susceptibility and average magnetization. (After G. T. Rado [18]). On the right: Parallel magnetoelectric susceptibility versus temperature for Cr_2O_3 computed using single-ion and two-ion theories. The single-ion theoretical curve involves the spin-orbit and g -factor mechanisms, while the two-ion theory compiles is based on the antisymmetric exchange induced by the applied electric field. (After R. Hornreich <i>et al.</i> [20])	12
1.7	On the left: Dependence of the voltage magnetoelectric coefficient on the volume fraction of the piezomagnetic phase. The geometry of the composite structure can be described as piezoelectric pillars embedded in the piezomagnetic matrix. Parameter p denotes the aspect ratio of the pillars. On the right: changing the composite geometry leads to a significant modification of the magnetoelectric coefficients. (After C.-W. Nan <i>et al.</i> [32])	15
1.8	Schematic representation of the Newnham's definition of connectivity. The regions of the composite structure corresponding to different constituent materials are represented by arrangements of cubes of two different colors. Dark cubes correspond to the regions of material A while the light cubes are those occupied by material B . The connectivity of each phase is defined as the number of dimensions in which the phase is <i>self connected</i> . The connectivity of the composite structure is represented by a pair of connectivities corresponding to each phase. The figure illustrates the possible connectivities of the two phase composite. (After R. E. Newnham <i>et al.</i> [29])	18
1.9	(a) Schematic illustration of the minimal edge cut of the graph. In the depicted case it is sufficient to remove a single edge (marked with blue dashed line) in order to disconnect the biggest component of the "black" site sublattice into two disjoint sets. (b) Similar logic can be applied to three dimensional lattices: example of the minimal edge cut of the pillar structure dividing it into two disconnected pillars.	19
1.10	(a) Illustration of three consecutive iterations of the Menger sponge generation algorithm. At each iteration, the elementary cube is divided into 27 equal subcubes. The center of each face and the center of the original cube are then removed from the lattice. (b) Three iterations of the 3D Cantor dust generation algorithm. (c) Examples of the fractal clusters generated using the DLCA algorithm.	21
1.11	For differentiable manifolds, or in another words smooth surfaces Euler characteristic can be calculated using eq. 1.21. For the case of two dimensional surfaces adding one-dimensional or circular holes reduces the Euler characteristic by one. For instance for the torus with two handles the number of connected components is equal to one. Similar to the simple torus it also contains only one cavity, however the number of circular holes is equal to four leading to an Euler number of $\chi = -2$	22

1.12	Dependence of the Euler-number density on the occupied site fraction p for the square (χ_{sq} on the left) and triangular (χ_{tri}) two-dimensional lattices. The two-dimensional triangular lattice is self-matching and therefore the zero of χ_{tr} matches the percolation threshold p_c , which is not the case for a simple square lattice. (After R. A. Neher <i>et al.</i> [41])	23
1.13	Schematic representation of the BaTiO ₃ phase diagram. The compound undergoes three consecutive phase ferroelectric phase transitions: from the paraelectric cubic phase (C) to tetragonal ferroelectric phase (T) at $\sim 403\text{K}$, from tetragonal phase to orthorhombic (O) at $\sim 278\text{K}$, and from orthorhombic to rhombohedral phase (R) at $\sim 183\text{K}$. Blue arrows indicate the orientation of the macroscopic polarization. (the experimental values of transition temperatures are those given in Ref. [46])	27
1.14	Average homogeneous strains η_{xx} , η_{yy} , and η_{zz} as a function of temperature in heating-up (solid lines), and cooling-down simulations (dashed lines). (After T. Nishimatsu <i>et al.</i> [47])	28
1.15	Temperature dependence of piezoelectric coefficients of the tetragonal phase of BaTiO ₃ calculated from first-principles based effective Hamiltonian method. Open triangles and circles represent values computed from the strain response to an electric field and from polarization-strain correlations, respectively. (After A. Garcia <i>et al.</i> [50])	28
1.16	Schematic illustration of the ferroelectric rhombohedral phase of BiFeO ₃ . The macroscopic polarization stems from displacement of the ions in [111] direction relative to the anions. The AFD structure can be described using two cubic perovskite unit cells. The oxygen octahedra rotations around [111] axes alternate along [111] pseudocubic direction. (After C. Ederer <i>et al.</i> [62])	30
1.17	(a) Paraelectric to rhombohedral ferroelectric phase transition predicted from effective Hamiltonian model. The figure shows temperature dependence of the average value of the components of spontaneous polarization. (b) The predicted sequence of the AFD phase transitions. (After I. A. Kornev <i>et al.</i> [72])	31
1.18	Theoretically predicted magnetic structure of BiFeO ₃ reported in [62]. The spin-orbit coupling, leads to antisymmetric exchange (Dzyaloshinskii-Moriya interaction [68, 69]), which in turn results in a rotation of the magnetic moments of iron atoms in (111) plane. Appearing nonzero spontaneous magnetization M is referred to as weak magnetic moment. (Adapted from C. Ederer <i>et al.</i> [62])	32
1.19	The predicted values of transverse (λ_{31}) and longitudinal (λ_{33}) magnetosriction, and piezomagnetic (q_{33} and q_{31}) coupling coefficients. (After A. Kumar <i>et al.</i> [80])	33
1.20	Ferroelectric hysteresis loops measured at $T=100\text{K}$ for the composite films with 0.33 weight fraction of BiFeO ₃ at different values of the bias magnetic field ranging from 0 to 8T. (After M. Lorentz <i>et al.</i> [84])	34

1.21	Temperature and bias magnetic field dependence of the magnetoelectric voltage coefficient $\alpha = \partial E / \partial H$ exhibited by thin films of different structure and composition. Measurements (a) and (b) were performed for the multilayers consisting of 15 (BiFeO ₃)(BaTiO ₃) double layers (denoted as 15BTO/BFO) and for composite thin films with 0.67 BiFeO ₃ weight fraction. Measurements (c) and (d) were performed for the composite films with 0.33 BiFeO ₃ weight fraction. (After M. Lorentz <i>et al.</i> [84])	35
1.22	Dependence of the induced ferroelectric polarization upon the external magnetic field strength at different temperatures for (A) (BiFeO ₃)(BaTiO ₃) and (B) (BiFeO ₃)(PbTiO ₃) solid solutions with 0.95 BiFeO ₃ mole %. The curves corresponding to different temperatures are denoted by numbers. System (A): (1) 298K (2) 305K (3) 323K (4) 398K; System (b): (1) 298K (2) 333K (3) 373K (4) 413K. (After I. H. Ismailidze <i>et al.</i> [86])	36
1.23	Variation of the magnetoelectric output with temperature for (BiFeO ₃) _{0.75} (BaTiO ₃) _{0.25} system. (After M. M. Kumar <i>et al.</i> [87])	36
1.24	Variation of lattice parameters with decreasing content of BiFeO ₃ . (After M. M. Kumar <i>et al.</i> [138])	37
2.1	Schematic illustration of the domain walls corresponding to the systems of either (a) continuous or (b) discrete symmetries. In the case of the Ising model (\mathbb{Z}_2 symmetry), the domain wall energy is proportional to the surface of the wall, $\epsilon_{dw} \sim JL^{d-1}$. The possibility of continuous rotation of the spins results in the domain wall energy of JL^{d-1}/w , where w is the domain wall thickness. Assuming $w \sim L$ gives $\epsilon_{dw} \sim L^{d-2}$	48
2.2	Topological defects appearing at the crossing points of the domain walls. Two different types of the boundaries depicted as red and blue curves are associated with $h_i^x = 0$ and h_i^y conditions. The crossing points, where the magnitude of the local field vanishes $\mathbf{h}_i = 0$, represent the topological defect pinning centres. In the specific case of the two component Heisenberg model in 2D, the topological defects correspond to the well known vortex and anti-vortex field configurations. (After T. C. Proctor <i>et al.</i> [105])	50
2.3	Schematic illustration of metastable, topologically protected states in 3D for (a) XY model ($n = 2$) and (b) classical Heisenberg model ($n = 3$). In the former case, the vortex points schematically depicted in Fig. 2.2 coalesce, forming the vortex lines. In the case of the classical Heisenberg spin model the point hedgehog defects form a set of dimension zero. (After T. C. Proctor <i>et al.</i> [105])	51
2.4	Relaxation of the average magnetization from the initial ordered state for the spin systems characterized by dimensions $d = 3$ and $n = \{2, 3, 4, 5\}$. MCS stands for a full lattice update of the spins, i.e. one Monte Carlo simulation sweep. (After T. C. Proctor <i>et al.</i> [105])	51
2.5	Schematic phase diagram of the three-dimensional random-field magnets. The blue curve corresponds to the true, equilibrium phase transition line, while the red curve marks the onset of irreversible hysteretic behaviour. (Adapted from D. S. Fisher <i>et al.</i> [107])	52

2.6	Schematic representation of independent short-range interaction parameters. For the first nearest neighbours interactions can be described using two different constants j_1 and j_2 . They correspond to the interaction of local mode components parallel and perpendicular to the link connecting sites i and j , respectively. The coefficients j_{3-5} describe the interactions between second nearest neighbours, while the two constants j_6 and j_7 corresponds to third nearest neighbours interactions. (After W. Zhong <i>et al.</i> [148])	56
2.7	The schematic representation of the supercells used in the frozen-phonon calculations. Calculating the energy for different atomic displacements corresponding to a certain distribution of local modes allows to obtain the estimates for the interaction coefficients j_{1-7} and the on-site coefficients κ, α, γ . (After W. Zhong <i>et al.</i> [148])	57
2.8	(a) Temperature dependence of the magnetoelectric coupling obtained from Monte Carlo simulations (blue circles) and mean-field calculations (solid red line). (b) Evolution of the antiferromagnetic order parameter and the magnetic susceptibility with temperature. (After M. Mostovoy <i>et al.</i> [116])	62
3.1	(a) Red arrows represent local radial electric fields produced in the case of a single A-site substitution. Blue spheres represent B-sites while Black and white spheres correspond to the A-sites of perovskite ABO_3 structure (b) Schematic representation of the unit cell of the superlattices used to estimate local fields magnitude. The black and white spheres represent A-sites of different type, while the blue spheres correspond to the B-sites, carrying the local mode vectors.	68
3.2	A-site $\{\sigma_i\}_A$ and B- site $\{\sigma_i\}_B$ first nearest neighbours environments of site i . Depicted in the middle is the union of the sets $\{\sigma_i\}_{A,B}$, along with the local mode center i and the schematic representation of the oxygen octahedron.	69
3.3	Schematic representation of the auxiliary electrostatic problem used to estimate the error made in the long-range interaction energy due to the employed effective medium approximation. The multilayer geometry is described by considering two layers (of materials A and B respectively) and identifying the top interface of layer B with the bottom interface of layer A , i.e. imposing periodic boundary conditions. The thickness of each layer is assumed to be equal to h and the origin of the z Cartesian axis coincides with the position of the interface (1).	71
3.4	Graphical representation of equation (3.22). The values of ε_1 and ε_2 are taken to be equal to those of $BaTiO_3$ and $BiFeO_3$ compounds respectively. The roots of the depicted function correspond to the eigenvalues of considered problem. Dashed blue curve corresponds to the dispersion equation of the effective medium.	73
3.5	Comparison of the first nonzero eigenvalues λ_1 and λ_2 defined by equations (3.18 , 3.19) and the corresponding λ_{eff} obtained from the effective medium approximation. One clearly sees the occurring splitting. The resulting deviation from the adopted solution is proportional to $(1 - (\varepsilon_1 + \varepsilon_2)/\sqrt{\varepsilon_1\varepsilon_2}) \approx 0.013$ in the case of $BiFeO_3$ - $BaTiO_3$ system. . . .	74

- 3.6 (a) Representation of BiFeO₃-BaTiO₃ (001) superlattice unit cell. ξ_x and ξ_z correspond to Γ_5 and Γ_1 modes eigenvectors. Displacements of Bi³⁺ described by ξ_x and ξ_z are considerably bigger compared to other cations (b) Energy differences with respect to reference structure with atoms situated in ideal cubic positions. The energy is first minimized with respect to unit cell volume then the atoms are shifted according to eigenvectors ξ_x and ξ_z (blue and red curves respectively). Solid black curve represents the energy obtained using constructed effective Hamiltonian approximation. (c) Due to the effect of local electric field, the ferroelectric instability is no longer present. Instead of a double well potential one observes an energy profile with a single stable minimum. 75
- 3.7 Calculated dependence of the absolute value of polarization on BiFeO₃ concentration. Shaded region delimits the interval between the minimum and maximum polarization values within the probed cation distributions. The inset shows calculated dependence of lattice constants on BiFeO₃ concentrations for BaTiO₃ rich compounds. Tetragonal distortion gradually reduces until the average lattice symmetry become cubic at the critical concentration x_c 77
- 3.8 Variation of the average local mode amplitude $q = \langle |\langle Z_i^* u_i \rangle| \rangle_i$ with concentration x . In the dilute solid solution limits ($x \rightarrow 0$ and $x \rightarrow 1$), the value of q decreases with increasing the doping phase content. This can be attributed to the weakening of ferroelectric order. In the intermediate range of concentrations the curve has a bell shape reaching its maximum at $x \approx 0.6$. In this limit, local modes are effectively decoupled and the nonzero average local mode amplitude is related to the presence of strong local fields forcing cations to shift from ideal cubic positions. 78
- 3.9 Bound charge density distribution $\delta n = -Z^* \nabla(\mathbf{u})$ in arbitrarily picked cross sections of the supercell for two characteristic compositions $x = 0.04$ and $x = 0.16$. The red areas correspond to positive bound charge appearing around negative defects, i.e., around Fe³⁺ ions substituting Ti⁴⁺. The dark blue regions indicate the areas with excess negative charge $\delta n < 0$, while the light blue color corresponds to $\delta n = 0$ or ferroelectric phase. Line traces represent the interpolated integral lines of the local modes vector field. 79
- 3.10 Calculated dependence on concentration of the configurationally averaged densities of topological defects corresponding to the local modes vector field (n_*) and the distribution of the local random fields n_{f*} . The blue triangular markers correspond to the the previously presented dependence of the configurationally averaged value of polarization. Lines are guide for the eye. 80
- 3.11 Dependence of the volumes of the biggest clusters on the BiFeO₃ concentration x . The black triangular markers correspond to the volume of the second biggest cluster of local modes, i.e. volume of the second biggest locally ordered region, averaged over 40 different disorder realisations. The blue, red and green markers represent the average volumes of the third, fourth and fifth biggest clusters, respectively. The inset shows the dependence of the configurational average of the dielectric susceptibility (in arbitrary units) on the concentration x . The lines represent guides to the eye. 81

- 3.12 Calculated temperature dependence of the ferroelectric order parameter for different concentrations (1) $x = 1.0$ (2) $x = 0.98$ (3) $x = 0.96$ (4) $x = 0.94$ (5) $x = 0.92$. Increasing concentration of the doping agent (in this case BaTiO_3) leads to decrease of the ferroelectric transition temperature. Moreover, one observes gradual smearing of the phase transition intrinsic to systems with quenched disorder [159]. Each of the curves corresponds to a single realization of A- and B- site disorder. 82
- 3.13 Dependence of the estimated Curie temperature on BiFeO_3 concentration x . The solid line represents a polynomial fit of the data, while the dashed line marks the temperature $T = 300\text{K}$ at which the phase diagram 3.7 has been calculated. 83
- 3.14 The temperature evolution of the average local mode components in the case of the three-dimensional checkerboard structure (denoted as $S_{(0,0)}$) schematically depicted in the inset figure, where the blue and white cubes represent the unit cell of BiFeO_3 and BaTiO_3 , respectively. It can be seen that the system undergoes a single ferroelectric phase transition, at $T_C \approx 795\text{K}$ 86
- 3.15 Temperature evolution of (a) the diagonal homogeneous strain tensor components and (b) the homogeneous strain tensor off-diagonal components in the case of $S_{0,0}$ supercell geometry. 87
- 3.16 Temperature evolution of the diagonal components of the (a) dielectric and (b) magnetic susceptibility tensors for $S_{0,0}$ lattice structure. Figure (b) indicates a presence of an antiferromagnetic phase transition at $T_N \approx 134\text{K}$ 88
- 3.17 The temperature evolution of the average local mode components in the case of the two-dimensional checkerboard structure (denoted as $S_{(1,1)}$) schematically depicted in the inset figure. As in the case of $S_{(0,0)}$ supercell structure, the blue and white cubes represent the unit cell of BiFeO_3 and BaTiO_3 respectively. The system undergoes two ferroelectric phase transitions, at $T_{C1} \approx 680\text{K}$ and $T_{C2} \approx 547\text{K}$ 89
- 3.18 Temperature dependence of (a) the diagonal homogeneous strain tensor components and (b) the homogeneous off-diagonal strain tensor components in the case of $S_{(1,1)}$ supercell geometry. The tetragonal symmetry of the paraelectric phase manifests in the different slopes of the temperature dependence of the η_{ii} variables above the first ferroelectric phase transition, or in other words in different thermal expansion coefficients. 90
- 3.19 Temperature evolution of the diagonal components of the (a) dielectric and (b) magnetic susceptibility tensors in the case of $S_{(1,1)}$ lattice structure. Figure (b) indicates the presence of an antiferromagnetic phase transition at $T_N \approx 262\text{K}$. Moreover, the cusp of the magnetic susceptibility components present at the ferroelectric transition temperature indicates a possible coupling of the magnetic and ferroelectric order parameters. 91
- 3.20 The temperature evolution of the average local mode components in the case of the superlattice structure (denoted as $S_{(2,2)}$) schematically depicted in the inset figure, where the blue and white cubes represent the unit cell of BiFeO_3 and BaTiO_3 , respectively. The system undergoes a single ferroelectric phase transition, at $T_C \approx 427\text{K}$ 92

3.21	Temperature dependence of (a) the diagonal homogeneous strain tensor components and (b) the homogeneous off-diagonal strain tensor components in the case of $S_{2,2}$ BiFeO ₃ /BaTiO ₃ superlattice. Again, as in the case of $S_{(1,1)}$ structure, the strain components above the ferroelectric phase transition split according to the tetragonal point-group symmetry of the unit cell of the structure.	92
3.22	Temperature evolution of the diagonal components of the (a) dielectric and (b) the magnetic susceptibility tensors in the case of $S_{(2,2)}$ lattice structure. Figure (b) indicates the presence of an antiferromagnetic phase transition at $T_N \approx 82$ K.	93
3.23	The temperature evolution of the average local mode components in the case of the $S_{(3,3)}$ structure. The system undergoes a single ferroelectric phase transition at $T_C \approx 574$ K from paraelectric to a monoclinic ferroelectric phase.	93
3.24	Temperature dependence of the of (a) the diagonal homogeneous strain tensor components and (b) the homogeneous off-diagonal strain tensor components in the case of $S_{(3,3)}$ supercell geometry.	94
3.25	Temperature evolution of the diagonal components of the (a) dielectric and (b) magnetic susceptibility tensors in the case of $S_{(3,3)}$ lattice structure. Figure (b) indicates the presence of an antiferromagnetic phase transition at $T_N \approx 277$ K.	95
3.26	The temperature evolution of the average local mode components in the case of the $S_{(2,3)}$ structure. The system undergoes a single ferroelectric phase transition at $T_C \approx 574$ K from paraelectric to a monoclinic r phase.	95
3.27	Temperature dependence of (a) the diagonal homogeneous strain tensor components and (b) the homogeneous off-diagonal strain tensor components in the case of $S_{(2,3)}$ supercell geometry.	96
3.28	Temperature evolution of the diagonal components of the dielectric susceptibility tensor components in the case of $S_{(2,3)}$ geometry.	96
3.29	The temperature evolution of the average local mode components in the case of the $S_{(3,2)}$ structure. The system undergoes a single ferroelectric phase transition at $T_C \approx 574$ K from paraelectric to monoclinic phase.	97
3.30	Temperature dependence of the of (a) the diagonal homogeneous strain tensor components and (b) the homogeneous off-diagonal strain tensor components in the case of $S_{3,2}$ supercell geometry.	97
3.31	Temperature evolution of the diagonal components of the dielectric susceptibility tensor components in the case of $S_{(3,2)}$ lattice structure.	98
3.32	Temperature evolution of the absolute value of average magnetization of the $S_{(3,2)}$ lattice structure.	98

- 3.33 Schematic representation of the considered $(\text{Ba}_x, \text{Sr}_{1-x})\text{TiO}_3$ superlattice structures. On the right: the fractal inclusions of BaTiO_3 in the matrix of SrTiO_3 . The shape of inclusions corresponds to the second iteration of the Menger sponge (three dimensional analogue of the Sierpinski carpet) construction algorithm. Yellow cubes correspond to the BaTiO_3 unit cells. The Ba^{2+} concentration is equal to $x \approx 0.19$. Throughout the text, the described structure is referred to as $F_{0.2}$. The inverse structure obtained by replacing BaTiO_3 unit cells by those of SrTiO_3 and vice versa allows to construct $F_{0.8}$ supercell. On the right: Spatially uniform distribution of Ba^{2+} and Sr^{2+} cations. Such structures will be denoted as $R_{0.2}$ and $R_{0.8}$ with the subscript indicating the Ba^{2+} concentration x 100
- 3.34 Average local mode components $\langle \langle u_{x,y,z} \rangle_i \rangle$ for different lattice structures (a) $R_{0.2}$, $(\text{Ba}_{0.19}, \text{Sr}_{0.81})\text{TiO}_3$ solid solution (b) $R_{0.8}$, $(\text{Ba}_{0.81}, \text{Sr}_{0.19})\text{TiO}_3$ solid solution (c) $F_{0.2}$, BaTiO_3 fractal inclusions in SrTiO_3 matrix (d) $F_{0.8}$, SrTiO_3 fractal inclusions in BaTiO_3 matrix. The errorbars indicate the standard deviation estimated from the performed Monte Carlo simulations using $\sim 10^5$ thermalization and averaging sweeps. 102
- 3.35 Dielectric susceptibilities of two fractal structures $\chi = (\sum_i \langle \chi_{ii} \rangle) / 3$ (a) average susceptibility of $F_{0.2}$ structure and (b) $aF_{0.8}$ structure. On both figures one observes two distinct peaks, corresponding to the entrance into the transient region and the stabilization of the system in a ferroelectric ground-state. All the observed peaks are diffuse. The dielectric response of bulk BaTiO_3 structure diluted with fractal SrTiO_3 (structure $F_{0.8}$) inclusions shows the dielectric response which is approximately one order of magnitude larger than that of the $(\text{Ba}_{0.81}, \text{Sr}_{0.19})\text{TiO}_3$ solid solution. 103
- 3.36 Upper and lower panels illustrate the comparison of the temperature dependence of the specific heat at fixed pressure for two different Ba^{2+} concentrations x . (a) $x \approx 0.19$. The red markers indicate the specific heat of the system composed of fractal BaTiO_3 inclusions in SrTiO_3 matrix ($F_{0.2}$), while the blue markers correspond to the specific heat computed for the solid solution system ($R_{0.2}$). (b) $x \approx 0.81$. The red markers correspond to the SrTiO_3 fractal inclusions in BaTiO_3 matrix, the blue markers represent the solid solution system ($R_{0.8}$). 104
- 3.37 Comparison of the temperature dependence of the average strain components exhibited by $F_{0.2}$ (black dashed curves) and $R_{0.2}$ (η_{ij} strain tensor components) structures. In the case of the fractal $F_{0.2}$ supercell geometry, the three diagonal η_{ii}^f (graph (a)) and three off-diagonal (graph (b)) strain components are equal in the entire probed temperature range. The results indicate the presence of a structural phase transition from the cubic to the rhombohedral ferroelectric phase. 105
- 3.38 Comparison of the temperature dependence of the average strain components exhibited by $R_{0.8}$ (graphs (a) and (b)) and $F_{0.8}$ (graphs (c) and (d)) structures. One can clearly observe three consecutive structural phase transitions in the case of the disordered $R_{0.8}$ structure. $F_{0.8}$ undergoes a phase transition from cubic to rhombohedral phase via the transient state indicated by unusually high fluctuations of the strain components. 106

4.1	Schematic depiction of a free-standing multilayer containing odd number of identical ferromagnetic layers and even number of identical ferroelectric layers. The multilayer is symmetric with respect to the central ferromagnetic slab. The thicknesses of ferroelectric and magnetic layers are denoted by t_f and t_m , respectively.	109
4.2	Probable lattice matching in FeGaB-BaTiO ₃ and FeGaB-PZT epitaxial systems. The crystallographic [100] direction of FeGaB lattice is parallel to the [110] direction of the prototypic cubic lattice of BaTiO ₃ or PZT, which reduces misfit strain in the heterostructure.	114
4.3	Phase diagrams of PZT 50/50 (a) and BaTiO ₃ (b) nanolayers interleaved by FeGaB slabs. The prototypic cubic phase of these nanolayers has the (001) crystallographic direction orthogonal to their surfaces. Two variants of the stability ranges of various possible phases delimited by red and blue curves correspond to the multilayers comprising Fe _{85.38} Ga _{14.6} B _{0.02} and Fe _{81.72} Ga _{18.2} B _{0.08} slabs respectively. The temperature equals 25°C.	115
4.4	Sensitivities $S_{3\alpha\beta}$ of the out-of-plane polarization P_3 to the misfit strains $u_{m\alpha\beta}$ calculated for PZT 50/50 nanolayers interleaved by Fe _{85.38} Ga _{14.6} B _{0.02} slabs at different values of the biaxial misfit strain u_m indicated on the plots.	116
4.5	Sensitivities $S_{3\alpha\beta}$ of the out-of-plane polarization P_3 to the misfit strains $u_{m\alpha\beta}$ calculated for BaTiO ₃ nanolayers interleaved by Fe _{85.38} Ga _{14.6} B _{0.02} slabs at different values of the biaxial misfit strain u_m indicated on the plots.	117
4.6	Out-of-plane permittivity ε_{33} of PZT 50/50 nanolayers interleaved by Fe _{85.38} Ga _{14.6} B _{0.02} slabs calculated at different values of the biaxial misfit strain u_m indicated on the plots.	117
4.7	Out-of-plane permittivity ε_{33} of BaTiO ₃ nanolayers interleaved by Fe _{85.38} Ga _{14.6} B _{0.02} slabs calculated at different values of the biaxial misfit strain u_m indicated on the plots.	118
4.8	Longitudinal magnetostrictive deformation ν_{\parallel} of crystalline (Fe ₈₁ Ga ₁₉) _{1-x} B _x alloys with $x = 3\%$ and 6% [200]. Linear fit in the vicinity of inflection point allows to estimate maximal piezomagnetic coefficient $d_{\parallel}^m = \partial\nu_{\parallel}^{ms}/\partial H$	119
4.9	Electrical configuration maximizing the output charge signal of a ferroelectric-ferromagnetic multilayer.	121
4.10	Magnetic field sensitivity $\partial V/\partial H_1$ of the output voltage signal generated by the multilayer comprising PZT 50/50 nanolayers interleaved by Fe _{85.38} Ga _{14.6} B _{0.02} slabs calculated at different values of the biaxial misfit strain u_m indicated on the plots.	123
4.11	Magnetic field sensitivity $\partial V/\partial H_1$ of the output voltage signal generated by the multilayer comprising BaTiO ₃ nanolayers interleaved by Fe _{85.38} Ga _{14.6} B _{0.02} slabs calculated at different values of the biaxial misfit strain u_m indicated on the plots.	124

This page is intentionally left blank

Introduction

Multiferroic materials represent a growing family of compounds owing undeniable importance for both fundamental physics and state-of-the-art technological applications. The main characteristic of these materials, namely the coexistence of several types of ferroic orders, leads to a possibility of establishing coupling between different order parameters. Of the most celebrated examples of this phenomena are direct and inverse magnetoelectric (ME) effects, where the coupling between polarization and magnetization engenders a nonzero response of either macroscopic polarization to an external magnetic field or inversely magnetization to an applied electric field. This makes multiferroic materials potential candidates for building a variety of electronic and spintronic devices including magnetoelectric recording read heads [169], electrostatically tunable microwave devices [170], electric-write magnetoresistive memories [171, 172], and energy-harvesting devices [173].

Since the theoretical prediction of the ME effect by L. Landau [1] and the pioneering experimental measurements of linear magnetoelectric coefficients of Cr_2O_3 [2, 3] compounds, a variety of single-phase multiferroics have been discovered, however none of those known to date materials exhibit strong enough ME coupling as necessitated for practical applications. The requirement of coexistence of ferroelectricity and magnetism in a chemically homogeneous (single-phase) compound not only puts specific symmetry constraints on the crystalline structure of the material [5, 6], but also constrains the maximum value of the linear magnetoelectric response, thereby making the chase for single-phase magnetoelectric compounds all the more intricate [4]. In this context, the artificial design of multi-phase or composite materials appears to be the fastest shortcut to the desired goal. Specifically, ferroelectric-ferromagnetic nanocomposites and nanoscale heterostructures may exhibit strong magnetoelectric effects greatly exceeding those of single-phase magnetoelectrics due to the interfacial coupling between two ferroic order parameters [163]. For these materials, the coexistence of ferroic orders is simply satisfied via the coexistence of ferromagnetic and ferroelectric materials, while the coupling between the order parameters is mediated through the interface between chemically homogeneous regions. Moreover, artificially designing the material

also allows to locally tailor the symmetry of the structure, thereby permitting various interface interactions or couplings. Examples of the coupling mechanisms include the mechanical interaction, which enables transmission of strains across interfaces [164], spin-dependent screening of surface polarization charges [165, 166], and modifications of interfacial bonds [167]. Evidently, the role of interface-related and proximity effects increases drastically in nanoscale multiferroic heterostructures, that are especially suitable for microelectronics.

The design and optimization of properties of such nanostructured materials not only require a thorough understanding of the coupling mechanisms and physics of the interfaces, but also demand some insight into how the properties of phase transitions change with respect to geometrical characteristics of the system, such as its dimension and connectivity, as well as into understanding finite size effects. On that account, the practical material design problem rises the fundamental question as to how does the system's underlying geometry affects its physical properties, i.e., the question of establishing structure-properties relations.

The challenge related to the design of multiferroic nanostructured materials is twofold:

- 1.) Despite the technological promise of nanostructured multiferroic composites, very little is currently known about these structures. This lack of knowledge is related to the absence of efficient numerical and analytical tools able to mimic such complex nanosystems.
- 2.) The structural complexity of nanocomposites makes the modeling of such multiferroic systems an extremely challenging problem from the computational point of view.

Consequently, the main goal of this study is

To develop efficient analytical and computational tools for modeling and designing multiferroic nanocomposite materials.

The manuscript is organized in the following way. First two chapters contain an introduction to the background of the problem and a description of the numerical tools used as a framework for this work. Specifically, in the first chapter we discuss some aspects related to the physics of multiferroic materials as well as to the magnetoelectric effect. Additionally, the first chapter is meant to introduce the language essential to the description of the geometry of nanocomposite systems. We therein also give a description of some reported properties of the materials that are used in this work as model systems.

The second chapter consists in the description of the methods adopted to study multiferroic materials at different scales. It is conceptually divided into two parts. In the first part, we present a short introduction to the *density functional theory*, the cornerstone of modern computational chemistry. The second part is devoted to the description of the so-called second-principles methods, namely the *effective Hamiltonian models*, for predicting finite-temperature properties of multiferroic materials. The description of the effective Hamiltonian approach is complemented by a discussion of the effects of structural heterogeneity on the properties of the system within the context of lattice models. We mainly consider the effect of structural disorder manifested by the onset of random local fields, and explore the concept of the lower critical dimension in the presence of random field quenched disorder. We also examine the role of topological defects in weakening/modifying the ground-state properties of the system.

The last two chapters contain the main methodological developments and theoretical predictions obtained in the course of this work. Although enriched and complemented by the presentation of the theoretical background given in the first two chapters, both chapter 3 and 4 are meant to be sufficiently independent and self-standing.

Chapter 3 is devoted to the discussion of a specific modification of the effective Hamiltonian method, commonly used to predict finite-temperature properties of perovskite compounds [148, 146]. The validity of the introduced approximations is assessed by applying the constructed model to study finite-temperature properties of $(\text{BiFeO}_3)(\text{BaTiO}_3)$ solid solutions and nanocomposite structures.

Finally, the last chapter represents a study of the properties of piezoelectric/piezomagnetic epitaxial heterostructures, namely $\text{BaTiO}_3/\text{FeGaB}$ and $\text{Pb}(\text{Zr}_{0.5}\text{Ti}_{0.5})\text{O}_3/\text{FeGaB}$ freestanding multilayers, using Ginzburg-Landau theory of phase transitions. In this chapter, we present the predicted room-temperature phase diagrams of these structures depending on their composition along with dielectric and magnetoelectric properties.

Chapter 1

Muliferroic Nanocomposites

Initially, the term *multiferroic* was used to describe the class of “*single-phase materials that possess two or all three of the ferroic properties (ferroelectricity, ferromagnetism, and ferroelasticity)*”. However, nowadays this definition has been significantly broadened and refers to systems possessing coexisting long-range orders of any nature, or equivalently, described by several order parameters. As an example, one might refer to bismuth ferrite or BiFeO_3 , undergoing both ferroelectric and magnetic phase transitions and whose equilibrium magnetic state at low temperatures can be described as G -type antiferromagnetism modulated with superimposed cycloid spin structure. Naturally, in order to understand the physics of multiferroic systems, it is essential to have a solid knowledge about fundamental properties of both ferroelectric and magnetic systems. This chapter contains some fundamental definitions and concepts which will introduce the reader to the subject of the thesis. Moreover, since the subject of the current work is related to spatially heterogeneous systems, this introductory chapter will also provide the necessary terminology and mathematical tools essential to the geometrical description of nanocomposite systems. Finally, concluding the introduction, we will provide a brief summary of recent experimental advances in the field.

1.1 Ferroelectric and Magnetic materials

Ferroelectric materials exhibit spontaneous polarization below a certain temperature, that can be reverted (switched) by an applied external electric field. Since the appearance of macroscopic polarization \mathbf{P} is associated with collective polar displacements of the ions (see Fig. 1.1), the transition temperature is marked by the change of the

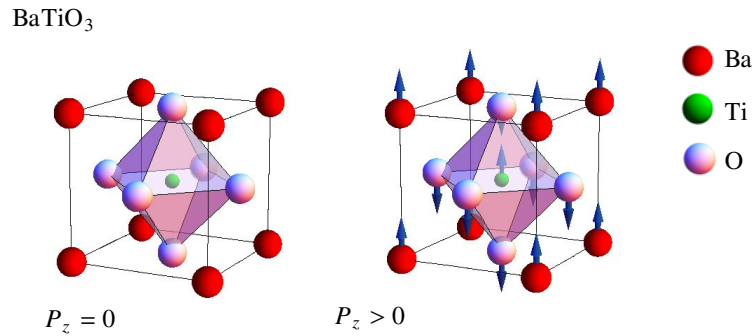


FIGURE 1.1: Schematic illustration of the collective polar displacements of the ions. On the left image, the ions of the unit cell of perovskite BaTiO₃ compounds are situated in high symmetry cubic positions. On the right: displacement of the ions leads to the appearance of a nonzero polarization component P_z . This situation corresponds to the room-temperature tetragonal phase of BaTiO₃.

space-group describing the symmetry of the crystal. Similar *symmetry-breaking* occurs in the case of ferromagnetic phase transition. However, in this latter case, the non zero macroscopic magnetization \mathbf{M} appearing at the transition temperature breaks the time reversal symmetry of the system. On the macroscopic level, the aforementioned conceptual similarity between ferromagnetic and ferroelectric systems can be described using the Landau theory of phase transitions, within which both \mathbf{M} and \mathbf{P} are seen as *order parameters* describing the “degree” of symmetry breaking. The structure of this theory can be conveniently exemplified by a system with a single component (scalar) order parameter ξ . The simplicity of this case can be naturally ascribed to the only possible high-temperature symmetry described by the 2 element cyclic permutations group $\mathbb{Z}_2 = \{E, I\}$. In the case of ferroelectric and ferromagnetic phase transitions, the only nontrivial element I of this group represents the spatial inversion operation and the operation of time reversal, respectively. Above the phase transition temperature, the properties of the system are assumed to be invariant under the action of the elements of \mathbb{Z}_2 , specifically under the inversion $I \xi \rightarrow -\xi$. Therefore, the high temperature equilibrium state corresponds to $\xi = 0$ while the nonequilibrium free energy describing thermal fluctuations of the order parameter can be represented as a Taylor expansion in powers of ξ :

$$\mathcal{F}(\xi) = \alpha\xi^2 + \beta\xi^4 + O(\xi^6) \quad (1.1)$$

Within this model, the symmetry breaking occurs when the sign of the quadratic coefficient α is reversed. Indeed, as it can be seen from the Fig. 1.2, the symmetric phase is associated with $\alpha > 0$, whereas for $\alpha < 0$, the double-well shape of the thermodynamic potential indicates the existence of two equivalent equilibrium states related by the inversion operation symmetry. It can be easily seen that the simple model of symmetry

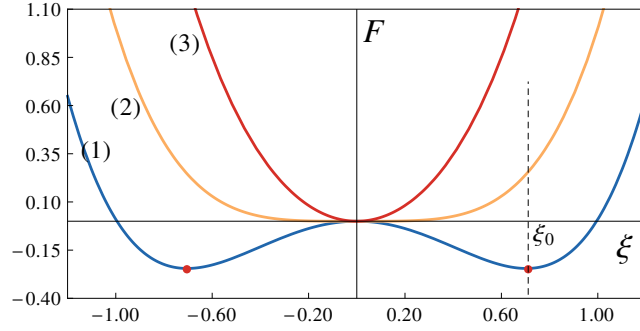


FIGURE 1.2: Schematic illustration of the nonequilibrium free energy describing thermal fluctuations of the order parameter ξ at different temperatures. (1) At low temperature the \mathbb{Z}_2 symmetry is broken. The symmetric double-well shape of the thermodynamic potential indicates the existence of two equivalent equilibrium states, related to each other via the inversion operation I . (2) At the phase transition temperature, the quadratic coefficient becomes equal to zero, whereas above T_c (3) $\alpha > 0$ and $\xi_0 = 0$.

breaking described by eq. (1.1) also captures the reversal of the equilibrium state under an applied external field linearly coupled to the order parameter. In this latter case, the free energy becomes $\mathcal{F}(\xi, \mathcal{E}) = \mathcal{F}(\xi) - \xi\mathcal{E}$, and the corresponding dependence of the $\xi_0(\mathcal{E})$ on the applied field at different temperatures is shown in Fig. 1.3. For real systems, the form of the expansion given by eq. (1.1) is more complicated since it has to be performed for the three-component order parameters. Also, by including higher order terms, one might adjust the theory so as to capture the behaviour of the systems exhibiting several consequent ferroelectric or magnetic phase transitions. However, on the other hand, Landau theory suffers from several considerable drawbacks among which one can list the neglected effects of the spatial fluctuations of the order parameter field as well as the phenomenological nature of the theory.

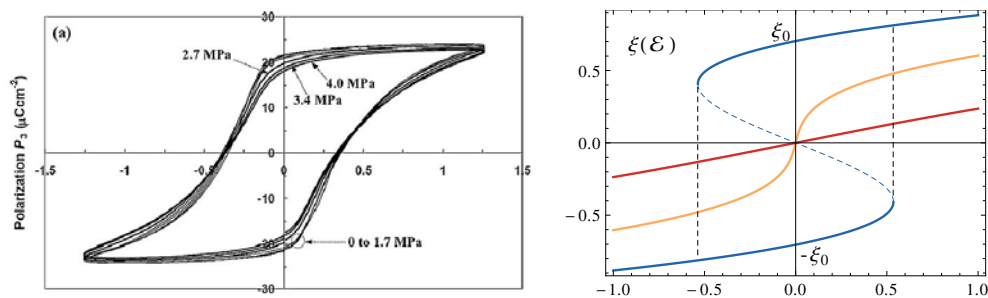


FIGURE 1.3: On the left: Experimentally observed ferroelectric hysteresis loop $P(\mathcal{E})$ exhibited by the samples of single-crystal BaTiO_3 (after [7]). On the right: Dependence of equilibrium order parameter magnitude $\xi(\mathcal{E})$ on the value of the external field with the model (eq. (1.1)). Different colors correspond to different temperatures, in accordance with those used in Fig. 1.2

Indeed, there is no universal way to estimate the values of the coefficients appearing in the expansion, and one is often led to resort to experimentally obtained values. Therefore, the symmetry-based approach illustrated above provides a universal description

of the symmetry breaking phenomena on the macroscopic scale while overlooking its microscopic origin.

Despite the conceptual similarity between ferroelectric and ferromagnetic phase transitions, the difference in the microscopic origin of these phenomena can often be mutually exclusive, resulting in a relative rarity of single-phase multiferroic compounds. Stemming from a revival of interest in multiferroic and magnetoelectric materials, a lot of attention has been devoted to answering the question pertaining to the rarity of multiferroic compounds in nature (see for instance [8], [9] and references therein). Indeed, only a small fraction of ferroelectric materials having perovskite structure exhibits magnetically ordered phases. However, it seems that the answer to this question cannot be put in terms of a theorem [10], but rather represents a matter of numbers. For instance, among the restrictions required by the coexistence of ferromagnetic and ferroelectric orders, one can enlist considerations related to *symmetry*, *electronic properties*, and the so-called “*d⁰-ness*” problem. The first two are fundamental and in reality do not explain the scarcity of multiferroic compounds. For instance, as we have seen before, the primary requirement for the existence of ferroelectricity is the possibility of the distortion of the high-symmetry phase removing the center of inversion from the symmetry elements of the structure. Similarly, taking into account the magnetic symmetry, it can be shown that among 122 Shubnikov point groups, only thirteen allow for the coexistence of ferromagnetic and ferroelectric orders. However, taking into account magnetic orders different from ferromagnetism, this list can be extended. The second restriction, namely that relying on the *electronic properties* simply refers to the fact that ferroelectric materials are naturally required to be insulators in order to exhibit polarization, whereas a wide range of ferromagnets are metallic. Although this restriction greatly reduces the number of compounds of interest, it remains non strictly exclusive, since some magnetic compounds are actually either insulators or semiconductors. The last point which we will briefly mention here is the “*d⁰-ness*”, which is also sometimes referred to as “*d⁰ vs dⁿ problem*”. Specifically, whereas for magnetism it is required to have partially filled *d* shells, a majority of the ferroelectric perovskite compounds contain transition metal ions with empty *d* shell, as Ti⁴⁺, Ta⁵⁺, W⁶⁺... Ferroelectricity in such compounds stems from the ability of the transition metal cation to form a strong covalent bond with one or three oxygen ions using the empty *d* states. The presence of the *d* electrons of *d* transition metals thus suppresses this mechanism of ferroelectricity in magnetic perovskites. One of the possible ways to overcome this problem is to make a “mixed” perovskite structure, i.e. a solid solution, comprising transition metal cations with both partially filled and empty *d* shells (see Fig. 1.4). This approach represents a step towards spatially heterogeneous compounds or nanocomposites. Another way is to involve other mechanisms driving ferroelectric phase transitions. For example, in single-phase multiferroic

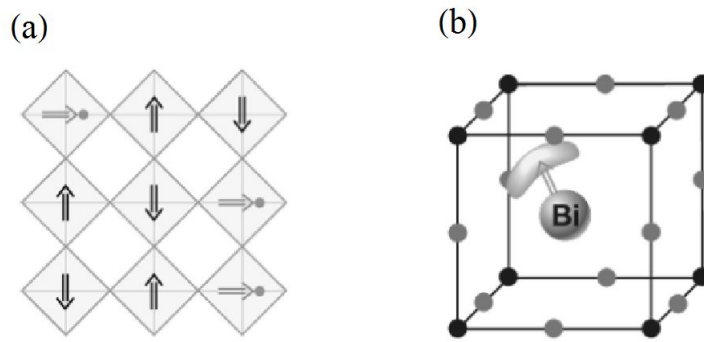


FIGURE 1.4: (a) Schematic representation of mixed perovskite structure. Gray arrows represent local dipole moments, while black arrows correspond to magnetic moments. Multiferroicity is achieved by combining transition metal ions with empty and partially filled d shells in a single structure. (b) Schematic representation of polarization appearing due to ordering of lone pairs associated with $6s$ outer electrons of Bi^{3+} cations. (After D. I. Khomskii [10])

BiFeO_3 , the ferroelectric polarization appears due to the dangling bonds, also called *lone pairs*, associated with two outer $6s$ electrons of the Bi^{3+} cation (see Fig. 1.4). The ordering of these lone pairs in a specific direction (with a certain admixture of p orbitals) leads to the nonzero net polarization [10].

1.2 Magnetolectric effect

Magnetolectric coupling may exist whatever the nature of magnetic and electrical order parameters, and can for example occur in paramagnetic ferroelectrics [11] (see Fig. 1.5). However, as it will be discussed later, in order to exhibit magnetolectric effect that would be relevant for practical applications it is necessary for the compound to possess both high dielectric permittivity and magnetic permeability.

This makes single-phase multiferroics a promising class of materials, within which the compounds are expected to exhibit strong magnetolectric coupling. Unfortunately, a close examination often reveals limitations in the sought properties. Indeed, in general, one can divide single-phase multiferroics into two classes [10], namely, compounds for which ferroelectricity and magnetism have different microscopic origins, and compounds where ferroelectricity is improperly caused by magnetism [12, 13]. In the case of the first class, the magnetolectric coupling is usually rather small, as in BiFeO_3 . Generally, for this class of compounds, the temperature of the ferroelectric transition exceeds that of the magnetic one, and the remnant polarization is often large ($P \approx 10\text{--}100 \mu\text{C}/\text{cm}^2$). In the case of magnetically triggered ferroelectricity, one expects the antagonistic situation: a large microscopic coupling between magnetic and ferroelectric order parameters, yet a

small absolute value of polarization, naturally reducing the macroscopic magnetoelectric response. These considerations moderate the expectations related to single-phase mul-

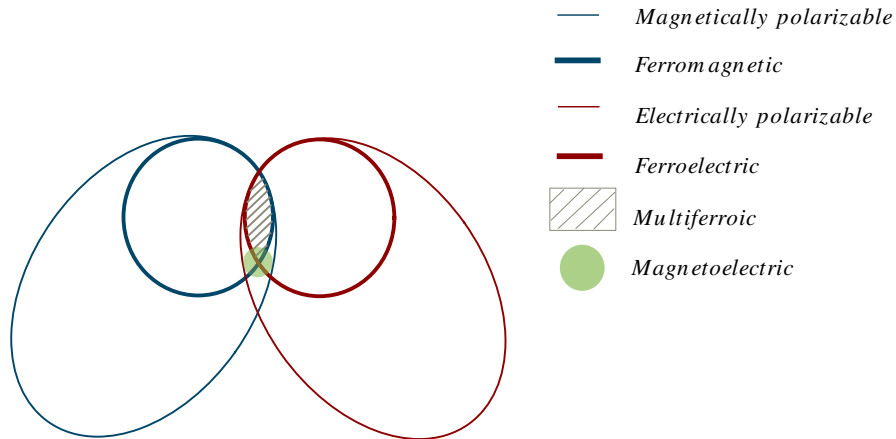


FIGURE 1.5: Schematic representation of the relationship between multiferroic and magnetoelectric materials, indicating their noncomplete overlap. Ferromagnets (ferroelectrics) form a subset of magnetically (electrically) polarizable materials such as paramagnets and antiferromagnets (paraelectrics and antiferroelectrics). The intersection (gray hatching) represents materials that are multiferroic. Magnetoelectric coupling (green) is an independent phenomenon that can, but need not, arise in any of the materials that are both magnetically and electrically polarizable. In practice, it is likely to arise in all such materials, either directly or via strain. (Adapted from D. I. Khomskii [10])

tiferroics. In order to better understand the origin of the aforementioned limitations, it is beneficial to follow the derivation of the famous upper bound inequality [14] restricting the magnetoelectric response of single-phase compounds.

1.2.1 Single-phase multiferroics

First let's consider an equilibrium thermodynamical approach to describe magnetoelectric coupling in single-phase compounds. Assuming that the applied external electric and magnetic fields are small, causing a small change of the free energy of the system [15] one can write

$$F = F_0 - \left(\frac{1}{2} \varepsilon_{ij} E_i E_j + \frac{1}{2} \chi_{ij} H_i H_j + \alpha_{ij} E_i H_j \right) - \frac{1}{2} \beta_{ijk} E_i H_j H_k - \frac{1}{2} \gamma_{ijk} H_i E_j E_k, \quad (1.2)$$

where F_0 represents the free energy of the system in the absence of applied external fields, E_α and H_α denote the cartesian components of electric and magnetic fields, while the coefficients of the expansion $\varepsilon_{ij}, \chi_{ij}, \alpha_{ij}$ represent the components of the dielectric, magnetic and magnetoelectric susceptibility tensors respectively. The expansion is truncated at first nonlinear magnetoelectric terms defined by the tensors γ_{ijk} and β_{ijk} . From the

expression given in eq. (1.2) one immediately obtains the equations of state describing the equilibrium components of polarization P_i and magnetization M_i

$$P_i = \varepsilon_{ij}E_j + \alpha_{ij}H_j + \frac{1}{2}\beta_{ijk}H_jH_k + \gamma_{ijk}E_jH_k \quad (1.3)$$

$$P_i = \chi_{ij}H_j + \alpha_{ji}E_j + \frac{1}{2}\gamma_{ijk}E_jE_k + \beta_{ijk}E_jH_k \quad (1.4)$$

These expressions make explicit the physical meaning of the introduced tensors. Moreover, neglecting the nonlinear contributions, from eq. (1.2) it immediately follows that there is an upper bound for the components of the magnetoelectric tensor. Specifically, the stability of the system with respect to applied fields requires the bilinear form defined by the tensors ε_{ij} , χ_{ij} and α_{ij} to be positive definite. Latter leads to the condition of positive sign of the determinant

$$\begin{vmatrix} \hat{\varepsilon} & \hat{\alpha} \\ \hat{\alpha} & \hat{\chi} \end{vmatrix} > 0 \quad (1.5)$$

where the hat indicates that the tensor is taken in the matrix form. In the specific case of isotropic medium this condition reduces to the widely known formula $\alpha^2 < \varepsilon\chi$ [16], giving a thermodynamic estimate for the upper bound of the magnitude of magnetoelectric coefficient. Similar estimate [14] can be obtained considering the thermodynamic perturbation theory [17]. Specifically, considering the perturbation of the electron many-body hamiltonian of the form

$$V = \sum \left(\frac{e}{mc} \mathbf{p} \mathbf{A} + \frac{e^2}{2mc^2} A^2 - e\phi - \boldsymbol{\mu}_s \nabla \times \mathbf{A} \right) \quad (1.6)$$

resembling the spin dependent terms in the single electron Pauli equation, Brown, Hornreich and Shtrikman [14] have derived similar theoretical supremum value for α_{ij} . In the above formula, the applied magnetic and electric fields appear in the form of electrostatic and vector potentials ϕ and \mathbf{A} , \mathbf{p} denotes the momentum of the electron while $\boldsymbol{\mu}_s$ stands for electron spin magnetic moment operator. The summation goes over all electrons in the system and the electrostatic Coulomb gauge fixing is assumed. Assuming constant external magnetic and electric field it is therefore straightforward to express perturbation V in the following form

$$V = a^i H_i + b^i E_i + \frac{1}{2} d^i H_i^2 \quad (1.7)$$

where the operators a^i , b^i and d^i are algebraic functions of the operators of orbital and spin magnetic moment of the electron and the position operator r . Calculating the corresponding corrections to the free energy of the crystal and imposing the condition

similar to eq. (1.5), again leads to the estimate

$$\alpha_{ij} < (\mu_{ii}\varepsilon_{jj})^{1/2}. \quad (1.8)$$

Despite the generality of the estimate obtained in [14], it is important to recall the utilized approximation which allowed to treat the problem analytically, especially since it seems that eq. (1.8) have caused a considerable confusion in the field. Specifically, in eq. (1.7) the cross terms of the form $c^{ij}H_iE_j$ were neglected, since they arise as a contribution from the spin-orbit coupling of the order $(v/c)^2$. In the presence of such terms the estimate given in eq. (1.8) does not hold since the matrix elements of c^{ij} operators can give either positive or negative contributions to α_{ij} and therefore should be calculated explicitly. On the other hand, in [14] authors have demonstrated that compared to terms appearing in eq. (1.6) which are of the order zero in (v/c) this contribution can be neglected. However, the lattice contributions that can give rise to cross terms $c^{ij}H_iE_j$ have not been discussed. It is also important to mention that the tensor μ in eq. (1.8) corresponds to the paramagnetic susceptibility of the material. Latter fact is not surprising, since the single-particle Pauli Hamiltonian (eq. (1.6)) does not describe strong exchange interactions of the electrons leading to ferromagnetic or antiferromagnetic ground states. Similar critic applies to the equilibrium thermodynamic formulation (eq. (1.2)).

In order to illustrate the connection of linear magnetoelectric coefficients α_{ij} to electric and magnetic susceptibilities one might consider the work of George T. Rado [18, 19], where the author has proposed a simple phenomenological model explaining the temperature-dependent magnetoelectric effect exhibited by Cr_2O_3 compound. This strikingly simple and therefore illuminating model has also suggested a microscopic mechanism explaining the observed phenomena. Specifically, Rado has proposed that the effect of applied external electric field can be translated in terms of the fictitious magnetic field h inducing the nonzero average magnetization δM in antiferromagnetic compound. Due to linearity of the magnetoelectric response one can suggest that $h \sim E$ and therefore the parallel and transverse magnetoelectric susceptibilities (denoted by α_{\parallel} and α_{\perp}) can be written in the form [18]

$$\alpha_{\parallel,\perp} \sim \delta M/E = \chi_{\parallel,\perp} h/E = \chi_{\parallel,\perp} A \quad (1.9)$$

where we have introduced the coefficient of proportionality A , so that $h = AE$. Moreover, since the magnetoelectric effect vanishes in the paramagnetic state one can exclude the leading dependence of A on temperature by stating proportionality to average magnetization of the system $A = a_{\parallel,\perp} \langle M \rangle$. Therefore, $\alpha_{\parallel,\perp} = a_{\parallel,\perp} \chi_{\parallel,\perp} \langle M \rangle$. Using this

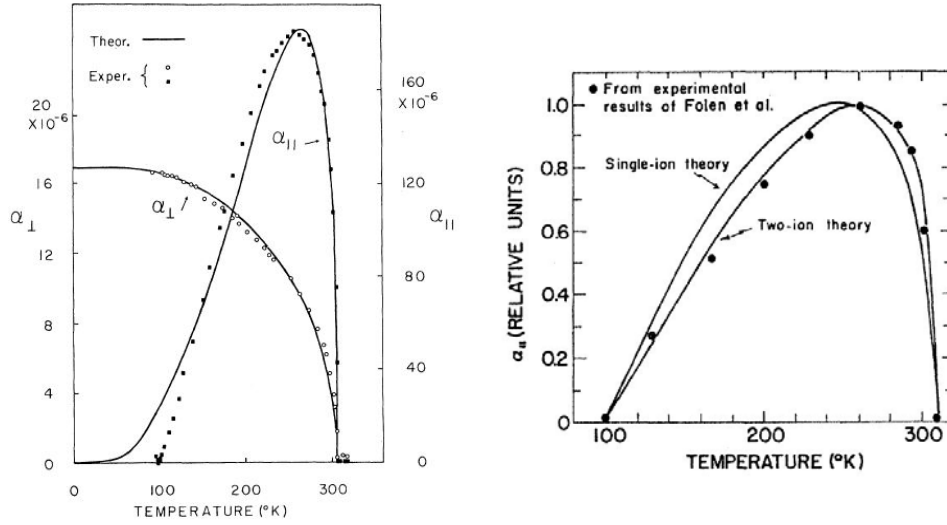


FIGURE 1.6: On the left: Temperature dependence of parallel and transverse magneto-electric susceptibilities (α_{\parallel} and α_{\perp} respectively) of Cr_2O_3 estimated from phenomenological theory of G. T. Rado [18, 19]. Temperature dependence is described as a product of magnetic susceptibility and average magnetization. (After G. T. Rado [18]). On the right: Parallel magneto-electric susceptibility versus temperature for Cr_2O_3 computed using single-ion and two-ion theories. The single-ion theoretical curve involves the spin-orbit and g -factor mechanisms, while the two-ion theory compiled is based on the antisymmetric exchange induced by the applied electric field. (After R. Hornreich *et al.* [20])

formula it is easy to estimate the temperature dependence of magneto-electric susceptibility. In the mean field approximation, the resulting dependencies are presented in Fig. 1.6. It can be seen, that despite the simplicity of the proposed phenomenological theory the predicted temperature dependence resembles strikingly well the experimental results. It was proposed that for the case of Cr_2O_3 the microscopic origin of the effective magnetic field h induced by applied electric field stems from the modification of the spin-orbit coupling energy of the electrons. This effect is referred to as the “single-ion anisotropy” mechanism. It describes the systems comprised of transition metal ions whose ground state in the total crystalline field is an orbital singlet, energetically well separated from the first excited orbital state. The coefficients $a_{\parallel,\perp}$ are proportional [19] to the following matrix elements

$$a_{\parallel} \sim \langle i|z|j\rangle \langle j|z|k\rangle \langle k|L_z|l\rangle \langle l|L_z|i\rangle \quad (1.10)$$

$$a_{\perp} \sim \langle i|z|j\rangle \langle j|x|k\rangle \langle k|L_z|l\rangle \langle l|L_x|i\rangle \quad (1.11)$$

stemming from the spin orbit coupling term ($L_{x,z}$ denote the cartesian components of the orbital momentum operator).

The works [18, 19] have inspired the theoretical investigations of the microscopic mechanisms of magneto-electric effect guided by the idea that magneto-electric interactions

can be generally ascribed to a certain modification of the parameters of spin-dependent terms of the Hamiltonian by the external electric field. For instance, different models have been developed in order to describe the modifications of the two-ion exchange [21], the g -factor term [22] and Dzyaloshinskii “ D -term” [20, 23] arising from the anisotropic exchange between ions.

One of the possible mechanisms leading to modification of aforementioned parameters of the spin Hamiltonian is the combined action of piezoelectricity and piezomagnetism [24, 25]. The idea behind it can be conveniently illustrated using the thermodynamic approach. Considering ferromagnetic phase transition in a ferroelectric material, the contributions to F of particular interest can be written in the following form

$$\Delta F = -\alpha_{ijk}M_iH_jE_k - d_{ijk}E_j\sigma_{jk} - q_{ijkm}M_iH_j\sigma_{km} - \frac{1}{2}s_{ijkm}\sigma_{ij}\sigma_{km}. \quad (1.12)$$

which contains the linear ME term α_{ijk} , a piezoelectric term, magnetostriction and the contribution due to the elastic deformations of the crystal. Specifically, d_{ijk} , q_{ijkm} and s_{ijkm} denote respectively the piezoelectric, magnetostriction and elastic compliance coefficients while σ_{ij} represent the components of the stress tensor. Then, equations of state are given by

$$P_i = \alpha_{jki}M_jH_k + d_{ijk}\sigma_{jk} \quad (1.13)$$

$$\eta_{ij} = d_{kij}E_k + q_{lmij}M_lH_m + s_{lmij}\sigma_{lm} \quad (1.14)$$

Assuming $\hat{\eta} = 0$, i.e. condition of the zero strain, and resolving the stress components yields

$$P_y^H = \alpha_{kky}^* M_k^2 |H| \quad (1.15)$$

for the part of P_y , which is proportional to H . In the above, for simplicity we have assumed that $\mathbf{H} \parallel \mathbf{M}$ and that the only nonvanishing component of the electric fields is E_y . The coefficient α^* represents the magnetoelectric susceptibility at zero strain, or in another words it would correspond to a quantum mechanical calculation based on an assumption of rigid lattice. One can similarly show that the magnetoelectric susceptibility α calculated at zero stress, corresponding to the case of experimental measurement setup is related to α^* by the following relation $\alpha_{kky} = \alpha_{kky}^* - \Delta\alpha_{kky}$, where the difference $\Delta\alpha_{kky}$ represents the lattice mediated magnetoelectric effect which is proportional to $\Delta\alpha \sim pd/s$ and is therefore not restricted by eq. (1.8). Evidently, in order to increase this contribution to ME effect it is necessary to have a material exhibiting both considerable piezoelectric and piezomagnetic effects. Latter can be achieved by making a composite material comprising piezomagnetic and piezoelectric phases.

1.2.2 Magnetolectric composites

Magnetolectric effect in composite materials comprising piezomagnetic and piezoelectric phases mentioned in the previous section can be schematically represented by the following formula

$$\text{ME} = \frac{\text{polarization}}{\text{strain}} \times \frac{\text{strain}}{\text{magnetic field}}$$

explicitly stating that in such materials the arising coupling is a product composite property [26]. The coupling between ferroic orders in this case is indirect and is mediated by the strain. Moreover, such composite compounds exhibit linear magnetolectric response even if the constituent phases are not magnetolectric.

The simplest, yet rigorous, theoretical description of strain mediated magnetolectric effect in composite materials with mesoscopic characteristic structural scale can be obtained using different homogenization techniques [27]. Using this approach Ce-Wen Nan [28] has obtained a reliable estimates for static magnetolectric effect exhibited by piezoelectric-piezomagnetic ceramics with various structure geometries. In order to better understand the limitations of this approach, we will briefly outline the main approximations employed. Following [28] one can write the constituent equations describing equilibrium state of the magnetolectric composite as

$$\begin{aligned} \hat{\sigma} &= \hat{C}\hat{\eta} - \hat{d}^{-1}\mathbf{E} - \hat{q}^{-1}\mathbf{H} \\ \mathbf{D} &= \hat{d}\hat{\eta} + \hat{\varepsilon}\mathbf{E} + \hat{\alpha}\mathbf{H} \\ \mathbf{B} &= \hat{q}\hat{\eta} + \hat{\alpha}^{-1}\mathbf{E} + \hat{\mu}\mathbf{H} \end{aligned} \quad (1.16)$$

where the variables $\hat{\sigma}, \hat{\eta}, \hat{C}, \hat{d}, \hat{q}$ denote the stress, strain tensors and elastic, piezoelectric and piezomagnetic coefficients tensors respectively. For the inhomogeneous system these equations hold locally at any given spatial point \mathbf{x} . The goal of the homogenization procedure is to obtain the properties of the effective medium that would describe the spatially averaged response of the real material. Specifically, introducing the volume averaging procedure $\langle A \rangle = (1/V) \int d^3x A(x)$ and rewriting eq. (1.16) one obtains the set of equations defining the effective medium properties

$$\begin{pmatrix} \langle \hat{\sigma} \rangle \\ \langle \mathbf{D} \rangle \\ \langle \mathbf{B} \rangle \end{pmatrix} = \begin{pmatrix} \hat{C}_* & -\hat{d}_*^{-1} & -\hat{q}_*^{-1} \\ \hat{d}_* & \hat{\varepsilon}_* & \hat{\alpha}_* \\ \hat{q}_* & \hat{\alpha}_*^{-1} & \hat{\mu}_* \end{pmatrix} \begin{pmatrix} \langle \hat{\eta} \rangle \\ \langle \mathbf{E} \rangle \\ \langle \mathbf{H} \rangle \end{pmatrix} \quad (1.17)$$

where star suffices indicate that the property corresponds to the effective medium. Therefore the problem mainly consists in finding the average values of the fields $\hat{\sigma}, \hat{\eta}, \mathbf{E}$,

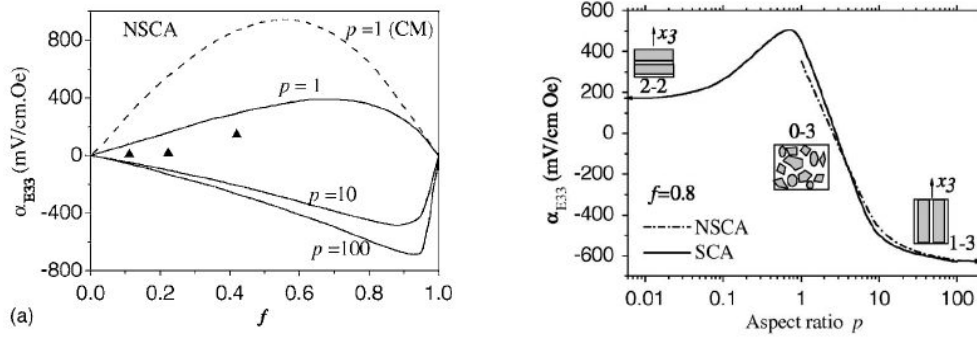


FIGURE 1.7: On the left: Dependence of the voltage magneto-electric coefficient on the volume fraction of the piezomagnetic phase. The geometry of the composite structure can be described as piezoelectric pillars embedded in the piezomagnetic matrix. Parameter p denotes the aspect ratio of the pillars. On the right: changing the composite geometry leads to a significant modification of the magneto-electric coefficients. (After C.-W. Nan *et al.* [32])

e.t.c. under specified boundary conditions or equivalently of solving the system of linear integral equations. The solution can be expressed in the operator form using the Green's functions method, and evaluated numerically given a specific spatial distribution of coefficients entering in eq. (1.16). In the work [28] the approximate expressions for the magneto-electric coefficients of composites constructed as piezoelectric pillars embedded in the piezomagnetic matrix has been obtained. Specifically, it was shown that the longitudinal effective ME coefficient is given by

$$\alpha_{33*} = -\frac{2f(1-f)d_{31}q_{31}}{(C_{11}^e + C_{11}^e) + (C_{11}^m - C_{12}^m) - f((C_{11}^e + C_{11}^e) - (C_{11}^m - C_{12}^m))} \quad (1.18)$$

where f denotes the volume fraction of the piezomagnetic phase and the superscripts e and m indicate elastic coefficients of piezoelectric and piezomagnetic phases respectively. The characteristic dependence of the linear magneto-electric response on the volume fraction of the piezomagnetic phase is depicted in Fig. 1.7. It can be described as a bell-shape with maximum ME response amplitude around $f \sim 0.7$ – 0.9 . For $f \rightarrow 1$ and $f \rightarrow 0$, α_{33*} vanishes indicating the fact that constituent phase are not magneto-electric. Asymmetry of the curve is explained by different elastic properties of constituent phases. The described approach can be also applied to study different geometrical arrangements of the constituent phases within the composite structure [32]. As can be seen from Fig. 1.7 this factor can drastically affect the resulting properties.

1.3 Geometrical characteristics of binary mixtures

In the following, unless specifically mentioned, we will be concerned with describing properties of phase transitions in a composite multiferroic systems comprised of two

chemically different phases. Specifically each of the phases can be either a ferromagnetic(antiferromagnetic), ferroelectric, or multiferroic material. This narrows down the class of geometries to that of binary mixtures or alloys. Given such system and generating a mesh (lattice) over it's volume we can therefore discretize the regions corresponding to different phases. Introducing a marker function σ_i defined on the set of the nodes i of the mesh we will define $\sigma_i = 0$ if node i falls into the region of material A and $\sigma_i = 1$ otherwise, or belonging to the region of material B . Although this construction might appear artificial, it proposes a rather clear way to geometrically classify the structure of binary alloys. In the case of macroscopic systems the choice of the mesh is not constrained, however it appears beneficial to choose a mesh that would capture the symmetry of the constituent phases. For instance, in the case of crystalline phases the mesh can be picked according to one of the Bravais lattices, while for an amorphous material an appropriate choice would be a random triangulation of the region. Naturally, the geometry of this discretization can be chosen differently for the regions corresponding to different materials. This procedure allows to generalize the visual representation of the composite systems with macroscopic morphological scale proposed by [29]. In the case of the nanostructures, the mesh corresponds to a crystalline lattice of the material with nodes i corresponding to positions of the atoms (see for example [144, 110]). This the representation scale invariant. Moreover, such discretization also allows to geometrically define the interface in a scale invariant manner. If for a given node i it's nearest neighbours environment $j \in \text{nn}(i)$ contains a node with a different value of a marker function $\sigma_i \neq \sigma_j$ then both nodes i and j belong to the *interface* between phases A and B . The *interface* is therefore defined as a set $\{i | \forall i \exists j \in \text{nn}(i): \sigma_i \neq \sigma_j\}$, consisting of a set of nodes connected with nearest neighbours links. It is important to mention that such definition is an attempt of formalizing a notion of the interface. For instance, in the case of a perfect epitaxial interface in multilayer nanostructures it will define a two dimensional (2D) surface according to the commonly accepted intuition. However in the presence of compositional gradient or in the case of a random homogeneous mixture the interface might acquire non-zero volume and the definition will become meaningless (these cases will be considered in more detail later).

Given a lattice representation of binary composite structure of volume N ($i = 1 \dots N$) and a certain volume of phase A : $V_A = \sum_i \sigma_i$ (or volume fraction $x = V_A/N$) it is obvious that the number of possible formally different lattice structures is given by the binomial coefficients $C(N; V_A)$, growing exponentially with the lattice volume and V_A . Taking into account symmetry considerations the volume of configurational space of a composite structure can be reduced by the factor $O(N)$. In order to divide binary configurations into classes several classifications have been proposed. Leaving aside the symmetry classification that follows the standard theory of point and space groups for crystalline

lattices in this section we will describe another related geometrical characteristics such as composite connectivity [29], fractality, shape of inclusions and more abstract topological characteristics.

1.3.1 Composite connectivity

Connectivity [29] is a concept that have proven to be useful in geometrical classification of composite materials. The commonly used definition states that connectivity of a constituent phase of a composite material is equal to the number of dimensions in which the phase is *self-connected*. Examples of different connectivities according to this definition are presented in Fig. 1.8. Considering two constituent phases the structure is classified with a pair of connectivities corresponding to each phase. As a matter of convention, connectivity of the active phase is listed first followed by inactive or inert phase. In the case of multiferroic composites we will be putting first the connectivity of ferroelectric constituent. Typical polycrystalline material is described by the connectivity of (0-3), meaning that the grains of active material are not inter connected between each other while the matrix, or in this case the grain boundaries form a simply connected set. Similarly a nearly dense ceramic with isolated pores can be described by a connectivity of (3-0). For two-phase composites 16 possible connectivities exist ten of which are geometrically distinct: (0,0), (1,0), (2,0), (3,0), (1,1), (2,1), (3,1), (2,2), (3,2), (3,3). Another important classes are the composites with connectivity of the type (2,2) and (1,3). They correspond to the so-called laminar structures and structures composed of *wires* of active material embedded in an inert matrix.

Connectivity of a composite frequently gives insight into it's physical properties. For instance, considering structure presented in Fig. 1.8 one can readily estimate the symmetry of tensor properties of the material [31] - tensors of elastic constants or stiffnesses, dielectric and magnetic susceptibilities, linear magnetoelectric tensor [32]. A more detailed analysis using linear homogenization techniques [39] shows that for composites within the same connectivity class these properties show similar dependencies on the volume fractions of the phases [32, 33] making Neuhm's definition of connectivity a good classification parameter for composites with macroscopic characteristic scales. Indeed, when description of material is governed by a linear model (either systems of linear [32] equations or linear differential equations [39]) boundary conditions defined by geometry play the key role in determining properties of the solution.

In the case of nanocomposite materials, with characteristic length scales comparable to lattice parameters of the constituent phases ($\lambda \sim 1\text{nm}-10\text{nm}$) connectivity becomes even

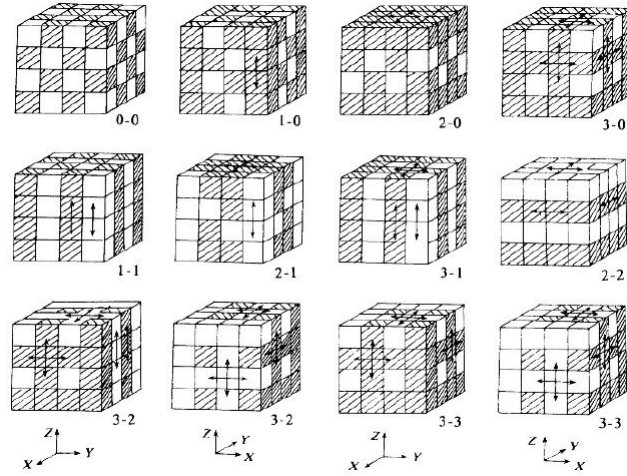


FIGURE 1.8: Schematic representation of the Newnham's definition of connectivity. The regions of the composite structure corresponding to different constituent materials are represented by arrangements of cubes of two different colors. Dark cubes correspond to the regions of material *A* while the light cubes are those occupied by material *B*. The connectivity of each phase is defined as the number of dimensions in which the phase is *self connected*. The connectivity of the composite structure is represented by a pair of connectivities corresponding to each phase. The figure illustrates the possible connectivities of the two phase composite. (After R. E. Newnham *et al.* [29])

more important especially in the case of systems exhibiting phase transitions. Inspecting the Newnham's definition one can notice that connectivity is tightly linked to the definition of *dimensionality* used in material science to classify nanostructures defined as the dimension of the space $d_{R^3} = 3$ minus the number of *nanoscale* dimensions of the structure $d = 3 - d_\lambda$. From this point of view, nanocomposite material described by a connectivity of (1,3) can be described as one-dimensional (1D) nanowires embedded in a bulk (3D) matrix. Similarly, dimensionality of epitaxial thin films and slabs of multilayers is equal to $d = 2$ (2D). In (3,0) nanocomposites, for instance nanoporous materials, the dimension of the pores is equal to zero. Therefore connectivity can be represented as a couple of numbers corresponding to the dimensionalities of constituent phases (d_A, d_B). This link emphasizes the importance of connectivity in nanoscale systems, since the properties of phase transitions depend strongly on systems dimensionality [34, 35].

Another important analogy can be deduced from noticing that the introduced lattice representation of the composite material can be seen as a three dimensional network or undirected graph[36]. This allows to define dimensionality as number of dimensions in which subgraphs corresponding to sets of nodes $\sigma_i = 0, 1$ percolates [37] and introduce the quantitative measure of connectivity. In graph theory latter is defined as follows: given a one-connected component of the graph, it's edge connectivity λ is given by the smallest edge cut disconnecting the graph into two disjoint sets [36]. Connectivity λ

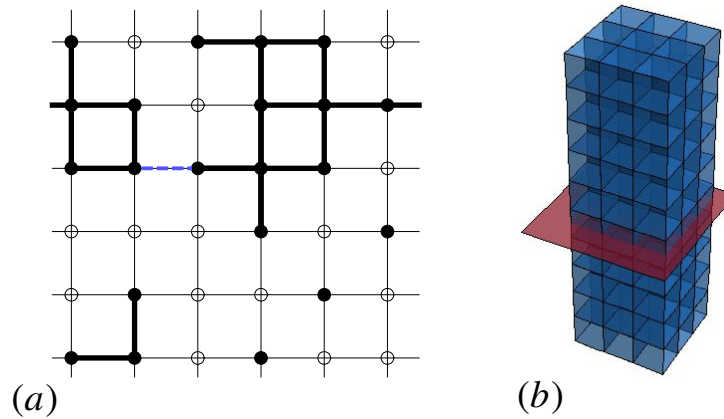


FIGURE 1.9: (a) Schematic illustration of the minimal edge cut of the graph. In the depicted case it is sufficient to remove a single edge (marked with blue dashed line) in order to disconnect the biggest component of the “black” site sublattice into two disjoint sets. (b) Similar logic can be applied to three dimensional lattices: example of the minimal edge cut of the pillar structure dividing it into two disconnected pillars.

therefore defines the minimal volume cross-section of the graph. Noticing that the volume of the set changes as $V \sim L^d$ with the characteristic length L while the cross-section $\lambda \sim L^{d-1}$ and remembering the link between connectivity and dimensionality one can define connectivity as $d = (1 - \log_V \lambda)^{-1}$. Obviously this definition is scale invariant and therefore cannot be used to identify zero connectivities according to Newnham’s definition. This follows from the fact that connectivity d appearing in this formula is proportional to the topological dimension d_T , which is equal to zero only for a disconnected sets of points.

1.3.2 Fractal dimension

As we have seen in the previous section, dimensionality is an important parameter characterizing geometry of nanostructures and nanocomposite materials. Yet another way to define dimensionality is the notion of fractal or Hausdorff dimension. Contrary to topological dimension, Hausdorff dimension d_H can take noninteger values ranging from zero to infinity and defines the *space-filling ability* of the set as well as its geometrical self-similarity. The literature on defining and calculating fractal dimensions is exhaustive and its review falls out of the scope of the current study. However, here we will describe one of the methods to calculate the so-called *correlation* dimension. Belonging to the family of fractal dimensions this measure, commonly used in chaos theory has the

advantage of being straightforwardly calculated as well as being less noisy when only a small number of points is available.

In order to calculate *correlation dimension* first the pair distance distribution function is calculated. It's integral that can be defined as $F(\epsilon) = \lim_{N \rightarrow \infty} g/N^2$, where g is the total number of pairs of points which have a distance between them that is less than ϵ . When the number of points is sufficiently large, for small values of ϵ the correlation integral $F(\epsilon)$ can be approximated with a power law $F(\epsilon) = \epsilon^d + o(\epsilon)$, where exponent d defines the correlation dimension of the set. In most of the cases correlation dimension is equal to the Hausdorff and box-counting dimensions.

Examples: Menger sponge, Cantor Dust and random fractals

Menger sponge and Cantor dust represent two perfect three-dimensional fractals ($d_T = 3$). Menger sponge is obtained by the following iterative procedure: (i) Begin with a homogeneous cubic lattice ($\sigma_i = 0$ for all i) (ii) Divide the lattice into 27 equal nonintersecting cubic sublattices (smaller cubes) (iii) Set $\sigma_i = 1$ for the nodes belonging to the smaller cube in the middle of each face, and the cube in the very center of the larger cube (iv) iterate steps (ii)-(iii). Cantor dust is obtained using the similar procedure, however only the sublattices located in 8 vertices on the initial lattice are filled. Several iterations of two-dimensional versions of these constructions are presented in Fig. 1.10. The sponge has a Hausdorff dimension of $d_H = \log 20 / \log 3 \sim 2.7268$, while $d_H = 2 \log 2 / \log 3 \sim 1.2619$. While it is hard to imagine that those perfect fractal structures can be realized experimentally, we can nevertheless consider them as theoretical examples of structures possessing non integer dimensional connectivities falling in between 2 and 3 in the case of Menger sponge and in between 1 and 2 for the case of Cantor dust. Another, more realistic examples of the fractal structures encountered in the field of nanocomposite materials are the so called random fractals, structures obtained using a random iterative procedure, therefore having random shape but fixed Hausdorff dimension. For instance, the example of such structures are random fractal structures generated using diffusion-limited cluster-cluster aggregation algorithm (DLCA)[40]. The generation algorithm is rather simple and can be summarized in the following way: (i) Start with a certain fraction of randomly occupied sites ($\sigma_i = 1$) (ii) The particles corresponding to occupied sites carry out random walk on the lattice. Whenever the two particles occupy neighbouring sites they form a cluster. Such cluster is considered inseparable and clusters of particles move together during random walk process. Whenever two clusters meet they form a bigger cluster. At sufficiently low starting concentration DLCA algorithm produces fractal clusters with fractal dimension $d_H = 1.75$. Examples of generated fractals are presented in Fig. 1.10.

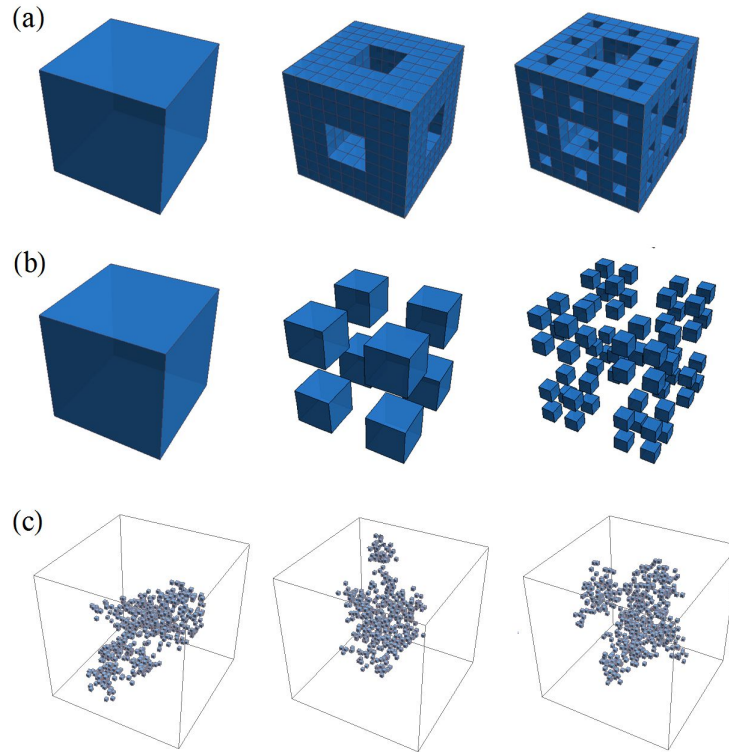


FIGURE 1.10: (a) Illustration of three consecutive iterations of the Menger sponge generation algorithm. At each iteration, the elementary cube is divided into 27 equal subcubes. The center of each face and the center of the original cube are then removed from the lattice. (b) Three iterations of the 3D Cantor dust generation algorithm. (c) Examples of the fractal clusters generated using the DLCA algorithm.

1.3.3 Euler-Poincaré characteristic

The Euler number or Euler-Poincaré characteristic χ is a topological characteristic of the set (more generally manifold) invariant under its smooth deformations (diffeomorphisms). The formal algebraic definition starts with defining the value χ of a simply connected compact convex body K , or in another words a ball with nonzero interior. Since all such sets are related via diffeomorphisms we set $\chi(K) = 1$. For the empty set $\chi(\emptyset) = 0$. Since the intersection $K_1 \cap K_2$ of two convex bodies K_1 and K_2 is either convex or empty then

$$\chi(K_1 \cup K_2) = \chi(K_1) + \chi(K_2) - \chi(K_1 \cap K_2) \quad (1.19)$$

Therefore for a disjoint union $\chi(K_1 \cup K_2) = 2$ and $\chi(K_1 \cup K_2) = 1$ otherwise. This formula can be generalized to sets corresponding to unions of m convex bodies $X = \cup_{i=1}^m K_i$

$$\chi(X) = \sum_{i=1}^m \chi(K_i) - \sum_{i=1}^m \sum_{j=i+1}^m \chi(K_i \cap K_j) + \dots + (-1)^{m+1} \chi(\cap_{i=1}^m K_i) \quad (1.20)$$

and is known as an inclusion-exclusion principle. Latter allows to calculate Euler number for an arbitrary set of convex bodies. Keeping in mind the description of composite geometry, we can already conclude that a structure with high positive Euler characteristic most likely resembles an array of inclusions with a compact convex shape. Another possibility follows from the formula [38]

$$\chi = \sum_{i=0}^{\infty} (-1)^i \beta_i = \beta_0 - \beta_1 + \beta_2, \quad (1.21)$$

where $\{\beta_i\}$ denotes the set of the so-called Betti numbers. The last equality is obtained assuming that the dimensionality of the set for which χ is calculated is lower than or equal to three, since $\beta_i = 0$ for all $i \geq (d - 1)$. Informally, the i th Betti number refers to the number of i -dimensional holes on a topological surface. For $d = 3$ the meaning of nonzero Betti numbers are the following. β_0 is the number of connected components, β_1 represents the number of one-dimensional or "circular" holes, while β_2 corresponds to the number of two-dimensional "voids" or "cavities". A torus has one simply connected component β_0 , two circular holes β_1 , the one in the center and the one in the middle of the "donut", and one two-dimensional void (β_2 , the interior cavity of the "donut") yielding Betti numbers of $\{1, 2, 1\}$ and a zero Euler characteristic, $\chi = 0$ (Fig. 1.11). On the same figure we can see other examples of two dimensional surfaces characterized by different values of χ . Obviously, increasing the number of circular holes while conserving one single cavity (eq. 1.21) reduces the Euler characteristic. Therefore, we see that to another geometrical configurations yielding high positive Euler number can be obtained by introducing cavities, or tunnels, into the structure, while to obtain negative Euler characteristic the only possibility consists in increasing the number of handles (Fig. 1.11) or in duplicating multi-handled toruses.

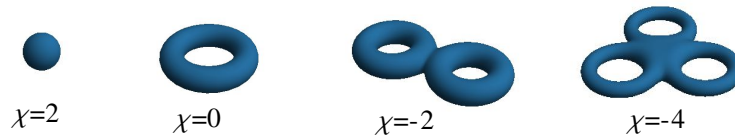


FIGURE 1.11: For differentiable manifolds, or in another words smooth surfaces Euler characteristic can be calculated using eq. 1.21. For the case of two dimensional surfaces adding one-dimensional or circular holes reduces the Euler characteristic by one. For instance for the torus with two handles the number of connected components is equal to one. Similar to the simple torus it also contains only one cavity, however the number of circular holes is equal to four leading to an Euler number of $\chi = -2$.

An expression very close to eq. 1.21 can be obtained if instead of the differentiable manifolds one considers discrete sets, such as polytopes, graphs, lattices or meshes. Indeed, for instance any two dimensional surface can be triangulated, or in another

words represented by a three dimensional graph, while three dimensional structures can be represented with meshes as explained in the introduction to Section 1.3. Graphs, meshes and lattices can be defined using common notions of vertices, edges and faces. For polytopes (which are discrete versions of convex bodies with nonempty interior) the analogue of eq. 1.21 is the Euler-Poincaré formula. Let F^k be the set of k dimensional phases of the polytope, e.g. F^0 denotes the set of faces, F^1 set of edges and F^3 is a polytope itself. Denoting by $\#F^k$ number of elements in F^k one can compute the Euler characteristic as

$$\chi = \sum_{k=0}^3 (-1)^k \#F^k \quad (1.22)$$

The generalization of eq. 1.22 to cubical complexes or lattices, e.g. structures introduced in section 1.3 to describe composite materials is far more complicated, however carries similar features. An instructive example of the relevance of Euler characteristic for lattices is it's relation to percolation threshold. Considering the site percolation problem on the planar two dimensional lattices, it was observed [42, 41] that the percolation threshold p_c is related to the concentration p_0 at which the volume density of Euler characteristic is zero (notably, the volumetric density of Euler-number is an intensive property in contrast to Euler characteristic itself and therefore represents a better parameter for characterizing bulk materials). For the *self-matching* [42] lattices it was theoretically shown that $p_c = p_0$ enabling the exact calculation of percolation thresholds. In the case when *self-matching* is not satisfied, the zero of Euler characteristic curve deviates from the percolation threshold p_c , however both values still remain close, i.e. $(1 - p_0/p_c) \ll 1$ still holds.

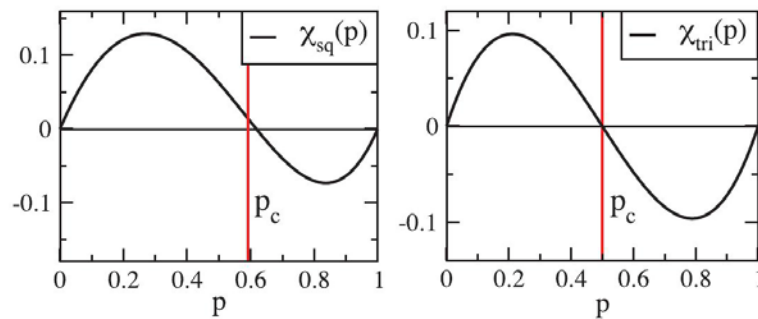


FIGURE 1.12: Dependence of the Euler-number density on the occupied site fraction p for the square (χ_{sq} on the left) and triangular (χ_{tri}) two-dimensional lattices. The two-dimensional triangular lattice is self-matching and therefore the zero of χ_{tri} matches the percolation threshold p_c , which is not the case for a simple square lattice. (After R. A. Neher *et al.* [41])

As can be seen from Fig. 1.12 the form of the curves describing Euler characteristic densities of clusters appearing in randomly occupied two-dimensional lattices is rather

universal. At low concentration, both χ_{sq} and χ_{tri} are positive and increase with increasing p . Indeed, the system geometrically can be described as a set of randomly distributed disconnected inclusions, and as discussed previously, increasing the number of inclusions leads to a linear increase of χ (see eq. 1.20). Similar situation is observed for $p \rightarrow 1$, however since the same geometrical description now holds for cavities in a fully occupied lattice, χ linearly reaches zero from the region of negative values. Therefore zero of Euler characteristic corresponds to a situation when the number of disconnected clusters and the number of circular cavities compensate each other. In the case of three dimensional lattices, $(1 - p_0/p_c) \ll 1$ relation does not hold; the percolation threshold deviation from p_0 becomes considerable. However, the shape of $\chi(p)$ still remains invariant for different lattice geometries. For the three dimensional case, contrary to the two-dimensional one, approaching full occupation limit yields positive χ linearly decreasing to zero, since the cavities now make positive contribution according to eq. 1.21. In the intermediate range of concentrations the sets of occupied sites and unoccupied free regions are geometrically similar, representing an interwoven handles geometry. Similar to the case of toruses with multiple handles. The circular holes dominate and the Euler number becomes negative (see Fig. 6 in Ref. [41]). This leads to the presence of two distinct zero points related to the percolation of clusters of occupied sites and clusters of non occupied, free regions.

Apart from quantitative description of the geometry of the structure, Euler characteristic provides an important link between physical properties of the system and its geometry. Generally, almost any physical property can be considered as a certain function or functional with domain in 3-dimensional Euclidean space. Local properties correspond to functions $f : \mathbb{R}^3 \rightarrow \mathbb{R}^n \times \mathbb{R}^m$, e.g. scalar functions ($n = 1$ and $m = 0$) such as particle densities, vector functions $k \geq 2, m = 0$ such as vector fields of velocities, magnetization, atomic shifts, and higher rank tensor fields $k \geq 1$ and $m \geq 1$ - local strain tensor etc. In the case of spatially confined systems, for instance nanostructures or composite materials in general, the domain of definition of f becomes restricted to a subset or a submanifold $\mathcal{M} \subset \mathbb{R}^3$. Remarkably, Euler characteristic of the definition domain $\chi(\mathcal{M})$ restricts the properties of any function defined on \mathcal{M} by imposing a conservation law of the topological charge known as *Morse index theorem*, or in the specific case of n -component vector fields also referred to as *Hopf-Poincaré theorem*.

Hopf-Poincaré theorem

Given a compact orientable differentiable manifold \mathcal{M} and a vector field $v : \mathcal{M} \rightarrow \mathbb{R}^n$ with isolated zeroes the following relationship holds

$$\chi(M) = \sum_i \text{ind}_{x_i}(v), \quad (1.23)$$

where the summation goes over all critical points x_i of the vector field v and $\text{ind}_{x_i}(v)$ denotes the index of the map $u = v(z)/|v(z)| : \partial D \rightarrow S^{n-1}$ of the boundary of the ε -neighbourhood D of the point x_i onto a $(n-1)$ -dimensional sphere. In the case of manifolds with boundary ∂M , the theorem is restricted to vector fields perpendicular to the boundary at any point $x \in \partial M$.

This theorem has been proven by Henri Poincaré for two-dimensional case followed by a generalization to higher dimensions by Heinz Hopf. In practice, the calculation of the u mapping index in the case of differentiable manifolds takes the following form [38, 43]

$$\text{ind}_{x_i}(v) = \frac{1}{\Omega} \int_{S^{n-1}} \begin{vmatrix} u^1 & \cdots & \cdots & u^n \\ \frac{\partial u^1}{\partial y^1} & \cdots & \cdots & \frac{\partial u^n}{\partial y^1} \\ \cdots & \cdots & \cdots & \cdots \\ \frac{\partial u^1}{\partial y^{n-1}} & \cdots & \cdots & \frac{\partial u^n}{\partial y^{n-1}} \end{vmatrix} dy^1 \cdots dy^{n-1} \quad (1.24)$$

where y^1, \dots, y^{n-1} are coordinates specified on the sphere S^{n-1} surrounding the defect, and a normalizing coefficient $\Omega = \int_{S^{n-1}} dy^1 \cdots dy^{n-1}$ equals 4π for $n = 3$ and 2π for $n = 2$. In the case of $n = 2$, eq. 1.24 yields

$$\text{ind}_{x_i}(v) = \frac{1}{2\pi} \oint \left(u^1 \frac{du^2}{dl} - u^2 \frac{du^1}{dl} \right) dl = 0, \pm 1, \pm 2, \dots \quad (1.25)$$

where l is a parameter defined along the loop surrounding the defect point. In this specific case we see that $\text{ind}_{x_i}(v)$ has a simple geometrical interpretation. Indeed, since any two-dimensional field can be parametrized as $v = |v|(\cos(\theta), \sin(\theta))$, the mapping u can be simply written as $u = (\cos(\theta), \sin(\theta))$ and eq. 1.25 reduces to

$$\text{ind}_{x_i}(v) = \frac{1}{2\pi} \oint \left(-\cos^2(\theta) \frac{d\theta}{dl} - \sin^2(\theta) \frac{d\theta}{dl} \right) = \frac{2\pi w}{2\pi} = w, \quad (1.26)$$

where we have introduced the integer number w commonly referred to as the winding number or topological charge of the point, indicating how many full turns of the vector u occur during the motion along the circle neighbourhood of the point x_i . For point defects in three-dimensional vector field eq. 1.24 yields

$$\text{ind}_{x_i}(v) = \frac{1}{4\pi} \oint \mathbf{u} \left[\frac{\partial \mathbf{u}}{\partial y^1} \times \frac{\partial \mathbf{u}}{\partial y^2} \right] dy^1 dy^2 \quad (1.27)$$

and indicates how many times one meets all possible orientations of the vector field while moving along the closed surface enclosing the defect center.

Now, once the meaning of the topological charge is clear, one can fully appreciate the meaning of the Hopf-Poincaré theorem. Indeed, eq. (1.23) means that given a specific manifold, the sum of the indexes of the critical points of any vector field defined on this manifold is constant! For instance, considering the two-dimensional sphere we immediately conclude that any tangent vector field will necessarily have at least one critical point where v vanishes, or in another words, it is impossible to define a zero gradient field on S^2 .

1.4 Finite-Temperature properties of model materials

In this section we will present the previously reported finite-temperature properties (both theoretically predicted and experimentally observed) of the compounds used as model materials in the present work. Main focus will be put on the classical ferroelectric material BaTiO_3 , and the single-phase multiferroic bismuth ferrite (BiFeO_3). Following, we will discuss the finite-temperature properties of $(\text{BiFeO}_3)_x(\text{BaTiO}_3)_{1-x}$ solid solutions and 2-2 heterostructures. As we will see, the former represents an especially interesting system. First, as described in Sec. 1.3, solid-solution structures can be thought of as a degenerate case of nanocomposite geometry, i.e. disordered binary mixture. For this type of system, the interface contribution is maximized and therefore the enhancement of product composite properties, such as ME effect, can be anticipated. The “composite” nature of these structures is also confirmed by the nature of inspiration which led to experimental synthesis of $\text{BiFeO}_3/\text{BaTiO}_3$ solid-solutions. Indeed, apart from the composite ME effect, mixtures of BiFeO_3 and BaTiO_3 were also expected to exhibit enhanced electronic properties (sum composite property), i.e. lower dielectric losses, giving advantage over single-phase bismuth ferrite. However, in contrary with the initial expectations $\text{BiFeO}_3/\text{BaTiO}_3$ solid-solutions were found to be paraelectric in a wide concentration range at room temperature. The nature of this phenomena has not been yet rigorously established and has recently inspired several thorough experimental studies. In contrast to the $\text{BiFeO}_3/\text{BaTiO}_3$ solid solutions, compounds which have been first synthesized in the 20th century, the nanocomposite epitaxial heterostructures comprising both bismuth ferrite and barium titanate have been fabricated only recently. Their experimental properties will be as well discussed in the present section.

1.4.1 BaTiO₃

Due to the simplicity of the crystalline structure, perovskite compounds present a special opportunity to theoretically investigate ferroelectric phase transitions [44]. Among other compounds of this class, the much-studied barium titanate [45] represents perhaps one of the most interesting prototypical example of perovskite ferroelectric material. The single-crystal BaTiO₃ undergoes a succession of ferroelectric phase transitions, from the high-temperature high-symmetry cubic perovskite phase to slightly distorted polar structures with tetragonal, orthorhombic and rhombohedral symmetries (see Fig. 1.13). The maximum saturation polarization values are $P_s^T \sim 26 \mu\text{C}/\text{cm}^2$ [59], $P_s^O \sim 33 \mu\text{C}/\text{cm}^2$ [58] and $P_s^R \sim 34 \mu\text{C}/\text{cm}^2$ [51]. Each transition is accompanied by the change of the per-

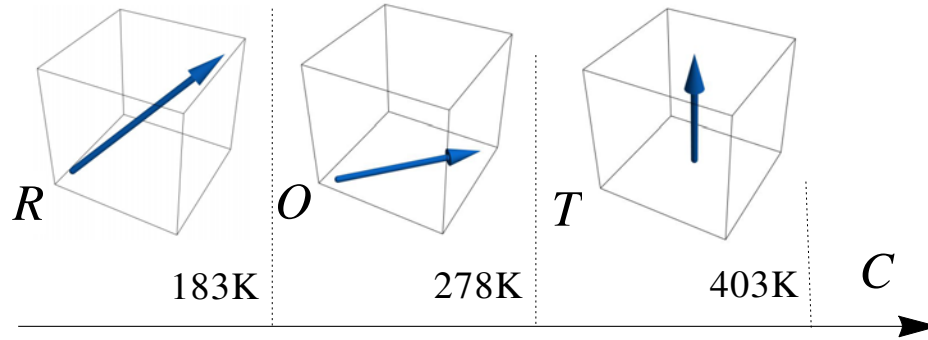


FIGURE 1.13: Schematic representation of the BaTiO₃ phase diagram. The compound undergoes three consecutive ferroelectric phase transitions: from the paraelectric cubic phase (C) to tetragonal ferroelectric phase (T) at $\sim 403\text{K}$, from tetragonal phase to orthorhombic (O) at $\sim 278\text{K}$, and from orthorhombic to rhombohedral phase (R) at $\sim 183\text{K}$. Blue arrows indicate the orientation of the macroscopic polarization. (the experimental values of transition temperatures are those given in Ref. [46])

ovskite unit cell shape, as a result of a considerable electromechanical coupling intrinsic to BaTiO₃. The corresponding theoretically predicted distortions [47] represented by the macroscopic strain components are presented in Fig. 1.14.¹ The first-order nature of the $R - O$ and $O - T$ phase transitions is indicated by the temperature hysteresis obtained from heating-up and cooling-down molecular dynamics simulations, in contrast to the weakly first-order tetragonal-to-cubic ferroelectric phase transition [49]. (The absence of the temperature hysteresis in Fig. 1.14 is explained by the fact that the temperature step used in the simulation exceeds the temperature range $\sim 5\text{K}$ of the coexistence of the tetragonal and cubic phases [48]).

¹The predicted phase transition temperatures deviate from the experimentally obtained values. This flaw is attributed to the use of LDA approximation to calculate the parameters of the effective Hamiltonian model used in [47].

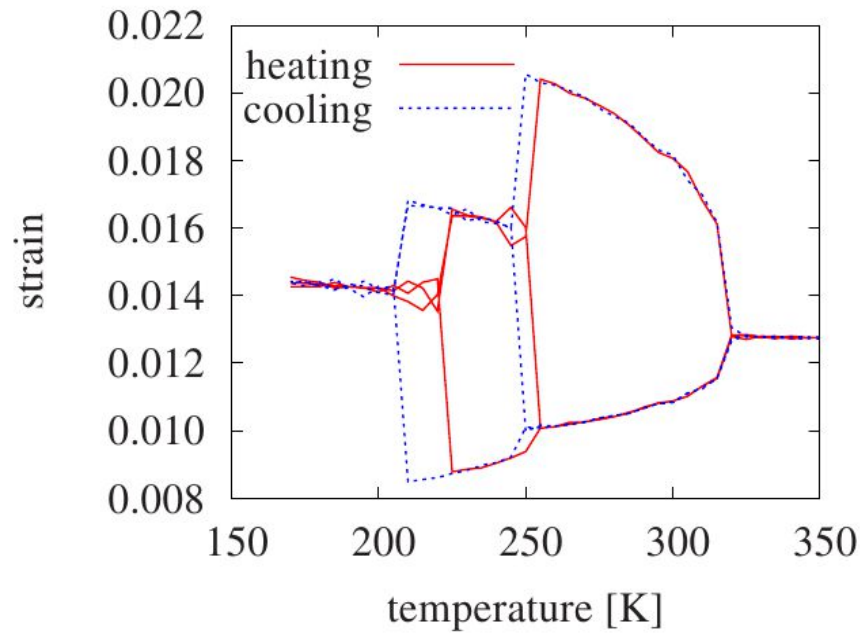


FIGURE 1.14: Average homogeneous strains η_{xx} , η_{yy} , and η_{zz} as a function of temperature in heating-up (solid lines), and cooling-down simulations (dashed lines). (After T. Nishimatsu *et al.* [47])

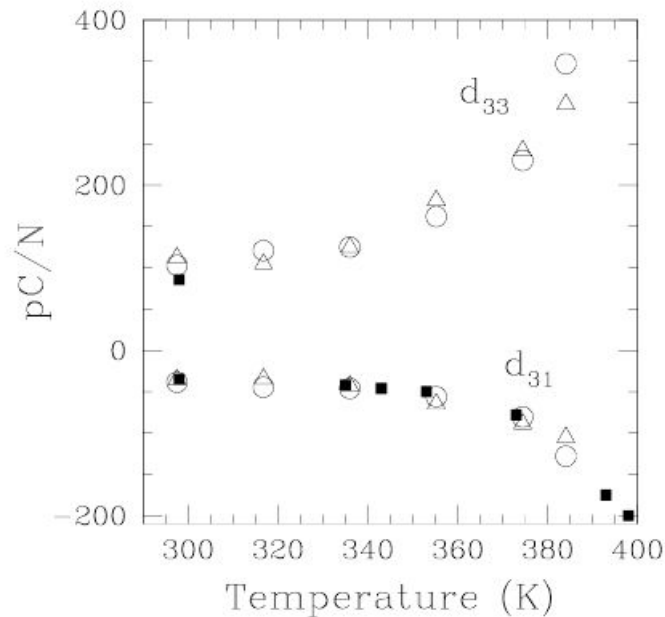


FIGURE 1.15: Temperature dependence of piezoelectric coefficients of the tetragonal phase of BaTiO_3 calculated from first-principles based effective Hamiltonian method. Open triangles and circles represent values computed from the strain response to an electric field and from polarization–strain correlations, respectively. (After A. Garcia *et al.* [50])

Another important characteristic of BaTiO_3 is its electromechanical properties, especially since in the present work BaTiO_3 is envisioned as a constituent material for multiferroic composite compounds exhibiting strain mediated ME effect (see eq. (1.18)). The

temperature dependence of the theoretically predicted piezoelectric coefficients [50] of the tetragonal phase of BaTiO₃ are presented in Fig. 1.15. In the paraelectric cubic phase, i.e. above the $T - C$ transition temperature, the piezoelectric coefficients are equal to zero due to the presence of the inversion center, while in the vicinity of the phase transition temperature one observes a significant increase of the electromechanical response [49]. The calculated piezoelectric coefficients at room temperature [50] are consistent with experimentally measured values. The comparison of room-temperature piezoelectric coefficients along with electrostriction coefficients of paraelectric BaTiO₃ is presented in Table 1.1. Similar information related to the elastic coefficients of tetragonal and cubic phase of BaTiO₃ is presented in Table 1.2.

d_{ij} (pC/N)	Exp. [52]	Exp. [51]	Ref. [50]	Q_{ij} (m ⁴ C ⁻²)	Ref.[53]
d_{33}	106	85.6	100	Q_{11}	0.1
d_{31}	-50	-34.5	-45	Q_{12}	-0.034
d_{15}	580	392		Q_{44}	0.029

TABLE 1.1: On the left: Comparison of the experimental and theoretically predicted values of room-temperature piezoelectric coefficients of BaTiO₃. The first two columns contain two different sets of experimentally obtained values, while the third column contains the calculated d_{ij} coefficients using effective Hamiltonian method [50]. On the right: experimental values of electrostriction coefficients in the cubic phase.

C_{ij}^T (GPa)	Exp. [52]	Exp. [54]	Exp. [51]	C_{ij}^c (GPa)	Exp. [51]
C_{11}	211±6	242	275	C_{11}	255
C_{33}	160±11	148	165		
C_{12}	107±5	128	179	C_{12}	82
C_{13}	114±8	122	151		
C_{44}	56±2	55	54	C_{44}	108
C_{66}	127±4	120	113		

TABLE 1.2: On the left: Comparison of the experimental values of room-temperature elastic coefficients of the tetragonal BaTiO₃ (C_{ij}^T). The first two columns contain two different sets of experimentally obtained values, while the third column contains the calculated d_{ij} coefficients using effective Hamiltonian method [50]. On the right: Experimental values of elastic coefficients (C_{ij}^c) of the cubic phase of BaTiO₃.

Finally, concluding the bibliographical review of some properties of barium titanate relevant to the present work, we would like to mention that despite the fact that BaTiO₃ is a classical ferroelectric that has been known and studied for more than 60 years², some debate regarding the mechanism of the ferroelectric-to-paraelectric phase transition in this compound is still going on (for instance see [56] and references therein). Without

²Interestingly, according to [55], BaTiO₃ was discovered during World War II. The initial reports were based on doping studies of TiO₂ with BaO, which produced ceramic materials with enhanced dielectric permittivities. Naturally, such materials were extremely important for electronic applications and the necessity all the more pronounced by the war has accelerated the research.

exploring this subject in more details, we would only like to mention that one of the consequences of this debate can be found in increasing number of different sets of Landau expansion coefficients (see for instance [57]).

1.4.2 BiFeO₃

Bismuth ferrite (BFO) is one of the most studied single-phase multiferroic materials since 2003 [60]. It has a rhombohedrally distorted perovskite structure with space group R3c [63, 64] (see Fig. 1.16) (the ferroelectric phase transition temperature $T_c \sim 1100\text{K}$ [65]). The magnetic structure is a G-type antiferromagnetism ($T_N \sim 640\text{K}$ [66]), modulated

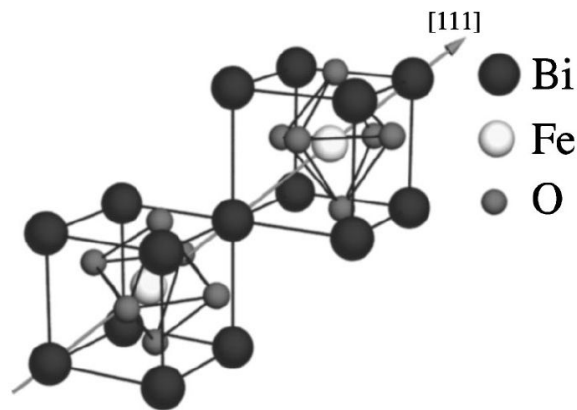


FIGURE 1.16: Schematic illustration of the ferroelectric rhombohedral phase of BiFeO₃. The macroscopic polarization stems from displacement of the ions in [111] direction relative to the anions. The AFD structure can be described using two cubic perovskite unit cells. The oxygen octahedra rotations around [111] axes alternate along [111] pseudocubic direction. (After C. Ederer *et al.* [62])

with a spin spiral structure [67], in which the antiferromagnetic axis rotates through the crystal with an incommensurate period of $\sim 620\text{\AA}$. The spiral modulation leads to the cancellation of any macroscopic magnetization that might occur through the canting of the antiferromagnetic sublattices magnetization directions, i.e. weak ferromagnetism [68, 69] (see Fig. 1.18), and inhibits the observation of the linear [70] magnetoelectric effect. The sequence of both structural and magnetic phase transitions have been successfully reproduced using first-principles based effective Hamiltonian methods (see for instance [72, 73, 74]). An example of the reported results are presented in Fig. 1.17.

The spiral magnetic structure of BiFeO₃ can be suppressed, allowing the observation of the linear magnetoelectric effect. Latter can be achieved by doping or by application of a high external magnetic field [70]. In the absence of external magnetic fields, single crystals of BiFeO₃ exhibit quadratic magnetoelectric effect. Such nonlinear magnetoelectric coefficients have been measured in 1985 by C. Tabarez-Munoz *et al.* [71],

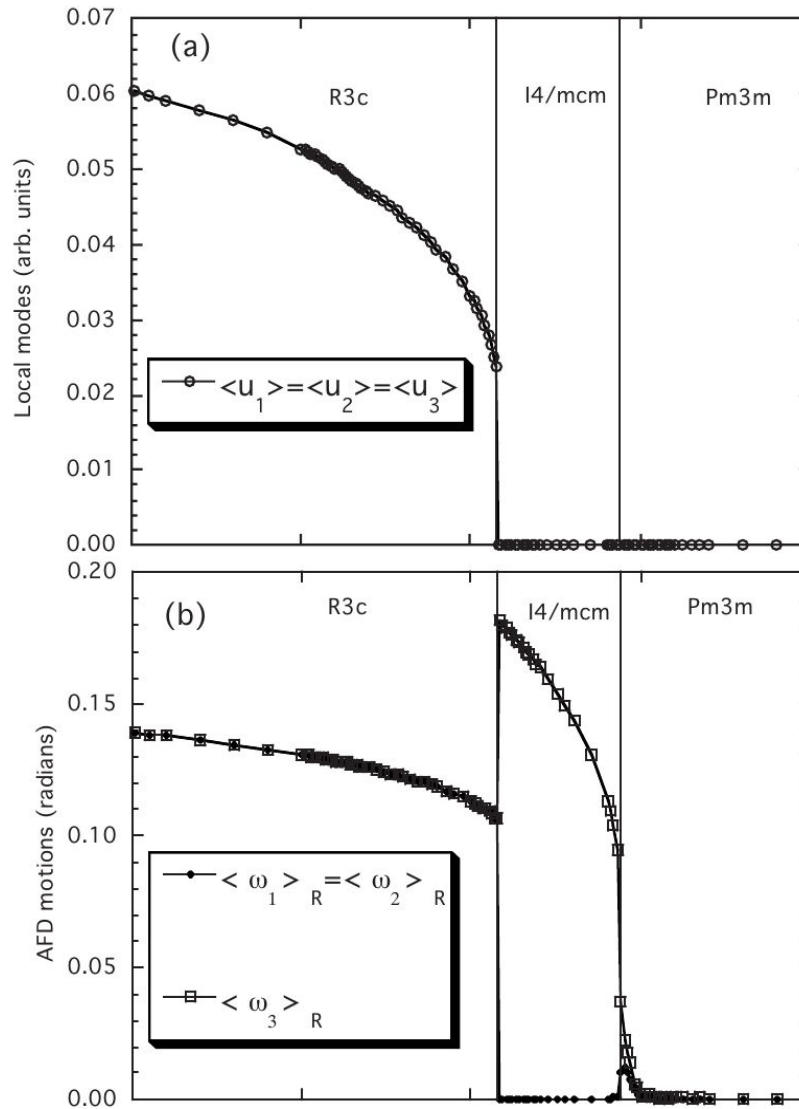


FIGURE 1.17: (a) Paraelectric to rhombohedral ferroelectric phase transition predicted from effective Hamiltonian model. The figure shows temperature dependence of the average value of the components of spontaneous polarization. (b) The predicted sequence of the AFD phase transitions. (After I. A. Kornev *et al.* [72])

however the theoretical estimates, both zero- and finite-temperature have been obtained only recently [75, 76, 77].

According to the theoretical predictions of J. C. Wojdel [75] and the recent experimental study of Sanghyun Lee *et al.* [78], the magnetoelectric effect exhibited by bismuth ferrite mainly consists of the lattice-mediated contribution. Specifically, the negative magnetoelectric coupling stemming from magnetostriction appears to outweigh the spin current contributions [78]. Therefore, the small values of linear magnetoelectric coefficients measured under applied bias magnetic field are related to the relatively small

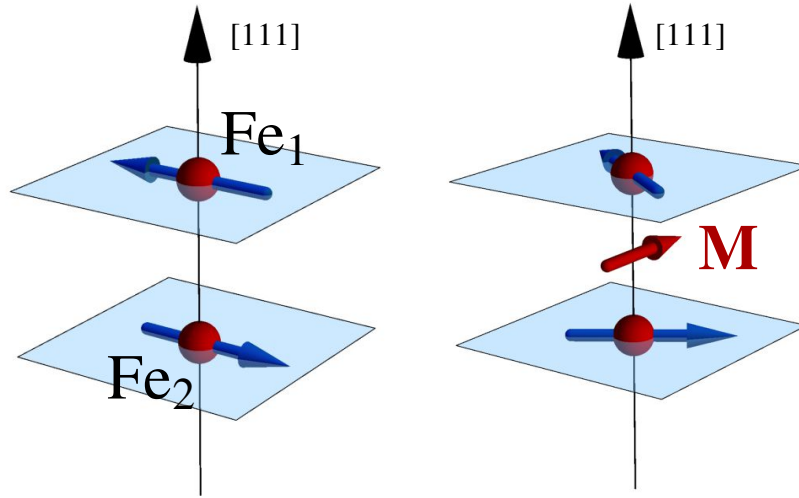


FIGURE 1.18: Theoretically predicted magnetic structure of BiFeO_3 reported in [62]. The spin-orbit coupling, leads to antisymmetric exchange (Dzyaloshinskii-Moriya interaction [68, 69]), which in turn results in a rotation of the magnetic moments of iron atoms in (111) plane. Appearing nonzero spontaneous magnetization M is referred to as weak magnetic moment. (Adapted from C. Ederer *et al.* [62])

values of piezoelectric and piezomagnetic coefficients of BiFeO_3 [60, 75] (elastic and electromechanical properties of bismuth ferrite are presented in table 1.3 while the piezomagnetic and magnetostriction coefficients are presented in figure 1.19). In a way, latter is a consequence of the multiferroic nature of BiFeO_3 , i.e. the distortions mediating the magnetoelectric effect are dominated by nonmagnetic ions.

C_{ij}^R (GPa)		C_{ij}^c (GPa)	Q_{ij} (m^4C^{-2})	Ref. [79]
C_{11}	222	195	Q_{11}	0.032
C_{12}	110	191	Q_{12}	-0.0016
C_{13}	50		Q_{44}	0.01
C_{14}	16			
C_{33}	150			
C_{44}	49	62		

TABLE 1.3: Elastic, electromechanical and magnetomechanical properties of bismuth ferrite. The first two columns contain the theoretically predicted elastic coefficients [61] of the rhombohedral $R3c$ phase (G -type antiferromagnetic order) and the paraelectric cubic nonmagnetic phase denoted as C_{ij}^R and C_{ij}^c respectively. The third column contains the piezoelectric coefficients Q_{ij} .

On the other hand, as pointed out in [75], BiFeO_3 can become an excellent magnetoelectric material if its electromechanical or magnetomechanical properties are improved. Possible ways of achieving this goal include fabrication of solid solutions of bismuth ferrite with other perovskite compounds, doping, or otherwise by strain engineering and

fabrication of composite and nanocomposite materials comprising BiFeO_3 as one of constituent phases. Specifically, $\text{BiFeO}_3/\text{BaTiO}_3$ nanostructures can represent promising candidates due to good electromechanical properties of BaTiO_3 .

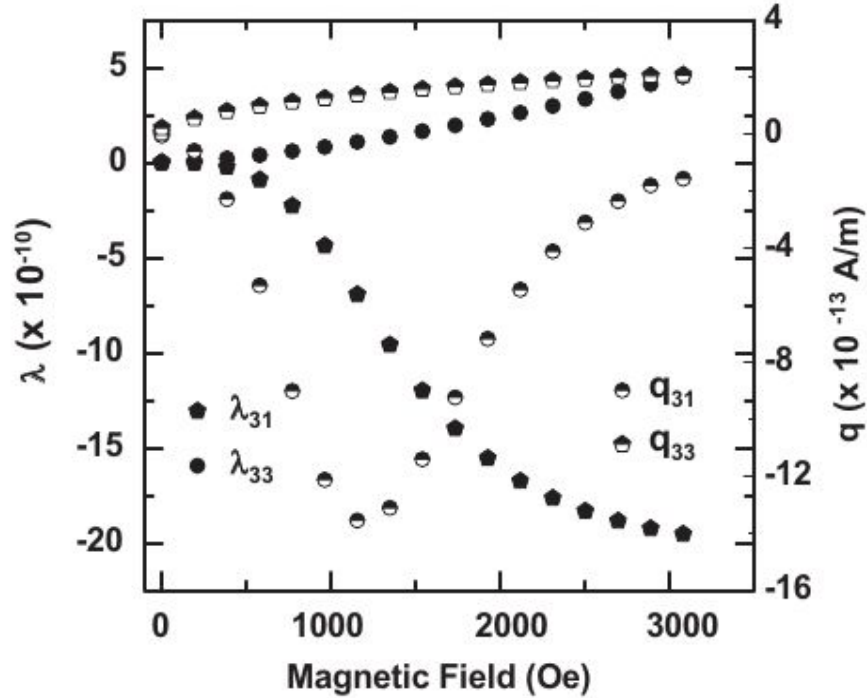


FIGURE 1.19: The predicted values of transverse (λ_{31}) and longitudinal (λ_{33}) magnetostriction, and piezomagnetic (q_{33} and q_{31}) coupling coefficients. (After A. Kumar *et al.* [80])

1.4.3 $(\text{BaTiO}_3)/(\text{BiFeO}_3)$ heterostructures

Unfortunately, despite the potential promise, only a few experimental studies have been devoted to the investigation of multiferroic properties of nanostructured $(\text{BiFeO}_3)(\text{BaTiO}_3)$ materials. Specifically, the main axis of study has been associated with $(\text{BiFeO}_3)_x(\text{BaTiO}_3)_{1-x}$ solid solutions³ and the $(\text{BiFeO}_3)_m(\text{BaTiO}_3)_n$ (m and n correspond to the thickness of corresponding layer in unit cells) multilayers epitaxially grown on SrTiO_3 substrates.

The experimental studies of $(\text{BiFeO}_3)(\text{BaTiO}_3)$ heterostructures with (2-2) connectivity have been initiated in 2008 by the work of H. Toupet *et al.* [81], where it was shown that the magnetization exhibited by such structures depends on the number of interfaces per unit thickness, therefore suggesting that the enhancement of magnetization originates at the $\text{BiFeO}_3/\text{BaTiO}_3$ interface. This observation was confirmed in the study conducted by P. Yang *et al.* [82], where the authors have also reported enhanced ferroelectric

³The properties of structurally disordered $(\text{BiFeO}_3)/(\text{BaTiO}_3)$ compounds will be discussed in the next section

properties and reduced leakage current. Moreover, it was found that using BaTiO_3 as a buffer layer leads to a larger in-plane and out-of-plane magnetization of BiFeO_3 thin films. The investigation continued in 2010, with an experimental study of the effect of the period of the superlattice on the magnetic properties of $(\text{BiFeO}_3)_m(\text{BaTiO}_3)_n$ (2,2) nanocomposites. In this study R. Ranjith *et al.* [83] have reported fabrication of the superlattices with different values of m and n ranging from 2 to 12. Once more, a weak ferromagnetic behaviour was observed with average magnetic moment per Fe^{3+} cation ranging from 0.01 to $0.015 \mu_B$ depending on the period of the superlattice.

To the best of our knowledge, the latest experimental study of $(\text{BiFeO}_3)(\text{BaTiO}_3)_3$ superlattices has been performed by M. Lorentz *et al.* in 2014 [84]. In their work, the authors have reported the fabrication of the composite $(\text{BiFeO}_3)(\text{BaTiO}_3)$ thin films with 33/67 and 67/33 mixing ratios as well as that of multilayer structures consisting of 15 bismuth ferrite-barium titanate double layers. The total thickness of the fabricated films ranged between 440 nm and 1850 nm. The highest saturation polarization of $75 \mu\text{C cm}^{-2}$ was exhibited by composite films with BiFeO_3 weight fraction of 0.33.

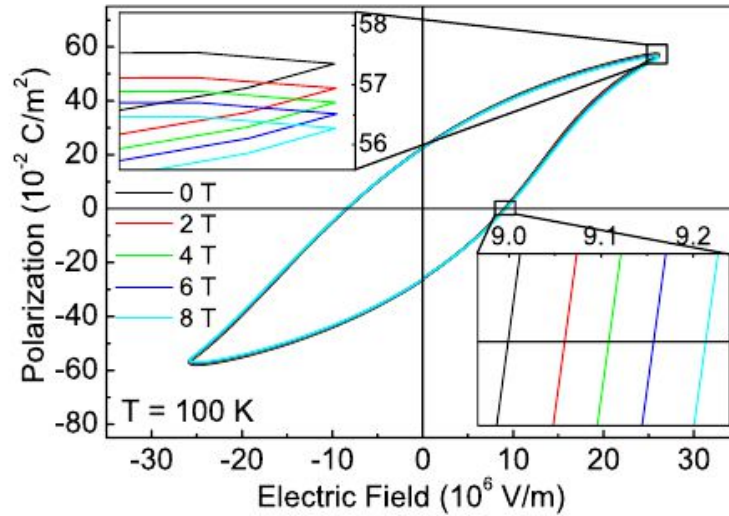


FIGURE 1.20: Ferroelectric hysteresis loops measured at $T=100\text{K}$ for the composite films with 0.33 weight fraction of BiFeO_3 at different values of the bias magnetic field ranging from 0 to 8T. (After M. Lorentz *et al.* [84])

Remarkably, in this work, the direct measurements of the magnetoelectric coupling exhibited by $(\text{BiFeO}_3)(\text{BaTiO}_3)$ multilayers have been reported for the first time. Specifically, the coupling between ferroelectric and ferromagnetic order parameters has been observed using two different techniques. First, the authors have performed the measurements of ferroelectric hysteresis loops under applied bias magnetic field. The corresponding reported results are presented in Fig. 1.20. Such method has revealed only minor changes of the loop shape which were estimated to be comparable to the effect of the change of the loop shape under fluctuations of the temperature of the sample.

This observation led authors to perform direct measurements of the longitudinal ac voltage response to an applied magnetic ac field at different values of temperatures and bias magnetic field, which are presented in Fig. 1.21. It was found that at room temperature and zero bias field, the maximum longitudinal magnetoelectric coefficient of $20.75 \text{ V cm}^{-1} \text{ Oe}^{-1}$ was exhibited by composite films with BiFeO_3 weight fraction of 0.33, a value comparable to the highest reported response for FeBSiC/PZT -fiber laminate structures. Similarly, it was found that $(\text{BaTiO}_3)(\text{BiFeO}_3)$ superlattices exhibit a magnetoelectric response exceeding that of the single-phase BiFeO_3 thin films.

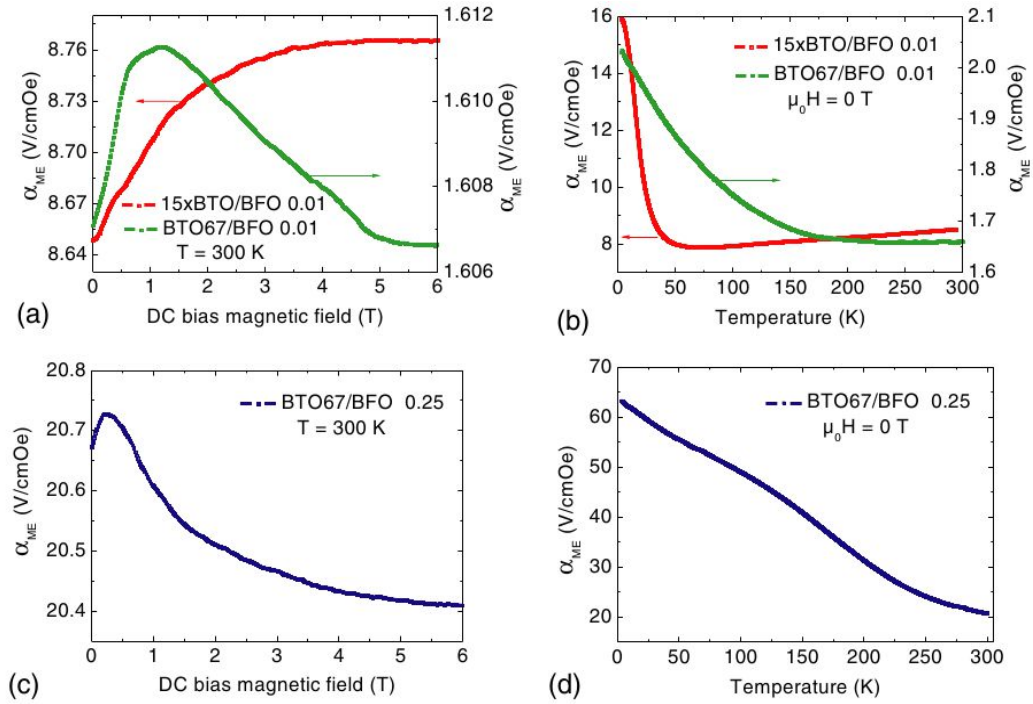


FIGURE 1.21: Temperature and bias magnetic field dependence of the magnetoelectric voltage coefficient $\alpha = \partial E / \partial H$ exhibited by thin films of different structure and composition. Measurements (a) and (b) were performed for the multilayers consisting of 15 $(\text{BiFeO}_3)(\text{BaTiO}_3)$ double layers (denoted as 15BTO/BFO) and for composite thin films with 0.67 BiFeO_3 weight fraction. Measurements (c) and (d) were performed for the composite films with 0.33 BiFeO_3 weight fraction. (After M. Lorentz *et al.* [84])

1.4.4 $(\text{BaTiO}_3)_x(\text{BiFeO}_3)_{1-x}$ solid solutions

In contrast to the case of epitaxial heterostructures, the experimental studies of the properties of structurally homogeneous $(\text{BiFeO}_3)_x(\text{BaTiO}_3)_{1-x}$ solid solutions have been performed more than fifty years ago (see for instance the study conducted by Yu. N. Venetsev *et al.* [85] in 1964), and the first evidence of the magnetoelectric coupling exhibited by these compounds has been first reported in 1981 by I. H. Ismailidze *et al.* [86] (see Fig. 1.22). Despite the fact that the measured magnetoelectric coupling was far too weak for practical applications, the interest to this system has resurfaced in 1999.

Specifically, M. M. Kumar *et al.* [87] have performed direct measurements of the magnetoelectric effect for compounds with different BiFeO_3 concentration x and its temperature dependence for the specific case of $x = 0.75$, thereby demonstrating the peaks of magnetoelectric response at the magnetic transition temperatures (see Fig. 1.23).

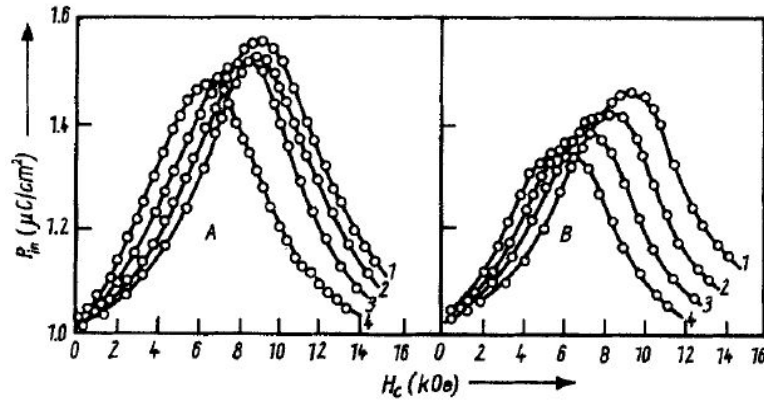


FIGURE 1.22: Dependence of the induced ferroelectric polarization upon the external magnetic field strength at different temperatures for (A) $(\text{BiFeO}_3)(\text{BaTiO}_3)$ and (B) $(\text{BiFeO}_3)(\text{PbTiO}_3)$ solid solutions with 0.95 BiFeO_3 mole %. The curves corresponding to different temperatures are denoted by numbers. System (A): (1) 298K (2) 305K (3) 323K (4) 398K; System (b): (1) 298K (2) 333K (3) 373K (4) 413K. (After I. H. Ismailidze *et al.* [86])

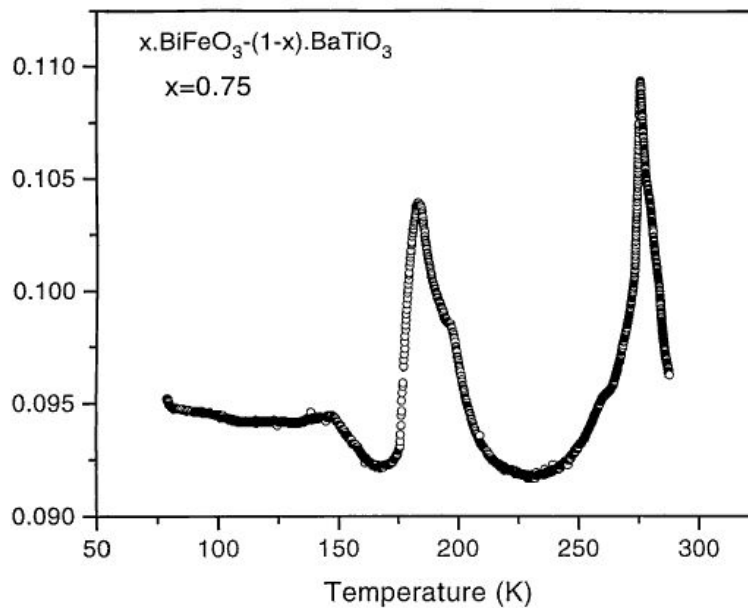


FIGURE 1.23: Variation of the magnetoelectric output with temperature for $(\text{BiFeO}_3)_{0.75}(\text{BaTiO}_3)_{0.25}$ system. (After M. M. Kumar *et al.* [87])

Finally, the temporal wheel of magnetoelectric measurements for $(\text{BiFeO}_3)(\text{BaTiO}_3)$ system has turned again in 2008, marked by the observation by A. Singh *et al.* [88] of an indirect evidence of the magnetoelectric coupling for the specific case of $x = 0.9$.

In contrast to the early yet persisting observations of magnetoelectric coupling exhibited by bismuth ferrite/barium titanate solid solutions, the studies pertaining to the structural properties of these compounds have led to a certain confusion regarding the nature of the observed structural phase transitions.

In the aforementioned work of Yu. N. Venevtsev *et al.* [85], it was first observed that at room temperature, the $(\text{BiFeO}_3)(\text{BaTiO}_3)$ solid solutions are found to exhibit three different phases depending on the concentration x . It was reported that for $x > 0.67$ the system stabilizes in rhombohedral ferroelectric phase, while for $x < 0.075$ it stabilizes in tetragonal phase. For the intermediate concentrations $0.075 < x < 0.67$, the symmetry of the structure was found to be cubic (see Fig. 1.24). Several subsequent studies confirmed these observations, however yielding different values of the critical concentrations at which the transitions from rhombohedral-to-cubic and tetragonal-to-cubic phases occur. For instance, A. Singh *et al.* [139] have reported a critical concentration of $x = 0.15$ at which the symmetry changes from tetragonal to cubic. Furthermore, it was found that only the global symmetry of the intermediate phase can be described as cubic, as suggested by studies proposing models involving local ferroic order.

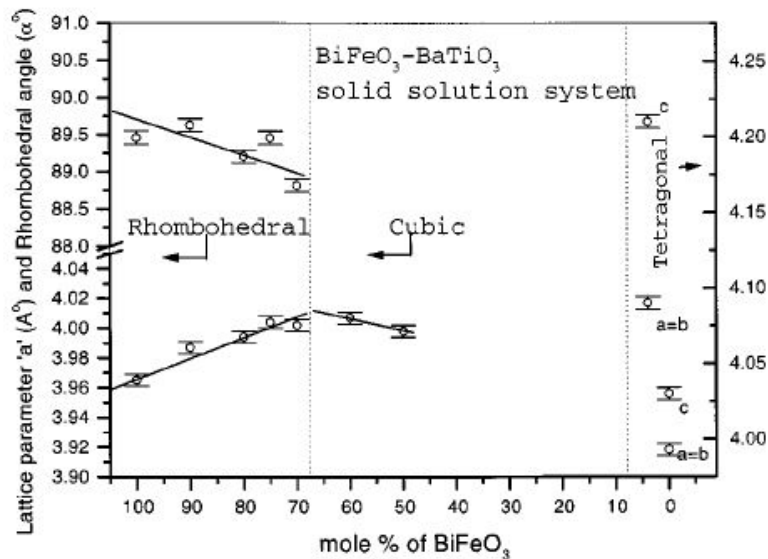


FIGURE 1.24: Variation of lattice parameters with decreasing content of BiFeO_3 . (After M. M. Kumar *et al.* [138])

The physical nature of this pseudocubic $Pm\bar{3}m$ phase has been debated in literature. Indeed, quantitative disagreement among experimental values of critical concentrations [138, 139, 140] on the one hand, and the absence of theoretical studies on the other, have led to vagueness in interpretations. For instance, in a study of A. Singh *et al.* [139], the pseudocubic phase formation was attributed to the presence of random electric fields and strain. Furthermore, it was suggested that the observed diffuseness of the dielectric response peak results from the cooperative freezing of off-centered Bi^{3+}

ions in $\langle 001 \rangle$ directions, while no relaxation of the dielectric response was observed. In a subsequent paper [140], the authors then indicated that the A-site ($\text{Bi}^{3+}/\text{Ba}^{2+}$) positional disorder rather gives rise to locally monoclinic structure with polarization vector continuously rotating from $[001]$ to $[111]$ pseudocubic direction, whereas Gotardo *et al* [142] proposed a model based on the coexistence of local tetragonal and monoclinic symmetries.

Chapter 2

Theoretical background

2.1 Introduction

This bibliographical chapter contains a brief summary of the theoretical approaches that are used throughout our study of the multiferroic properties of $\text{BiFeO}_3/\text{BaTiO}_3$ nanostructured compounds at different scales and temperatures. The ensuing discussion is subdivided into two main parts.

The first one is concerned with providing a short introduction to the *density functional theory*, the cornerstone of modern computational chemistry. The second part is devoted to the description of the so-called second-principles methods for predicting finite-temperature properties of multiferroic materials. We therein follow the works of K. Rabe, D. Vanderbilt, U. Waghmare and W. Zhong [148, 146] to detail the effective Hamiltonian scheme. This second part is of particular importance since it serves as the methodological foundation upon which our model is built.

The description of the effective Hamiltonian approach is complemented by a discussion of the effects of structural heterogeneity on the properties of the system within the context of lattice models. We mainly consider the effect of structural disorder manifested by the onset of random local fields, and explore the concept of the lower critical dimension in the presence of random field quenched disorder. We also examine the role of topological defects in weakening/modifying the ground-state properties of the system. As it will be seen in the next chapter, these concepts will reveal to be impactful in our investigation of the nature of the pseudocubic non-polar phase displayed by $(\text{BiFeO}_3)(\text{BaTiO}_3)$ solid solutions.

2.2 First principles approaches

2.2.1 Density Functional Theory

When considering a system consisting of N electrons and M nuclei, a first simplification naturally arises from the large mass difference between electrons and nuclei, enabling the decoupling of their dynamics and degrees of freedom within the so-called Born-Oppenheimer approximation. This leads to a reduction of the many-body problem to the study of interacting electrons in a frozen-in configuration of the nuclei whose positions, \mathbf{r}_α , are regarded as parameters. Within this first approximation, the ground state of N electrons is determined by solving the following Hamiltonian of a stationary many-body system:

$$\hat{H}_v = \hat{T} + \hat{U} + \hat{V}_{\text{ext}} \quad (2.1)$$

The constituent terms are explicitly given as

$$\hat{T} = -\frac{1}{2} \sum_i \nabla_i^2 \quad (2.2)$$

$$\hat{U} = \sum_i u(\mathbf{r}_i) = \sum_i \sum_{i>j} \frac{1}{|\mathbf{r}_i - \mathbf{r}_j|} \quad (2.3)$$

$$\hat{V}_{\text{ext}} = \sum_i v(\mathbf{r}_i) = \sum_i \sum_\alpha \frac{-Z_\alpha}{|\mathbf{r}_i - \mathbf{r}_\alpha|} \quad (2.4)$$

where the latin subindices refer to the electrons while the Greek subindices refer to the nuclei, and where the operators denote the kinetic energy of the electrons, the two-particle Coulomb interaction and the external potential arising from the nuclei, respectively. For all N-electrons systems, \hat{T} and \hat{U} are the same, they are said to be universal, or system-independent, so that the specificity of the system is encapsulated in the external potential v_{ext} . The Hamiltonian \hat{H}_v is thereby denoted with a sub-index v indicating that the operator can be regarded as a functional of the external potential. This is in particular the case for the ground state wave function $|\psi_0[v]\rangle$ and the ground state energy $E_0[v]$, which are related by the Schrödinger equation

$$(\hat{T} + \hat{U} + \hat{V}_{\text{ext}}) |\psi_0[v]\rangle = E_0[v] |\psi_0[v]\rangle \quad (2.5)$$

The ground state $|\psi_0[v]\rangle$ gives rise to a ground state electronic density $n(\mathbf{r})$

$$n(\mathbf{r}) = \langle \psi_0 | \hat{n} | \psi_0 \rangle = \langle \psi_0 | \sum_{i=1}^N \delta(\mathbf{r} - \mathbf{r}_i) | \psi_0 \rangle = N \int \prod_{i=2}^N d\mathbf{r}_i |\psi_0(\mathbf{r}, \mathbf{r}_2, \dots, \mathbf{r}_N)|^2 \quad (2.6)$$

Hohenberg-Kohn theorems

The first Hohenberg-Kohn theorem demonstrates that the density may be used in place of the potential as the fundamental function uniquely characterizing the system, rather than the many electron wave function. It may be stated as: *the ground-state density $n(\mathbf{r})$ uniquely specifies the potential, to within a constant, and hence the ground state wave function, to within a phase factor.* This means that the external potential is a well defined functional $v[n]$ of the density. In the original Hohenberg-Kohn paper [89], this theorem is proven by *reductio ad absurdum* for densities with non-degenerate ground states. Assuming that there exist two different external potentials V_{ext} and V'_{ext} which both give the same electron density $n(\mathbf{r})$. Then the corresponding Hamiltonians H and H' have the same ground state density but different ground state wave functions, $|\psi_0\rangle$ and $|\psi'_0\rangle$, respectively. Using the variational principle, and taking $|\psi'_0\rangle$ as a trial function for H yield the strict inequality

$$\begin{aligned} E_0 < \langle \psi'_0 | H | \psi'_0 \rangle &= \langle \psi'_0 | H' | \psi'_0 \rangle + \langle \psi'_0 | (H - H') | \psi'_0 \rangle \\ &= E'_0 + \int d\mathbf{r} n(\mathbf{r}) [V_{\text{ext}}(\mathbf{r}) - V'_{\text{ext}}(\mathbf{r})] \end{aligned} \quad (2.7)$$

Whereas taking $|\psi_0\rangle$ as a trial function for H' gives

$$\begin{aligned} E'_0 < \langle \psi_0 | H' | \psi_0 \rangle &= \langle \psi_0 | H | \psi_0 \rangle + \langle \psi_0 | (H' - H) | \psi_0 \rangle \\ &= E_0 - \int d\mathbf{r} n(\mathbf{r}) [V_{\text{ext}}(\mathbf{r}) - V'_{\text{ext}}(\mathbf{r})] \end{aligned} \quad (2.8)$$

Adding these two equations results in the contradiction

$$E_0 + E'_0 < E_0 + E'_0 \quad (2.9)$$

from which it is concluded that different ground states must yield different densities. The first Hohenberg-Kohn theorem¹ thus indicates that there is a unique invertible mapping between the external potential v and the ground state density $n(\mathbf{r})$. This implies that

¹Lieb [91] was the first to point out the connection between density-functional theory and Legendre transforms. In this approach, potential and density are conjugate variables, and the first Hohenberg-Kohn theorem simply trades one set of variational parameters for another via a Legendre transform: writing the ground state energy as a functional of the external potential $E_0[v]$ and taking its functional derivative result in the following expression for the density $n(\mathbf{r}) = \delta E[v] / \delta v(\mathbf{r})$. The one-to-one correspondence between v and n is thus due to the fact that the Legendre transform $F_{\text{HK}}[n(\mathbf{r})] = E_0[v(\mathbf{r})] - \int n(\mathbf{r})v(\mathbf{r})d\mathbf{r}$ of the ground state energy $E_0[v]$ is the $F_{\text{HK}}[n]$ functional.

the total energy is a functional of the density, $E = E[n]$. The universal Hohenberg-Kohn functional $F_{\text{HK}}[n]$ given by

$$F_{\text{HK}}[n] = \langle \psi[n] | \hat{T} + \hat{U} | \psi[n] \rangle \quad (2.10)$$

defines the energy functional $E[n]$ as

$$E[n] = \int n(\mathbf{r})v(\mathbf{r})d\mathbf{r} + F_{\text{HK}}[n] \quad (2.11)$$

The second Hohenberg-Kohn theorem [89] generalises the *variational principle* from wave functions to electron densities, in that it states that the functional for the ground state energy is minimized by the ground state electron density. If n_0 is the ground state density corresponding to an external potential v_0 and \tilde{n} an arbitrary other ground state density satisfying $\tilde{n}(\mathbf{r}) \geq 0$ and $\int \tilde{n}(\mathbf{r})d\mathbf{r} = N$, then

$$\begin{aligned} E_{v_0}[n_0] &\leq E_{v_0}[\tilde{n}] \\ \langle \psi[n_0] | \hat{T} + \hat{U} + \hat{V}_0 | \psi[n_0] \rangle &\leq \langle \psi[\tilde{n}] | \hat{T} + \hat{U} + \hat{V}_0 | \psi[\tilde{n}] \rangle \end{aligned} \quad (2.12)$$

This second Hohenberg-Kohn theorem thus states that $E[n]$ has an extremum in correspondence with the ground state electron density. This theorem demonstrated the *existence* of such a functional but did not provide any explicit instructions as for how to build or find this functional.

The Kohn-Sham ansatz

The central assertion of Kohn and Sham's reformulation of DFT [90] stands in the mapping of the intractable system of interacting electrons in a external potential v_{ext} onto a fictitious system of independent electrons, chosen to have the same density as the physical system and evolving in a effective potential v_s . In this approach, the exact kinetic energy functional can be written as

$$T[n] = T_s[n] + T_c[n] \quad (2.13)$$

where $T_s[n]$ is the kinetic energy of the auxiliary non interacting N-electron system, and where $T_c[n]$ is the remainder. The subscripts s and c stand for single-particle and correlation, respectively. Similarly, the exact Coulomb functional $U[n]$ is written as $U[n] = E_H[n] + \Delta U[n]$ where the Hartree term $E_H[n]$ describes the electron-electron repulsion and where $\Delta U[n]$ is a contribution that accounts for the quantum nature of

the interacting electrons. The exact energy functional is then rewritten as:

$$E[n] = T_s[n] + \int n(\mathbf{r})v_{\text{ext}}(\mathbf{r}) \, d\mathbf{r} + E_H[n] + E_{\text{xc}}[n] \quad (2.14)$$

where the exchange-correlation function $E_{\text{xc}}[n]$ corresponds by definition to

$$E_{\text{xc}}[n] = (T[n] - T_s[n]) + (U[n] - E_H[n]) \quad (2.15)$$

and should account for the exchange effects (Pauli repulsion), the correction that compensates for the self-interaction term in $E_H[n]$ and the correlations effects. The variational equation in its Euler-Lagrange form for the exact functional is thus:

$$\frac{\delta E[n]}{\delta n(\mathbf{r})} = \frac{\delta T_s[n]}{\delta n(\mathbf{r})} + v_{\text{ext}}(\mathbf{r}) + \int \frac{n(\mathbf{r}')}{|\mathbf{r} - \mathbf{r}'|} \, d\mathbf{r}' + \frac{\delta E_{\text{xc}}[n]}{\delta n(\mathbf{r})} = \mu \quad (2.16)$$

where μ is a Lagrange multiplier constraining the number of electrons to N . Kohn and Sham introduced an auxiliary non interacting system S of N particles with the property that it yields the same ground state density as the real interacting system in a given external potential $v_{\text{ext}}(\mathbf{r})$. This correspondence implies that the non interacting electrons must be subjected to another external potential $v_s(\mathbf{r})$, which must compensate the contributions arising from the electron-electron interactions. For the virtual system S , the variational equation writes:

$$\frac{\delta E[n]}{\delta n(\mathbf{r})} = \frac{\delta T_s[n]}{\delta n(\mathbf{r})} + v_s(\mathbf{r}) = \mu \quad (2.17)$$

Equations (2.16) and (2.17) coincide whenever:

$$v_s(\mathbf{r}) = v_{\text{ext}}(\mathbf{r}) + \int \frac{n(\mathbf{r}')}{|\mathbf{r} - \mathbf{r}'|} \, d\mathbf{r}' + v_{\text{xc}}[n](\mathbf{r}) \quad v_{\text{xc}}(\mathbf{r}) = \frac{\delta E_{\text{xc}}[n]}{\delta n(\mathbf{r})} \quad (2.18)$$

Consequently, one can calculate the density of the interacting (many-body) system in potential $v_{\text{ext}}(\mathbf{r})$, described by a many-body Schrödinger equation of the form given by eq. (2.5), by solving the equations of a non-interacting (single-body) system in potential $v_s(\mathbf{r})$. In particular, the Schrödinger equation of the auxiliary system

$$\left\{ -\frac{1}{2}\nabla^2 + v_s(\mathbf{r}) \right\} \phi_i(\mathbf{r}) = \epsilon_i \phi_i(\mathbf{r}) \quad (2.19)$$

yields orbitals that reproduce the density $n(\mathbf{r})$ of the original system:

$$n(\mathbf{r}) = \sum_i^N f_i |\phi_i(\mathbf{r})|^2 \quad (2.20)$$

where f_i is the occupation of the i th orbital.

Given a practical approximation for $E_{xc}[n]$, one obtains $v_{xc}(\mathbf{r})$, and can thus find $v_s(\mathbf{r})$ from $n(\mathbf{r})$ for a given $v_{ext}(\mathbf{r})$. The set of coupled non linear equations (2.18), (2.19) (2.20) are the Kohn-Sham equations, and should hold simultaneously. In particular, the density must be self-consistent. The computational procedure usually starts with an initial guess for the input density $n(\mathbf{r})$, leading to a potential $v_s(\mathbf{r})$ which in turn gives rise to a set of orbitals ϕ_i from which a new density is constructed. This procedure is reiterated until reaching a convergence criteria (equality of the input and output densities to required precision) within this self-consistency cycle. Again, this scheme only holds for an explicit form of $E_{xc}[n]$ that is *a priori* unknown but can be efficiently approximated.

The local density approximation

As stated previously, the quality of the results using DFT depends on the ability of the universal exchange-correlation functional $E_{xc}[n]$ to model the many-body electronic interactions. The first, and most widely used approach is the Local Density Approximation (LDA) [90], which treats the inhomogeneous system locally as an homogeneous electron gas. It assumes (i) that the exchange-correlation energy per particle at point \mathbf{r} , $\epsilon_{xc}(\mathbf{r})$, only depends on the density at this point, and (ii) that it is equal to the exchange-correlation energy per particle of a homogeneous electron gas of density $n(\mathbf{r})$ in a neutralizing background.

$$E_{xc}^{LDA}[n] = \int n(\mathbf{r}) \epsilon_{xc}^{LDA}(\mathbf{r}) d\mathbf{r} \quad \epsilon_{xc}^{LDA}(\mathbf{r}) = \epsilon_{xc}^{hom}[n(\mathbf{r})] \quad (2.21)$$

The quantity $\epsilon_{xc}^{hom}[n(\mathbf{r})]$ can be further split into exchange and correlation contributions:

$$\epsilon_{xc}^{hom}[n(\mathbf{r})] = \epsilon_x^{hom}[n(\mathbf{r})] + \epsilon_c^{hom}[n(\mathbf{r})] \quad (2.22)$$

The exchange part describes the energy lowering due to antisymmetrization (Pauli repulsion) and can be evaluated analytically by the method of Bloch and Dirac, and scales as

$$\epsilon_x^{hom}[n(\mathbf{r})] = -\frac{3}{4\pi} \left(\frac{3}{\pi} n(\mathbf{r}) \right)^{1/3} \quad (2.23)$$

For the correlation part, that describes the propensity for two electrons of unequal spin to choose different orbitals and to mutually avoid along their motion in space, one may rely on accurate values obtained by Ceperley-Alder [92] from Monte-Carlo simulations of the energy of the homogeneous electron gas. By its very construction, the LDA is expected to be a good approximation for spatially slowly varying densities. Although this condition is hardly ever met for real electronic systems, LDA has proved to be remarkably accurate

for a wide variety of systems² providing access to the ground state energy and thereby to structural and dynamical properties of solids such as equilibrium structures, elastic, dielectric and vibrational properties. Atomic positions and lattice constants reproduce the experiment within 1% whereas phonon frequencies are usually obtained within 5%. Although an accuracy of 1% on the lattice constant might be considered as successful for a method without any adjustable parameter, it can constitute a limitation in some cases. In perovskite oxides for example, the ferroelectric instability is very sensitive to pressure, and thus to the lattice constant. In this context, in order to avoid this problem, it appeared convenient in some circumstances to fix the lattice parameters to their experimental values, or to apply a negative pressure [93] in the calculation that compensates for the typical LDA underestimate of the lattice constant.

2.3 Lattice models

While offering an exceptional opportunity to avoid any phenomenological input, the density functional theory is limited to describing only the ground-state properties of the many-electron systems, i.e., it represents an approach applicable only in the case of the zero-temperature studies. On the other hand, the problem of obtaining the finite-temperature properties of the strongly interacting systems (in general both quantum and classical) is still far from being solved, especially in the case of the absence of translational invariance and other global symmetries.

In order to reduce the complexity of the problem under investigation, one usually resorts to studying a simplified model, which captures the essential physics of the original system while being simple enough to be approachable either numerically or via different analytical approximations. Lattice models of statistical physics represent a perfect example of such a complexity reduction scheme. The two models that will be extensively used throughout this work are the classical Heisenberg lattice model and the so-called lattice ϕ^4 theory.

★ *The Classical Heisenberg model*

The classical Heisenberg model deals with the problem of obtaining finite-temperature properties of a system of spins \mathbf{s}_i (three dimensional vectors of a fixed norm

²This is due in part to the fact that the LDA fulfills the sum rule on the exchange-correlation hole, $\int d\mathbf{r}' n_{xc}(\mathbf{r}, \mathbf{r}') = -1$, $\forall \mathbf{r}$, which must be obeyed by the real functional, and which describes how an electron at \mathbf{r} completely depletes the total density of the other electron at \mathbf{r}' . This gives rise to error compensation when computing the exchange-correlation energy (typically, the LDA overestimates E_x and underestimates E_c)

$|\mathbf{s}_i| = 1$) situated at the nodes i of a lattice L , the interaction of which is described by the following Hamiltonian

$$H = - \sum_{i,j \in L} J_{ij} s_i^\alpha s_j^\alpha \quad (2.24)$$

where s_i^α denotes the α Cartesian component of the classical spin situated at site i . This Hamiltonian has a global spherical symmetry, that is, rotating all the spins with the same orthogonal transformation $s^\alpha \rightarrow \hat{O}_{\alpha\beta} s^\beta$ leaves the interaction energy invariant. The constants J_{ij} describe the quantum exchange interaction energy between the spins situated at the sites i and j . The bilinear exchange J_{ij} term along with the fixed magnitude of the lattice spins s_i are the main characteristic features of the classical Heisenberg model. Then, depending on the considered lattice geometry, additional on-site terms or modified range of exchange interactions can lead the model to exhibiting a wide spectrum of behaviours.

★ *The ϕ^4 model*

The ϕ^4 theory can be seen as a truncated version of the Heisenberg model. Its generalized form is described by the following lattice Hamiltonian

$$H = - \sum_{i,j} J_{ij} \phi_i^\alpha \phi_j^\beta + \sum_i (\kappa_{2,\alpha\beta} \phi_i^\alpha \phi_i^\beta + \kappa_{4,\alpha\beta\gamma\delta} \phi_i^\alpha \phi_i^\beta \phi_i^\gamma \phi_i^\delta) \quad (2.25)$$

acting on the n -component real-valued field ϕ_i defined on the set of the lattice sites. The formal correspondence between this Hamiltonian and the generalized Heisenberg model can be established via the Hubbard-Stratonovich transformation. Yet, even without exploring this question in further details, one can readily note that the expression given in eq. (2.25) can be seen as a soft-magnitude version of the expression given in eq. (2.24). Indeed, allowing the change of amplitude of the vectors \mathbf{s}_i leads to the requirement of convergence of the partition function, the latter being satisfied at the expense of introducing the κ_2 and κ_4 terms.

2.3.1 Effects of structural disorder

The physical properties of phase transitions exhibited by spatially heterogeneous systems are intrinsically different from those exhibited by the systems possessing translational symmetry such as infinite volume crystalline lattices. Specifically, spatial heterogeneity introduces an artificial ladder of scales in addition to the scale at which the spatial fluctuations of the order parameter field occur. For

instance, let us consider the isotropic soft Heisenberg spin Hamiltonian of the following form

$$H = \sum_{\langle i,j \rangle, \alpha} J_{ij} s_i^\alpha s_j^\alpha + \sum_{i, \alpha} U_{\text{loc}}(s_i^\alpha) \quad (2.26)$$

where the amplitude of the spin component variables s_i^α takes values $(-\infty, \infty)$. The convergence of the partition function is ensured by introducing the local potential U_{loc} . Translational invariance in this case leads to a simplification of the form of the exchange interaction parameters. Specifically, J_{ij} can only depend on the distance between sites i and j , i.e. $J_{ij} = J(|i - j|)$. This allows to diagonalize the bilinear terms in the sum appearing in eq. (2.26) by evaluating it in the reciprocal space. In contrast, this trick ceases to be directly applicable to spatially heterogeneous systems with broken translational invariance. Naturally, the exchange couplings describing heterogeneous systems can be cast in the form of $J_{ij} = J(|i - j|) + \delta J_{ij}$, where the Fourier transformation of δJ_{ij} will obviously generate off-diagonal contribution. Apart from the modification of the interactions between fluctuations of the order parameter at different scales, spatial heterogeneity can couple directly to the order parameter field. This is achieved by the spatial modulation of the local potential U_{loc} . The simplest case of such a modification lies in the local fields term, $-\sum_{i, \alpha} h_i^\alpha s_i^\alpha$, arising from the compositional asymmetry of the structure.

The coupling between the order parameter fluctuations and the heterogeneity scale can significantly modify the critical behaviour of the system [94], or even suppress the phase transition [95, 96, 97, 98]. The most intriguing situation of this kind is perhaps that of infinitesimally weak disorder breaking the low-temperature ordered state. The underlying mechanism of this phenomena has been heuristically proposed by Imry and Ma (IM) [95]. Considering the case of “statistically” translationally invariant system, i.e., the case of non correlated random-field type of disorder

$$\langle h_i \rangle = 0, \quad \langle h_i h_j \rangle = h^2 \delta_{ij} \quad (2.27)$$

as well as the continuous symmetry of the Hamiltonian ³, they have concluded that the ordered low-temperature state is unstable against arbitrarily weak random field in less than four dimensions. The argumentation was based on the estimate of the energy of the domain walls appearing in the case of the breaking of the globally ordered state into locally ordered microscopic domains. For the systems possessing continuous order-parameter symmetry, the domain-wall energy ϵ_{dw} is proportional to L^{d-2} , where L is the characteristic domain size and d is

³in the case of eq. (2.26), this consideration implies the continuous symmetry of U_{loc} term.

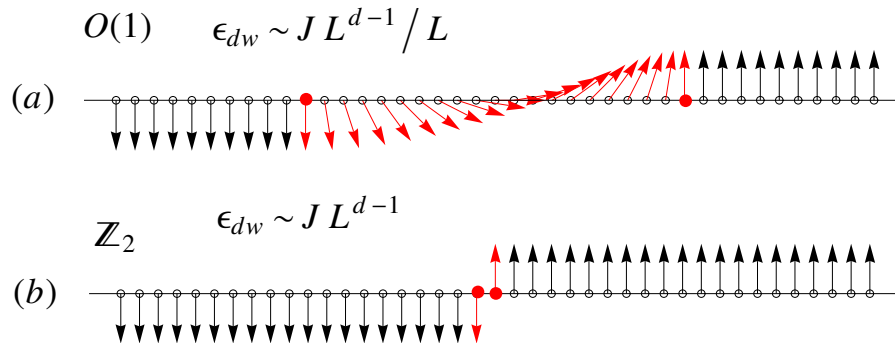


FIGURE 2.1: Schematic illustration of the domain walls corresponding to the systems of either (a) continuous or (b) discrete symmetries. In the case of the Ising model (\mathbb{Z}_2 symmetry), the domain wall energy is proportional to the surface of the wall, $\epsilon_{dw} \sim J L^{d-1}$. The possibility of continuous rotation of the spins results in the domain wall energy of $J L^{d-1}/w$, where w is the domain wall thickness. Assuming $w \sim L$ gives $\epsilon_{dw} \sim L^{d-2}$.

the topological dimension of the system. This is illustrated in Fig. 2.1, where one can see that the possibility of continuous rotation of the spins within the domain wall indeed results in a surface energy density of the order $J\pi/L$. On the other hand, within the volume of the domain, the fluctuations of the random fields might lead to a gain of the energy proportional to $\langle |\sum_L h_i| \rangle$. The averaging over configurational disorder is performed on the absolute value of the sum of the local fields within the domain since the domain magnetization is assumed to be aligned with the average field. Then, the asymptotic behaviour of the estimator $\langle |(\sum_L h_i)/L| \rangle \sim L^{-d/2}$ given by the central limit theorem leads to the estimate of a bulk energy gain contribution of the order $L^{d/2}$. The ordered state will break into domains if the bulk energy gain overcomes the energy loss due to the domain wall contribution. Therefore for $d/2 \geq d - 2$, or equivalently $d \leq 4$, there will always be a big enough size L which will allow the ferroelectric order to break into locally ordered state. The dimension $d = 4$ is therefore special and carries the name of *lower critical dimension* d_l .

Similar arguments can be also applied in the case of systems described by spin Hamiltonians with discrete symmetry. For instance, in the case of Ising model, $\epsilon_{dw} \sim L^{d-1}$ and therefore the lower critical dimension equals $d_l = 2$. More generally, in principal, the argument of Imry and Ma can be applied to any system, given that the energy contribution of the domain wall can be properly estimated⁴.

⁴L. F. Pontin et al. [101] have discussed the sensitivity of the Imry and Ma argument to a more complex geometries of the domains, specifically the possibility of the presence of the so called internal Peierls contours, or equivalently non convex domain shapes, within the context of dilute antiferromagnets in the

It is however worth noting that such illustrative considerations do not allow to conclude that the obtained critical dimension is exact. For instance, four years after the publication of Imry and Ma, G. Parisi and N. Surlas [100] have proposed a critical dimension $d_l = 3$ for the Ising model based on the argument of *dimensional reduction*, stating that there is a correspondence between the randomly disordered system in d dimensions and its pure counterpart of dimension $d - 2$. This disagreement has been resolved by the two papers [103, 104], where it has been proved that the ground state in three or more dimensions is ferromagnetic, while in dimensions less than two the ferromagnetic ordering is unstable at any given finite temperature. This confirmed the Imry and Ma intuitive argument thereby infirming the dimensional reduction conjecture.

Despite the fact that the heuristic indications of Imry and Ma have proven to be reliable for different models subject to quenched random-field disorder, the question of the exact lower critical dimensions still remains obscure. For instance, Z.-G. Ye et al. [106] have experimentally studied the validity of the IM argument in the case of ferroelectric $\text{Pb}(\text{Zr}_x\text{Ti}_{1-x})\text{O}_3$ (PZT), where the B-site disorder in the system leads to the appearance of weak quenched local fields. In their work, it has been proposed that the PZT system represents a compound described by the Hamiltonians of either discrete or continuous symmetries depending on the concentration x . It was found that the systems behaviour is in agreement with IM scenario in the vicinity of the morphotropic phase boundary, when the symmetry of the system becomes pseudo continuous. In this case where $x \sim 0.5$, the ferroelectric state corresponds to coexisting nanoscale domains strongly resembling the IM state. For compositions $0.25 < x < 0.5$, where a first-order phase transition is observed, it was suggested that the discrete-symmetry system can be described by an Ising-like Hamiltonian, thus resulting in $d_l = 2$. However, let us note that systems with discrete order-parameter symmetry can be far more complex, and thus should be handled with care. As an example, one can mention the exactly solvable spherical model with cubic anisotropy, for which it has been shown that $d_l = 4$ [96].

Among other studies assessing the validity of the Imry and Ma argument, we would like to mention a recent work by T. C. Proctor et al. [105], where the energy balance statement proposed in [95] was modified in order to capture the energy contribution appearing from the unavoidable singularities in the order parameter vector field associated with the crossing points of the domain boundaries (see

presence of an external magnetic field. They have concluded that in the case of $d \geq 3$ such structures are necessary to consider and the IM argument by itself is not sufficient for a proof of a phase transition.

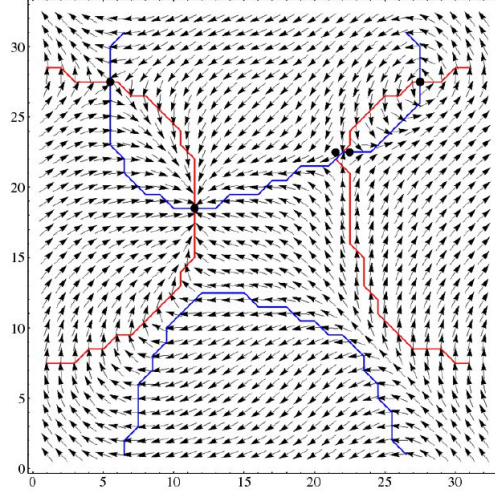


FIGURE 2.2: Topological defects appearing at the crossing points of the domain walls. Two different types of the boundaries depicted as red and blue curves are associated with $h_i^x = 0$ and h_i^y conditions. The crossing points, where the magnitude of the local field vanishes $\mathbf{h}_i = 0$, represent the topological defect pinning centres. In the specific case of the two component Heisenberg model in 2D, the topological defects correspond to the well known vortex and anti-vortex field configurations. (After T. C. Proctor *et al.* [105])

Fig. 2.2). Considering the general n -component classical Heisenberg model, the authors have suggested that IM construction holds only for $n > d + 1$ where the generation of topological defects is impossible. In this case, topologically protected configurations of the vector field are absent and the ground state is unique and independent of the initial conditions of the relaxation. In case of violation of this inequality, as illustrated by the three dimensional Heisenberg model on three dimensional lattices, the energy contributions associated with the hedgehog-type topological defects has to be taken into account. Moreover, the presence of random fields leads to the locally reduced activation energy of the topological defects. Therefore, the hedgehogs appearing in the vicinity of the pinning centres in the course of relaxation towards the IM state form a metastable state (see Fig. 2.3) protected topologically by the condition of topological charge conservation. The dependence of the relaxation process on initial conditions is all the more pronounced with increasing d and decreasing n . Indeed, the measure of the topological defects set increases, resulting in a considerable contribution to the energy of the system. Latter can be seen in Fig. 2.4, where the variation of the average supercell magnetization in the course of Monte-Carlo simulation is presented for $d = 3$ and $n = \{2, 3, 4, 5\}$. In the case of $n \leq 5 = d + 2$, the presence of topological defects leads to a nonzero value of the average magnetization, clearly indicating a deviation from IM domain state characterized by $m = \langle s_i \rangle = 0$.

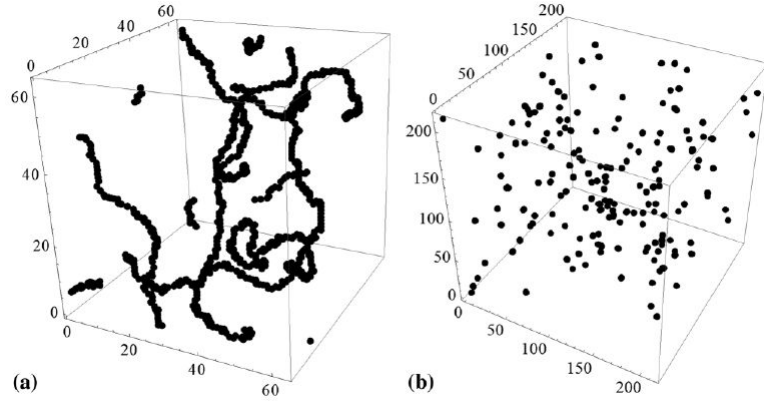


FIGURE 2.3: Schematic illustration of metastable, topologically protected states in 3D for (a) XY model ($n = 2$) and (b) classical Heisenberg model ($n = 3$). In the former case, the vortex points schematically depicted in Fig. 2.2 coalesce, forming the vortex lines. In the case of the classical Heisenberg spin model the point hedgehog defects form a set of dimension zero. (After T. C. Proctor *et al.* [105])

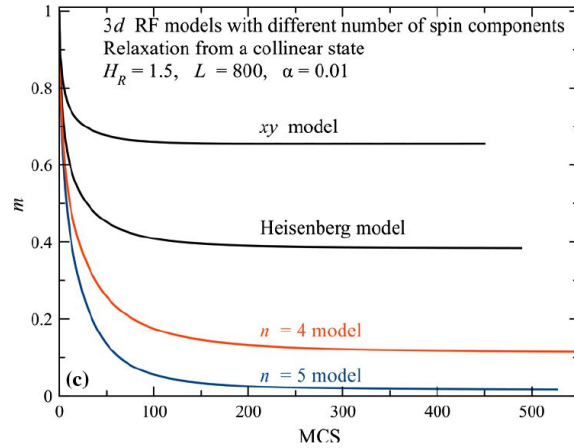


FIGURE 2.4: Relaxation of the average magnetization from the initial ordered state for the spin systems characterized by dimensions $d = 3$ and $n = \{2, 3, 4, 5\}$. MCS stands for a full lattice update of the spins, i.e. one Monte Carlo simulation sweep. (After T. C. Proctor *et al.* [105])

We have just discussed the influence of structural disorder that manifests in the coupling of the order parameter to randomly distributed local fields on the behaviour of the system in the case of $d \leq d_l$. While for $d \leq d_l$, arbitrarily weak disorder prevents the occurrence of the phase transition, above the lower critical dimension the situation is different. Specifically, it is expected that there will always be a strong enough field sufficient to destabilize the ground state [99]. Under the assumption of the zero mean local field value $\langle h_i \rangle = 0$, the strength of disorder is governed by the variance $\langle h_i^2 \rangle$. In this case, the approximate shape of the Temperature-Random-field phase diagram resembles that of the three dimensional random-field Ising ferromagnet (see Fig. 2.5). The two transition lines correspond to the true equilibrium phase transition (blue curve) and to the onset

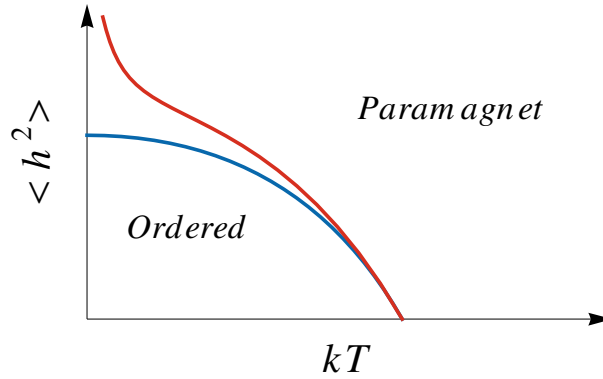


FIGURE 2.5: Schematic phase diagram of the three-dimensional random-field magnets. The blue curve corresponds to the true, equilibrium phase transition line, while the red curve marks the onset of irreversible hysteretic behaviour. (Adapted from D. S. Fisher *et al.* [107])

of irreversible hysteretic behaviour (red line). Unfortunately, as it is the case for $d \leq d_l$, an analytical treatment of the problem is hardly achievable. Among the general approximations, one can envisage the *replica trick* based methods. While being relatively simple, these approaches allow to access the approximate solution in a closed analytical form. A remarkable example of the application of the replica based mean-field theory to real compounds lies in the spherical random bond random field model (SRFRB) of R. Pirc and R. Blinc [108].

2.4 Second principles models: Effective Hamiltonian approach

In the previous sections, we have discussed some specific aspects of spin lattice models without exploring in detail the origin of the parameters of the effective Hamiltonian itself. This section will be devoted to the description of the method that enables linking together the lattice models of statistical physics with *ab initio* approaches.

2.4.1 Perovskite compounds

In the case of perovskite compounds, the explicit link between first-principles calculations and microscopic lattices models that are formulated in terms of reduced basis of local modes has been developed in the works of K. Rabe, Z. Zhong, D. Vanderbilt and U. Waghmare (see [148, 146] and references therein). Specifically, the authors have shown that frozen-phonon calculations performed within LDA

approximation yield reliable estimates of the expansion coefficients. Moreover, the authors have introduced several approximations, which allowed to drastically reduce the computational complexity of the proposed scheme, such as the approximation of local anharmonicity. In this section, we will follow the works given in Ref. [148, 146, 110, 111] and describe in detail the construction of effective Hamiltonian models for BaTiO₃ and BiFeO₃ compounds.

Considering the perovskite crystalline lattice structure, one can construct the localized basis using a set of local mode vectors $\{\mathbf{u}_i\}$ parametrizing the Γ_{15} optical phonon branch, a set $\{\boldsymbol{\omega}_i\}$ describing the oxygen octahedra tilts, and a set of vectors $\{\mathbf{v}_i\}$ representing the acoustic phonon modes. In order to keep the discussion as general as possible, each of these sets of variables will be equivalently denoted by $\{\boldsymbol{\xi}_{\Lambda i}\}$ with different phonon branch index Λ . The tilt variables are especially important for constructing the effective Hamiltonian of BiFeO₃. Moreover, in order to describe the multiferroic behaviour of this compound, it is as well necessary to introduce the set of spin variables $\{\mathbf{m}_i\}$ representing the magnetic moments of Fe³⁺ cations.

Assuming that the atomic displacements from the reference structure are small, one can expand the energy of the system in terms of the components of the introduced variables $\{\xi_{\Lambda i}^\alpha\}$. The terms of such Taylor expansion series can be conveniently classified according to the range of interactions and their nature. First, it appears profitable to separate the terms diagonal in phonon branch indexes Λ . These terms will be denoted as $H_\Lambda(\{\boldsymbol{\xi}_{\Lambda i}\})$. The interactions between phonon modes transforming according to different irreducible representations are assumed to be "pairwise" in the Λ space. They are described by off-diagonal functions $H_{\Lambda\Lambda'}(\{\boldsymbol{\xi}_{\Lambda i}\}, \{\boldsymbol{\xi}_{\Lambda' i}\})$. Therefore, using the introduced notations the effective Hamiltonian can be written as

$$H_{eff} = \sum_{\Lambda} H_{\Lambda}(\{\boldsymbol{\xi}_{\Lambda i}\}) + \frac{1}{2} \sum_{\Lambda, \Lambda'} H_{\Lambda\Lambda'}(\{\boldsymbol{\xi}_{\Lambda i}\}, \{\boldsymbol{\xi}_{\Lambda' i}\}) + H_{mag}(\{\mathbf{m}_i\}, \{\boldsymbol{\xi}_{\Lambda i}\}) \quad (2.28)$$

The last term, $H_{mag}(\{\mathbf{m}_i\}, \{\boldsymbol{\xi}_{\Lambda i}\})$, describes the magnetic energy of the system. It stands separately from the energy contributions associated with displacements of the ions, since H_{mag} should be invariant under the action of the elements of the magnetic space group of the prototype phase. Similarly to the decomposition of the energy terms associated with lattice vibrations, one can deconstruct H_{mag} into purely spin Hamiltonian and the interaction of the spins with the phonon modes

$$H_{mag} = H_M(\{\mathbf{m}_i\}) + \sum_{\Lambda} H_{M,\Lambda}(\{\boldsymbol{\xi}_{\Lambda i}\}) \quad (2.29)$$

The functions H_{Λ} and H_M can be further decomposed into terms describing the local energy contributions, short-range and long-range interactions. Once again, this decomposition can be formally achieved by separating diagonal and off diagonal terms. The on-site energies correspond to the diagonal elements of the interaction tensors, however this time one considers the spatial indexes i . The long-range interactions describe the electrostatic (or magnetostatic) energy of the system of interacting dipoles. This contribution slowly decays with distance between sites as $\sim 1/R_{ij}^5$. The remaining energy contributions are referred to as short-range interactions.

In order to reduce the number of coefficients appearing in the Taylor expansion of the energy, it is reasonable to take the high symmetry phase as the reference structure. In the case of perovskite lattice, the reference cubic structure is described by $Pm3m$ (221) space group. Since the variables $\{\boldsymbol{\xi}_{\Lambda}\}$ transform according to different irreducible representations, it is required to construct each of the energy terms described above individually. First we will start with the description of the energy contributions associated with the local modes $\{\mathbf{u}_i\}$.

By definition, the variables $\{\mathbf{u}_i\}$ transform according to Γ_{15} irreducible representation. In other words, variables \mathbf{u}_i are polar vectors. Therefore, the construction of the on-site energy term is fairly straightforward. Specifically, invariance under the action of the elements of the cubic O_h point group requires it to be a symmetric polynomial containing only even powers of the local mode cartesian components $u_{i,\alpha}$. Truncating the series at the order of $u_{i,\alpha}^4$, one obtains

$$\begin{aligned} H_{loc}(\{\mathbf{u}_i\}) &= \sum_i (\kappa(u_{ix}^2 + u_{iy}^2 + u_{iz}^2) + \alpha(u_{ix}^2 u_{iy}^2 + u_{iy}^2 u_{iz}^2 + u_{ix}^2 u_{iz}^2)) \\ &+ \gamma(u_{ix}^4 + u_{iy}^4 + u_{iz}^4) \end{aligned} \quad (2.30)$$

where the summation goes over all the unit cells of the crystalline lattice. It is important to remember that truncating the series at the fourth power of local mode components, strictly speaking, imposes a constraint on the construction of other energy terms. Indeed, in order to conserve the accuracy it is required to keep all the interactions up to the same order of magnitude in $u_{i,\alpha}$. This mainly applies to the short range interactions since the electrostatic multipole energy terms that are higher than the dipolar ones can usually be neglected. On the other

hand, this leads to a rather big set of interaction parameters requiring, as we will later see, a large number of frozen phonon first-principles calculations. In order to relieve the involved computational effort, one introduces the approximation of "local anharmonicity" by keeping the short range interaction terms bilinear. Under this assumption, the short-range interaction energy of the local modes takes the form of Heisenberg exchange interaction

$$H_{sr}(\{\mathbf{u}_i\}) = \sum'_{ij} J_{ij}^{\alpha\beta} u_{i\alpha} u_{j\beta} \quad (2.31)$$

The prime symbol indicates that only off-diagonal terms, i.e. $i \neq j$, are participating in the summation. The number of independent short-range interaction parameters $J_{ij}^{\alpha\beta}$ can be obtained by considering the constraint of symmetry of the reference phase. Generally, given a certain distance R_{ij} between the local mode sites, the maximum number of independent coefficients is equal to six. This follows from the invariance of the tensor components $J_{ij}^{\alpha\beta}$ under the permutation of the Cartesian indexes α and β . This property does not depend on the symmetry of the reference phase and results from the bilinear nature of the term H_{sr} . Taking into account the symmetry of the prototype phase allows to further reduce the amount of independent interaction parameters. For instance, considering the symmetry of the first nearest neighbours link, one can immediately conclude that the off-diagonal components of the tensor J_{ij} are equal to zero. Indeed, the presence of the mirror planes always allows to find the symmetry operation reversing the sign of the product $u_{i\alpha} u_{j\beta}$ for $R_{ij} = a_0$ and $\alpha \neq \beta$. Furthermore, in contrast to the case of the quadratic on-site energy contributions given by eq. (2.30), the cubic anisotropy splits the diagonal terms $J_{ij}^{\alpha\alpha}$. This can be simply seen by remembering that the Hamiltonian of the system should be invariant under the rotations around the axes passing through the edges of the conventional cubic unit cell. This operation not only acts on the local mode components, but also permutes the lattice site indexes. Therefore, keeping this consideration in mind, one arrives at the conclusion that the first nearest neighbours interactions can be described by two independent parameters which we will denote by j_1 and j_2 . Specifically, the j_1 coefficient describes the interaction of local mode components perpendicular to the link connecting sites i and j , while j_2 is ascribed to the interactions of the components parallel to this link. This is schematically depicted in Fig. 2.6.

Similar considerations can be used to derive the number of independent parameters describing interactions of the second and third nearest neighbours. These

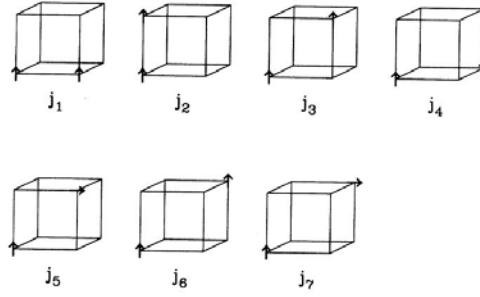


FIGURE 2.6: Schematic representation of independent short-range interaction parameters. For the first nearest neighbours interactions can be described using two different constants j_1 and j_2 . They correspond to the interaction of local mode components parallel and perpendicular to the link connecting sites i and j , respectively. The coefficients j_{3-5} describe the interactions between second nearest neighbours, while the two constants j_6 and j_7 corresponds to third nearest neighbours interactions. (After W. Zhong *et al.* [148])

considerations lead to three coefficients associated with the interactions between second nearest neighbours, and to two coefficients associated with the third nearest neighbours interactions. All the introduced parameters can be generally expressed in the following way

$$1\text{NN} : J_{ij}^{\alpha\beta} = (j_1 + (j_2 - j_1)|R_{ij}^\alpha|)\delta_{\alpha\beta} \quad (2.32)$$

$$2\text{NN} : J_{ij}^{\alpha\beta} = (j_3 + \sqrt{2}(j_4 - j_3)|R_{ij}^\alpha|)\delta_{\alpha\beta} + 2j_5|R_{ij}^\alpha||R_{ij}^\beta|(1 - \delta_{\alpha\beta}) \quad (2.33)$$

$$3\text{NN} : J_{ij}^{\alpha\beta} = j_6\delta_{\alpha\beta} + 3j_7|R_{ij}^\alpha||R_{ij}^\beta|(1 - \delta_{\alpha\beta}) \quad (2.34)$$

where R_{ij}^α denotes the Cartesian components of the normalized vector connecting sites i and j . Similarly to the case of the first nearest neighbours interactions, the schematic representations of interactions described by coefficients j_{3-7} are summarized in Fig. 2.6.

By definition, the short-range interaction coefficients are assumed to decay exponentially with the distance between the interacting local mode sites. Therefore, it is sensible to introduce a certain radial cut-off beyond which the short-range interaction terms are neglected. For the perovskite compounds, it has been shown that keeping short-range interactions only up to the third nearest neighbours does not introduce significant errors and allows for a satisfactory description of the phonon dispersion branches throughout the volume of the first Brillouin zone.

The link between first-principles calculations and lattice model described by eq. (2.28) can be maintained via the so called frozen-phonon calculations scheme. This procedure allows to estimate the coefficients introduced in eqs. (2.30, 2.31). For this one

performs DFT calculations for the supercells depicted in Fig. 2.7. The displacements of the cations are fixed, i.e. the structural relaxation is not performed. This allows to obtain a set of values for the energies of different atomic displacement patterns corresponding to the set of different local modes states. Latter, in fact, allows to construct a linear system of equations determining the coefficients j_{1-7} and the on-site parameters κ, α and γ .

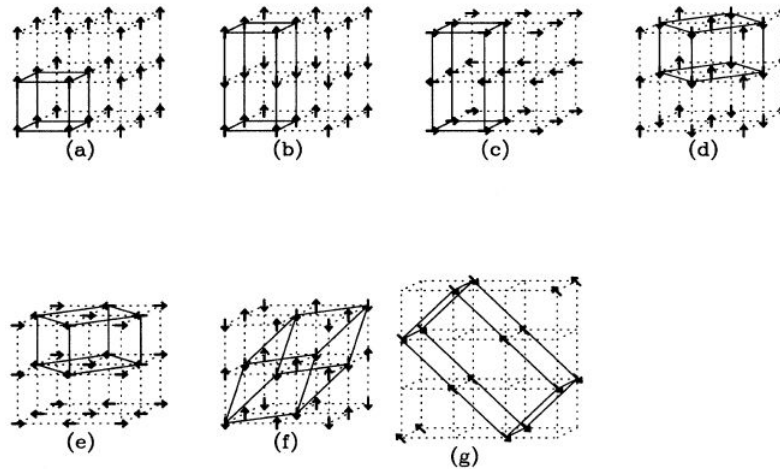


FIGURE 2.7: The schematic representation of the supercells used in the frozen-phonon calculations. Calculating the energy for different atomic displacements corresponding to a certain distribution of local modes allows to obtain the estimates for the interaction coefficients j_{1-7} and the on-site coefficients κ, α, γ . (After W. Zhong *et al.* [148])

Notably, the recent development of the first-principles methods has lead to the adoption of another, probably, more practical way of estimating the on-site and short-range interaction coefficients using the density functional perturbation theory techniques (see [109] for a recent review).

Another, bilinear term appearing in the expression of $H_u(\{\mathbf{u}_i\})$ is associated with the long-range dipolar interactions between the local modes located at different sites. Its expression has a form similar to that of eq. (2.31), with the interaction coefficients $D_{ij}^{\alpha\beta}$ equal to [148]

$$D_{ij}^{\alpha\beta} = \frac{2Z^{*2}}{\varepsilon_\infty} \left[\sum_{\mathbf{G} \neq 0} \frac{\pi}{\Omega_c} \frac{1}{|\mathbf{G}|^2} \exp\left(-\frac{|\mathbf{G}|^2}{4\lambda^2}\right) \cos(\mathbf{R}_{ij} \cdot \mathbf{G}) G_\alpha G_\beta - \frac{\lambda^3}{3\sqrt{\pi}} \delta_{\alpha\beta} \delta_{ij} \right] \quad (2.35)$$

where the summation is carried out over the reciprocal lattice vectors \mathbf{G} . Z^* denotes the Born effective charge associated with the local modes u , while ε_∞ is the optical dielectric constant of the material. Parameter λ controls the convergence

of the series. The sum of the on-site “ ϕ^4 ” terms, the short-range harmonic interactions and the dipole-dipole interaction described above constitute together the Λ -diagonal terms $H_\Lambda(\{\boldsymbol{\xi}_\Lambda\})$ of the effective Hamiltonian H_{eff} .

The form of the energy of the AFD degrees of freedom $\{\boldsymbol{\omega}_i\}$ have the same form as the one associated with the local modes $\{\mathbf{u}_i\}$ describing the ferroelectric phase transition. The only two differences reside in (i) the symmetry consideration allowing to reduce the number of the independent short-range interaction coefficients and (ii) the absence of the long range dipolar interactions. Therefore, the energy contribution associated with the oxygen octahedra tilts can be written as [110]

$$H_\omega = \sum_i (\kappa_A \omega_i^2 + \alpha_A \omega_i^4 + \gamma_A (\omega_{ix} \omega_{iy} + \omega_{ix} \omega_{iz} + \omega_{iy} \omega_{iz})) + \sum_{ij, \alpha\beta} K_{ij}^{\alpha\beta} \omega_{i\alpha} \omega_{j\beta} \quad (2.36)$$

The magnetic part of the Hamiltonian, has the form resembling that of the modified classical Heisenberg model. Following [111], in addition to the magnetic exchange interactions, we also include the contribution of the magnetic dipole-dipole interactions, along with the interactions with other degrees of freedom, namely the AFD $\{\boldsymbol{\omega}_i\}$ variables, local modes $\{\mathbf{u}_i\}$ and the local strain tensors $\eta_{i,\alpha\beta}$.

Both the interactions within the set of degrees of freedom related to atomic displacements and their interactions with the spin variables have essentially the same biquadratic form. Specifically [110, 111], the off-diagonal term $H_{u,\omega}(\{\mathbf{u}_i\}, \{\boldsymbol{\omega}_i\})$ is given by the on-site contribution

$$H_{u,\omega}(\{\mathbf{u}_i\}, \{\boldsymbol{\omega}_i\}) = \sum_i F^{\alpha\beta\gamma\delta} u_{i\alpha} u_{i\beta} \omega_{i\gamma} \omega_{i\delta} \quad (2.37)$$

while the interaction of the local mode degrees of freedom $\{\boldsymbol{\xi}_i\} = \{\mathbf{u}_i, \boldsymbol{\omega}_i\}$ with $\{\mathbf{m}_i\}$ reduces to the modification of the Heisenberg exchange interaction constants

$$H_{M,\Lambda}(\{\boldsymbol{\xi}_i\}, \{\mathbf{m}_i\}) = \sum_{i,j} \delta J^{\alpha\beta\gamma\delta} \xi_{i\alpha} \xi_{i\beta} m_{i\gamma} m_{j\delta} \quad (2.38)$$

along with the appearance of the induced Dzyaloshinskii-Moriya antisymmetric exchange

$$H_{DM}(\{\boldsymbol{\omega}_i\}, \{\mathbf{m}_i\}) = \sum_{i,j} K_{ij} (\boldsymbol{\omega}_i - \boldsymbol{\omega}_j) \cdot (\mathbf{m}_i \times \mathbf{m}_j) \quad (2.39)$$

Finally, the part of the Hamiltonian associated with the elastic deformations of the crystal is expressed in terms of the local strain tensor variables as [148, 110, 111]

$$H_\eta(\{\eta_i\}, \{\xi_i\}, \{\mathbf{m}_i\}) = \sum_i \left(C^{ll'} \eta_{i,l} \eta_{i,l'} + q^{l\alpha\beta} \eta_{i,l} \xi_{i\alpha} \xi_{i\beta} \right) + \sum_{ij} d_{ij}^{l\alpha\beta} \eta_{i,l} m_{i\alpha} m_{j\beta} \quad (2.40)$$

where the components of the strain tensor in the unit cell i are denoted by $\eta_{i,l}$ with the Voigt component index l . The variables $C^{ll'}$, $q^{l\alpha\beta}$ and $d_{ij}^{l\alpha\beta}$ denote the microscopic elastic moduli, piezoelectric and local piezomagnetic tensor components.

2.4.2 Monte Carlo simulations

Let us now consider the problem of evaluating the static equilibrium properties of the system at finite temperature T . For this, as a starting point, we will assume that the system's Hamiltonian, which defines the energy of the system at each point of the configuration space, is known. After achieving the thermodynamic equilibrium, the probability π_s of the system to be found in a specific point s of configuration space is proportional to the Boltzmann factor $\pi_s \sim e^{-E_s/kT}$. The temperature-dependent coefficient of proportionality is the partition function $Z(T) = \sum_s e^{-E_s/kT}$, where E_s denotes the classical energy of the system in the state s . Once the normalization factor $Z(T)$ is evaluated, any thermodynamic average $\langle A \rangle$ of the macroscopic variable A is given by

$$\langle A \rangle = \frac{1}{Z(T)} \sum_s A_s e^{-E_s/kT} \quad (2.41)$$

where A_s denotes the value of the macroscopic variable A for the system in the state s . In practice, in the specific case of strongly interacting many-body systems, the evaluation of the sums of the type given in eq. (2.41) represents an extremely complex problem. Therefore, facing the practical impossibility of obtaining the exact solution, one has to choose between resorting to either analytical approximations or numerical integration techniques.

In this study we have chosen to resort to the second option by implementing the commonly used Metropolis-Hastings algorithm. This method belongs to the family of Markov chain Monte Carlo schemes and is therefore technically simple and straightforward to implement. Moreover, it has proven to be reliable for obtaining finite-temperature properties of ferroelectric systems described by the Hamiltonians presented in the previous sections.

We will here briefly describe the method along with the main drawbacks and artefacts common to Markov-chain Monte Carlo schemes.

★ *Metropolis-Hastings algorithm*

Usually, the direct numerical sampling of the Boltzmann distribution (or equivalently the numerical integration of the partition function using either a regular or a random uniform mesh) associated with a strongly interacting many-body system is difficult given that only a small fraction of the configuration space volume gives a non-negligible contribution to the partition function. These regions are hard to identify since the the properties of a multivariate energy landscape cannot be easily predicted. The Markov chain Monte Carlo integration scheme avoids this problem by sampling a set of distributions π^t with $t \in \mathbb{Z}$ and $\lim_{t \rightarrow \infty} \pi^t = \pi$. This is achieved by constructing a Markov chain at each time step t of which the transition probabilities $P_{s1 \rightarrow s2}$ between two states $s1$ and $s2$ of the system satisfy the conditions of *ergodicity* and *global balance*. These conditions which ensure that the Markov chain exponentially converges with Monte Carlo time t to a unique limiting distribution π^t can be defined as follows

- 1.) *Ergodicity* is satisfied if each state s of the chain is aperiodic (i.e., there is no period T at which the state i occurs), but has a finite recurrence time.
- 2.) *Global balance* condition requires that the flow into each configuration at each step t is equal to the flow out of it, specifically

$$\sum_{s2} P_{s \rightarrow s2} = \sum_{s2} P_{s2 \rightarrow s} \quad (2.42)$$

The Metropolis-Hastings algorithm satisfies the global balance condition by imposing a more strict condition of local or *detailed balance*. Indeed, one can easily note that eq. (2.42) is satisfied in particular if $P_{s \rightarrow s2} = P_{s2 \rightarrow s}$. Moreover, within the Metropolis algorithm the choice of the transition probability is given by $P_{s1 \rightarrow s2} = \min(\pi_{s1}, \pi_{s2})$. In terms of a more practical conditional probabilities $p_{s1 \rightarrow s2} = P_{s1 \rightarrow s2} / \pi_{s1}$, latter can be rewritten in a commonly used form

$$p_{s1 \rightarrow s2} = \min(1, \pi_{s2} / \pi_{s1}) \quad (2.43)$$

Equation (2.43) is advantageous for applications in statistical physics since at each Monte Carlo time step t , one only needs to know the ratio of Boltzmann probabilities π_s , which alleviate us from the need of knowing beforehand the partition

function $Z(T)$. Notably, the presented choice of the transition probability is not the only one satisfying the global balance and ergodicity conditions. This means that there are many different valid Monte Carlo algorithms, and probably even more to be discovered.

On the other hand, any algorithm which follows the general scheme described in this section will most probably suffer from some drawbacks common to Markov Chain Monte Carlo Methods. For instance, while the exponential convergence to the target distribution, i.e. $(\pi^t - \pi) \propto e^{-t/\tau}$, is ensured by the conditions enlisted above, the convergence interval, or in other words the correlation time τ , can be rather difficult to estimate. Usually, the estimate of τ is obtained by performing preliminary numerical experiments for each specific model Hamiltonian under investigation. In the case of the model Hamiltonian describing the ferroelectric phase transition, the correlation time was estimated to be equal to $\tau \approx 100$ Monte Carlo sweeps. Similarly, it was “experimentally” found that for the specific case of BaTiO₃, the necessary amount of Monte Carlo simulation sweeps ensuring acceptable quality of statistical averages is of the order of $\approx 10^4$.

Among other technical difficulties associated with the use of Monte Carlo methods are the finite-size scaling and the estimation of the variance for the obtained observables. Both questions deserve special attention and have been extensively discussed in literature devoted to numerical simulation methods (see for instance [114, 115]). For the specific example of BaTiO₃, the acceptable simulation cell size was found to be equal to 12x12x12=1728 unit cells, i.e. the cubic supercell with the size of 12 unit cells along each of the Cartesian directions.

★ *Estimates of the linear response coefficients*

Interestingly, the Markov Chain Monte Carlo methods give a direct access not only to the thermodynamic averages of the macroscopic observables A , such as average polarization, homogeneous strain components, etc., but also to their derivatives $\partial A/\partial \mathcal{E}$ with respect to the conjugated forces \mathcal{E} . Specifically, given the Hamiltonian of the form $\tilde{H} = H - A\mathcal{E}$, where H does not explicitly depend on the force \mathcal{E} , the derivatives $\partial^m A/\partial \mathcal{E}^m$ can be readily expressed via the moments of the variable A . For instance,

$$\frac{\partial A}{\partial \mathcal{E}} = \frac{\partial \sum_s A_s e^{-\tilde{H}_s/kT}}{\partial \mathcal{E} \sum_s e^{-\tilde{H}_s/kT}} = \frac{1}{kT} (\langle A^2 \rangle - \langle A \rangle^2) = \frac{\kappa_2(A)}{kT} \quad (2.44)$$

Generally, the m -th derivative is equal to the cumulant $\kappa_m(A)/(kT)^m$.

2.4.3 Temperature dependent ME effect

Despite all the possible technical issues, the Metropolis Monte Carlo Simulations introduced in the previous section can give reliable estimates for the values of the magnetoelectric coupling coefficients. One of the recent examples of the success of Monte Carlo methods lies in the work of M. Mostovoy *et al.* [116], where the temperature-dependent magnetoelectric effect exhibited by a prototypical magnetoelectric oxide Cr_2O_3 has been evaluated from a first-principles based model.

Following the approach described in the previous chapters, the authors have constructed a rather simple Heisenberg-type classical spin model in order to describe the magnetoelectric properties of Cr_2O_3 . The bare exchange and magnetoelectric interaction coefficients of the model were fitted to first principles calculations. The

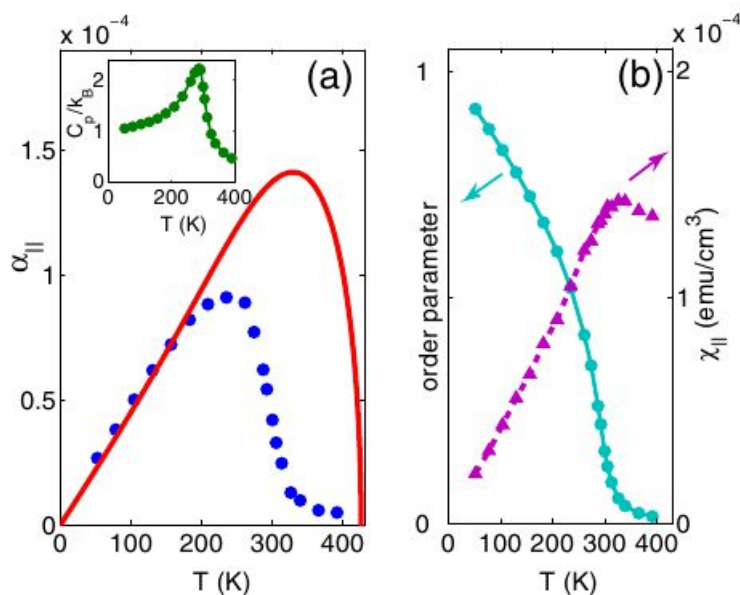


FIGURE 2.8: (a) Temperature dependence of the magnetoelectric coupling obtained from Monte Carlo simulations (blue circles) and mean-field calculations (solid red line). (b) Evolution of the antiferromagnetic order parameter and the magnetic susceptibility with temperature. (After M. Mostovoy *et al.* [116])

fluctuation renormalized exchange-driven longitudinal magnetoelectric coefficient obtained within the same model from Monte Carlo simulations or using the mean field approximation are presented in figure 2.8a. Comparing these results to the experiments, one can see that the mean-field transition temperature is significantly overestimated, while the value obtained from Monte Carlo simulations is in good agreement with the experimental data.

Despite the significance of the aforementioned work [116], the authors have employed a substantially simplified model, accounting for the ferroelectric degrees

of freedom only effectively. Therefore, in order to obtain the values of magnetoelectric coupling, it was only necessary to calculate the magnetic susceptibility along with the temperature dependence of the antiferromagnetic order parameter. Let us note that a more complex model, especially for describing systems possessing structural inhomogeneity, could lead to a drastic decrease of the quality of the Monte Carlo estimates of the linear response functions, such as dielectric, magnetic and magnetoelectric susceptibilities. Indeed, given a relatively small magnitude of the magnetoelectric coupling, the correlated changes of the average magnetization and polarization of the system can be significantly smaller than the standard deviation of the predicted susceptibilities.

Therefore it is not surprising that the number of works devoted to studying the temperature dependence of magnetoelectric coefficients using Monte Carlo techniques is rather small. Among them one can mention a study of J.-M. Liu et al. [117] devoted to the investigation of the effect of bare magnetoelectric coupling magnitude on the finite-temperature properties of the system.

Chapter 3

Effective Hamiltonian approach for heterogeneous systems

In this chapter we present a study of possible generalizations of the effective Hamiltonian method applicable to nanocomposite systems. In contrast to the existing generalised approaches commonly relying on the virtual crystal approximation (VCA) [144, 143, 145] (and thereby limited to describing compounds comprising chemically close constituent materials), we resort to simple phenomenological approximations, which allow us to reduce the computational complexity of the scheme while capturing the main physical features of the system.

In order to explore the validity of the introduced approximations, we apply the constructed model to study the finite-temperature properties of $(\text{BiFeO}_3)_x(\text{BaTiO}_3)_{1-x}$ solid solutions and nanocomposites. The theoretical description of this specific system represents an interesting challenge. Indeed, on the one hand, the application of VCA approximation for such compounds is not straightforward due to several inter-related lattice instabilities occurring along with antiferromagnetic phase transition in BiFeO_3 . On the other hand, the theoretical investigation of the properties of this compounds appears to be appealing due to the experimentally discovered unusual ferroelectric behaviour of $(\text{BiFeO}_3)_x(\text{BaTiO}_3)_{1-x}$ solid solutions [128, 140, 142].

The comparison of the proposed model with both first-principles calculations and experimental results allows us to justify the employed approximations, while the

obtained results give the necessary microscopical insight into the mechanism driving the pseudocubic phase formation [139, 140] in $(\text{BiFeO}_3)_x(\text{BaTiO}_3)_{1-x}$ compounds. The assessment of the model is continued with a study of the multiferroic properties of $(\text{BiFeO}_3)(\text{BaTiO}_3)$ bicrystals with different lattice geometries. Finally, in order to show the importance of the impact of the geometry of the composite material on its properties, we present a study of a “toy model” system — ferroelectric $(\text{Ba,Sr})\text{TiO}_3$ fractal nanostructures.

3.1 Model: methodology and assessment

3.1.1 Introductory background

Multiferroic compounds represent a quickly growing family of materials, having undeniable importance for both fundamental physics and cutting edge technological applications [119, 120, 121, 122, 123]. Among them, promising candidates are complex perovskite compounds, namely nanostructured composites [124, 125, 126] and solid solutions [127, 128, 129] comprising single phase multiferroic BiFeO_3 [130].

In order to reveal the full potential of bismuth ferrite hindered by relatively high conductivity, solid solutions with insulating perovskite materials have been fabricated [129, 132, 133]. It has been shown that partially substituting either Bi^{3+} or Fe^{3+} cations by Ba^{2+} [135, 134] or Ti^{4+} [136, 137] respectively, leads to improved ferromagnetic and ferroelectric properties, while substituting both cations simultaneously suppresses ferroelectric order in $(\text{BiFeO}_3)_x(\text{BaTiO}_3)_{1-x}$ solid solutions [138, 139, 140, 142]. Surprisingly, in contrast to the scenario of a crossover between the two systems through a sequence of phases with intermediate symmetries, it was unexpectedly observed [138, 139, 140] that increasing barium titanate content leads to a structural phase transition from a parent $R3c$ phase to pseudocubic $Pm\bar{3}m$ phase at a critical concentration x_c'' . Similar phenomenon was observed for solid solutions rich in barium titanate: upon increasing x , the tetragonal distortion of the lattice inherited from BaTiO_3 gradually reduces, vanishing at the critical concentration x_c' . The physical nature of the aforementioned $Pm\bar{3}m$ phase has been debated in literature, and is yet to be uncovered. Indeed, quantitative disagreement among experimental values of critical concentrations x_c' and x_c'' [138, 139, 140] on one hand, and the absence of theoretical studies on the other, have lead to vagueness in interpretations. For instance, in a study of A. Singh *et*

al. [139], the pseudocubic phase formation was attributed to the presence of random electric fields and strain. Furthermore, it was suggested that the observed diffuseness of the dielectric response peak results from the cooperative freezing of off-centered Bi^{3+} ions in $\langle 001 \rangle$ directions, while no relaxation of the dielectric response was reported. In a subsequent paper [140], the authors then indicated that the A-site ($\text{Bi}^{3+}/\text{Ba}^{2+}$) positional disorder gives rise to locally monoclinic structure with polarization vector continuously rotating from $[001]$ to $[111]$ pseudocubic direction, whereas Gotardo *et al* [142] proposed a model based on the coexistence of local tetragonal and monoclinic symmetries.

In this section we will present an effective-Hamiltonian model able to predict finite-temperature properties of multiferroic solid-solutions and nanocomposite materials along with its comparison with first-principles calculations and experimental results.

3.1.2 Methodology

Conventionally, the effective Hamiltonian is built using a reduced set of degrees of freedom [147, 146] parametrizing unstable phonon branches (set of local modes $\{\mathbf{u}_i\}$ proportional to dipole moments in each unit cell i [148] and $\{\boldsymbol{\omega}_i\}$ representing octahedra tilts [149]), acoustic phonons (local strain tensors $\{\eta_i^{\alpha\beta}\}$ [148]) and magnetic moments of the ions $\{\mathbf{m}_i\}$ [149]. The energy of the crystal can be split into several parts depending on the nature and range of the interactions

$$H_{eff} = H_{loc}(\{\mathbf{u}_i, \boldsymbol{\omega}_i, \mathbf{m}_i\}) + H_{dip}(\{\mathbf{u}_i, \mathbf{m}_i\}) + H_{str}(\{\eta_i^{\alpha\beta}\}, \{\mathbf{u}_i, \boldsymbol{\omega}_i, \mathbf{m}_i\}) \quad (3.1)$$

Here H_{loc} denotes the combination of on-site energy and nearest neighbours (short-range) interactions while H_{dip} represents long-range dipolar interactions. The last term H_{str} is associated with elastic deformations of the crystal and contains contributions of the self energy of acoustic phonons and their interactions with other degrees of freedom [148]. In order to construct an effective Hamiltonian model for a compositionally heterogeneous material, we assume that the effective Hamiltonians of constituent compounds are known. In the specific case under study, we refer to them as H_{eff}^{bto} for the effective Hamiltonian of pure BaTiO_3 [148] and H_{eff}^{bfo} for that of BiFeO_3 [149]. Then, the local contribution $H_{loc}(\{\mathbf{u}_i\})$ associated with

the local mode degrees of freedom only can be represented in the following way

$$H_{loc}(\{\mathbf{u}_i\}) = \sum_{i=1}^N \left(\sigma_i H_{loc\,i}^{bto} + (1 - \sigma_i) H_{loc\,i}^{bfo} + \delta H_i \right), \quad (3.2)$$

where the summation goes over all N sites i of the lattice carrying local mode vectors. Formally, in the used parametrizations [148, 149], local modes lattice is mapped onto B site sublattice of the perovskite ABO_3 structure. This allows to introduce a marker function σ_i describing details of microscopic structure of the material [144, 143, 145]. Its value is set to $\sigma_i = 1$ if site i is occupied by Ti^{4+} , and $\sigma_i = 0$ for Fe^{3+} . The first two terms in eq. (3.2) constitute an initial approximation for the local energy contribution. H_{loc}^{bfo} and H_{loc}^{bto} expressions are given by

$$H_{loc\,i} = \kappa_2 u_i^2 + \alpha u_i^4 + \gamma (u_{ix}^2 u_{iy}^2 + u_{iy}^2 u_{iz}^2 + u_{ix}^2 u_{iz}^2) + \sum_{j \in \text{NN}_B} J_{ij}^{\alpha\beta} u_i^\alpha u_j^\beta \quad (3.3)$$

with a different set of coefficients $\{\kappa_2, \alpha, \gamma, J_{ij}^{\alpha\beta}\}$ ¹. The correction term δH_i (eq. (3.2)) depends on the nearest neighbours environment of the site i . Conceptually, following the methodological scheme described in Ref. [148], it is possible to account for the effect of local environment precisely by choosing the appropriate form of δH_i . Extending the definition of σ_i to A sites of the lattice ($\sigma_i = 1$ for Ba^{2+} and $\sigma_i = 0$ for Bi^{3+}), we arrive at the following general expression

$$\delta H_i = \mathcal{E}_i(\{\sigma_i\}_{A,B}) \mathbf{u}_i + \delta \kappa_2^{\alpha\beta}(\{\sigma_i\}_A) u_i^\alpha u_i^\beta + \sum_{j \in \text{NN}_B} \delta J_{\sigma_i \sigma_j}^{\alpha\beta} u_{i\alpha} u_{j\beta} \quad (3.4)$$

The first term describes the energy of the local mode \mathbf{u}_i subject to random local field \mathcal{E}_i appearing on site i due to compositional breaking of local inversion symmetry. It depends on the first nearest neighbours A- and B-site atomic configuration $\{\sigma_i\}_{A,B}$ of the site i and can be approximated in the following way

$$\mathcal{E}_i = \sum_{j \in \text{1NN}_A} (1 - \delta_{\sigma_i \sigma_j}) (\sigma_i f_{Ti}^{Bi} + (1 - \sigma_i) f_{Fe}^{Ba}) \mathbf{e}_{ij} + \sum_{j \in \text{1NN}_B} (1 - \delta_{\sigma_i \sigma_j}) (\sigma_i f_{Ti}^{Fe} + (1 - \sigma_i) f_{Fe}^{Ti}) \mathbf{e}_{ij}, \quad (3.5)$$

¹In the following discussion, NN_B and NN_A denote B-site and A-site nearest neighbours environments of site i . 1NN_A and 1NN_B denote first nearest A- and B-site neighbours of the node i respectively, while $\text{1NN}_{A,B}$ corresponds to the union of these sets

where \mathbf{e}_{ij} is the unit vector connecting site i and j . Coefficients f can take four different values depending on the interacting pair of sites. Their physical meaning can be understood considering the following examples: in the case of an A site substitution of Ba^{2+} for Bi^{3+} in BaTiO_3 on site j , the magnitude of the local field acting on \mathbf{u}_i will be equal to $f_{\text{Ti}}^{\text{Bi}}$. Similar case with a B site substitution of Ti^{4+} for Fe^{3+} is described by the force constant $f_{\text{Ti}}^{\text{Fe}}$ while substituting single Fe^{3+} cation in pure BiFeO_3 corresponds to $f_{\text{Fe}}^{\text{Ti}}$.

In order to estimate the magnitude of the local electric fields from first-principles, one can adopt the following procedure. As we have previously mentioned, a single A-site substitution produces a local radial field acting on the surrounding local modes located at the B-sites (Fig. 3.1a). Therefore, in the case of the [001] superlattice geometry depicted in Fig. 3.1b local fields will be pointing in the [001] direction with their magnitude decreasing with increasing distance from the substituted A-site monolayer.

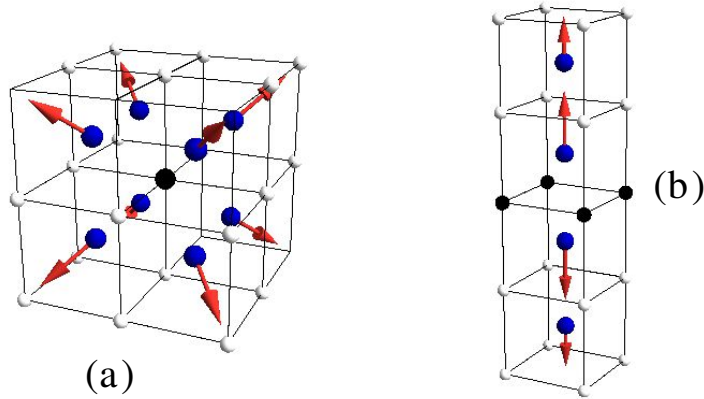


FIGURE 3.1: (a) Red arrows represent local radial electric fields produced in the case of a single A-site substitution. Blue spheres represent B-sites while Black and white spheres correspond to the A-sites of perovskite ABO_3 structure (b) Schematic representation of the unit cell of the superlattices used to estimate local fields magnitude. The black and white spheres represent A-sites of different type, while the blue spheres correspond to the B-sites, carrying the local mode vectors.

The fields acting on the atoms can be directly calculated from the DFT calculations. For this purpose, the superlattice geometry presented in Fig. 3.1b is more suitable than the study of a supercell with a single A-site substitution, since it allows to drastically reduce the volume of the supercell. For instance, associating the layer of black spheres with BiO^{1+} oxide layer, white spheres with BaO oxide layers and blue atoms with Ti^{4+} allows to estimate $f_{\text{Ti}}^{\text{Bi}}$ coefficient. First, one calculates the forces acting on the atoms situated at ideal cubic positions by performing a single self-consistent groundstate energy calculation. The evaluated forces are

then multiplied by the displacements given by the coordinates of the normalized local mode eigenvector. The resulting coefficient has the units of energy and is equal to f_{Ti}^{Bi} .

The second term in eq. (3.4) describes the modification of on-site quadratic coefficients. According to the local nature of this contribution, we have explicitly assumed that this correction depends only on the first nearest neighbours A-site atomic configuration $\{\sigma_i\}_A$ of local mode center i . It is worth noting that even within this approximation, the evaluation of $\delta\kappa_2^{\alpha\beta}$ corrections from first principles appears to be practically infeasible since the number of geometrically distinct $\{\sigma_i\}_A$ configurations is equal to 20, leading to 40 different $\delta\kappa_2^{\alpha\beta}$ sets. In order to estimate the number of distinct coefficients, we need to enumerate all possible $\{\sigma_i\}_{A,B}$ configurations. As we can see from Fig. 3.2, the set $\{\sigma_i\}_A$ represents a unit cube. Each of the 8 vertices of this cube can be occupied by either Ba^{2+} or Bi^{3+} cations, summing up to 2^8 possible configurations. However, only 20 of these

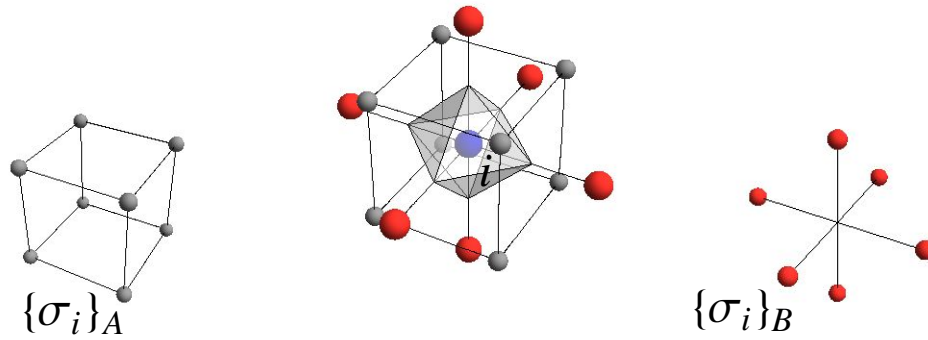


FIGURE 3.2: A-site $\{\sigma_i\}_A$ and B- site $\{\sigma_i\}_B$ first nearest neighbours environments of site i . Depicted in the middle is the union of the sets $\{\sigma_i\}_{A,B}$, along with the local mode center i and the schematic representation of the oxygen octahedron.

configurations are geometrically different. The main goal now is to evaluate the number of distinct nonzero $\kappa_2^{\alpha\beta}(\{\sigma_i\}_A)$ coefficients in eq. (3.4). Taking into account the operation of the replacement of all Ba^{2+} by Bi^{3+} , one can see that finally only 12 configurations should be considered, since such an inversion does not change the spatial symmetry of the structure. To visually represent the aforementioned 12 situations, we will say that the vertex is colored in white if it is occupied by Bi^{3+}

and black otherwise. For instance  represents a configuration with only one Bi^{3+} cation located at the 111 vertex. All other configurations with a single Bi^{3+} cation can be obtained from the latter one using the O_h symmetry operations. All configurations containing a single Ba^{2+} are obtained using chemical inversion. The

number of distinct configurations with two Bi^{3+} cations is equal to three. They

can be visualized as . Similarly, the number of configurations with three and four white vertices is equal to three and six, respectively. Taking into account that site i itself can be either Ti^{4+} or Fe^{3+} , we conclude that overall one has to consider 40 different situations leading to over 60 distinct $\delta\kappa_2^{\alpha\beta}$.

The last term appearing in eq. (3.4) introduces corrections to short-range interaction coefficients. As in the case of on-site quadratic coefficients, large number of local atomic configurations would require far too much computational time to calculate $\delta J_{ij}^{\alpha\beta}$. In order to overcome this difficulty, we propose the following approximation. Since $\delta\kappa_2^{\alpha\beta}$ and $\delta J_{ij}^{\alpha\beta}$ introduce corrections of the same order of magnitude, we allow ourselves to neglect the $\delta\kappa_2^{\alpha\beta}$ term and to set

$$\delta J_{ij}^{\alpha\beta} = \frac{1}{4}(\delta_{\sigma_i\sigma_j} - 1)(J_{ij}^{\alpha\beta\text{ } bto} + J_{ij}^{\alpha\beta\text{ } bfo}) \quad (3.6)$$

This corresponds to setting short-range interaction coefficients equal to that of pure BaTiO_3 or BiFeO_3 in the case of $\text{Ti}\Leftrightarrow\text{Ti}$ or $\text{Fe}\Leftrightarrow\text{Fe}$ interacting local mode pairs, and to an arithmetic average otherwise. Similar approximations have been already used to theoretically describe phase transitions in ferromagnetic alloys [150] and ferroelectric superlattices [154]. However, in contrast to [154], where $\delta J_{ij}^{\alpha\beta}$ were neglected and κ_2 coefficients averaged, the approximations given in eq.(3.5) and eq.(3.6) allow to capture the symmetry of both A- and B-site nearest neighbours environments. The remaining terms contributing to local energy $H_{loc}(\{\mathbf{u}_i, \boldsymbol{\omega}_i, \mathbf{m}_i\})$ are related to $\{\boldsymbol{\omega}_i\}$ and $\{\mathbf{m}_i\}$ degrees of freedom. Since phonon modes associated with oxygen octahedra rotations can be neglected for BaTiO_3 , we assume the same form for $H_{loc}(\{\boldsymbol{\omega}_i, \mathbf{m}_i\})$ as the one reported in [149], however setting ω_i and m_i degrees of freedom on Ti^{4+} sites to zero.

The long-range dipolar interaction between local modes does not need to be essentially modified. Using the same formula as in [148] for dipole-dipole interaction coefficients $Q_{ij,\alpha\beta}$, we put the prefactor $Z^{*2}/\varepsilon_\infty$ under the summation over the lattice sites and set it equal to $Z_i^* Z_j^*/\varepsilon_\infty^{eff}$ ², where Z_i^* is the Born effective charge of the local mode at site i [148]. For ε_∞^{eff} , we use the Maxwell-Garnett effective medium approximation [151]. The introduced error in the long-range interaction energy can be estimated by considering the system with (2-2) composite geometry.

²Formula (5) in reference [148]

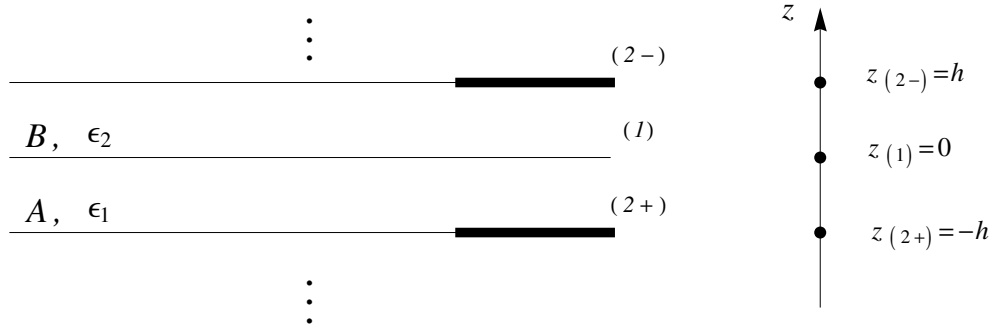


FIGURE 3.3: Schematic representation of the auxiliary electrostatic problem used to estimate the error made in the long-range interaction energy due to the employed effective medium approximation. The multilayer geometry is described by considering two layers (of materials A and B respectively) and identifying the top interface of layer B with the bottom interface of layer A , i.e. imposing periodic boundary conditions. The thickness of each layer is assumed to be equal to h and the origin of the z Cartesian axis coincides with the position of the interface (1).

For this specific case, the solution of the electrostatic problem

$$\nabla \varepsilon(\mathbf{r}) \nabla G(\mathbf{r}, \mathbf{r}_0) = \delta(\mathbf{r} - \mathbf{r}_0) \quad (3.7)$$

of finding the electrostatic potential Green's function $G(\mathbf{r}, \mathbf{r}_0)$ can be straightforwardly obtained. Later can be achieved by finding the spectrum of the Poisson operator for the boundary problem schematically described in Fig. 3.3. Once the sets of the eigenvalues $\{\lambda_i\}$ and the corresponding eigenfunction $\{e_i(\mathbf{r})\}$ are found, $G(\mathbf{r}, \mathbf{r}_0)$ can be obtained via the spectral representation

$$G(\mathbf{r}, \mathbf{r}_0, \lambda) = \sum_i \frac{e_i(\mathbf{r}) e_i^*(\mathbf{r}_0)}{\lambda - \lambda_i} \quad (3.8)$$

$$G(\mathbf{r}, \mathbf{r}_0) = \oint_C d\lambda G(\mathbf{r}, \mathbf{r}_0, \lambda) \quad (3.9)$$

where the integration is performed over the contour C enclosing all the poles of the function $G(\mathbf{r}, \mathbf{r}_0, \lambda)$. The eigenvalue problem for the geometry presented in Fig. 3.3 is defined in the following way

$$\varepsilon_1 \Delta e(\mathbf{r}) = \lambda e(\mathbf{r}) \quad , \text{ for } \mathbf{r} \in A \quad (3.10)$$

$$\varepsilon_2 \Delta e(\mathbf{r}) = \lambda e(\mathbf{r}) \quad , \text{ for } \mathbf{r} \in B \quad (3.11)$$

$$e(x, y, 0+) = e(x, y, 0-), \quad \varepsilon_2 \partial_z e(x, y, z)|_{0+} = \varepsilon_1 \partial_z e(x, y, z)|_{0-} \quad (3.12)$$

$$e(x, y, h) = e(x, y, -h), \quad \varepsilon_2 \partial_z e(x, y, z)|_h = \varepsilon_1 \partial_z e(x, y, z)|_{-h} \quad (3.13)$$

where equations (3.12) and (3.13) represent the conditions of continuity of the

electrostatic potential and the continuity of the normal component of the electric displacement vector at the interface. Finally, the conditions of the continuity of the tangent component of the electric field

$$\partial_x e(x, y, 0+) = \partial_x e(x, y, 0-), \quad \partial_y e(x, y, 0+) = \partial_y e(x, y, 0-) \quad (3.14)$$

$$\partial_x e(x, y, h) = \partial_x e(x, y, -h), \quad \partial_y e(x, y, h) = \partial_y e(x, y, -h) \quad (3.15)$$

close the formulation of the Sturm-Liouville problem for the eigenfunctions $e(\mathbf{r})$.

The usual ansatz $e(x, y, z) = X(x)Y(y)Z(z)$ allows to split the variables and to convert the partial differential equation problem into the problem of solving three ordinary differential equations. For instance, the introduced function $Z(z)$ satisfies the following equations in the regions occupied by layers A and B

$$\varepsilon_1 Z''(z) = \lambda_z Z(z), \quad \text{for } z < 0 \quad (3.16)$$

$$\varepsilon_2 Z''(z) = \lambda_z Z(z), \quad \text{for } z > 0 \quad (3.17)$$

The equations for the functions $X(x)$ and $Y(y)$ have the similar form, yet with different auxiliary eigenvalues, which we will denote as λ_x and λ_y . Naturally, the eigenvalues λ_i appearing in equation (3.8) can be recovered as a sum $\lambda_i = \lambda_{x,i_1} + \lambda_{x,i_2} + \lambda_{x,i_3}$ from all possible combinations of the indexes i_{1-3} . From eqs. (3.18-3.19) one readily finds

$$Z = A_1 \exp^{ik_1 z} + A_2 \exp^{-ik_1 z}, \quad \text{for } z < 0 \quad (3.18)$$

$$Z = B_1 \exp^{ik_2 z} + B_2 \exp^{-ik_2 z}, \quad \text{for } z > 0 \quad (3.19)$$

where we have introduced the notations $k_{1,2} = \sqrt{\lambda/\varepsilon_{1,2}}$ in order to keep the formulas compact. The boundary conditions allow to obtain the coefficients $\{A_1, A_2, B_1, B_2\}$ up to a common multiplier and therefore the eigenvalues $\lambda_{x,i}$. Using equations (3.12, 3.12) one obtains the following matrix equations on the coefficients $A_{1,2}$ and $B_{1,2}$

$$\begin{pmatrix} 1 & 1 \\ 1 & -1 \end{pmatrix} \begin{pmatrix} A_1 \\ A_2 \end{pmatrix} = \begin{pmatrix} 1 & 1 \\ \sqrt{\varepsilon_2/\varepsilon_1} & -\sqrt{\varepsilon_2/\varepsilon_1} \end{pmatrix} \begin{pmatrix} B_1 \\ B_2 \end{pmatrix} \quad (3.20)$$

and

$$\begin{pmatrix} e^{-ik_1 h} & e^{ik_1 h} \\ e^{-ik_1 h} & -e^{ik_1 h} \end{pmatrix} \begin{pmatrix} A_1 \\ A_2 \end{pmatrix} = \begin{pmatrix} e^{ik_2 h} & e^{-ik_2 h} \\ \sqrt{\varepsilon_2/\varepsilon_1} e^{ik_2 h} & -\sqrt{\varepsilon_2/\varepsilon_1} e^{-ik_2 h} \end{pmatrix} \begin{pmatrix} B_1 \\ B_2 \end{pmatrix} \quad (3.21)$$

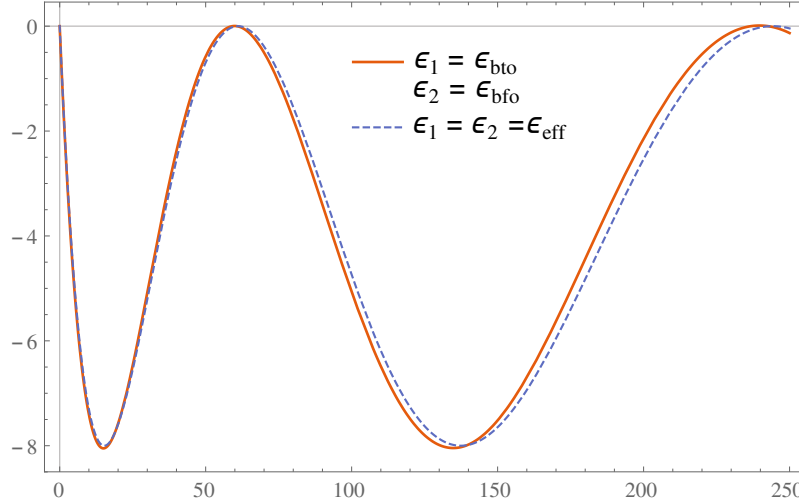


FIGURE 3.4: Graphical representation of equation (3.22). The values of ε_1 and ε_2 are taken to be equal to those of BaTiO₃ and BiFeO₃ compounds respectively. The roots of the depicted function correspond to the eigenvalues of considered problem. Dashed blue curve corresponds to the dispersion equation of the effective medium.

Resolving this system of equations yields the following dispersion relation defining the eigenvalues λ_z

$$-1 + \cos(k_1 h) \cos(k_2 h) - \frac{1}{2} \left(\sqrt{\frac{\varepsilon_1}{\varepsilon_2}} + \sqrt{\frac{\varepsilon_2}{\varepsilon_1}} \right) \sin(k_1 h) \sin(k_2 h) = 0 \quad (3.22)$$

As expected this expression is symmetric with respect to the dielectric permittivities ε_1 and ε_2 . Moreover, one immediately obtains the parameter governing the deviation of the problem from the effective medium solution. Comparing eq. (3.22) to the equation holding for $\varepsilon_1 = \varepsilon_2 = \varepsilon_\infty^{eff}$, we see that the deviation of the eigenvalues from the corresponding effective medium values can be obtained as a series expansion

$$\delta\lambda \sim \sum_k c_k \left(1 - \frac{\varepsilon_1 + \varepsilon_2}{\sqrt{\varepsilon_1 \varepsilon_2}} \right)^k \quad (3.23)$$

Indeed, assuming $(1 - \varepsilon_1/\varepsilon_2) \ll 1$, and keeping only the terms of the lowest order of perturbation theory, the equation (3.22) can be rewritten as

$$\left(-1 + \cos(kh)^2 - \sin(kh)^2 \right) + \frac{1}{2} \left(-3kh \cos(kh)\sin(kh) - \sin(kh)^2 \right) \left(\frac{\delta\varepsilon}{\varepsilon_\infty^{eff}} \right)^2 = 0 \quad (3.24)$$

where $k = \sqrt{\lambda_x / \varepsilon_{\text{inf}}^{eff}}$ and $\delta\varepsilon = \varepsilon_1 - \varepsilon_\infty^{eff} \approx -\varepsilon_2 + \varepsilon_\infty^{eff}$. A graphical representation of equation 3.22 is provided in Fig. (3.4).

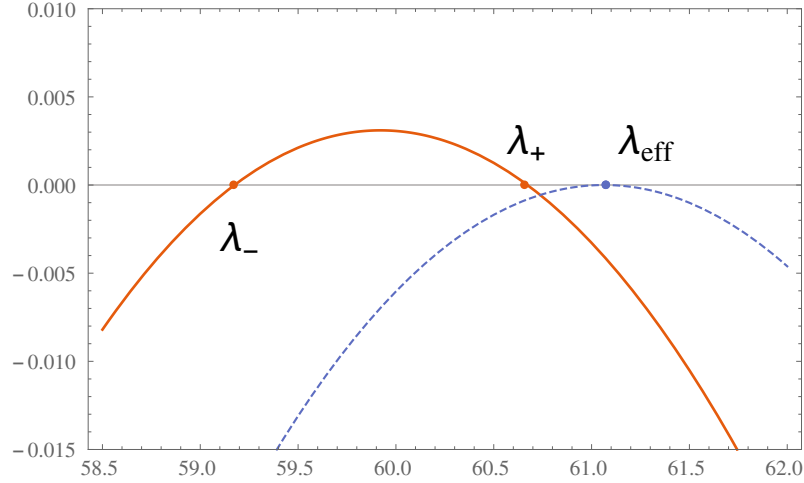


FIGURE 3.5: Comparison of the first nonzero eigenvalues λ_1 and λ_2 defined by equations (3.18 , 3.19) and the corresponding λ_{eff} obtained from the effective medium approximation. One clearly sees the occurring splitting. The resulting deviation from the adopted solution is proportional to $(1 - (\varepsilon_1 + \varepsilon_2)/\sqrt{\varepsilon_1\varepsilon_2}) \approx 0.013$ in the case of BiFeO₃-BaTiO₃ system.

The energy contribution associated with the elastic degrees of freedom is treated similarly to the above described approximation for the local modes part of the effective Hamiltonian. The effect of local chemical pressure due to the difference of ionic radii of the atoms is explicitly accounted for using the approach described in Ref. [143, 144].

3.1.3 Assessment of the model

In order to test the validity of the introduced approximations for (BiFeO₃)(BaTiO₃) systems, we have performed first principles calculations of local mode energy profiles for (BiFeO₃)_{0.5}(BaTiO₃)_{0.5}[001] superlattices (Fig. 3.6a). This structure has been chosen in order to clearly separate contributions coming from the quadratic terms (see eq. (3.4)) from the effect of the local fields associated with compositional breaking of inversion symmetry. Since the symmetry of the structure can be described by 4mm point group, we can readily see that in-plane local electric field components are equal to zero $\mathcal{E}_i^{x,y} = 0$ at any site i . Therefore for $u_i^{x,y}$ components, only $\delta J_{ij}^{\alpha\beta}$ terms contribute to δH_i .

The LDA calculations were performed with PWscf package [152] using standard set of ultrasoft pseudopotentials [153]. An $8 \times 8 \times 4$ k-point grid was used to compute integrals over the Brillouin-zone of the 10-atom perovskite cell depicted in Fig. 3.6a. The cutoff for wavefunctions basis was set to 70 Ry with kinetic energy cutoff of 700 Ry. In the spirit of the approximation described by eq. 3.2, we have

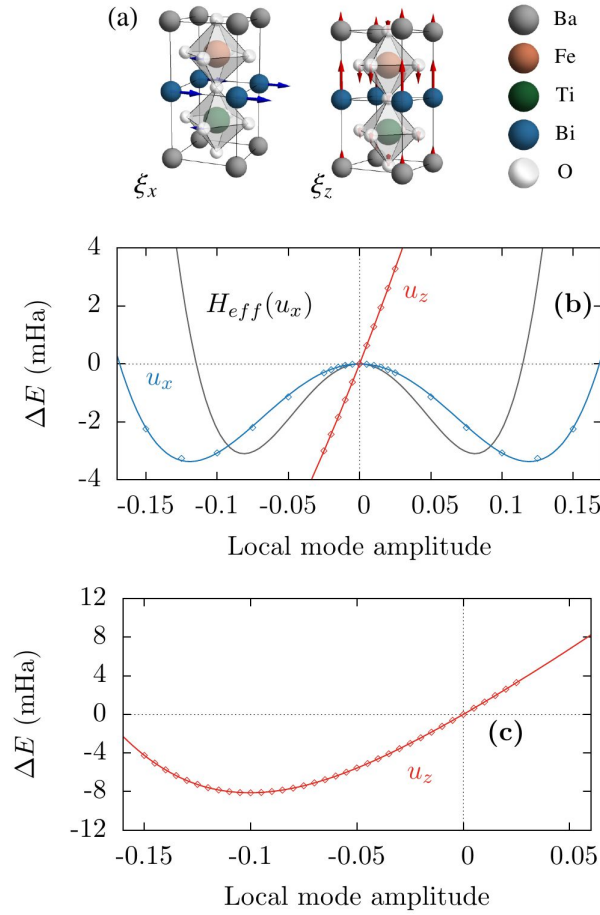


FIGURE 3.6: **(a)** Representation of BiFeO₃-BaTiO₃ (001) superlattice unit cell. ξ_x and ξ_z correspond to Γ_5 and Γ_1 modes eigenvectors. Displacements of Bi³⁺ described by ξ_x and ξ_z are considerably bigger compared to other cations **(b)** Energy differences with respect to reference structure with atoms situated in ideal cubic positions. The energy is first minimized with respect to unit cell volume then the atoms are shifted according to eigenvectors ξ_x and ξ_z (blue and red curves respectively). Solid black curve represents the energy obtained using constructed effective Hamiltonian approximation. **(c)** Due to the effect of local electric field, the ferroelectric instability is no longer present. Instead of a double well potential one observes an energy profile with a single stable minimum.

first optimized the unit cell volume while keeping the shape of the unit cell and atomic positions fixed. This configuration was chosen as a reference structure. Evaluating the eigenvectors of Γ_1 and Γ_5 phonon modes ξ_z , ξ_x and displacing the atoms by either $u_z \xi_z$ or $u_x \xi_x$ (see Fig. 3.6a) we have obtained the mean-field energy profiles associated with the local modes contributions (Figs. 3.6b and 3.6c). In agreement with [155], we find that different oxidation states of the ions comprising the structure lead to the destruction of the double well potential associated with atomic displacements along [001] direction. Instead we observe an energy profile with a single stable minimum (Fig. 3.6c). In the vicinity of the reference structure, the energy depends linearly on the local modes amplitude u_z (Fig 3.6b), clearly

indicating the dominant effect of quenched local fields associated with compositionally broken inversion symmetry.

For ξ_x and ξ_y modes transforming according to the Γ_5 representation, the absence of the in-plane force components allows to reveal the ferroelectric double-well instability (Fig. 3.6b) and therefore, to test the validity of the chosen approximation for $\delta J_{ij}^{\alpha\beta}$. Despite the fact that the positions of the minima of H_{eff} model and those of the double-well potential obtained from ab initio calculations differ, the depth of the wells are in good correspondence. By construction, the adopted model (Eqs. (3.2)) should approximate rather well the potential energy surfaces for compositions close to pure BaTiO₃ and BiFeO₃ compounds. The case of $x \approx 0.5$ thus represents the most challenging case where the introduced errors will be maximized. However, the agreement of the energy barrier heights shows that even in this case our model captures the energy scale correctly.

3.2 Room-temperature phase diagram of (BiFeO₃)_x(BaTiO₃)_{1-x} solid solutions

In order to obtain temperature dependent properties of (BiFeO₃)_x(BaTiO₃)_{1-x} solid solutions, we have performed Metropolis Monte Carlo simulations using the constructed effective Hamiltonian model H_{eff} . For all these simulations we have used superlattices containing 1728 (12×12×12) unit cells. At each given concentration, we first carry out a full temperature range annealing for a specific fixed random realization of A-site and B-site atomic distributions. Then the averaging over disorder realizations at room temperature is executed using forty different structural configurations. For each configuration the cations distribution over the A-site and B-site positions are assumed to be spatially uniform and statistically independent.

Figure 3.7 shows the obtained dependence of the absolute value of polarization $P \sim |\langle\langle Z_i^* \mathbf{u}_i \rangle\rangle|$ on BiFeO₃ concentration x . The $\langle\cdot\rangle$ operation represents thermal averaging, while $\langle\cdot\rangle_i$ stands for the averaging over the sites of the supercell. In order to illustrate the effect of disorder we also plot the interval between minimum and maximum values of polarization within the probed set of atomic configurations, which is shown as a shaded area. The dependence on x of the average polarization magnitude clearly indicates a gradual crossover from a ferroelectric to a nonpolar phase, the latter appearing in the intermediate range of concentrations $x'_c < x <$

x_c'' . The inset shows the dependence of lattice parameters on the composition for BaTiO₃ rich compounds. It can be clearly seen that the tetragonal distortion is gradually decreasing with increasing x . This allows us to estimate the critical value $x_c'=0.06$ as the concentration at which the average lattice symmetry becomes cubic. We have observed similar phenomena for compounds with compositions chemically close to pure BiFeO₃ crystal. Decreasing x leads to a gradual decrease of the rhombohedral distortion angle with an estimate of $x_c''=0.76$ for the concentration at which the value of the rhombohedral distortion becomes negligible. Qualitatively, the predicted behaviour of the macroscopic properties is in agreement with the experimental results reported in Ref.[138, 139, 140]. Moreover, the broadness of the prediction interval suggests that the phase diagram of the system strongly depends on the structural disorder realization, or in other words on the quality of mixture, which defines how close the specific disorder realization is to the average structure. It is important to stress that in our calculations we have assumed statistically independent and spatially homogeneous distributions for A-site and B-site cations, an approximation that appears to be a rather coarse one. Quantitative comparison of the theoretically obtained critical concentrations to the experimental ones would require a more rigorous structural study which lies beyond the scope of this study. However, the estimated values for x_c' and x_c'' appear to fall within the range of the experimentally obtained values found in literature [138, 140].

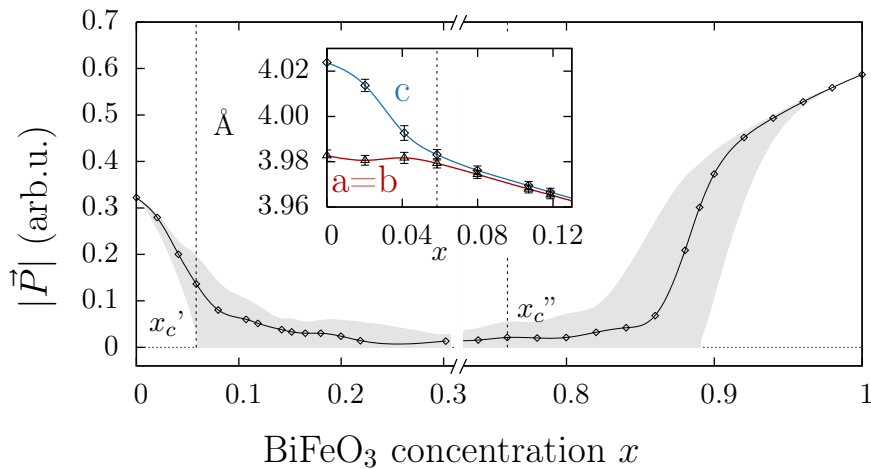


FIGURE 3.7: Calculated dependence of the absolute value of polarization on BiFeO₃ concentration. Shaded region delimits the interval between the minimum and maximum polarization values within the probed cation distributions. The inset shows calculated dependence of lattice constants on BiFeO₃ concentrations for BaTiO₃ rich compounds. Tetragonal distortion gradually reduces until the average lattice symmetry become cubic at the critical concentration x_c' .

In order to reveal the mechanism responsible for the observed weakening of ferroelectric order, we have probed the local properties of the system. Fig. 3.8 shows the dependence on concentration of the average on-site local mode amplitude $q = \langle |\langle Z_i^* u_i \rangle| \rangle_i$ [145] for the full composition range, where $|\langle Z_i^* u_i \rangle|$ represents the absolute value of the thermal average of local mode vector centered on site i . Normally, nonzero values of the introduced parameter q indicate the deviation of the system's state from the paraelectric one. It can be seen that in the dilute limits ($x \approx 0$ or $x \approx 1$), increasing the percentage of the dopant material first leads to a decreasing average dipole magnitude, while for concentrations close to $x \approx 0.6$ the magnitude of q reaches its maximum.

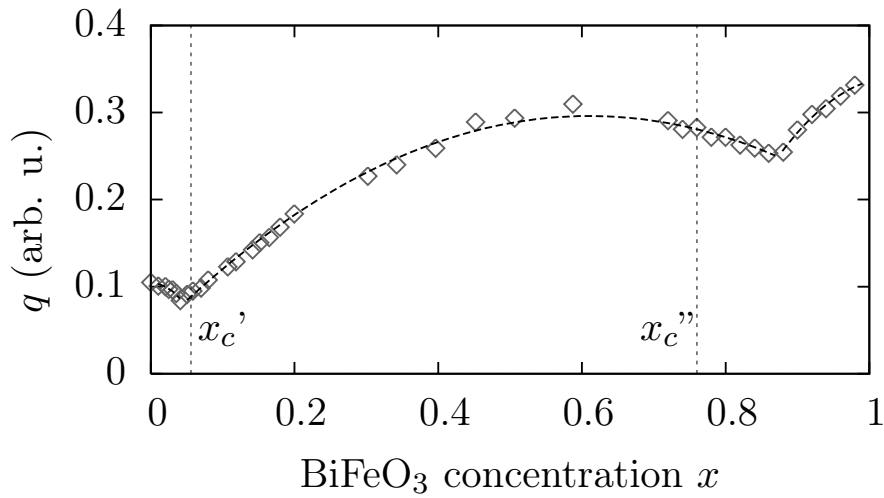


FIGURE 3.8: Variation of the average local mode amplitude $q = \langle |\langle Z_i^* u_i \rangle| \rangle_i$ with concentration x . In the dilute solid solution limits ($x \rightarrow 0$ and $x \rightarrow 1$), the value of q decreases with increasing the doping phase content. This can be attributed to the weakening of ferroelectric order. In the intermediate range of concentrations the curve has a bell shape reaching its maximum at $x \approx 0.6$. In this limit, local modes are effectively decoupled and the nonzero average local mode amplitude is related to the presence of strong local fields forcing cations to shift from ideal cubic positions.

This is a natural consequence of the local charge imbalance present in the system due to compositional asymmetry. Indeed, local dipole moments created by the displacements of ions are forced to screen the built-in charges [156] leading to local quenching of \mathbf{u}_i variables. For instance, in solid solutions rich in BaTiO₃, the substitution of Bi³⁺ for Ba²⁺ represents a local positively charged defect which is screened by a bound charge density $\delta n = -Z^* \nabla(\mathbf{u})$ surrounding it. Therefore, the average local mode amplitude q can be split into two distinct contributions $q(x) = q^0(x) + q^f(x)$, representing the quenched part and the free one, respectively. For the unit cells surrounding the charged defect, the local potential has a shifted

single-well shape (as in Fig. 3.6), meaning that the appearing polarization is non-switchable, i.e., it is quenched. These cells mainly contribute to q^0 . As for the rest of the volume of the crystal, local modes are not constrained by local random fields and can potentially adopt collinear configurations. The ferroelectric contribution $q^f(x)$ vanishes in the intermediate concentration range $x'_c < x < x''_c$, where $q^0(x)$ reaches its maximum, whereas in the ferroelectric phase $q^0(0) = q^0(1) = 0$. From this point of view, for any composition x , the system at room temperature can be described in terms of two coexisting phases: a paraelectric phase, associated with regions with nonzero bound charge density δn and a ferroelectric one, for which $\delta n = 0$. In order to illustrate our argument, we have plotted the bound charge density distribution and the integral lines of the local modes vector field in an arbitrary cross sections of the supercell for two characteristic compositions: $x = 0.04$ and $x = 0.16$, as shown in Fig. 3.9. Due to the radial symmetry of the local electric field produced by a single defect, regions where $\delta n \neq 0$ (red and dark blue areas in Fig. 3.9) carry negligible average polarization. Therefore, these regions can be seen as paraelectric. At $x = 0.04$, the volume of the ferroelectric phase still dominates and the average polarization is not equal to zero, while at $x = 0.16$ the state of the system becomes globally paraelectric.

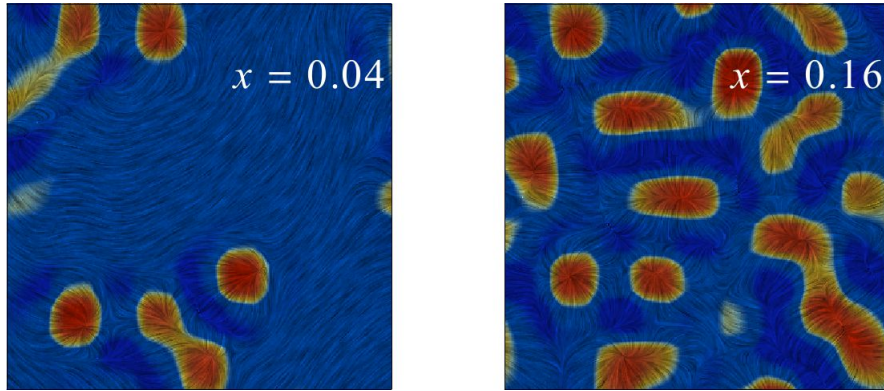


FIGURE 3.9: Bound charge density distribution $\delta n = -Z^* \nabla(\mathbf{u})$ in arbitrarily picked cross sections of the supercell for two characteristic compositions $x = 0.04$ and $x = 0.16$. The red areas correspond to positive bound charge appearing around negative defects, i.e., around Fe^{3+} ions substituting Ti^{4+} . The dark blue regions indicate the areas with excess negative charge $\delta n < 0$, while the light blue color corresponds to $\delta n = 0$ or ferroelectric phase. Line traces represent the interpolated integral lines of the local modes vector field.

The process of the formation of the paraelectric state can be equivalently described using an alternative measure of the ferroelectric properties of the system, namely the density of the topological defects n_* of the local modes vector field. The calculated dependence of this parameter upon concentration is presented in Fig. 3.10. Moreover, in this figure, we also present the density n_{f*} of the topological defects

associated with the local random fields distribution and the previously presented concentration dependence of the configurationally averaged value of polarization (see Fig. 3.7).

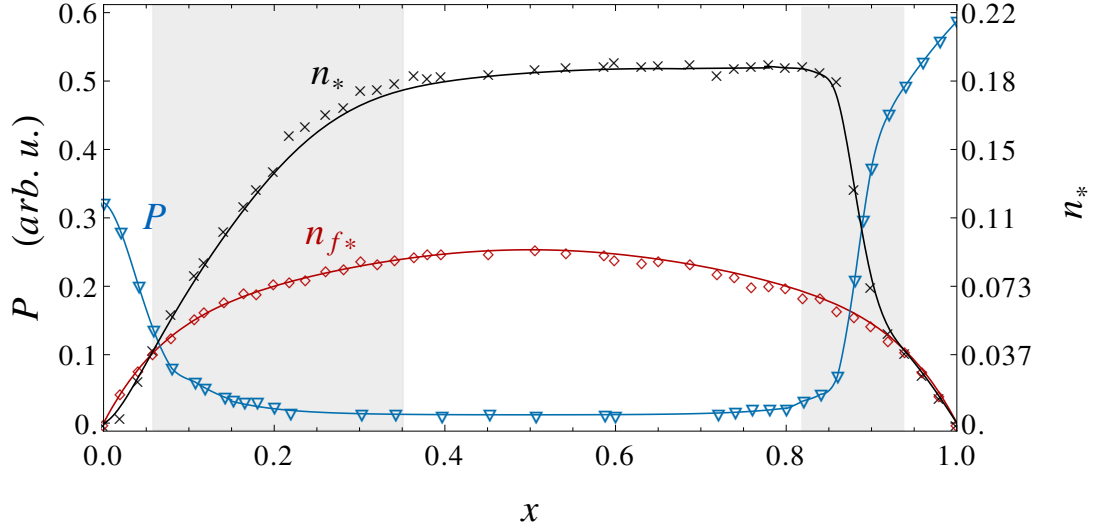


FIGURE 3.10: Calculated dependence on concentration of the configurationally averaged densities of topological defects corresponding to the local modes vector field (n_*) and the distribution of the local random fields n_{f*} . The blue triangular markers correspond to the the previously presented dependence of the configurationally averaged value of polarization. Lines are guide for the eye.

As expected, one can see that upon increasing the concentration of the doping agent, n_{f*} monotonically increases reaching its maximum at $x = 0.5$. This, in turn, leads to the increase of the density n_* . Indeed, as discussed in the section 2.3.1, the points at which the topological defects corresponding to the \mathcal{E}_i distribution are located represent pinning centers for the local modes, or in other words – points at which the activation energy for the topological defect of the \mathbf{u}_i field is lowered. This argument is confirmed by the fact that the n_* density follows the n_{f*} curve in the dilute limits $x < 0.06$ and $x > 0.90$. Naturally, topological defects appearing at the pinning centers gradually destroy ferroelectric order, all the more lowering the activation energy finally resulting in a fully disordered state.

Naturally, the presented arguments incline one to investigate the possibility of the presence of local order. Indeed, the regions devoid of the influence of local fields might still be ferroelectric. For instance, such situation might occur even in the presence of a percolating network of nonzero bound charge. In order to study this possibility, we have implemented the clustering algorithm, which allowed us to automatically access the information about the characteristic of the regions in which the local modes adopt collinear configurations. Specifically, the implemented algorithm was designed as a two-step labelling-clustering procedure. The first step,

namely the labelling of the local modes consists in attributing a label to each of the local mode vectors according to its orientation. Specifically, the set of possible orientation $\theta \in [0, \pi)$, $\phi \in [0, 2\pi)$ has been divided into twenty equal solid angles. Local modes whose direction falls within the same spherical region are attributed the same directional label. Then, it is straightforward to perform spatial clustering of the sublattice of local modes having equal label values. In our case we have chosen to use a simple back-tracking algorithm [158].

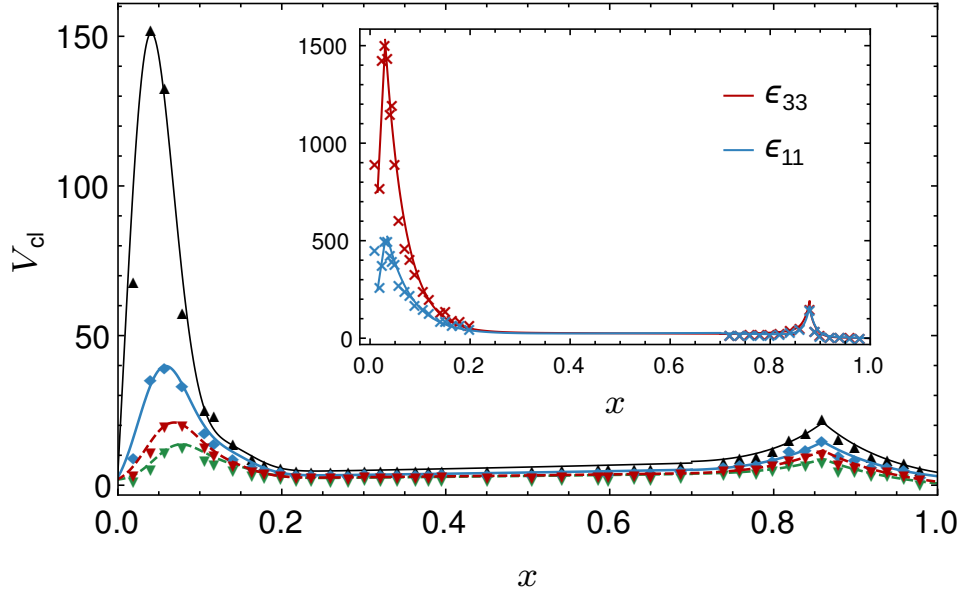


FIGURE 3.11: Dependence of the volumes of the biggest clusters on the BiFeO_3 concentration x . The black triangular markers correspond to the volume of the second biggest cluster of local modes, i.e. volume of the second biggest locally ordered region, averaged over 40 different disorder realisations. The blue, red and green markers represent the average volumes of the third, fourth and fifth biggest clusters, respectively. The inset shows the dependence of the configurational average of the dielectric susceptibility (in arbitrary units) on the concentration x . The lines represent guides to the eye.

The obtained results do not reveal any signature of the presence of local order in the intermediate concentration range, indicating that within our model the pseudocubic phase is indeed paraelectric. However, we find that before undergoing ferroelectric-paraelectric phase transition, the system breaks into ferroelectric domains. Figure 3.11 shows the dependence of the configurationally averaged volumes of the second, third, fourth and fifth biggest clusters on BiFeO_3 concentration x (the volume of the biggest cluster at each concentration simply follows the normalized polarization (see Fig. 3.7) and is therefore not presented). The obtained results clearly show that all these quantities increase with increasing the concentration of the dopant material, reaching their maximum values below the critical concentration x'_c and above x''_c . The corresponding peaks coincide with the peaks of the dielectric susceptibility, depicted in the inset of Fig. 3.11. Such

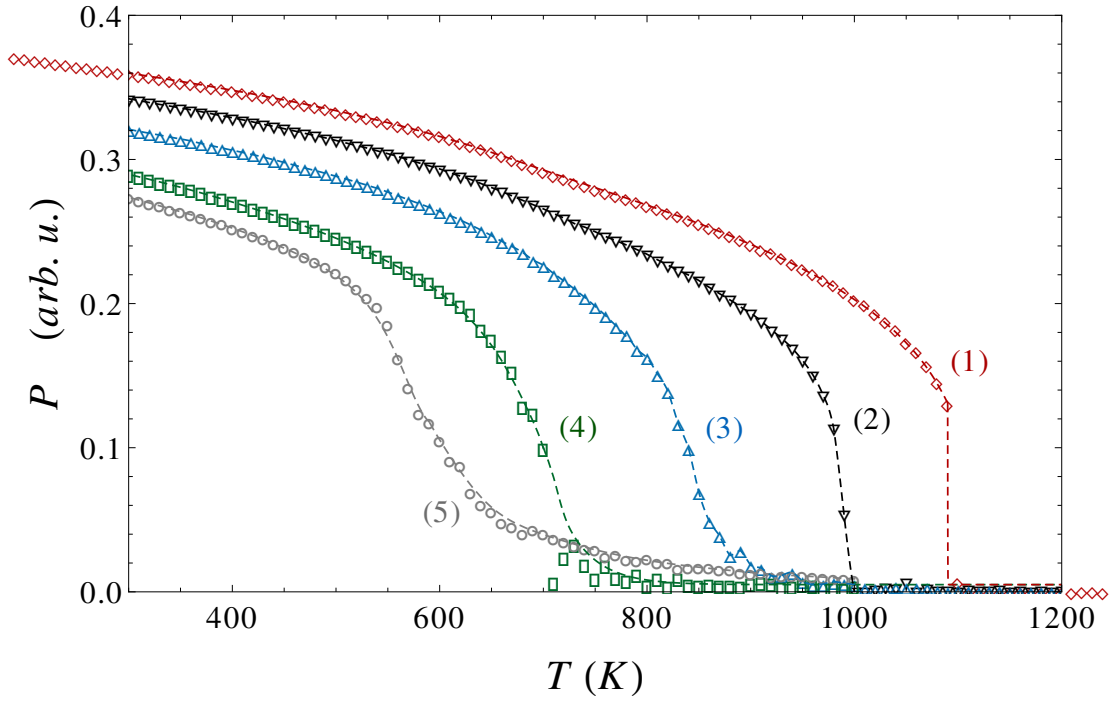


FIGURE 3.12: Calculated temperature dependence of the ferroelectric order parameter for different concentrations (1) $x = 1.0$ (2) $x = 0.98$ (3) $x = 0.96$ (4) $x = 0.94$ (5) $x = 0.92$. Increasing concentration of the doping agent (in this case BaTiO_3) leads to decrease of the ferroelectric transition temperature. Moreover, one observes gradual smearing of the phase transition intrinsic to systems with quenched disorder [159]. Each of the curves corresponds to a single realization of A- and B- site disorder.

correspondence is common for models with intrinsic quenched disorder, which exhibit thermally stable locally ordered regions [159]. On the other hand, increasing the concentration of the dopant material leads to the decrease of the ferroelectric Curie temperature. This can be clearly seen in the case of compounds rich in bismuth ferrite. The corresponding temperature variations of the ferroelectric order parameter for different compositions with $x > 0.9$ are presented in Fig. 3.12³. Since the dielectric response exhibits an anomaly at the Curie temperature, the peaks present in the inset of Fig. 3.11 can potentially be associated with the concentration at which the Curie temperature becomes equal to 300K, i.e. to the temperature at which we have calculated the characteristics of the locally ordered regions (Fig. 3.11).

The estimated dependence of the Curie temperature T_c on concentration for BiFeO_3 rich compounds is presented in Fig. 3.13. As it can be seen, the polynomial fit of the obtained data gives an estimate of $x_* \approx 0.89$ for the concentration at which the Curie temperature becomes equal to $T_c = 300\text{K}$. For the BaTiO_3 rich compounds, i.e. for $x < 0.1$, the accuracy of the performed Monte Carlo simulations

³Each of the curves correspond to a single realization of A- and B- site disorder.

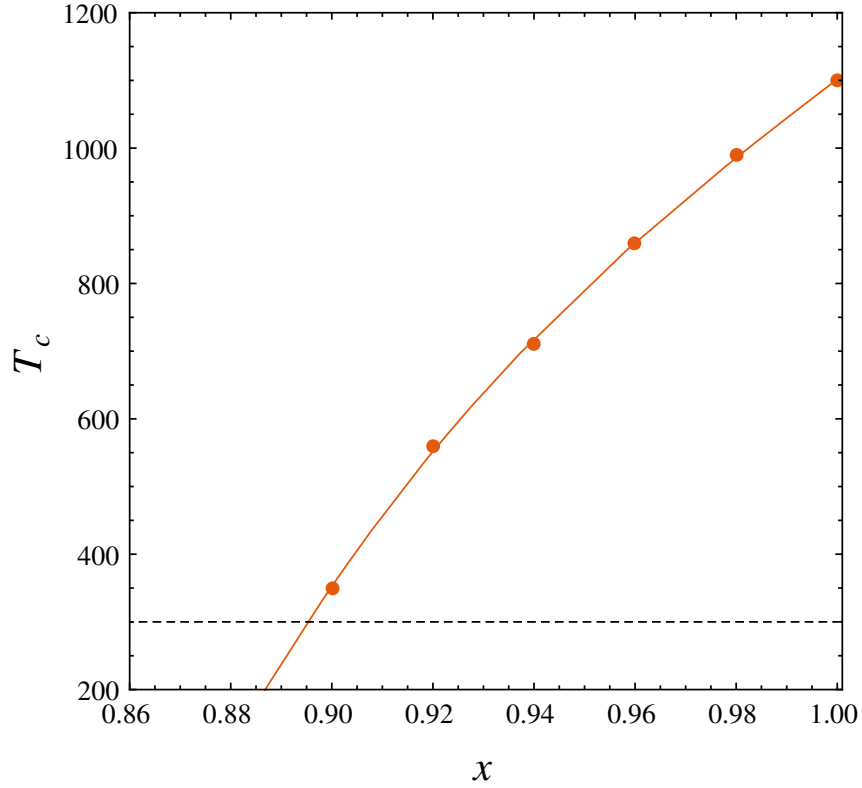


FIGURE 3.13: Dependence of the estimated Curie temperature on BiFeO₃ concentration x . The solid line represents a polynomial fit of the data, while the dashed line marks the temperature $T = 300K$ at which the phase diagram 3.7 has been calculated.

is not sufficient to obtain reliable estimates for the Curie temperature. Moreover, the fact that the temperature dependence of the order parameter for different concentrations has been performed only for a specific randomly selected realization of disorder does not allow to clearly establish the nature of the peaks of the dielectric response.

In order to further investigate the effect of local random fields and identify the mechanism driving the pseudocubic phase formation, we have investigated the zero-local-field limit of our model. Specifically, performing Monte Carlo simulations under the assumption $\mathcal{E}_i = 0$ at each site i , we have found that at room temperature the system remains ferroelectric in the entire concentration range. Hence, within our model, local fields are primarily accountable for the weakening of the ferroelectric order. It is important to note that both zero-field limit and the case of $\{\mathcal{E}_i\} \neq 0$ do not reproduce locally monoclinic structure of the pseudocubic phase reported in some recent experimental studies [140, 142]. This discrepancy is not surprising and represents a consequence of the introduced approximations. For instance, a more elaborated estimate of $\delta J_{ij}^{\alpha\beta}$ and $\delta \kappa_i^{\alpha\beta}$, rather than averaging described by eq. (3.6), is required in order to precisely capture the on-site anisotropy.

Another simplification lies in the assumption of a uniform uncorrelated distribution of A- and B-site cations. Indeed, chemical correlations will obviously change the distribution of local fields and introducing short-range chemical order might naturally result in a locally ordered ferroelectric phase [157].

In summary, in this section we have presented a first-principles based model suitable for predicting finite-temperature properties of multiferroic materials comprising chemically distinct constituents. In the case of (BiFeO_3) (BaTiO_3) compounds, the validity of the model was assessed by comparison with performed first principles calculations. The application of our model to the case of $(\text{BiFeO}_3)_x(\text{BaTiO}_3)_{1-x}$ solid solutions yields results supporting the hypothesis of the dominant role of local random fields in driving the formation of the experimentally observed pseudocubic phase [139]. Whereas in the dilute limits the influence of the local fields is only quantitative in that it induces the weakening of ferroelectric order, in the intermediate concentrations region they result in a nonpolar equilibrium state.

3.3 Finite-temperature properties of $(\text{BiFeO}_3)(\text{BaTiO}_3)$ bicrystals

The question of the effect of the geometry of the structure on the properties of phase transitions is mostly pronounced when the characteristic structural length-scale ⁴ becomes comparable to the lattice constant of the constituent materials. In this section, we will exemplify this question by considering the ferroelectric, magnetic and structural properties of yet another limiting case of nanocomposite $\text{BiFeO}_3/\text{BaTiO}_3$ structures which can be described as bicrystals, and will apply the model developed and tested in the previous section.

The definition of bicrystal structures as a subclass of nanocomposite materials can be most simply established by resorting to the notion of the marker function σ_i , introduced in the section 1.3. Indeed, since we are considering the arrangements of unit cells of two different types ($\sigma_i = \pm 1$) on the cubic lattice within a periodic supercell, we can equivalently describe the structure by introducing the Fourier transformation $\sigma_q = \sum_i \sigma_i e^{iq\mathbf{r}_i}$. Then, the simplest nontrivial periodic arrangements of the $\sigma_i = \pm 1$ nodes would be described by the vectors $\{\sigma_q\}$ whose nonzero components correspond only to the high symmetry points q located at the

⁴By characteristic structural length-scale we refer to the period of compositional modulation of the structure, i.e. the thickness of the layers in the case of epitaxial (2,2) multilayer structures, radius of the nanopillar or the period of the nanopillar array, lateral size of the nanodot, etc.

boundary of the Brillouin zone. Notably, such structural representation of bicrystals can be put into correspondence with the Newnham's definition of connectivity (see section 1.3).

In order to exclude the effect of the local fields which significantly suppress ferroelectricity, in this section, we only consider geometries in which the local fields are prohibited by symmetry. First, we will perform a study of the bicrystals described by symmetric connectivity index, specifically the (0,0), (1,1), (2,2) and (3,3) structures. The presence of the mirror planes and local inversion centres for these structures will be assured by the assumption of the (0,0) A-sites distribution. Then, an example of a more complex asymmetric geometry will be examined by looking into the case of the (3,2) and (2,3) structures.

For all considered structures, the finite-temperature properties were obtained from the Metropolis Monte Carlo simulations. Specifically, we have performed a temperature annealing, decreasing the temperature from 2000 K down to 10 K with steps of 10 K. At each step, a thermalization over 20000 Monte Carlo sweeps followed by the same amount of averaging sweeps have been performed. In contrast to the case of disordered systems, this amount of Monte Carlo simulation sweeps have been verified to be sufficient for obtaining reliable estimates of macroscopic observables. The following sections will contain the summary of the most important results related to each of the aforementioned geometries.

3.3.1 Lattice geometry with (0,0) connectivity

The (0,0) structure can be seen as a three-dimensional "checkerboard" with unit cells of BaTiO₃ and BiFeO₃ alternating along each of the Cartesian directions. The marker function in this case can be expressed as $\sigma_i = (-1)^{i_x+i_y+i_z}$, where the set of variables $\{i_x, i_y, i_z\}$ label the three dimensional coordinate i of the unit cell. The schematic representation of the (0,0) supercell used in Monte Carlo simulations is presented in the inset of Fig. (3.14)⁵. It can be seen that for each unit cell i of the structure, all unit cells belonging to its first nearest neighbours environment have a chemical type different from that of the cell i , i.e. for all $j \in 1\text{NN}(i)$ $\sigma_j \neq \sigma_i$. Therefore, in the approximation where only the first nearest neighbours short-range interactions are considered, the $S_{(0,0)}$ structure can be seen as a virtual or average crystal, as understood within the VCA approximation. On the other hand, the sets of the second and third next nearest neighbours are chemically identical to

⁵In the following discussion the supercells resembling the bicrystals with (α, β) connectivity index will be denoted as $S_{(\alpha, \beta)}$

the center site i under consideration. Latter makes it possible to distinguish two different cubic face centered sublattices corresponding to the sets of the unit cells of BiFeO_3 and BaTiO_3 . The global cubic symmetry and local cubic anisotropy are conserved.

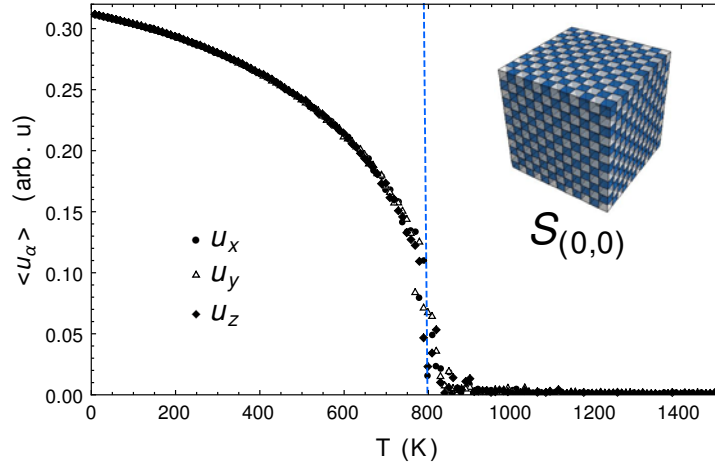


FIGURE 3.14: The temperature evolution of the average local mode components in the case of the three-dimensional checkerboard structure (denoted as $S_{(0,0)}$) schematically depicted in the inset figure, where the blue and white cubes represent the unit cell of BiFeO_3 and BaTiO_3 , respectively. It can be seen that the system undergoes a single ferroelectric phase transition, at $T_C \approx 795$ K.

Figure (3.14) shows the temperature evolution of the obtained average local mode components $\langle u_\alpha \rangle$. It can be seen that the system undergoes a single ferroelectric phase transition from the paraelectric to the rhombohedral ferroelectric phase at the temperature $T_C \approx 795$ K. Latter is confirmed by the temperature dependence of the average homogeneous strain tensor components presented in Fig. (3.15).

The temperature dependences of the dielectric and magnetic susceptibilities are presented in Fig. (3.16). At the ferroelectric transition temperature, one observes a divergence of the dielectric response. The temperature dependence of the magnetic susceptibility shows a slight change of the slope at the ferroelectric transition temperature T_C . Moreover, one observes a clear signature of an antiferromagnetic phase transition at $T_N = 134$ K.

3.3.2 Lattice geometry with (1,1) connectivity

Bicrystals possessing the (1,1) connectivity correspond to the two-dimensional analogue of the three-dimensional checkerboard structure considered in the previous section. In this case, the marker function does not depend on the i_z index, and the only nonzero component of the Fourier transformation vector σ_q corresponds

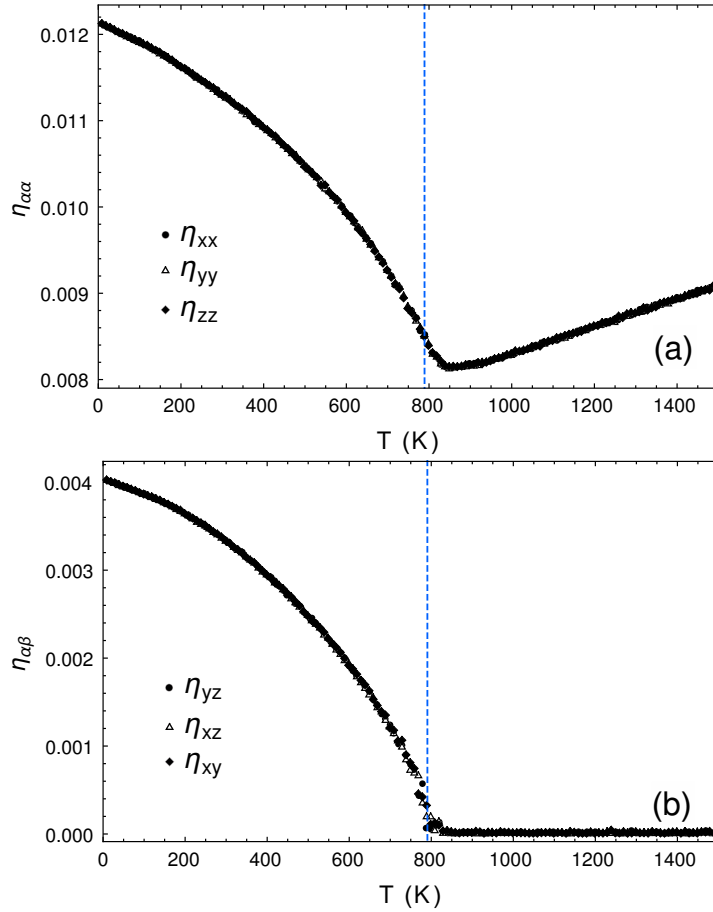


FIGURE 3.15: Temperature evolution of (a) the diagonal homogeneous strain tensor components and (b) the homogeneous strain tensor off-diagonal components in the case of $S_{0,0}$ supercell geometry.

to the M point of the first Brillouin zone. In contrast to the $S_{(0,0)}$ case, the global point-group symmetry is tetragonal. The presence of a single four-fold axis passing through the axis of the nanowires (or equivalently along the z Cartesian direction) of the constituent phases leads to the expectation of a more complex sequence of phase transitions. The results of the Monte Carlo simulations are presented in Fig. (3.17-3.19).

Indeed, Fig. 3.14 shows that the $S_{(1,1)}$ system undergoes two ferroelectric phase transitions from the paraelectric tetragonal phase to the orthorhombic aa ferroelectric phase ($\langle u_x \rangle = \langle u_y \rangle, \langle u_z \rangle = 0$) at $T_{C1} \approx 680$ K, and from the orthorhombic to the monoclinic ferroelectric r phase ($\langle u_x \rangle = \langle u_y \rangle \neq \langle u_z \rangle$) at $T_{C2} \approx 547$ K.

The temperature dependences of the homogeneous strain tensor components are presented in Fig. (3.18). As expected, the paraelectric phase does not possess cubic symmetry due to the aforementioned tetragonal symmetry of the $S_{(1,1)}$ structure unit cell. Indeed, at $T > T_{C1}$, the strain components split in such a way that

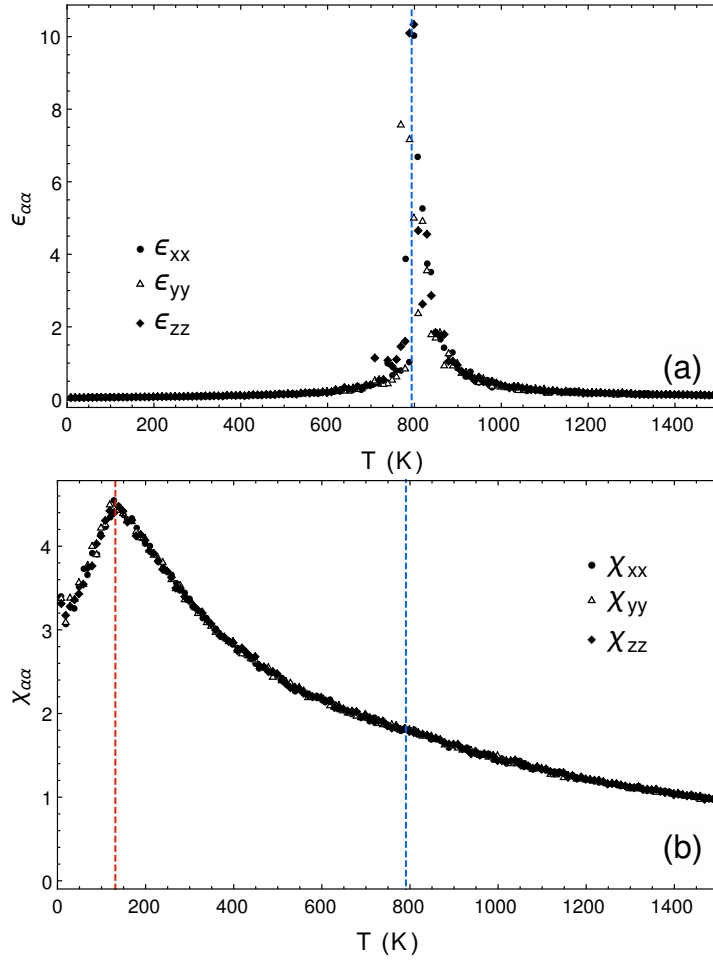


FIGURE 3.16: Temperature evolution of the diagonal components of the (a) dielectric and (b) magnetic susceptibility tensors for $S_{0,0}$ lattice structure. Figure (b) indicates a presence of an antiferromagnetic phase transition at $T_N \approx 134\text{K}$.

the components perpendicular to the four-fold symmetry axis are equal, $\eta_{xx} = \eta_{yy} \neq \eta_{zz}$. Accordingly, one observes similar splitting of the thermal expansion coefficients.

Each of the aforementioned ferroelectric phase transitions, similarly to the case of $S_{(0,0)}$ structure, is associated with a divergence of the components of dielectric susceptibility, as it can be seen in Fig. (3.19). The temperature evolution of the magnetic susceptibility is presented in Fig. (3.19b). The system undergoes an antiferromagnetic phase transition at $T_N \approx 262\text{ K}$.

3.3.3 Lattice geometry with (2,2) connectivity

Increasing the connectivity of each of the constituent phases leads to the superlattice geometry presented as an inset in Fig. (3.20). Similarly to the case of the

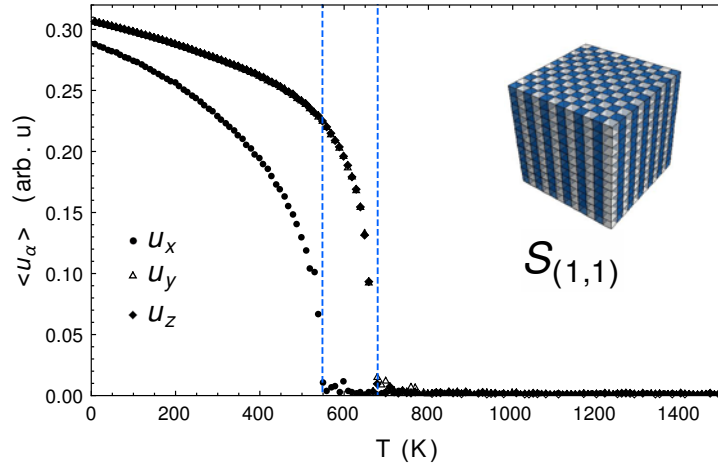


FIGURE 3.17: The temperature evolution of the average local mode components in the case of the two-dimensional checkerboard structure (denoted as $S_{(1,1)}$) schematically depicted in the inset figure. As in the case of $S_{(0,0)}$ supercell structure, the blue and white cubes represent the unit cell of BiFeO_3 and BaTiO_3 respectively. The system undergoes two ferroelectric phase transitions, at $T_{C1} \approx 680$ K and $T_{C2} \approx 547$ K.

checkerboard arrangement of nanopilars, the unit cell of such atomic structure has a tetragonal point-group symmetry. However, the finite-temperature properties of the $S_{(2,2)}$ superlattice differ drastically from those of the $S_{(1,1)}$ structure considered in the previous section. As it can be seen from Fig. (3.20), the transition temperature is significantly lowered: at $T_C \approx 427$ K, the system directly undergoes a ferroelectric phase transition from the tetragonal paraelectric to a monoclinic ferroelectric r phase. In contrast to the previously considered nanocomposite geometries, the symmetry changes abruptly at the transition temperature. The ferroelectric phase transition possesses features that are qualitatively similar to those of the pure BiFeO_3 .

This is manifested in the temperature dependence of the dielectric and magnetic susceptibilities of the system (see Fig. (3.22)). Both curves possess characteristic features of the BiFeO_3 single crystal, such as the signature of the magnetoelectric coupling in the peak of the dielectric susceptibility at the antiferromagnetic phase transition, as well as in the kink of the magnetic susceptibility at the paraelectric to ferroelectric phase transition. The antiferromagnetic transition is also significantly lower than that featured by the $S_{(1,1)}$ structure and is equal to $T_N \approx 82$ K.

3.3.4 Lattice geometry with (3,3) connectivity

The $(\text{BiFeO}_3)(\text{BaTiO}_3)$ bicrystals with (3,3) connectivity represent the most interesting geometry among compositionally symmetric structures. As in the case

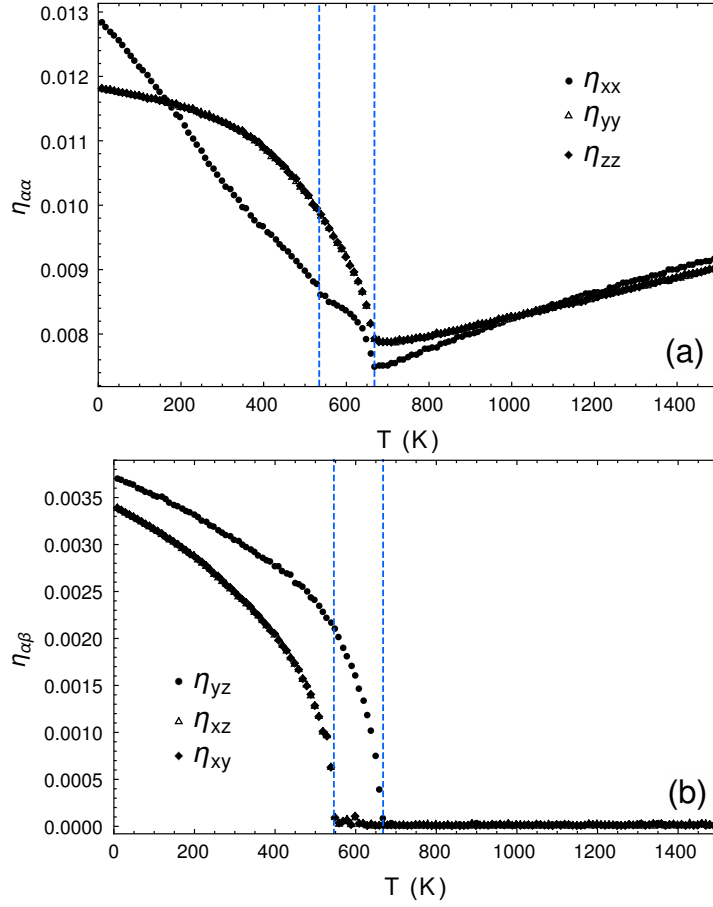


FIGURE 3.18: Temperature dependence of (a) the diagonal homogeneous strain tensor components and (b) the homogeneous off-diagonal strain tensor components in the case of $S_{(1,1)}$ supercell geometry. The tetragonal symmetry of the paraelectric phase manifests in the different slopes of the temperature dependence of the η_{ii} variables above the first ferroelectric phase transition, or in other words in different thermal expansion coefficients.

of the $S_{(0,0)}$ structure, the point-group symmetry of the unit cell is cubic. Yet, the change of connectivity is expressed in the fact that each unit cell now possesses a set of first nearest neighbours that are of the same chemical type as the center cell i , while all the second and third next nearest neighbours are labelled with a marker function value different from σ_i . Moreover, the Fourier transform of the marker function now has more than one nonzero component.

Figure (3.23) shows the temperature dependence of the calculated average local mode components. As it can be seen, the phase diagram is qualitatively similar to that of the $S_{(2,2)}$ with the paraelectric to rhombohedral transition occurring at $T_C \approx 574$ K.

However, the global cubic symmetry of the supercell structure now results in a simpler shape of the temperature dependence of the strain tensor components

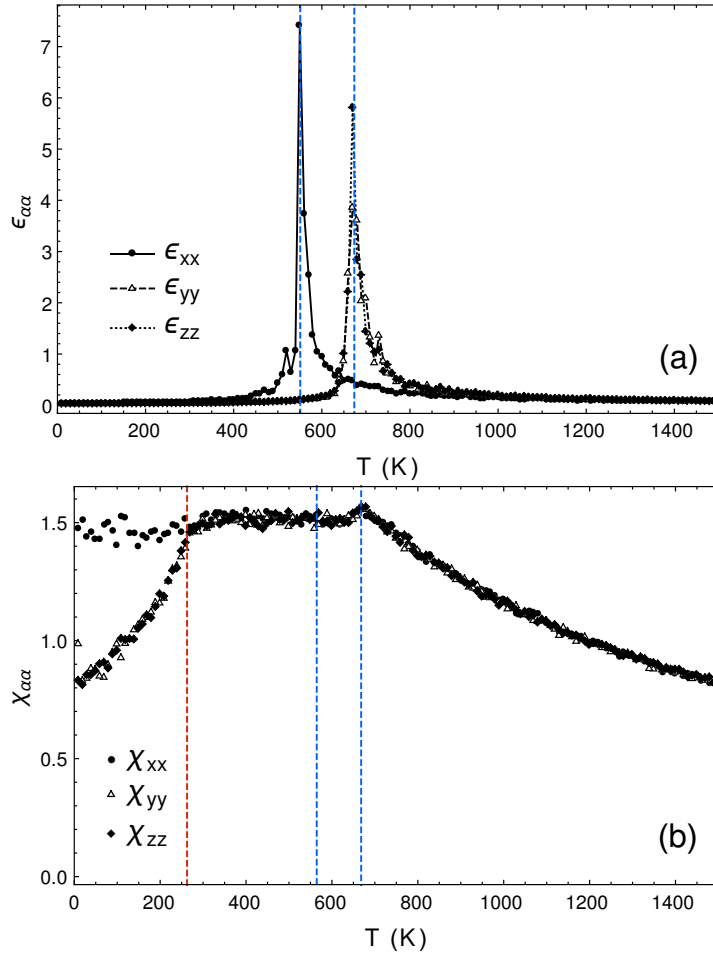


FIGURE 3.19: Temperature evolution of the diagonal components of the (a) dielectric and (b) magnetic susceptibility tensors in the case of $S_{(1,1)}$ lattice structure. Figure (b) indicates the presence of an antiferromagnetic phase transition at $T_N \approx 262$ K. Moreover, the cusp of the magnetic susceptibility components present at the ferroelectric transition temperature indicates a possible coupling of the magnetic and ferroelectric order parameters.

presented in Fig. (3.24). From the temperature dependence of the diagonal homogeneous strain tensor components, one also observes an indication of the AFD phase transition happening at $T_{AFD} \approx 800$ K.

The antiferromagnetic transition temperature is also increased (see Fig. (3.25) and is equal to $T_N \approx 277$ K. Again, similarly to the case of $S_{(2,2)}$ superlattice structure, one observes a kink in the magnetic susceptibility at the ferroelectric phase transition.

3.3.5 Compositionally asymmetric structures: (3,2) and (2,3)

In the previous sections, we have only considered the compositionally symmetric supercell geometries. Specifically, for all the described structures, volume fractions

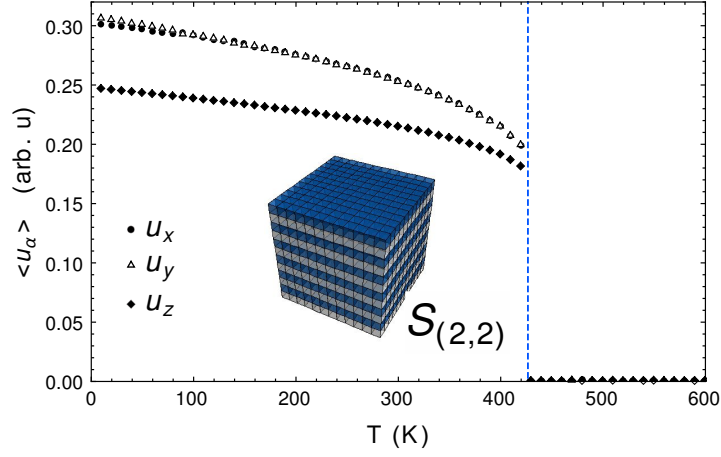


FIGURE 3.20: The temperature evolution of the average local mode components in the case of the superlattice structure (denoted as $S_{(2,2)}$) schematically depicted in the inset figure, where the blue and white cubes represent the unit cell of BiFeO_3 and BaTiO_3 , respectively. The system undergoes a single ferroelectric phase transition, at $T_C \approx 427$ K.

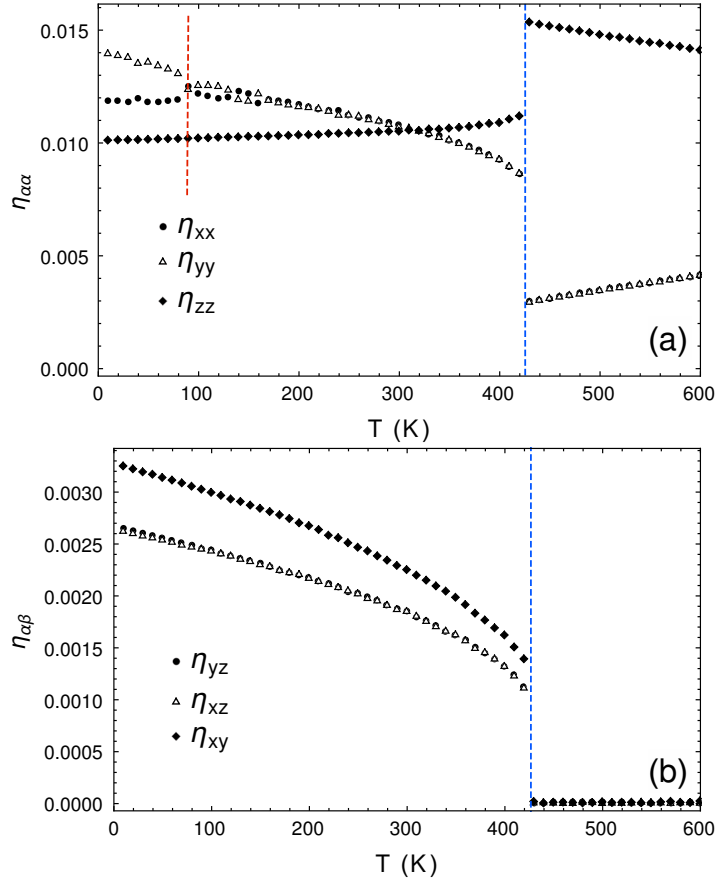


FIGURE 3.21: Temperature dependence of (a) the diagonal homogeneous strain tensor components and (b) the homogeneous off-diagonal strain tensor components in the case of $S_{2,2}$ $\text{BiFeO}_3/\text{BaTiO}_3$ superlattice. Again, as in the case of $S_{(1,1)}$ structure, the strain components above the ferroelectric phase transition split according to the tetragonal point-group symmetry of the unit cell of the structure.

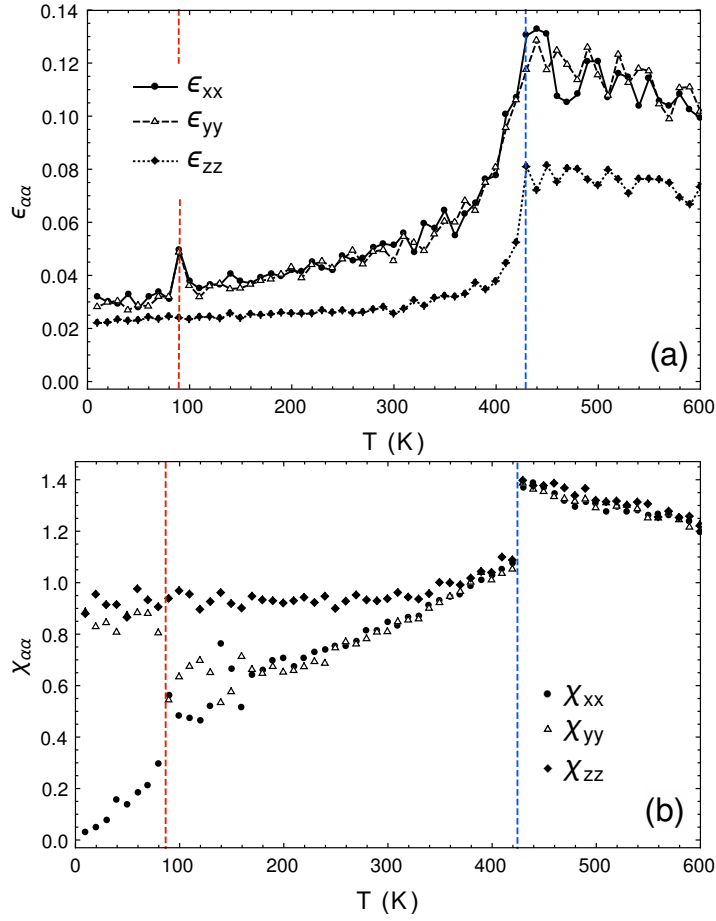


FIGURE 3.22: Temperature evolution of the diagonal components of the (a) dielectric and (b) the magnetic susceptibility tensors in the case of $S_{(2,2)}$ lattice structure. Figure (b) indicates the presence of an antiferromagnetic phase transition at $T_N \approx 82$ K.

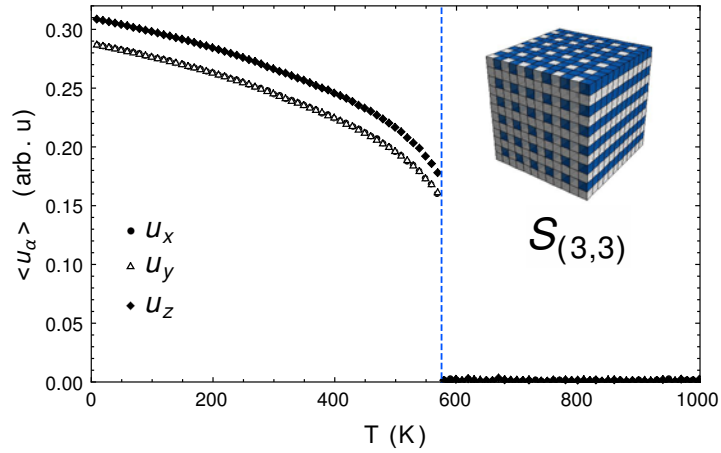


FIGURE 3.23: The temperature evolution of the average local mode components in the case of the $S_{(3,3)}$ structure. The system undergoes a single ferroelectric phase transition at $T_C \approx 574$ K from paraelectric to a monoclinic ferroelectric phase.

of both phases along with their connectivity indexes were equal. In this section we will describe the properties of two structures with BiFeO_3 concentrations of $x =$

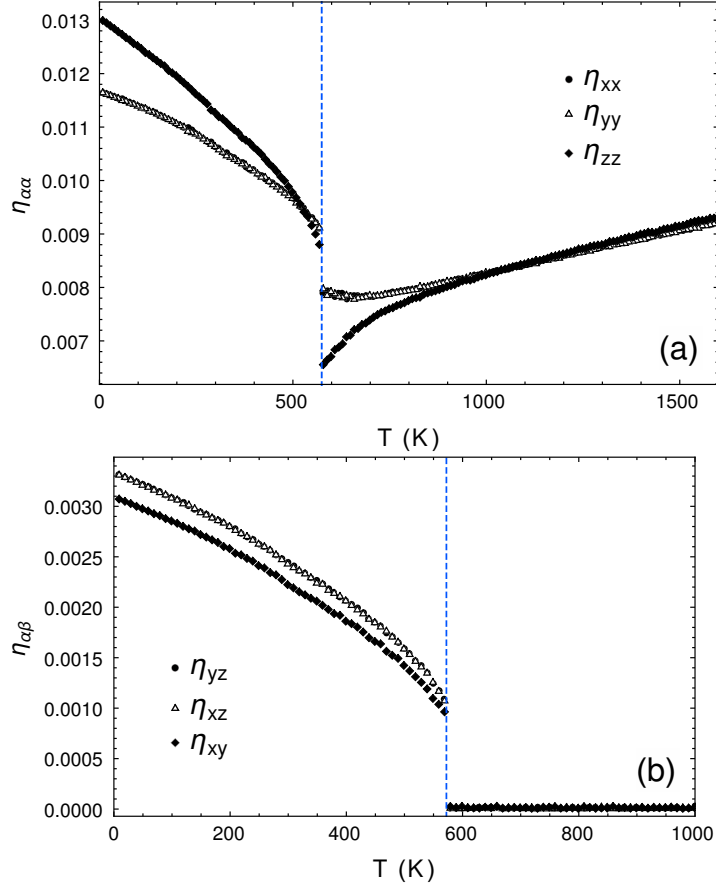


FIGURE 3.24: Temperature dependence of the of (a) the diagonal homogeneous strain tensor components and (b) the homogeneous off-diagonal strain tensor components in the case of $S_{(3,3)}$ supercell geometry.

0.625 and $x = 0.375$ possessing the connectivities of (3,2) and (2,3) respectively.

The $S_{(2,3)}$ structure consists of alternating layers of BiFeO_3 and BaTiO_3 , as in the case of $S_{(2,2)}$ superlattice, however, the layers of BaTiO_3 are now interconnected. This is achieved by adding the BaTiO_3 sublattice in each of the BiFeO_3 layers. The $S_{(2,3)}$ $12 \times 12 \times 12$ supercell used in the Monte Carlo simulations is schematically depicted in the inset of Fig. (3.26).

The $S_{(2,3)}$ structure undergoes two structural phase transitions, namely the AFD phase transition at $T_{\text{AFD}} \approx 636$ K, followed by the ferroelectric transition from the paraelectric to the monoclinic ferroelectric phase at $T_C \approx 134$ K.

As expected, the phase diagram is qualitatively similar to that of $S_{(2,2)}$ $\text{BiFeO}_3/\text{BaTiO}_3$ superlattices, with however lower transition temperatures, result that can be explained by the decrease of the volume fraction of the BiFeO_3 phase. Similar sequence of structural phase transitions is also observed in the case of the $S_{(3,2)}$

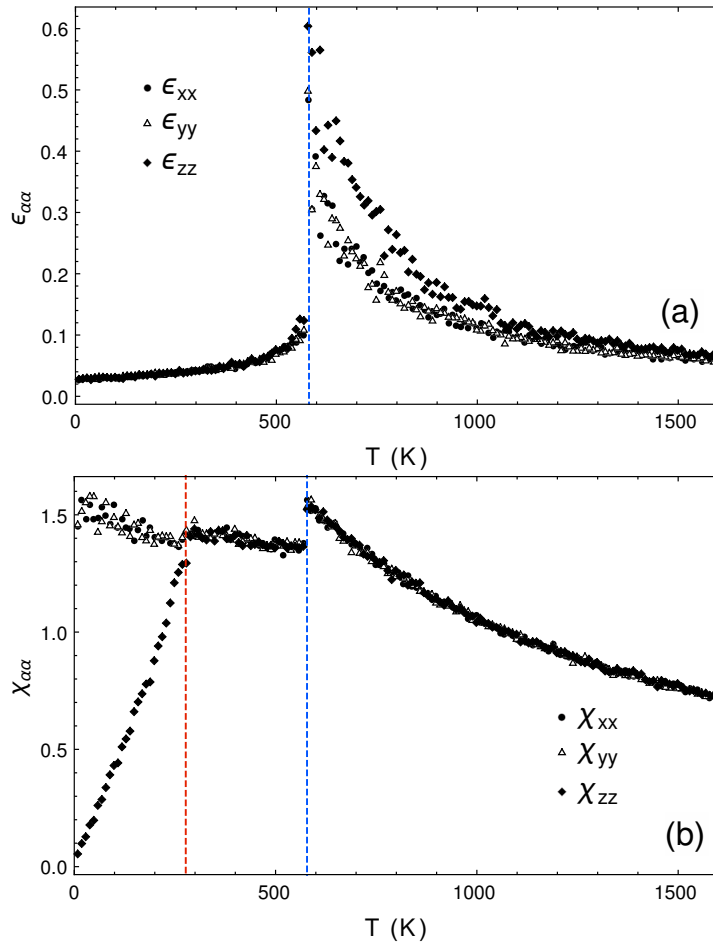


FIGURE 3.25: Temperature evolution of the diagonal components of the (a) dielectric and (b) magnetic susceptibility tensors in the case of $S_{(3,3)}$ lattice structure. Figure (b) indicates the presence of an antiferromagnetic phase transition at $T_N \approx 277$ K.

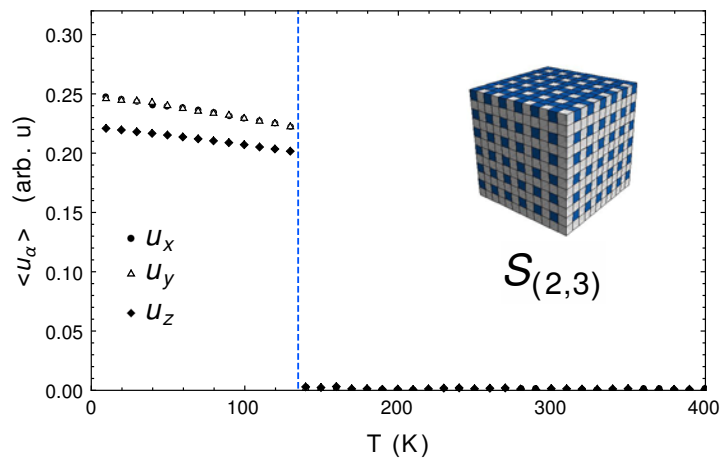


FIGURE 3.26: The temperature evolution of the average local mode components in the case of the $S_{(2,3)}$ structure. The system undergoes a single ferroelectric phase transition at $T_C \approx 574$ K from paraelectric to a monoclinic r phase.

structure. As can be seen from Fig. (3.29-3.31), the transition temperatures in this case are: $T_{AFD} \approx 1146$ K and $T_C \approx 654$ K.

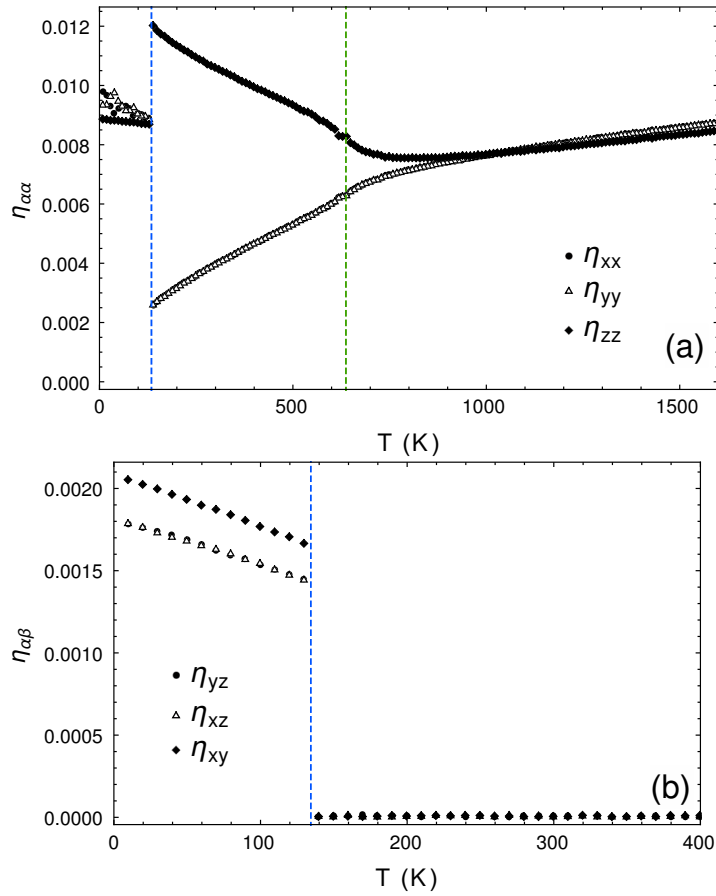


FIGURE 3.27: Temperature dependence of (a) the diagonal homogeneous strain tensor components and (b) the homogeneous off-diagonal strain tensor components in the case of $S_{(2,3)}$ supercell geometry.

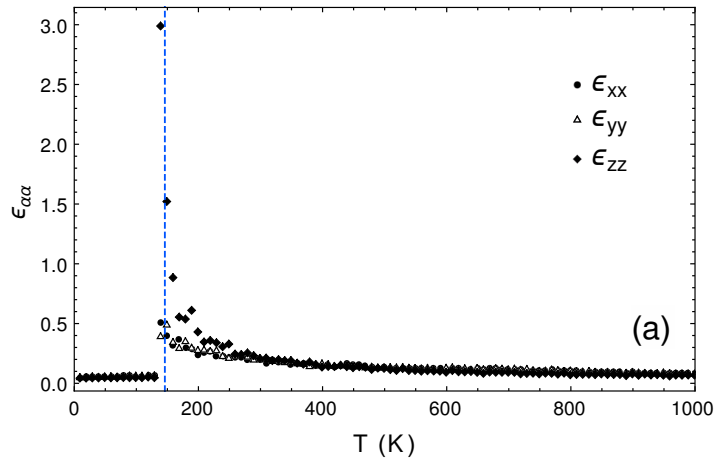


FIGURE 3.28: Temperature evolution of the diagonal components of the dielectric susceptibility tensor components in the case of $S_{(2,3)}$ geometry.

Remarkably, the magnetic properties of both $S_{(3,2)}$ and $S_{(2,3)}$ structures are drastically different from all other considered cases. This can be seen by observing the temperature evolution of the magnitude of the supercell average magnetization presented in the Fig. (3.32).

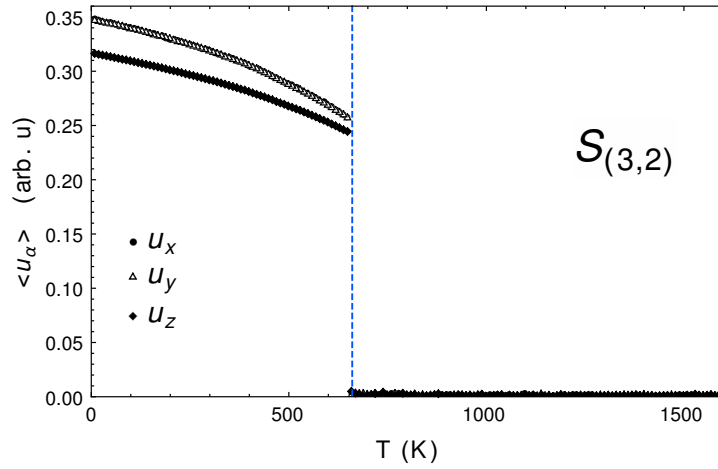


FIGURE 3.29: The temperature evolution of the average local mode components in the case of the $S_{(3,2)}$ structure. The system undergoes a single ferroelectric phase transition at $T_C \approx 574$ K from paraelectric to monoclinic phase.

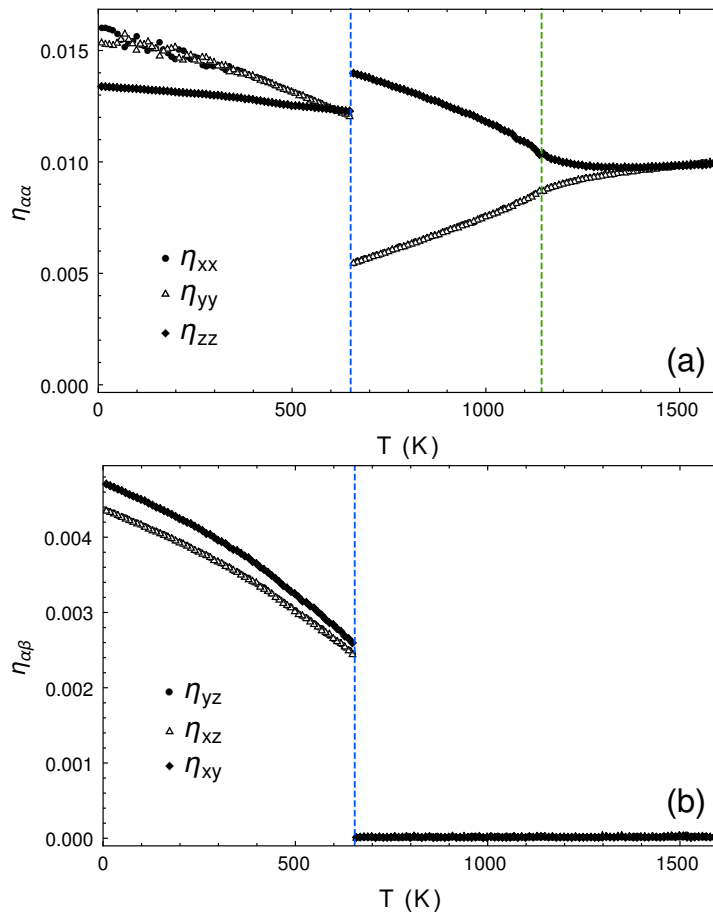


FIGURE 3.30: Temperature dependence of the of (a) the diagonal homogeneous strain tensor components and (b) the homogeneous off-diagonal strain tensor components in the case of $S_{3,2}$ supercell geometry.

Indeed, the $S_{(3,2)}$ structure undergoes a magnetic phase transition at $T_N \approx 450$ K. For both $S_{(2,3)}$ and $S_{(3,2)}$ geometries, the lattice structure constrains the possible

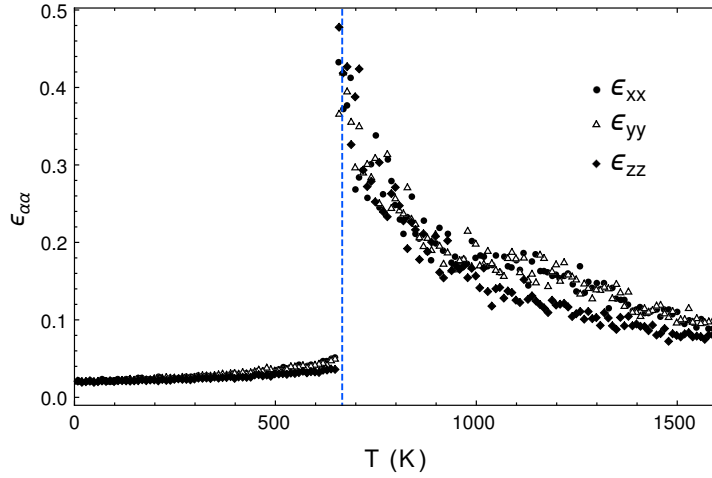


FIGURE 3.31: Temperature evolution of the diagonal components of the dielectric susceptibility tensor components in the case of $S_{(3,2)}$ lattice structure.

ground-state spin configuration leading to average magnetization values several orders of magnitude higher than the weak magnetic moment of pure the BiFeO_3 . The antiferromagnetic order parameter $L = \sum_{x,y,z} (-1)^{x+y+z} \mathbf{s}_i$ in this case is equal to $2.5 \mu_B$.

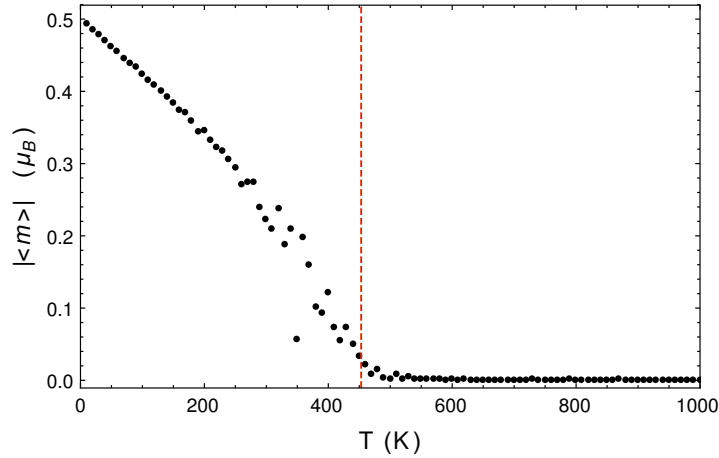


FIGURE 3.32: Temperature evolution of the absolute value of average magnetization of the $S_{(3,2)}$ lattice structure.

In the case of $S_{(2,3)}$ geometry, the decreased volume fraction of BiFeO_3 lowers the magnetic transition temperature, however, the ground state magnetization still exceeds that of the pure BiFeO_3 by one order of magnitude.

3.3.6 Summary of the obtained results

Table 3.1 summarizes the obtained transition temperatures for the bicrystal $(\text{BiFeO}_3)(\text{BaTiO}_3)$ lattices with different geometries.

Supercell structure	x	T_C (K)	T_{AFD} (K)	T_N (K)
$S_{(0,0)}$	0.5	(<i>C-R</i>) 795	—	134
$S_{(1,1)}$	0.5	(<i>T-O</i>) 680 (<i>O-M</i>) 547	—	262
$S_{(2,2)}$	0.5	(<i>T-M</i>) 427	—	82
$S_{(3,3)}$	0.5	(<i>C-M</i>) 574	800	277
$S_{(2,3)}$	0.325	(<i>T-M</i>) 134	636	—
$S_{(3,2)}$	0.625	(<i>T-M</i>) 654	1146	450

TABLE 3.1: Summary of the transition temperatures predicted for the considered $(\text{BiFeO}_3)(\text{BaTiO}_3)$ bicrystals. The first column contains the label of the structure, the second column presents the corresponding BiFeO_3 concentration x . The third column summarizes the ferroelectric transition temperatures. Here, labels *C*, *T*, *R*, *O*, *M* denote cubic, tetragonal, rhombohedral, orthorhombic and monoclinic phases respectively. The last two columns contain the AFD and antiferromagnetic transition temperatures.

As can be seen from table 3.1, the multiferroic properties of $(\text{BiFeO}_3)(\text{BaTiO}_3)$ compounds strongly depend on the geometry of the lattice. For instance, increasing the connectivity of bismuth ferrite and its concentration leads to the increase of the AFD transition temperature. On the other hand, the behaviour of the Curie and Neel temperatures do not follow this trend. For the structures with equal volume fractions of constituent materials, the magnetic transition temperature reaches its maximum in the case of the (3,3) connectivity, while the ferroelectric transition temperature is maximized in the case of (0,0) three-dimensional checkerboard geometry. Most importantly, our results suggest that composite $(\text{BiFeO}_3)(\text{BaTiO}_3)$ structures can exhibit magnetoelectric response exceeding that of BiFeO_3 single crystals. Latter is indicated by the presence of pronounced kinks of the magnetic susceptibility at the ferroelectric transition temperatures.

3.4 Example of structure-property relations: fractal $(\text{Ba,Sr})\text{TiO}_3$ structures

In this section, we briefly present a study pertaining to a specific morphology of inclusions, that is, of the fractal type. The motivation of this study is twofold. First, it allows to further asses the relevance of the Nehwnham's composite materials classification relying on the concept of the geometrical connectivity (see section 1.3). Second, as it is now well established [160, 161, 162], critical phenomena can involve spatially self-similar fluctuations. The idea is thus to probe

whether fractal ferroelectric inclusions can structurally underpin the critical fluctuations.

Specifically, we will consider the example of the fractal BaTiO_3 inclusions in SrTiO_3 matrix (such structure will be referred to as $R_{0.2}$) and conversely SrTiO_3 fractal inclusions in the BaTiO_3 matrix ($R_{0.8}$ structure). The fractal shape is chosen to be represented by the second iteration of the Menger sponge construction algorithm (see section 1.3). Such inclusions, having the side length of nine unit cells are embedded in the $12 \times 12 \times 12$ simulation supercell subject to periodic boundary conditions and are depicted in Fig. 3.33. Therefore, the volume fraction of the material contained within the array of fractal inclusions is approximately equal to ~ 0.19 , while the volume fraction of the matrix material is ≈ 0.81 . Naturally, according to Newnham's definition, such supercell structures would correspond to the (0-3) connectivity. The same connectivity can be achieved by uniformly distributing the active material contained within the inclusions over the volume of the supercell. In this latter case, the obtained structure would mimic the $(\text{Ba}_x\text{Sr}_{1-x})\text{TiO}_3$ solid solution with $x \approx 0.19$ or $x \approx 0.81$ (solid solution structures will be denoted as $R_{0.2}$ and $R_{0.8}$ with the subscript indicating the approximate concentration of Ba^{2+} cations).

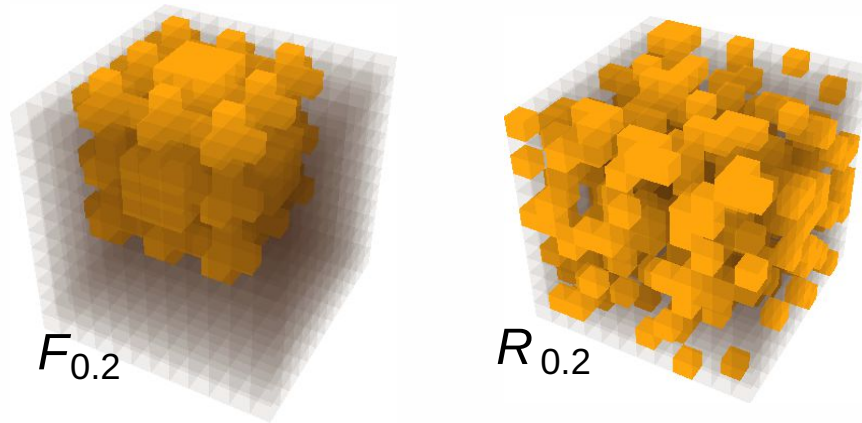


FIGURE 3.33: Schematic representation of the considered $(\text{Ba}_x\text{Sr}_{1-x})\text{TiO}_3$ superlattice structures. On the right: the fractal inclusions of BaTiO_3 in the matrix of SrTiO_3 . The shape of inclusions corresponds to the second iteration of the Menger sponge (three dimensional analogue of the Sierpinski carpet) construction algorithm. Yellow cubes correspond to the BaTiO_3 unit cells. The Ba^{2+} concentration is equal to $x \approx 0.19$. Throughout the text, the described structure is referred to as $F_{0.2}$. The inverse structure obtained by replacing BaTiO_3 unit cells by those of SrTiO_3 and vice versa allows to construct $F_{0.8}$ supercell. On the right: Spatially uniform distribution of Ba^{2+} and Sr^{2+} cations. Such structures will be denoted as $R_{0.2}$ and $R_{0.8}$ with the subscript indicating the Ba^{2+} concentration x .

The comparison of the geometrical characteristics of all the considered supercell geometries is presented in table (3.2). As one can see, the F_x and R_x structures have the same connectivities along with equal active phase concentration x , while exhibiting drastically different Euler characteristic and fractal dimension of the set of the active phase unit cells. Let us note that the fractal dimension of the F_x structures is comparable to the fractal dimension of the critical spin clusters featured by 3D Ising model [160].

Supercell structure	x	β_1	β_2	β_3	χ_E	d_B	C
$F_{0.2}$	0.19	1	31	3	-27	2.22	(0-3)
$F_{0.8}$	0.81	1	28	0	-27	2.89	(3-0)
$R_{0.2}$	0.19	3	102	0	-99	1.42	(0-3)
$R_{0.8}$	0.81	1	3	151	149	1.79	(3-0)

TABLE 3.2: Summary of the geometric characteristics of the considered $(\text{Ba}_x, \text{Sr}_{1-x})\text{TiO}_3$ supercell structures. Columns β_{1-3} contain the first three Betti numbers of the set representing the union of the BaTiO_3 unit cells; χ_E denotes the Euler characteristic calculated as $\chi_E = \beta_1 - \beta_2 + \beta_3$, while x and d_B are Ba^{2+} concentration and the box counting fractal dimension respectively. The last column contains the connectivity of the structure, with BaTiO_3 is assumed to be the active phase.

In order to obtain the finite-temperature properties of the aforementioned $(\text{Ba}, \text{Sr})\text{TiO}_3$ nanostructures, we have performed Metropolis Monte Carlo simulations with temperature annealing using 10^5 thermalization sweeps and $9 \cdot 10^5$ averaging sweeps. Figure 3.34 presents the obtained average local mode components $\langle \langle u_{x,y,z} \rangle_i \rangle$. Both $R_{0.2}$ (graph (a)) and $R_{0.8}$ (graph (b)) structures undergo a similar sequence of ferroelectric phase transitions from paraelectric to tetragonal, orthorhombic and rhombohedral phases. The fractal $F_{0.2}$ (graph (c)) exhibits a single diffuse phase transition from paraelectric to ferroelectric rhombohedral phase. Let us note that despite the significant statistical sample volume ($\sim 10^6$ Monte Carlo sweeps), the standard deviation of the average local mode components remains relatively large, most likely indicating the presence of multiple accessible local energy minima. Similar phenomenon is observed in the case of $F_{0.8}$ fractal structure (graph (d)), where one witnesses the collapse of the three phase transitions exhibited by the disordered $R_{0.8}$ structure into a single diffuse and broad “critical” (or transient) region.

Naturally, the aforementioned broadened “critical” region can be clearly observed in the temperature dependence of the computed dielectric susceptibility. As it can be seen from Fig. 3.35, both $F_{0.2}$ and $F_{0.8}$ feature a double peaked dielectric susceptibility. Each of the peaks corresponds to the entrance into the transient region and the stabilization of the system in a ferroelectric ground-state as the

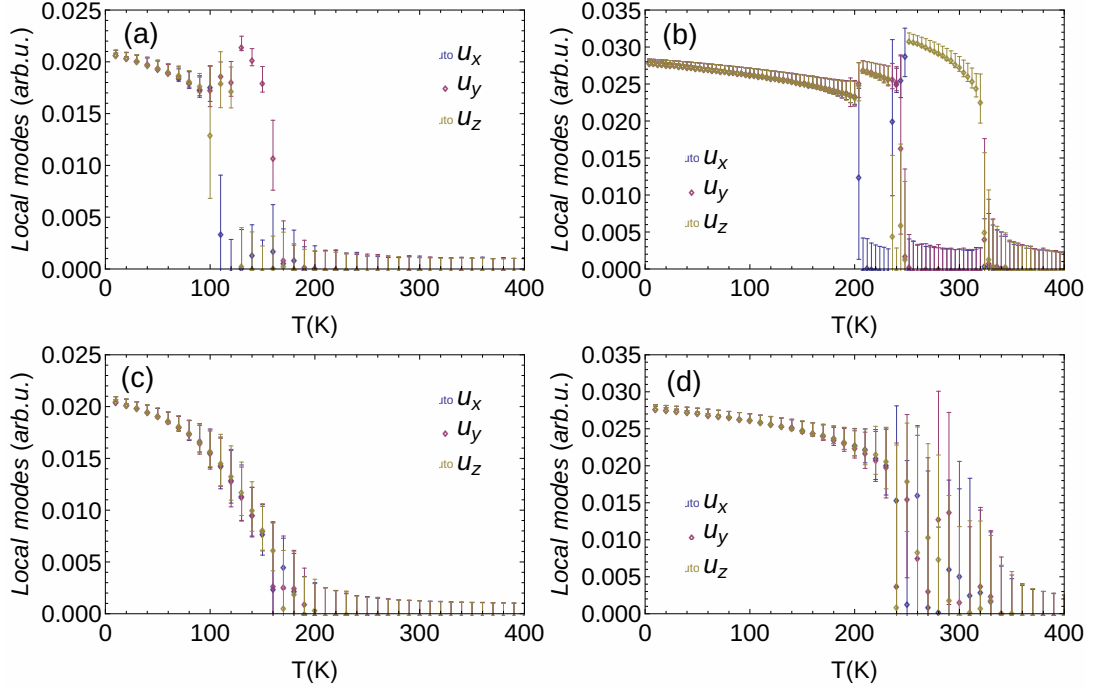


FIGURE 3.34: Average local mode components $\langle u_{x,y,z} \rangle_i$ for different lattice structures (a) $R_{0.2}$, $(\text{Ba}_{0.19}, \text{Sr}_{0.81})\text{TiO}_3$ solid solution (b) $R_{0.8}$, $(\text{Ba}_{0.81}, \text{Sr}_{0.19})\text{TiO}_3$ solid solution (c) $F_{0.2}$, BaTiO_3 fractal inclusions in SrTiO_3 matrix (d) $F_{0.8}$, SrTiO_3 fractal inclusions in BaTiO_3 matrix. The errorbars indicate the standard deviation estimated from the performed Monte Carlo simulations using $\sim 10^5$ thermalization and averaging sweeps.

temperature is decreased, respectively. Notably, the dielectric response of the $F_{0.8}$ structure is approximately one order of magnitude higher than that of the $(\text{Ba}_{0.81}, \text{Sr}_{0.19})\text{TiO}_3$ solid solution structure.

Figure 3.36 contains the calculated temperature dependence of the specific heat for all four considered structures. In contrast to the disordered systems, the specific heat of the fractal structures does not diverge at the transition temperatures. Moreover, one observes that the temperature region attributed to the transient phase exhibited by the fractal structures $F_{0.2}$ and $F_{0.8}$ is approximately delimited by the paraelectric to tetragonal and tetragonal to orthorhombic transition temperatures of the corresponding $R_{0.2}$ and $R_{0.8}$ disordered structures.

The absence of the orthorhombic phase in the phase diagram of fractal structures $F_{0.2}$ and $F_{0.8}$ is confirmed by the calculated temperature dependence of the average strain components. In the case of $F_{0.2}$ structure (Fig. 3.37), one observes a

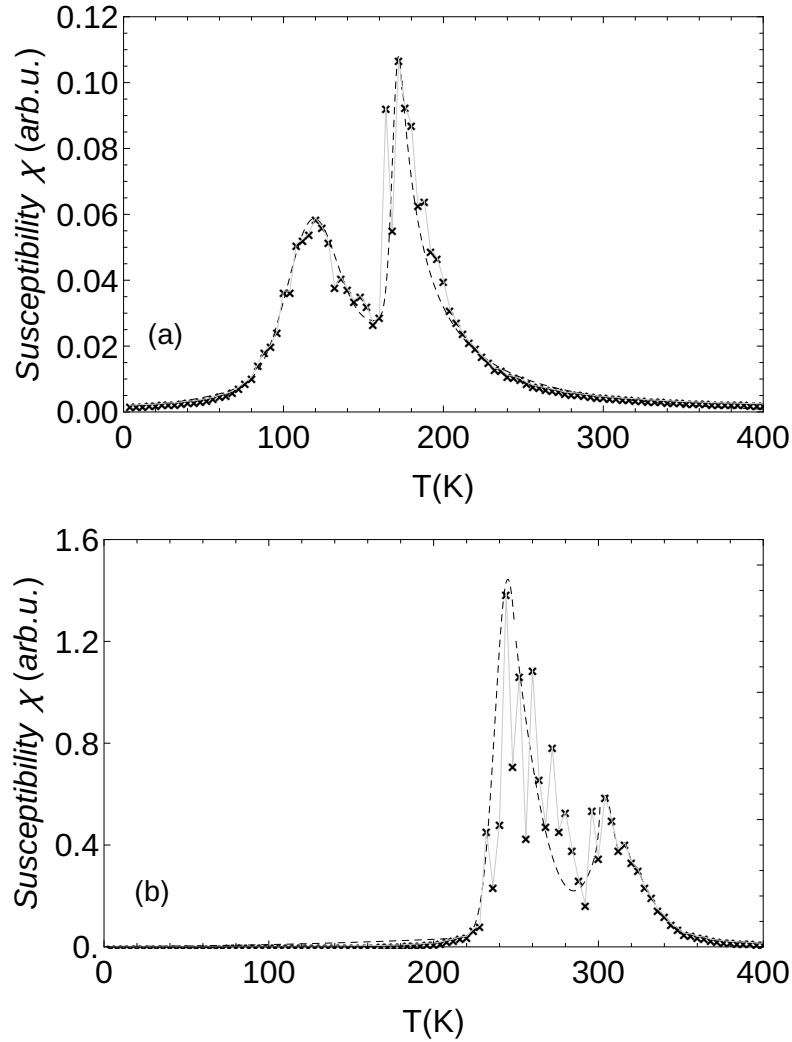


FIGURE 3.35: Dielectric susceptibilities of two fractal structures $\chi = (\sum_i \langle \chi_{ii} \rangle) / 3$ (a) average susceptibility of $F_{0.2}$ structure and (b) $aF_{0.8}$ structure. On both figures one observes two distinct peaks, corresponding to the entrance into the transient region and the stabilization of the system in a ferroelectric ground-state. All the observed peaks are diffuse. The dielectric response of bulk BaTiO_3 structure diluted with fractal SrTiO_3 (structure $F_{0.8}$) inclusions shows the dielectric response which is approximately one order of magnitude larger than that of the $(\text{Ba}_{0.81}, \text{Sr}_{0.19})\text{TiO}_3$ solid solution.

signature of a cubic to rhombohedral structural phase transition occurring around the first transition temperature of $R_{0.2}$ compound. Moreover, in contrast to the case of the disordered $R_{0.2}$ structure, the diagonal and off-diagonal strain tensor components remain equal in the entire probed temperature range.

The comparison of the temperature dependence of the average strain components exhibited by $R_{0.8}$ and $F_{0.8}$ structures is presented in Fig. 3.38. While one can clearly observe three consecutive structural phase transitions in the case of the disordered $R_{0.8}$ structure, the $F_{0.8}$ system undergoes a phase transition from cubic

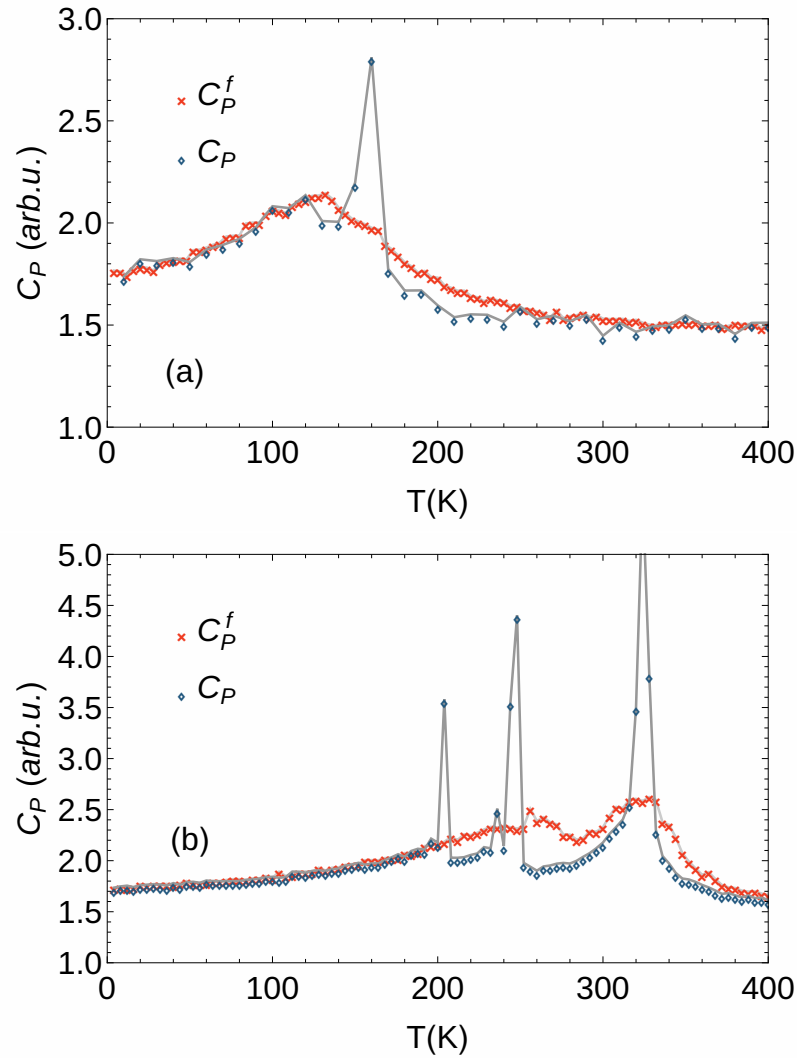


FIGURE 3.36: Upper and lower panels illustrate the comparison of the temperature dependence of the specific heat at fixed pressure for two different Ba^{2+} concentrations x . (a) $x \approx 0.19$. The red markers indicate the specific heat of the system composed of fractal BaTiO_3 inclusions in SrTiO_3 matrix ($F_{0.2}$), while the blue markers correspond to the specific heat computed for the solid solution system ($R_{0.2}$). (b) $x \approx 0.81$. The red markers correspond to the SrTiO_3 fractal inclusions in BaTiO_3 matrix, the blue markers represent the solid solution system ($R_{0.8}$).

to rhombohedral phase via a transient state characterised by unusually high level of strain components fluctuations.

The discussion presented above strongly suggests that the connectivity and other commonly used structural characteristics are not necessarily sufficient to classify nanocomposite materials. Indeed, in the context of phase transition studies, other properties such as the fractal dimension of the active phase sublattice might play an important role.

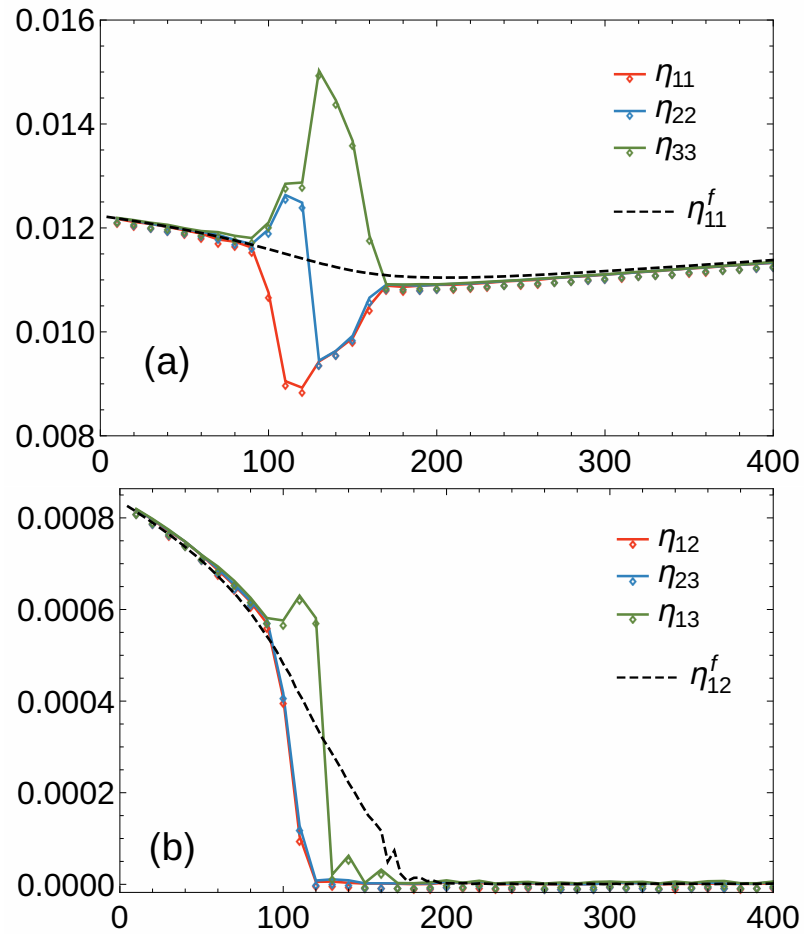


FIGURE 3.37: Comparison of the temperature dependence of the average strain components exhibited by $F_{0.2}$ (black dashed curves) and $R_{0.2}$ (η_{ij} strain tensor components) structures. In the case of the fractal $F_{0.2}$ supercell geometry, the three diagonal η_{ii}^f (graph (a)) and three off-diagonal (graph (b)) strain components are equal in the entire probed temperature range. The results indicate the presence of a structural phase transition from the cubic to the rhombohedral ferroelectric phase.

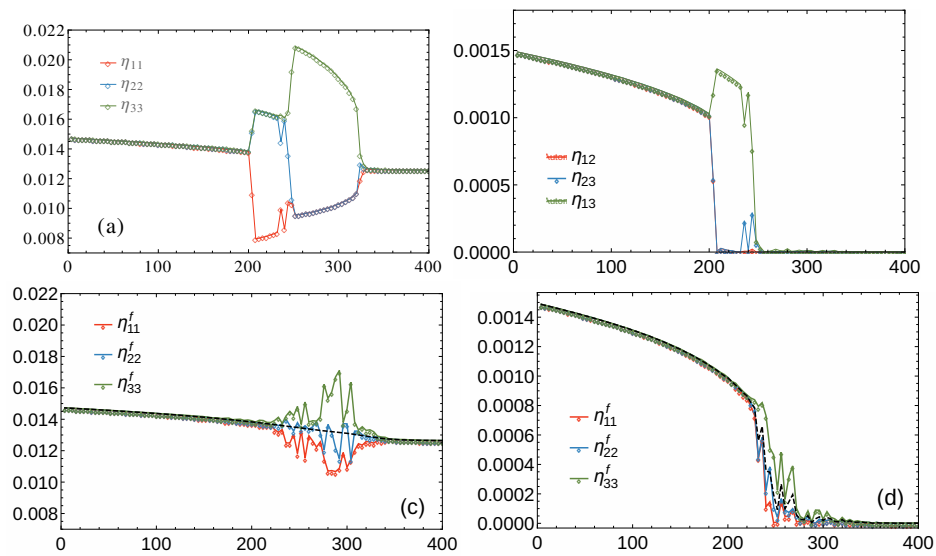


FIGURE 3.38: Comparison of the temperature dependence of the average strain components exhibited by $R_{0.8}$ (graphs (a) and (b)) and $F_{0.8}$ (graphs (c) and (d)) structures. One can clearly observe three consecutive structural phase transitions in the case of the disordered $R_{0.8}$ structure. $F_{0.8}$ undergoes a phase transition from cubic to rhombohedral phase via the transient state indicated by unusually high fluctuations of the strain components.

Chapter 4

Nonlinear thermodynamic theory of piezoelectric/piezomagnetic heterostructures

4.1 Introduction

Ferroelectric-ferromagnetic nanocomposites and nanoscale heterostructures may exhibit strong magnetoelectric (ME) effects owing the interfacial coupling between two ferroic order parameters [163]. The most important coupling mechanisms include the mechanical interaction providing transmission of strains across interfaces [164], spin-dependent screening of surface polarization charges [165, 166], and modifications of interfacial bonds [167]. Evidently, the role of interface-related and proximity effects increases drastically in nanoscale multiferroic heterostructures, which are especially suitable for microelectronics. In addition, the epitaxial growth of such heterostructures should ensure much better strain transfer between ferroic constituents than in the bulk piezoelectric-magnetostrictive composites suffering from poor coupling at the interfaces [168]. As a result, multiferroic nanostructures are considered as promising active elements for a variety of electronic and spintronic devices including ME recording read heads [169], electrostatically tunable microwave devices [170], electric-write magnetoresistive memories [171, 172], and energy-harvesting devices [173].

In particular, multilayered ME nanocomposites represent one of the leading contenders for ultrasensitive room-temperature magnetic-field sensors needed for biomedical applications (e.g., in magnetocardiography and magnetoencephalography) [174].

The strain-mediated ME response of these multilayers, however, becomes high only at the mechanical resonance because they are fabricated on thick passive substrates which strongly reduce the field-induced deformations of magnetic layers. Such mechanical clamping can be avoided by using *active* magnetostrictive [175, 176] and piezoelectric [177, 178, 179] substrates for the fabrication of ferroelectric and ferromagnetic films, respectively. The resulting ME film-substrate hybrids should have strongly enhanced quasi-static ME responses. In particular, it was predicted theoretically that the strain-mediated direct ME effect displayed by ferroelectric-ferromagnetic hybrids is characterized by high ME voltage coefficients [180, 181].

Another promising approach is to employ mechanically free ME multilayers since this geometry provides large interface area. Such multilayers can be obtained by removing the substrate after the deposition or by thinning it down to a thickness much smaller than that of the multilayer. This can be realized by substrate etching [182] or by using focused ion beam technique [183, 184]. Moreover, a substrate-free ferroelectric-ferromagnetic multilayer in the form of the nanolamellar BaTiO₃/CoFe₂O₄ bicrystal has been recently successfully fabricated [185].

In this chapter, we describe theoretically the strain-mediated direct ME effect exhibited by free-standing multilayers composed of single-crystalline ferroelectric nanolayers interleaved by conducting ferromagnetic slabs. Our analysis is restricted to multilayers that are symmetric with respect to the central slab, involving even number of ferroelectric and odd number of ferromagnetic layers (Fig. 4.1). Such multilayers do not bend under applied magnetic field, which greatly simplify theoretical calculations without changing the quasi-static ME effect significantly. We first determine the polarization states of ferroelectric nanolayers with the aid of a nonlinear thermodynamic approach developed in the paper [186], which properly takes into account specific mechanical boundary conditions of the problem. The room-temperature stability ranges of possible single-domain states are described by phase diagrams constructed using the misfit strain in the heterostructure and the volume fraction of ferromagnetic component as two independent variables. Then, using these diagrams, we calculate the strain sensitivity of the out-of-plane polarization component and the permittivity of ferroelectric nanolayers. Since this work focuses on the strain-mediated ME effect, the ferromagnetic component is modeled by a crystalline medium with linear elastic properties and lattice parameters varying with applied magnetic field \mathbf{H} (owing to the magnetostriction). Furthermore, the strain response of this component to a weak measuring ac field \mathbf{H}_{ac} is taken to be linear due to the presence of a bias field \mathbf{H}_{dc} in ME measurements [170]. Characterizing this response by effective piezomagnetic coefficients

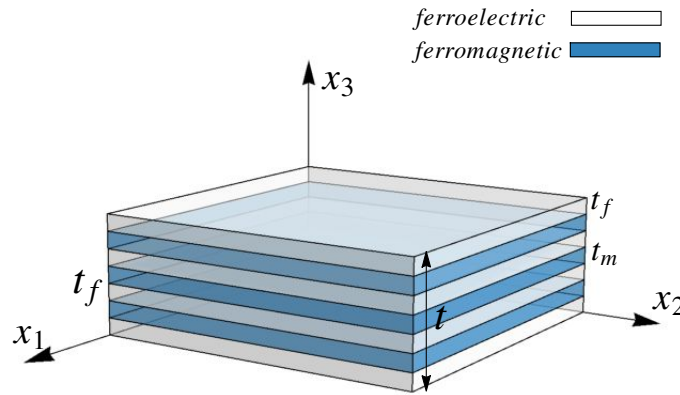


FIGURE 4.1: Schematic depiction of a free-standing multilayer containing odd number of identical ferromagnetic layers and even number of identical ferroelectric layers. The multilayer is symmetric with respect to the central ferromagnetic slab. The thicknesses of ferroelectric and magnetic layers are denoted by t_f and t_m , respectively.

of ferromagnetic slabs and using the calculated strain sensitivity of polarization and permittivity of ferroelectric ones, we finally evaluate low-frequency ME polarization and voltage coefficients of the discussed multilayers and their output charge and voltage signals. The numerical calculations, restricted to the room temperature $T = 25^\circ\text{C}$, are performed for multilayers comprising BaTiO_3 and $\text{Pb}(\text{Zr}_{0.5}\text{Ti}_{0.5})\text{O}_3$ layers interleaved by FeGaB slabs.

4.2 Nonlinear thermodynamic model

Consider a free-standing multilayer consisting of alternating ferroelectric and ferromagnetic slabs with the total thickness t much smaller than the multilayer sizes along the x_1 and x_2 axes (Fig. 4.1). Despite the absence of external mechanical forces acting on the multilayer, the interfacial coupling between dissimilar ferroic materials generally gives rise to considerable strains and internal stresses in this heterostructure. Since lattice strains have a strong impact of the phase states of ferroelectric thin films [187, 188, 189], we have to determine first the polarization state of ferroelectric component in the multilayer. To that end, we employ the Helmholtz free energy density F_f of ferroelectric layers written in terms of polarization components P_i and total strains u_{ij} ($i, j = 1, 2, 3$) counted from the prototypic paraelectric state [190]. For layers with nanoscale thicknesses, single-domain states may be assumed for poled ferroelectric slabs, as confirmed

by first-principles calculations [191, 192]. In contrast, we consider ferromagnetic layers with fine domain structures providing high linear response to a weak ac field \mathbf{H}_{ac} at intermediate bias fields \mathbf{H}_{dc} [170]. Since we are interested only in the mechanical effect of ferromagnetic layers on ferroelectric ones, the magnetization distribution in the former may be taken into account implicitly via average magnetostrictive strains ν_{ij}^{ms} depending on the applied magnetic field. Indeed, the total strains ν_{ij} in a ferromagnetic material, counted from the prototypic paramagnetic state, can be written as $\nu_{ij} = \nu_{ij}^{el} + \nu_{ij}^{ms}$, where ν_{ij}^{el} are the elastic strains related to internal stresses [1]. Hence the mean Helmholtz energy density F_m of conducting ferromagnetic layers may be set equal to the elastic energy (governed by ν_{ij}^{el}) in the first approximation.

To determine the strain state of the multilayer, we first employ the mechanical boundary conditions of the problem. In the reference frame (x_1, x_2, x_3) shown in Fig. 4.1, the classical interfacial compatibility condition [193] can be written as

$$\begin{aligned} u_{11} &= \nu_{11}^{el} + \nu_{11}^{ms} + u_{m11}^0, & u_{22} &= \nu_{22}^{el} + \nu_{22}^{ms} + u_{m22}^0, \\ u_{12} &= \nu_{12}^{el} + \nu_{12}^{ms} + u_{m12}^0 \end{aligned} \quad (4.1)$$

where u_{m11}^0 , u_{m22}^0 , and u_{m12}^0 are the *misfit strains* (normal and shear) in the prototypic paraelectric-paramagnetic multilayer, which result from the mismatch of two crystal lattices at the growth temperature (in the case of epitaxial growth) and the development of thermal strains during the cooling from the growth temperature to room temperature (these strains are governed by the difference in thermal expansion coefficients of two materials). Considering in-plane magnetostrictive strains $\nu_{\alpha\beta}^{ms}$ ($\alpha, \beta = 1, 2$) as a part of modified misfit strains, we can rewrite eq. 4.1 in the form $u_{\alpha\beta} = \nu_{\alpha\beta}^{el} + u_{m\alpha\beta}$, where $u_{m\alpha\beta} = u_{m\alpha\beta}(\mathbf{H})$ are the misfit strains characterizing the difference between the prototypic paraelectric state of free-standing ferroelectric layers and the stress-free state of ferromagnetic layers in a magnetic field \mathbf{H} .

Taking into account the absence of forces acting on the multilayer outer surface, we further obtain restrictions imposed on the internal mechanical stresses in ferroelectric and magnetic layers, which will be denoted as σ_{ij}^f and σ_{ij}^m , respectively. Since the equations of mechanical equilibrium [194] ensure the continuity of stresses σ_{i3} across the interfaces, the stresses σ_{i3}^f and σ_{i3}^m should be zero in the free-standing multilayer. In addition, the calculation of forces acting on the surface sections perpendicular to the x_1 and x_2 axes gives $\phi_f \sigma_{\alpha\beta}^f + \phi_m \sigma_{\alpha\beta}^m = 0$, where ϕ_f and ϕ_m are the volume fractions of ferroelectric and magnetic materials in the multilayer.

Since $\sigma_{ij}^f = \partial F_f / \partial u_{ij}$ and $\sigma_{ij}^m = \partial F_m / \partial \nu_{ij}^{el}$, in total we obtain twelve equations for twelve strains u_{ij} and ν_{ij}^{el} , which enable us to find the latter in terms of the misfit strains $u_{m\alpha\beta}$ and polarization components P_i in the ferroelectric component.

The energetically most favorable single-domain states of ferroelectric nanolayers can be found now via the minimization of the mean Helmholtz free energy density $\langle F \rangle (P_1, P_2, P_3)$ in the multilayer, which can be written as

$$\langle F \rangle = \phi_f F_f + \phi_m F_m \quad (4.2)$$

To allow the consideration of ferroelectrics with complex phase behaviors in the bulk such as BaTiO₃, the energy density F_f should be described by a polynomial including the polarization terms up to eighth order [195]. At the same time, it is sufficient to employ the linear-quadratic relationship [190] for the electrostrictive coupling between lattice strains and polarization, whilst the elastic energy of ferroelectric and ferromagnetic layers can be written in the harmonic approximation. Since only conductive ferromagnetic materials are considered in this work, we neglect the electrostatic contribution to the energy $\langle F \rangle$, which is caused by the polarization charges existing on the surfaces of ferroelectric layers [186]. However, the interaction of polarization P with the applied electric field E is included.

Owing to the electrostrictive coupling, the mechanical interaction between ferroelectric and ferromagnetic layers renormalizes thermodynamic coefficients of the second-order and fourth-order polarization terms in the energy density F_f . This modification, however, is different from the renormalization characteristic of ferroelectric films grown on dissimilar thick substrates [187, 189], because ferromagnetic interlayers generally impose only partial clamping on ferroelectric ones. For multilayers comprising ferroic slabs with (001)-oriented prototypic phases (paraelectric and paramagnetic) of cubic symmetry, the calculation of the mean energy density yields

$$\begin{aligned} \langle F \rangle = & \phi_f (\alpha_1^* P_1^2 + \alpha_2^* P_2^2 + \alpha_3^* P_3^2 + \alpha_6^* P_1 P_2 + \alpha_{11}^* (P_1^4 + P_2^4) + \\ & + \alpha_{33}^* P_3^4 + \alpha_{12}^* P_1^2 P_2^2 + \alpha_{13}^* (P_1^2 P_3^2 + P_2^2 P_3^2) + \alpha_{111} (P_1^6 + P_2^6 + P_3^6) + \\ & + \alpha_{112} (P_1^2 (P_2^4 + P_3^4) + P_2^2 (P_1^4 + P_3^4) + P_3^2 (P_1^4 + P_2^4)) + \alpha_{123} P_1^2 P_2^2 P_3^2 + \\ & + \alpha_{1111} (P_1^8 + P_2^8 + P_3^8) P_1^2 + P_3^2 + \alpha_{1112} (P_1^6 (P_2^2 + P_3^2) + P_2^6 (P_1^2 + \\ & + P_3^2) + P_3^6 (P_1^2 + P_2^2)) + \alpha_{1122} (P_1^4 P_2^4 + P_2^4 P_3^4 + P_1^4 P_3^4) + \\ & + \alpha_{1123} (P_1^4 P_2^2 P_3^2 + P_2^4 P_1^2 P_3^2 + P_3^4 P_1^2 P_2^2) - P_1 E_1 - P_2 E_2 - P_3 E_3) \end{aligned} \quad (4.3)$$

where the renormalized second-order coefficients are given by the relations

$$\begin{aligned}
\alpha_1^* &= \alpha_1 - \frac{\phi_m}{2} \left(\frac{(u_{m11} + u_{m22})(Q_{11} + Q_{12})}{(1 - \phi_m)(s_{11}^m + s_{12}^m) + \phi_m(s_{11} + s_{12})} + \frac{(Q_{11} - Q_{12})(u_{m11} - u_{m22})}{(1 - \phi_m)(s_{11}^m - s_{12}^m) + \phi_m(s_{11} - s_{12})} \right) \\
\alpha_2^* &= \alpha_1 - \frac{\phi_m}{2} \left(\frac{(u_{m11} + u_{m22})(Q_{11} + Q_{12})}{(1 - \phi_m)(s_{11}^m + s_{12}^m) + \phi_m(s_{11} + s_{12})} - \frac{(Q_{11} - Q_{12})(u_{m11} - u_{m22})}{(1 - \phi_m)(s_{11}^m - s_{12}^m) + \phi_m(s_{11} - s_{12})} \right) \\
\alpha_3^* &= \alpha_1 - \frac{\phi_m(u_{m11} + u_{m22})Q_{12}}{(1 - \phi_m)(s_{11}^m + s_{22}^m) + \phi_m(s_{11} + s_{22})} \\
\alpha_6^* &= \frac{\phi_m Q_{44} u_{m12}}{(1 - \phi_m)s_{44}^m + \phi_m s_{44}}
\end{aligned} \tag{4.4}$$

whilst the renormalized fourth-order coefficients α_{ij}^* coincide with those defined by equation (8) in the Ref. [186]. In eq. 4.3 and eq. 4.4, $\alpha_1 = \alpha_1(T)$, α_{1ij} , and α_{11ij} represent the temperature-dependent dielectric stiffness and higher-order stiffness coefficients of paraelectric phase at constant stress, Q_{11} , Q_{12} , and Q_{44} are the electrostrictive constants of this phase, and s_{11} , s_{12} , s_{44} and s_{11}^m , s_{12}^m , s_{44}^m are the elastic compliances of the paraelectric and paramagnetic phase, respectively, which are defined in the reference frame (x_1, x_2, x_3) with the x_i axes parallel to the principal cubic axes of the paraelectric phase.

At $\phi_m \rightarrow 1$, when the mechanical boundary conditions of ferroelectric layers become equivalent to those imposed on a thin film grown on a thick substrate, the expressions given in eq. 4.4 reduce to the relations for renormalized thermodynamic coefficients given in Ref. [189]. On the other hand, in the case of isotropic biaxial misfit strain ($u_{m11} = u_{m22} = u_m$, $u_{m12} = 0$), at any value of ϕ_m we obtain $\alpha_2^* = \alpha_1^*$, $\alpha_6^* = 0$, and the same formulae for α_1^* and α_3^* as in [186]. These results support the validity of our calculations.

In conclusion of this section we note that our thermodynamic model differs from the previous theoretical investigations of ferroelectric-ferromagnetic multilayers [196, 197] in several respects. In particular, a single-domain state was assumed for ferromagnetic layers in these studies, which cannot provide high linear strain response to the applied magnetic field. Moreover, Wang and Woo [196] employed the energy density of ferromagnetic component written as a polynomial in terms of magnetization components, which is valid near the Curie temperature only [1], while Livesey studied multilayers fully clamped in the direction orthogonal to interfaces [197], but not the free standing ones.

4.3 Polarization states and physical properties of ferroelectric nanolayers

The numerical minimization of the mean free energy $\langle F \rangle (P_1, P_2, P_3)$ given by eq. 4.3 with respect to three polarization components P_i makes it possible to determine the energetically most favorable single-domain states of ferroelectric nanolayers at various temperatures, misfit strains, and volume fractions of the ferromagnetic component. In this work, we studied two important ferroelectric materials - BaTiO₃ and Pb(Zr_{0.5}Ti_{0.5})O₃ (PZT 50/50) - and restricted our computations to the determination of their polarization states at room temperature. The numerical values of thermodynamic coefficients were taken from Refs. [195, 198], while those of electrostrictive constants and elastic compliances - from Refs. [187, 188, 198].

As a representative ferromagnetic material, we selected FeGaB because this galfenol alloy with small boron addition has exceptional magnetostrictive properties [199, 200], and BaTiO₃-Fe heterostructures probably may be grown epitaxially [167]. Below certain critical boron content, FeGaB has the crystalline structure with a cubic unit cell and lattice constant $b \approx 2.9 \text{ \AA}$ [200]. Accordingly, the lattice mismatch becomes reduced when the [100] crystallographic axis of FeGaB is parallel to a face diagonal of the prototypic cubic cell of BaTiO₃ or PZT (see Fig. 4.2). At this orientation, the lattice matching creates an isotropic biaxial misfit strain u_m ($u_{m11} = u_{m22} = u_m, u_{m12} = 0$), which in the case of coherent interface is defined by the formula $u_m = (\sqrt{2}b - a_0)/a_0$, where a_0 is the lattice parameter of the prototypic cubic phase of BaTiO₃ or PZT. Since a_0 is about 4 Å, the nominal misfit strain is still rather large ($u_m \approx 2.5\%$) so that the critical thickness for the generation of misfit dislocations should be small [201]. Hence the actual misfit strain in the considered multilayers can vary in a wide range depending on the thicknesses of ferroelectric and ferromagnetic layers. Furthermore, very small magnetostrictive strains $\sim 2 \times 10^{-5}$ induced by the bias magnetic field \mathbf{H}_{dc} (see next section) may be neglected in comparison with much bigger initial misfit strains u_{m11}^0 and u_{m22}^0 . This feature enables us to neglect the influence of \mathbf{H}_{dc} on the misfit strains $u_{m\alpha\beta}(\mathbf{H})$ in the multilayer and to determine the polarization states of ferroelectric layers as a function of u_m .

To evaluate the sensitivity of ferroelectric states to the elastic properties of ferromagnetic layers, we considered two different FeGaB alloys - Fe_{85.38}Ga_{14.6}B_{0.02} and Fe_{81.72}Ga_{18.2}B_{0.08}. The measured elastic stiffnesses of these alloys [202] are listed in the table below. These stiffnesses, given in the FeGaB crystallographic

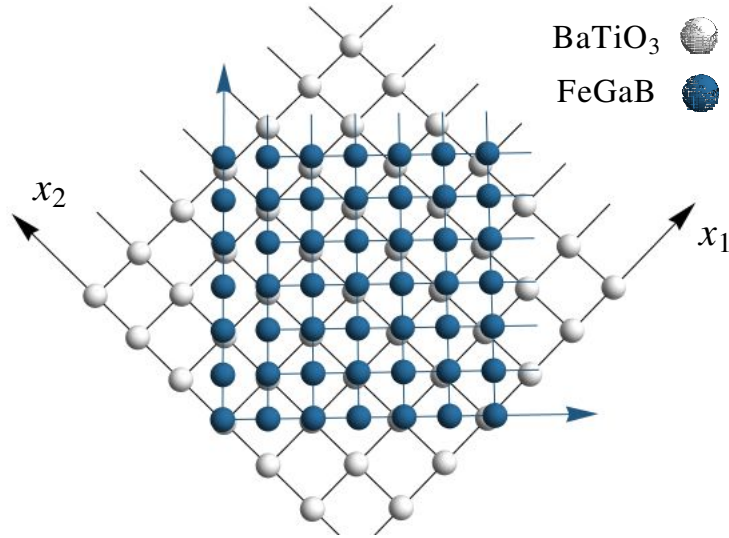


FIGURE 4.2: Probable lattice matching in FeGaB-BaTiO₃ and FeGaB-PZT epitaxial systems. The crystallographic [100] direction of FeGaB lattice is parallel to the [110] direction of the prototypic cubic lattice of BaTiO₃ or PZT, which reduces misfit strain in the heterostructure.

Composition	c_{11}^m (10^{11} N/m ²)	c_{12}^m (10^{11} N/m ²)	c_{44}^m (10^{11} N/m ²)
Fe _{85.38} Ga _{14.6} B _{0.02}	1.984	1.402	1.241
Fe _{81.72} Ga _{18.2} B _{0.08}	2.150	1.718	1.231

TABLE 4.1: Elastic constants of FeGaB alloys [202]

coordinate system, were transformed to the reference frame (x_1, x_2, x_3) rotated by 45° and then converted into the elastic compliances involved in eq. 4.4.

Figure 4.3 shows the calculated room-temperature phase diagrams of PZT 50/50 and BaTiO₃ nanolayers interleaved by FeGaB slabs, which are constructed using the biaxial misfit strain u_m and the volume fraction ϕ_m of ferromagnetic component as two independent variables. In the case of PZT 50/50, the diagram contains stability ranges of only four polarization states: the orthorhombic a ($P_1 \neq 0, P_2 = P_3 = 0$ or $P_2 \neq 0, P_1 = P_3 = 0$) and aa ($|P_1| = |P_2| \neq 0, P_3 = 0$) phases with in-plane polarizations, the tetragonal c phase ($P_1 = P_2 = 0, P_3 \neq 0$) with the polarization \mathbf{P} perpendicular to the interfaces, and the monoclinic r phase ($|P_1| = |P_2| \neq 0, P_3 \neq 0$) with \mathbf{P} inclined to them. The (u_m, ϕ_m) -diagram of BaTiO₃ involves additional monoclinic ac phase ($P_1 \neq 0, P_2 = 0, P_3 \neq 0$ or $P_1 = 0, P_2 \neq 0, P_3 \neq 0$). It should be emphasized that the a and ac phases were found to be unstable in the (001)-oriented PZT 50/50 and BaTiO₃ thin films and superlattices grown on thick substrates [188, 203, 204].

The inspection of Fig. 4.3 also shows that the phase diagrams are relatively weakly

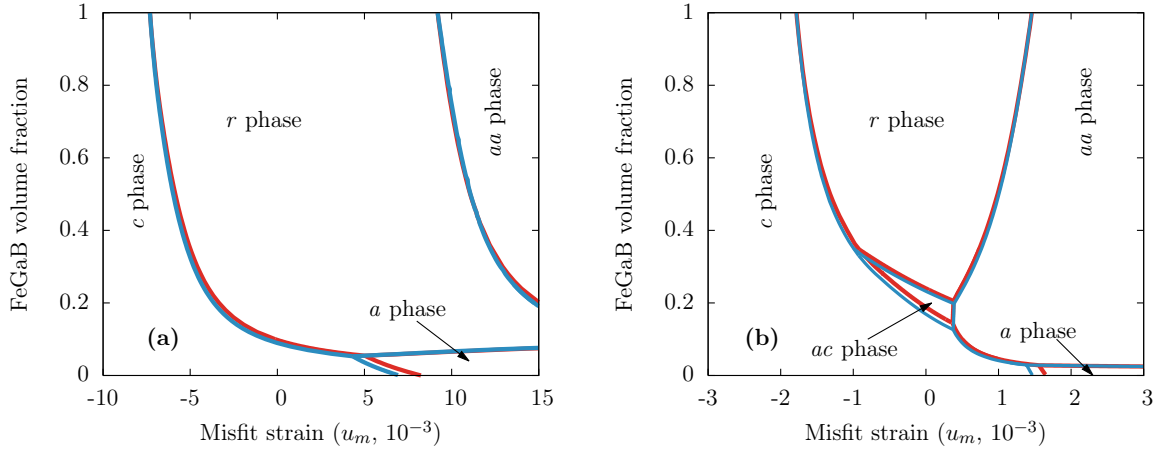


FIGURE 4.3: Phase diagrams of PZT 50/50 (a) and BaTiO₃ (b) nanolayers interleaved by FeGaB slabs. The prototypic cubic phase of these nanolayers has the (001) crystallographic direction orthogonal to their surfaces. Two variants of the stability ranges of various possible phases delimited by red and blue curves correspond to the multilayers comprising Fe_{85.38}Ga_{14.6}B_{0.02} and Fe_{81.72}Ga_{18.2}B_{0.08} slabs respectively. The temperature equals 25°C.

sensitive to the elastic properties of ferromagnetic slabs. Importantly, the considered variations of elastic constants do not alter the set of stable phases but only shift the boundaries of their stability ranges. These shifts are significant only at intermediate volume fractions $0 < \phi_m < 1$ of the ferromagnetic component. They become negligible at $\phi_m \rightarrow 1$ because thick ferromagnetic slabs with $t_m \gg t_f$ create almost rigid clamping of ferroelectric layers irrespective of their elastic stiffnesses. On the other hand, in the limit of $\phi_m \rightarrow 0$, the c and a phases become energetically equivalent so that they transform into the c and a domain variants of the same tetragonal phase. Therefore, the position of the c — a boundary actually loses significance near $\phi_m = 0$.

The developed phase diagrams of ferroelectric layers make it possible to determine the sensitivities $S_{i\alpha\beta} = \partial P_i / \partial u_{m\alpha\beta}$ of polarization components P_i to the misfit strains $u_{m\alpha\beta}$ and the electric permittivities ϵ_{ij} of these layers, which are necessary for the calculation of ME coefficients [181]. Since electrical responses of the multilayer to the applied magnetic field are detected via conductive ferromagnetic slabs employed as electrodes (see next sections), it is sufficient to evaluate the strain sensitivities $S_{3\alpha\beta}$ of the out-of-plane polarization component P_3 and the permittivity ϵ_{33} along the normal to the interfaces. From the general considerations it follows that $S_{3\alpha\beta}$ differ from zero in the c , r , and ac phases, where $S_{311} = S_{322}$ and $S_{311} \neq S_{322}$, respectively, while $S_{312} \neq 0$ in the r phase only.

Using eq. 4.3 and eq. 4.4 and performing numerical computations to find the

polarization changes δP_3 induced by small strain increments $\delta u_{m\alpha\beta}$ superimposed on the isotropic biaxial misfit strain u_m , we calculated the strain sensitivities $S_{3\alpha\beta}$ for PZT 50/50 and BaTiO₃ nanolayers as a function of the Fe_{85.38}Ga_{14.6}B_{0.02} volume fraction ϕ_m at various values of u_m . The results of calculations shown in Fig. 4.4 and Fig. 4.5 demonstrate that in the *c* phase the sensitivities $S_{311} = S_{322}$ increase monotonically with increasing FeGaB volume fraction ϕ_m and decreasing absolute value of the compressive misfit strain u_m . When ϕ_m reaches a critical value at which the *c* phase is replaced by the monoclinic *r* or *ac* phase in the diagram, the sensitivities display a step-like increase. Depending on the misfit strain, they may either decrease or increase within the stability range of the *r* phase.

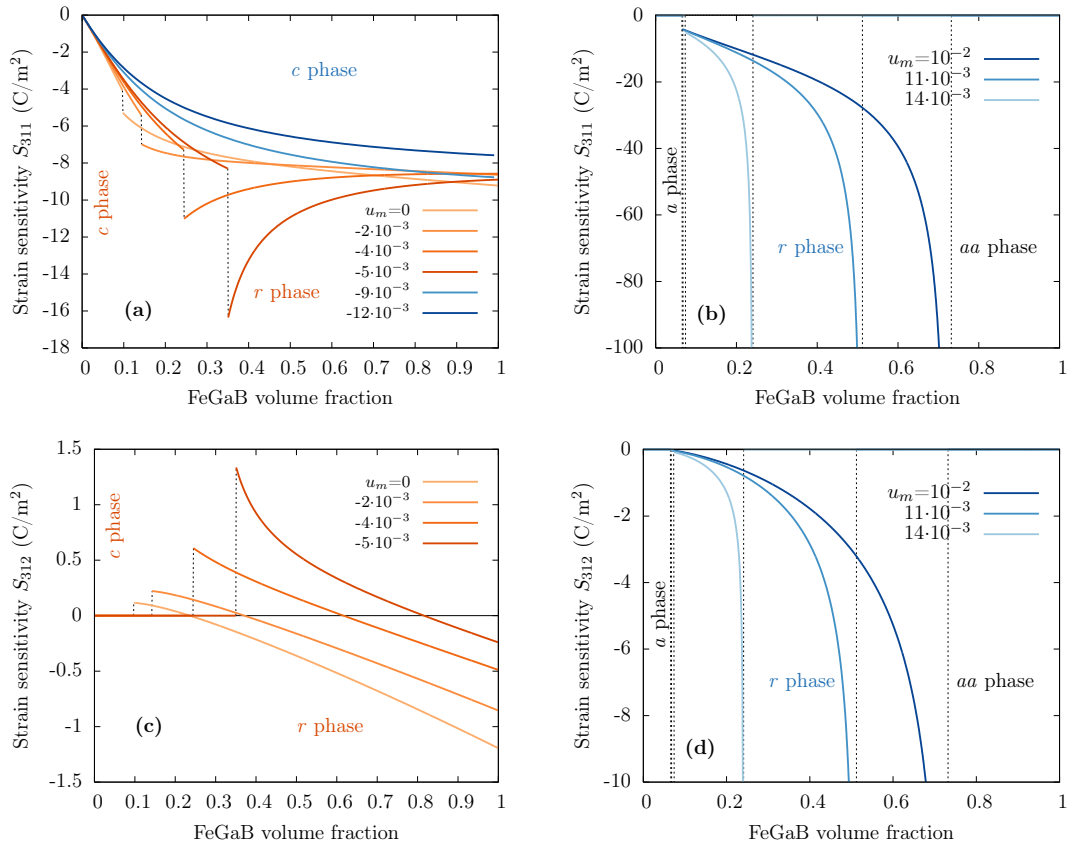


FIGURE 4.4: Sensitivities $S_{3\alpha\beta}$ of the out-of-plane polarization P_3 to the misfit strains $u_{m\alpha\beta}$ calculated for PZT 50/50 nanolayers interleaved by Fe_{85.38}Ga_{14.6}B_{0.02} slabs at different values of the biaxial misfit strain u_m indicated on the plots.

The relative out-of-plane permittivity ε_{33} of ferroelectric nanolayers was calculated numerically via the polarization change δP_3 induced by a weak applied electric field δE_3 . Figure 4.6 and Fig. 4.7 show ε_{33} of PZT 50/50 and BaTiO₃ layers calculated at various misfit strains u_m as a function of the FeGaB volume fraction ϕ_m . In the *c* phase, the permittivity is rather small (~ 200 - 300) and only weakly dependent

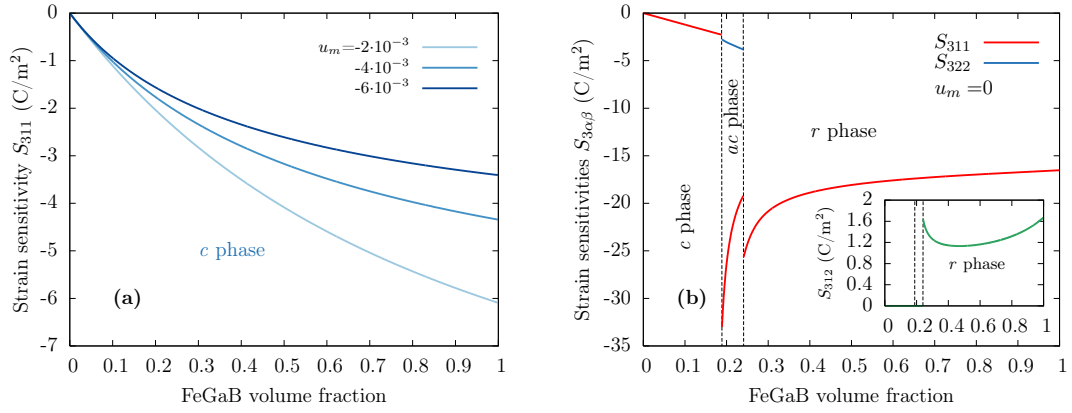


FIGURE 4.5: Sensitivities $S_{3\alpha\beta}$ of the out-of-plane polarization P_3 to the misfit strains $u_{m\alpha\beta}$ calculated for BaTiO₃ nanolayers interleaved by Fe_{85.38}Ga_{14.6}B_{0.02} slabs at different values of the biaxial misfit strain u_m indicated on the plots.

on ϕ_m . It increases in the r and ac phases but at zero misfit strain remains below 600 in PZT 50/50 nanolayers and below 800 in BaTiO₃ ones. The situation changes dramatically at positive misfit strains, where the out-of-plane permittivity becomes very high, especially near the critical FeGaB volume fraction separating stability ranges of the r and aa phases (see panel (c) in Fig. 4.6 and Fig. 4.7).

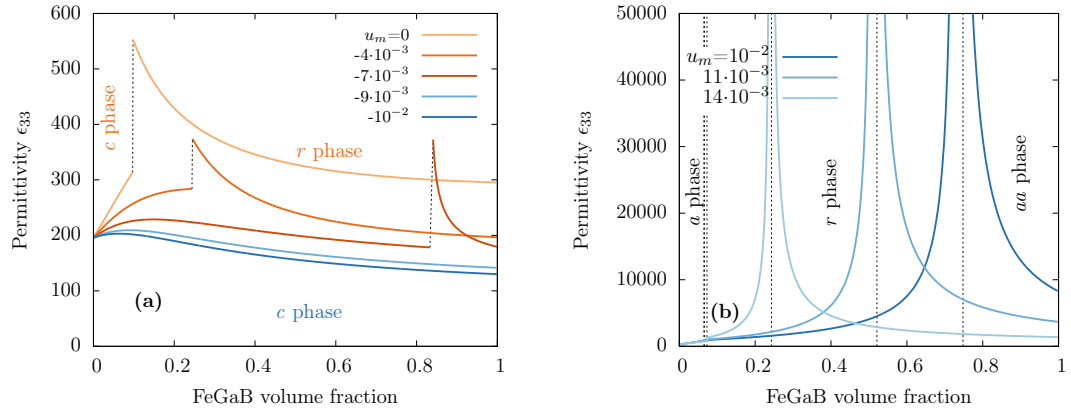


FIGURE 4.6: Out-of-plane permittivity ϵ_{33} of PZT 50/50 nanolayers interleaved by Fe_{85.38}Ga_{14.6}B_{0.02} slabs calculated at different values of the biaxial misfit strain u_m indicated on the plots.

4.4 Direct magnetoelectric effect displayed by ferroelectric-ferromagnetic multilayers

The set of fundamental characteristics of the direct ME effect involves the polarization coefficients $\alpha_{Pij} = \partial P_i / \partial H_j$ and the voltage coefficients $\alpha_{Eij} = \partial E_i / \partial H_j$, where \mathbf{P} and \mathbf{E} are the polarization and electric field in ferroelectric layers under

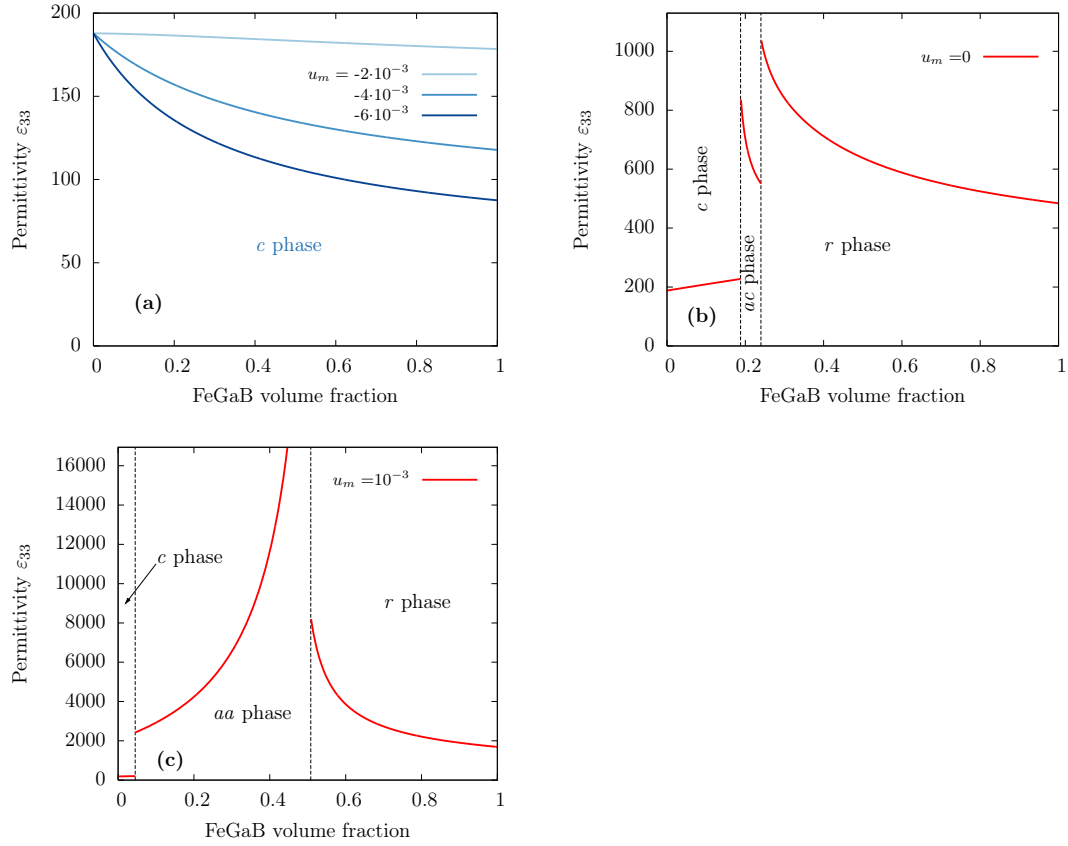


FIGURE 4.7: Out-of-plane permittivity ϵ_{33} of BaTiO_3 nanolayers interleaved by $\text{Fe}_{85.38}\text{Ga}_{14.6}\text{B}_{0.02}$ slabs calculated at different values of the biaxial misfit strain u_m indicated on the plots.

short-circuit and open-circuit conditions, respectively. For the strain-mediated ME effect displayed by ferroelectric-ferromagnetic multilayers, these coefficients can be calculated from the relations

$$\alpha_{Pij} = \frac{\partial P_i}{\partial u_{m11}} \frac{\partial u_{m11}}{\partial H_j} + \frac{\partial P_i}{\partial u_{m22}} \frac{\partial u_{m22}}{\partial H_j} + \frac{\partial P_i}{\partial u_{m12}} \frac{\partial u_{m12}}{\partial H_j} \quad (4.5)$$

and $\alpha_{Eij} = \chi_{i1}\alpha_{P1j} + \chi_{i2}\alpha_{P2j} + \chi_{i3}\alpha_{P3j}$ where $\chi_{ij} = \partial E_i / \partial P_j$ are the reciprocal susceptibilities of ferroelectric layers. Equation 4.5 shows that, in addition to the strain sensitivities $S_{i\alpha\beta} = \partial P_i / \partial u_{m\alpha\beta}$, we need to know the derivatives $\partial u_{m\alpha\beta} / \partial H_j$ in order to calculate ME coefficients. According to the definition given in section 4.2, the misfit strains $u_{m\alpha\beta}$ are the sum of strains $u_{m\alpha\beta}^0$ in the prototypic paraelectric-paramagnetic multilayer and the in-plane magnetostrictive deformations $\nu_{\alpha\beta}^{ms}$ of free-standing ferromagnetic slabs. Since $u_{m\alpha\beta}^0$ do not depend on the applied magnetic field, the sought derivatives may be set equal to the effective piezomagnetic coefficients $d_{j\alpha\beta}^m = \partial \nu_{\alpha\beta}^{ms} / \partial H_j$ of the ferromagnetic component.

To evaluate the piezomagnetic coefficients of FeGaB layers, we used the available experimental data [200] because the average magnetostrictive deformations of polydomain ferromagnetic crystals at intermediate values of the bias magnetic field \mathbf{H}_{dc} cannot be calculated with sufficient accuracy [181]. The linear fit of the measured longitudinal magnetostrictive deformation $\nu_{\parallel}^{ms}(H)$ curve [200] in the vicinity of the inflection point enabled us to estimate the maximum longitudinal piezomagnetic coefficient $d_{\parallel}^m = \partial\nu_{\parallel}^{ms}/\partial H$. The results obtained for crystalline $(\text{Fe}_{81}\text{Ga}_{19})_{1-x}\text{B}_x$ alloys with $x = 3\%$ and 6% are shown in Fig. 4.8. We find that the considered compositions have almost the same maximum piezomagnetic coefficient appearing at a moderate bias field of about 55 and 40 Oe, respectively. The value of $7 \times 10^{-6} \text{ Oe}^{-1}$ characteristic of the $(\text{Fe}_{81}\text{Ga}_{19})_{0.97}\text{B}_{0.03}$ alloy was taken for the coefficient d_{\parallel}^m in this work. Since we are not aware of experimental data on the magnetostrictive deformation ν_{\perp}^{ms} developing in FeGaB alloys in the direction orthogonal to the applied field \mathbf{H} , this deformation was estimated from the condition of volume conservation to be $\nu_{\perp}^{ms} = -\nu_{\parallel}^{ms}/2$. Accordingly, the piezomagnetic coefficient $d_{\perp}^m = \partial\nu_{\perp}^{ms}/\partial H$ was set equal to $-3.5 \times 10^{-6} \text{ Oe}^{-1}$.

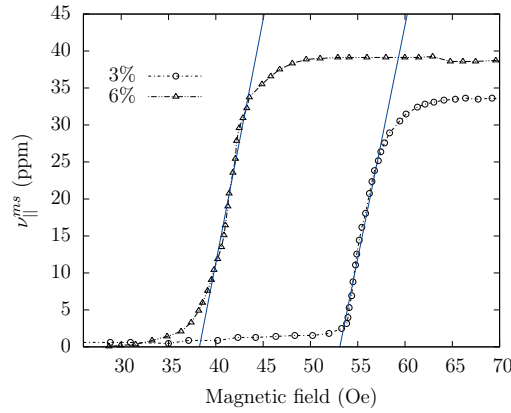


FIGURE 4.8: Longitudinal magnetostrictive deformation ν_{\parallel} of crystalline $(\text{Fe}_{81}\text{Ga}_{19})_{1-x}\text{B}_x$ alloys with $x = 3\%$ and 6% [200]. Linear fit in the vicinity of inflection point allows to estimate maximal piezomagnetic coefficient $d_{\parallel}^m = \partial\nu_{\parallel}^{ms}/\partial H$.

4.4.1 Magnetoelectric polarization coefficients and output charge signal

Using the strain sensitivities $S_{3\alpha\beta}$ of the out-of-polarization calculated in section 4.3 and the piezomagnetic coefficients d_{\parallel}^m and d_{\perp}^m given above, one can evaluate the ME polarization coefficients $\alpha_{P3\alpha}$ of PZT-FeGaB and BaTiO₃-FeGaB multilayers. The polarization response to the magnetic field orthogonal to the interfaces

($H_3 \neq 0$), however, should be relatively small because at this orientation the magnetic field inside ferromagnetic layers becomes much lower than the applied field owing to the presence of a strong demagnetizing field. Therefore, we restrict our consideration by the coefficients $\alpha_{P3\alpha}$ characterizing polarization changes induced by a magnetic field parallel to the interfaces.

In the *ac* phase, the strain sensitivities S_{311} and S_{322} differ from each other significantly (see Fig. 4.5(b)). For the ME coefficients of this phase, the calculation yields $\alpha_{P31} = S_{311}d_{\parallel}^m + S_{322}d_{\perp}^m \approx (S_{311} - S_{322}/2)d_{\parallel}^m$ and $\alpha_{P32} = S_{311}d_{\perp}^m + S_{322}d_{\parallel}^m \approx (S_{322} - S_{311}/2)d_{\parallel}^m$. These relations give $\alpha_{P31} \sim 10^{-6} \text{ s m}^{-1}$ and $\alpha_{P32} \sim -10^{-7} \text{ s m}^{-1}$ for the BaTiO₃-FeGaB multilayer with zero misfit strain. Hence the ME effect increases by an order of magnitude when the direction of applied magnetic field with respect to the in-plane polarization in the *ac* phase changes from perpendicular to parallel.

The revealed high ME coefficients of ferroelectric-ferromagnetic multilayers make them promising for the sensing of magnetic fields. The most important characteristic of such ME sensors is the output charge signal $Q(\mathbf{H})$ per unit volume of the multilayer. In order to maximize this signal, we propose to employ conductive ferromagnetic layers as interdigitated electrodes transferring the magnetically induced charge signal to the electrometer as shown in Fig. 4.9. This electrical configuration, which is similar to the one used previously to measure the ME voltage signal [206], renders possible to polarize neighboring ferroelectric layers in opposite directions during their preliminary poling. After switching off the applied electric field and short-circuiting two subsets of electrodes, a specific polarization distribution will be obtained in the set of ferroelectric nanolayers, where the out-of-plane polarization P_3 alternates in sign (see Fig. 4.9). The advantage of such distribution is that the magnetically induced polarization charges have the same sign on both sides of each ferromagnetic electrode. As a result, the sensitivity $\partial Q/\partial H_1$ of the output charge signal to the in-plane magnetic field increases up to $\partial Q/\partial H_1 = \alpha_{P31}(n+1)/(2t)$, where n is the total number of ferromagnetic and ferroelectric slabs in the multilayer.

To find the optimum multilayer geometry that maximizes $\partial Q/\partial H_1$, one has to take into account the dependence of α_{P31} on the ferromagnetic volume fraction ϕ_m . In the range of negative misfit strains where ferroelectric nanolayers stabilize in the *c* phase at any value of ϕ_m (see Fig. 4.3), the ME coefficient $\alpha_{P31} = S_{311}(d_{\parallel}^m + d_{\perp}^m)$ varies with ϕ_m monotonically. In accordance with Fig. 4.4(a) and Fig. 4.5(a) for the strain sensitivity S_{311} , we find that $\alpha_{P31}(\phi_m)$ can be approximated by the

inverse tangent function $\alpha_{P31} \approx \arctan(\phi_m/\phi_0)$, where ϕ_0 represents the fitting parameter taking different values depending on the misfit strain u_m . Hence at $n \gg 1$ we obtain $\partial Q/\partial H_1 \approx \arctan(t_m \phi_0^{-1}(t_m + t_f)^{-1})/(t_m + t_f)$, so that the magnetic-field sensitivity of charge signal maximizes at $t_m = t_f/k$ and $t_f \rightarrow 0$, where k varies from 1.35 at $u_m = -2 \times 10^{-3}$ to 1.77 $u_m = -6 \times 10^{-3}$ for PZT and $k \approx 2.3$ for BaTiO₃. However, the thickness of ferroelectric layers cannot be made smaller than the critical thickness $t_c(u_m) \approx 10$ nm, below which the single-domain polarization state becomes unstable [207]. The ferromagnetic layers also should be sufficiently thick ($t_m \geq t_{min}$) to exhibit high piezomagnetic coefficient $d_{||}^m$ since the magnetostrictive deformations of homogeneously magnetized films are usually small. All in all, the maximum sensitivity $\partial Q/\partial H_1$ is achieved when $t_f = t_c$ and $t_m = \max\{t_{min}, t_c/k\}$.

In the range of positive misfit strains where the r — aa phase-transition line appears on the (u_m, ϕ_m) -diagram (see Fig. 4.3), the ME coefficient $\alpha_{P31}(\phi_m)$ has a sharp peak in the r phase at the critical volume fraction $\phi_m^*(u_m)$ corresponding to this line. Therefore, the optimum FeGaB volume fraction equals $\phi_m^*(u_m)$ in the considered case. Since the sensitivity of charge signal may be written as $\partial Q/\partial H_1 \approx \alpha_{P31}(1 - \phi_m)/t_f$, we further find that the maximum sensitivity is achieved at $t_f = t_c$ if $\phi_m^*/(1 - \phi_m^*) \geq t_{min}/t_c$ and at $t_f = t_{min}(1 - \phi_m^*)/\phi_m^*$ when $\phi_m^*/(1 - \phi_m^*) < t_{min}/t_c$.

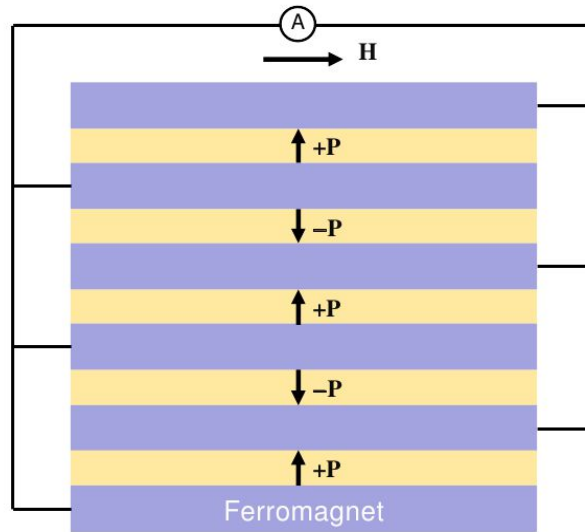


FIGURE 4.9: Electrical configuration maximizing the output charge signal of a ferroelectric-ferromagnetic multilayer.

4.4.2 Magnetolectric voltage coefficients and output voltage signal

Under open-circuit electrical conditions, the magnetically induced polarization charges create an internal electric field \mathbf{E} in ferroelectric layers. In the discussed multilayers with conductive ferromagnetic slabs, this field is orthogonal to the surfaces of ferroelectric layers ($E_3 \neq 0$), and the ME voltage coefficients $\alpha_{E3j} = \partial E_3 / \partial H_j$ can be found as $\alpha_{E3j} = -\alpha_{P3j} / (\varepsilon_0 \varepsilon_{33})$ [181]. These coefficients define the output voltage $V(\mathbf{H})$ which can be used for the sensing of magnetic fields with the aid of ferroelectric-ferromagnetic multilayers as well. However, the electrical scheme with interdigitated electrodes shown in Fig. 4.9 does not provide enhancement of the voltage signal. Therefore, the magnetically induced voltage should be measured using the conventional scheme, where only the top and bottom ferromagnetic slabs in the multilayer are connected to a voltmeter.

In this electrical configuration, the preliminary poling creates an out-of-plane polarization component P_3 of the same sign in all ferroelectric layers. Hence the output voltage signal per unit height of the multilayer is defined by the relation $V = E_3 t_f n_f / t$, where $n_f = (n - 1) / 2$ is the number of ferroelectric nanolayers. Accordingly, the sensitivity $\partial V / \partial H_j$ of the voltage signal to the magnetic field component H_j can be found as $\partial V / \partial H_j = \phi_f \alpha_{E3j} = -(1 - \phi_m) \alpha_{P3j} / (\varepsilon_0 \varepsilon_{33})$. Using this formula, we calculated the sensitivity $\partial V / \partial H_1$ of PZT50/50-FeGaB and BaTiO₃-FeGaB multilayers on the basis of the results obtained for their ME polarization coefficient $\alpha_{P31}(\phi_m)$ and the relative permittivity $\varepsilon_{33}(\phi_m)$ of ferroelectric nanolayers determined in section 4.3.

Figure 4.10 and Fig. 4.11 show the sensitivity $\partial V / \partial H_1$ plotted as a function of the FeGaB volume fraction ϕ_m for multilayers with different misfit strains u_m . It can be seen that this sensitivity always has a maximum at some optimum value of ϕ_m , which ranges from nearly 0.1 to about 0.5 at the considered strains. For the *c* phase, the maximum sensitivity is around $100 \text{ V cm}^{-1} \text{ Oe}^{-1}$ in the PZT50/50-FeGaB multilayers and about $50 \text{ V cm}^{-1} \text{ Oe}^{-1}$ in the BaTiO₃-FeGaB ones. Unlike the charge output signal, the sensitivity of the voltage signal does not increase strongly when ferroelectric nanolayers stabilize in the *r* phase. However, if the *ac* phase forms in BaTiO₃ layers, as it happens at zero misfit strain and $0.19 < \phi_m < 0.24$, the sensitivity $\partial V / \partial H_1$ rises markedly, reaching the value of about $250 \text{ V cm}^{-1} \text{ Oe}^{-1}$ at the optimum volume fraction $\phi_m \approx 0.19$. This value corresponds to the coefficient $\alpha_{E31} = \partial V / \partial H_1 / (1 - \phi_m) \approx 300 \text{ V cm}^{-1} \text{ Oe}^{-1}$ significantly exceeding ME voltage coefficients predicted by the thermodynamic theory for ferroelectric-ferromagnetic film-substrate hybrids [180, 181].

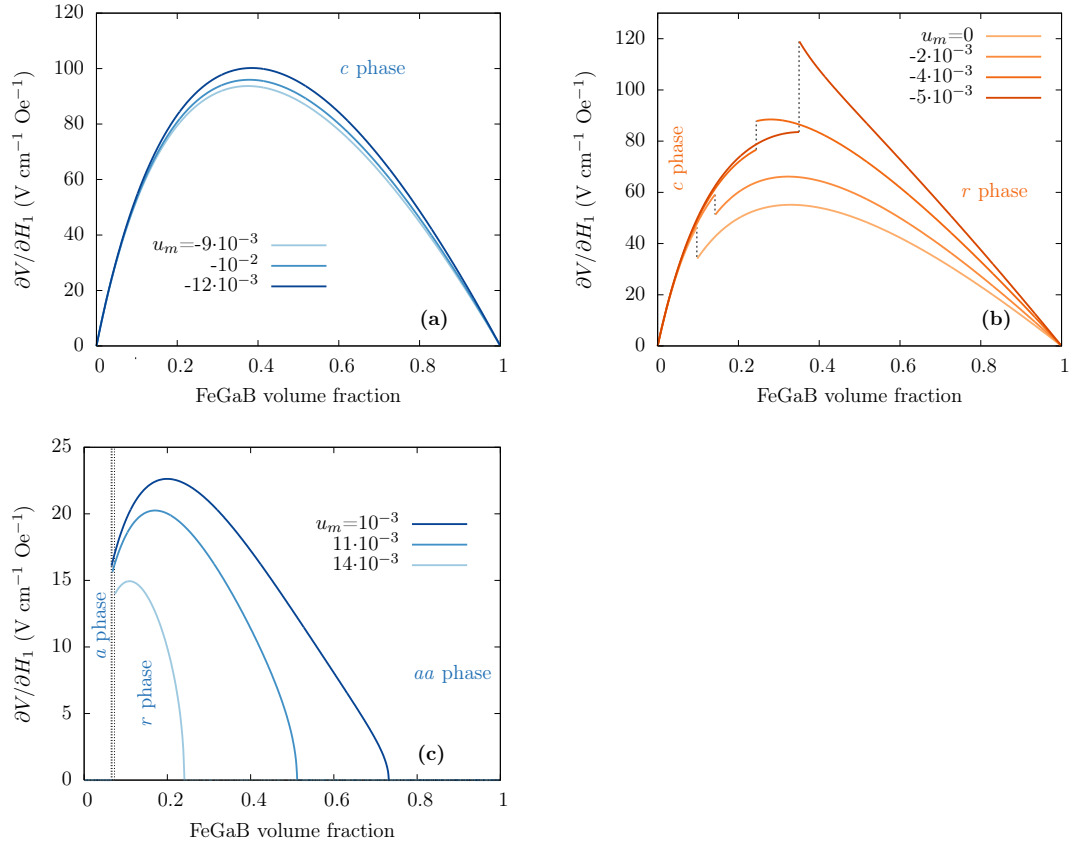


FIGURE 4.10: Magnetic field sensitivity $\partial V/\partial H_1$ of the output voltage signal generated by the multilayer comprising PZT 50/50 nanolayers interleaved by $\text{Fe}_{85.38}\text{Ga}_{14.6}\text{B}_{0.02}$ slabs calculated at different values of the biaxial misfit strain u_m indicated on the plots.

4.5 Conclusions

In conclusion, we presented a phenomenological model of biferroic multilayers comprising ferroelectric nanolayers interleaved by conducting ferromagnetic slabs. This nonlinear model renders possible to determine energetically favorable single-domain polarization states of ferroelectric layers with the account of their mechanical interaction with ferromagnetic ones in a free-standing multilayer and the misfit strains existing in the heterostructure. On this basis, the sensitivities of polarization to misfit strains and the permittivity of ferroelectric nanolayers can be calculated. Since these strains depend on the applied magnetic field via magnetostrictive deformations of ferromagnetic slabs, the strain-mediated direct ME effect exhibited by biferroic multilayers can be described quantitatively.

For the PZT50/50-FeGaB and BaTiO_3 -FeGaB multilayers considered as model biferroic systems, we performed numerical calculations of the room-temperature polarization states at different volume fractions ϕ_m of the ferromagnetic constituent

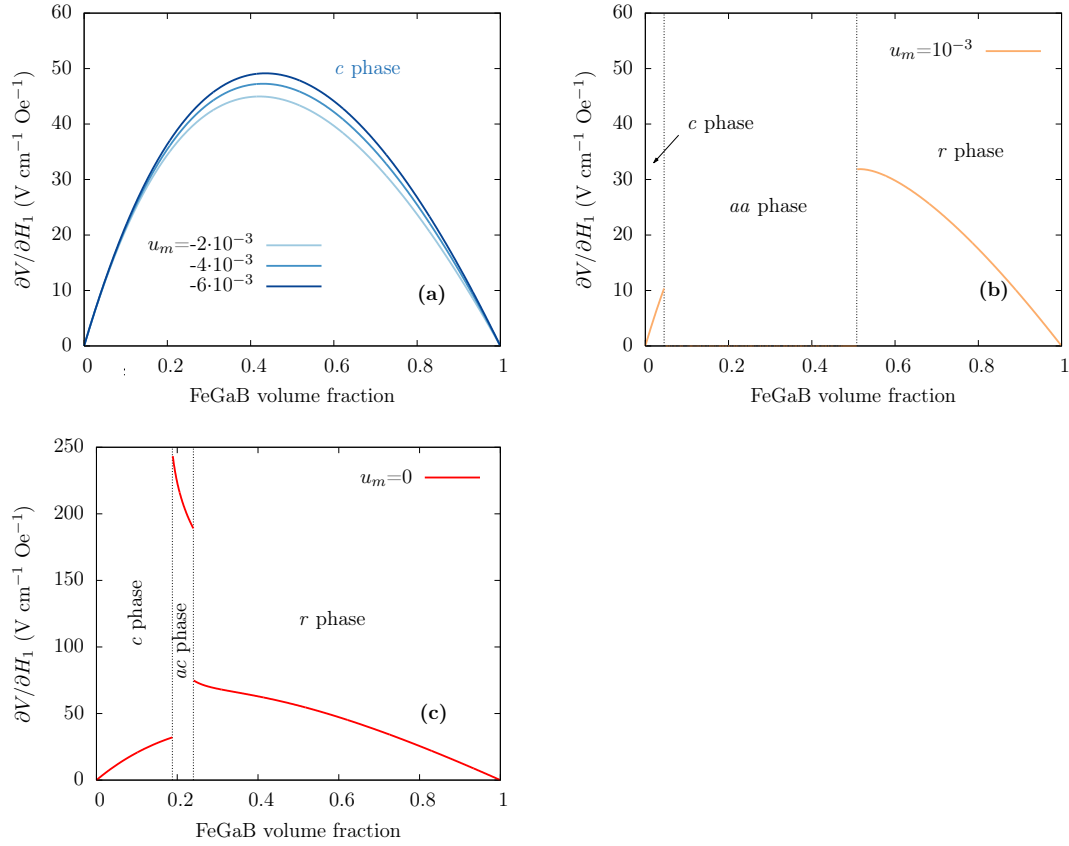


FIGURE 4.11: Magnetic field sensitivity $\partial V/\partial H_1$ of the output voltage signal generated by the multilayer comprising BaTiO_3 nanolayers interleaved by $\text{Fe}_{85.38}\text{Ga}_{14.6}\text{B}_{0.02}$ slabs calculated at different values of the biaxial misfit strain u_m indicated on the plots.

treated as a linear elastic medium. It is found that the set of possible single-domain states of PZT 50/50 and BaTiO_3 nanolayers involves the orthorhombic *a* phase not forming in epitaxial films subjected to isotropic biaxial misfit strains [188, 203, 204]. Furthermore, BaTiO_3 nanolayers may stabilize in the monoclinic *ac* phase, which disappears at large volume fractions ϕ_m owing to the increased elastic clamping.

In our theoretical description of the strain-mediated direct ME effect exhibited by PZT50/50-FeGaB and BaTiO_3 -FeGaB multilayers, we focused on electrical responses to a weak magnetic ac field \mathbf{H}_{ac} measured in the presence of a bias field \mathbf{H}_{dc} . It is shown that, for these typical ME measurements, the polarization coefficients α_{P3j} can be calculated by multiplying strain sensitivities of the out-of-plane polarization by appropriate effective piezomagnetic coefficients of FeGaB films. Remarkably, the theory predicts that the tuning of FeGaB volume fraction renders possible to increase α_{P31} above $2 \times 10^{-6} \text{ s m}^{-1}$, which strongly exceeds ME coefficients calculated for ferroelectric-ferromagnetic film-substrate hybrids [181]

and measured in PZT/Terfenol-D bulk laminate composites [205]. Moreover, we demonstrated that the output charge signal can be drastically enhanced additionally by using conductive ferromagnetic slabs as interdigitated electrodes. In this electrical scheme, the magnetically induced charge increases linearly with the number of ferroelectric layers, which opens the way for detection of ultralow magnetic fields.

Finally, we calculated the ME voltage coefficient α_{E31} and the sensitivity $\partial V/\partial H_1 = (1 - \phi_m)\alpha_{E31}$ of the output voltage signal per unit height of the multilayer to the in-plane magnetic field. It is found that $\partial V/\partial H_1$ always has a maximum at some optimum value of the FeGaB volume fraction in the multilayer. Unlike the output charge signal, the magnetically induced voltage should be measured in the conventional plate-capacitor setup and does not depend on the number of layers. For the PZT50/50-FeGaB multilayers, the maximum calculated sensitivity $\partial V/\partial H_1 \approx 100 \text{ V cm}^{-1} \text{ Oe}^{-1}$ is attained in the perpendicular-to-plane polarization state of PZT50/50 nanolayers (tetragonal c phase), which appears at compressive biaxial misfit strains and possesses considerable strain sensitivity of polarization combined with relatively low permittivity. In contrast, the BaTiO₃-FeGaB multilayers display the highest sensitivity $\partial V/\partial H_1 \approx 250 \text{ V cm}^{-1} \text{ Oe}^{-1}$ in the monoclinic ac phase, where the polarization is inclined to the surfaces of BaTiO₃ nanolayers. This sensitivity corresponds to the coefficient $\alpha_{E31} \approx 300 \text{ V cm}^{-1} \text{ Oe}^{-1}$ significantly exceeding the ME voltage coefficients predicted by the thermodynamic theory for ferroelectric-ferromagnetic film-substrate hybrids [180, 181].

Conclusion

The summary of the obtained results can be encompassed into the following. The first stage of the work is methodological and consists in several developments of the currently existing multiscale approaches with the aim of studying the properties of multiferroic compounds. Specifically,

- 1.) We have proposed an extension of the effective Hamiltonian, so as to predict finite-temperature properties of multiferroic nanostructures and solid solutions. Our scheme represents an alternative to methods relying on the VCA approximation and is shown to be more suitable for describing nanocomposite systems comprising chemically distinct constituents.

The first step of the envisioned methodological scheme lies in the construction of effective Hamiltonian models describing the properties of each of the constituent materials. In order to build the model for composite structures, it is then necessary to obtain correction terms which will account for the modification of the effective potential at the interface between different phases. However, although the analytical form of such correction terms can be easily evaluated using symmetry considerations, the numerical evaluation of the large number of the expansion coefficients is practically impossible. For the sake of reducing this computational complexity, we have thus proposed a phenomenological approximation for the interface correction terms. We have confronted our method with first-principles calculations performed for the case of $(\text{BiFeO}_3)(\text{BaTiO}_3)$ superlattices so as to test the validity of the proposed model.

- 2.) The second methodological development consists in the construction of the Ginzburg-Landau phenomenological model describing ferroelectric properties of the piezoelectric/piezomagnetic freestanding epitaxial multilayers. Particularly, we have derived the renormalized free energy expansion coefficients for

such structures, assuming the perfect strain transmission at the epitaxial interface. In contrast to similar phenomenological models reported previously, our model can address any arbitrary symmetry of the misfit strain tensor. Moreover, the assumed absence of the substrate allows to reveal the dependence of the expansion coefficients on the volume fractions of constituent phases.

In a second stage, the aforementioned constructed models were applied to studying the properties of different multiferroic compounds:

- 1.) In order to validate the constructed effective Hamiltonian model, we have conducted the study of $(\text{BiFeO}_3)_x(\text{BaTiO}_3)_{1-x}$ solid solutions. Being a specific limiting case of the composite geometry, such statistically homogeneous disordered structures have been chosen as the most challenging case for the proposed methodological scheme. The obtained results allowed to theoretically support the previously reported conjecture pertaining to the relevance of the local fields in the formation of the pseudocubic phase, which is experimentally observed in the intermediate concentration range $x'_c < x < x''_c$. The predicted critical concentrations x'_c and x''_c were found to fall within the range of the experimentally obtained values. Furthermore, we have carried out a numerical study for investigating the formation of locally ordered ferroelectric regions for compositions located in the vicinity of the critical concentrations.
- 2.) After having studied the properties of disordered compounds, we have probed the finite-temperature properties of $(\text{BiFeO}_3)(\text{BaTiO}_3)$ bicrystals with different lattice geometries. In order to eliminate the effect of local fields hindering ferroelectric behaviour, we have chosen to consider only structures for which each local modes lattice site is associated with an inversion symmetry center. The results of the performed Monte Carlo simulations show that the multiferroic properties of $(\text{BiFeO}_3)(\text{BaTiO}_3)$ compounds strongly depend on the geometry of the lattice. Specifically, we show that increasing the connectivity of bismuth ferrite and its concentration leads to the enhancement of the AFD transition temperature. In contrast, the behaviour of the Curie and Neel temperatures do not follow this trend. For structures with equal volume fractions of constituent materials, the magnetic transition temperature reaches its maximum for (3,3) connectivity, while the ferroelectric transition

temperature is maximized for (0,0) three-dimensional checkerboard geometry. Moreover, our results suggest that composite $(\text{BiFeO}_3)(\text{BaTiO}_3)$ structures can exhibit a magnetoelectric response exceeding that of BiFeO_3 single crystals.

- 3.) Based on the presented Ginzburg-Landau phenomenological model, we have performed numerical calculations of the room-temperature polarization states and linear magnetoelectric coefficients of $(\text{Pb}(\text{Zr}_{0.5},\text{Ti}_{0.5})\text{O}_3)(\text{FeGaB})$ and $(\text{BaTiO}_3)(\text{FeGaB})$ freestanding (2,2) multilayers at different volume fractions of the ferromagnetic constituent. It was found that the set of possible single-domain states of $\text{Pb}(\text{Zr}_{0.5},\text{Ti}_{0.5})\text{O}_3$ and BaTiO_3 nanolayers involves the orthorhombic a phase which does not form in epitaxial films subjected to isotropic biaxial misfit strains. Furthermore, we found that BaTiO_3 nanolayers may stabilize in the monoclinic ac phase, which disappears at large volume fractions ϕ_m owing to the increased elastic clamping. Within this study, we have also calculated the ME voltage coefficient and the sensitivity of the output voltage signal V per unit height of the multilayer to the in-plane magnetic field H_1 .

For the $(\text{Pb}(\text{Zr}_{0.5},\text{Ti}_{0.5})\text{O}_3)(\text{FeGaB})$ multilayers, the maximum calculated sensitivity $\partial V/\partial H_1 \approx 100 \text{ V cm}^{-1} \text{ Oe}^{-1}$ is attained in the perpendicular-to-plane polarization state of $\text{Pb}(\text{Zr}_{0.5},\text{Ti}_{0.5})\text{O}_3$ nanolayers (tetragonal c phase), which appears at compressive biaxial misfit strains and possesses considerable strain sensitivity of polarization combined with relatively low permittivity. In contrast, the $(\text{BaTiO}_3)\text{FeGaB}$ multilayers display the highest sensitivity $\partial V/\partial H_1 \approx 250 \text{ V cm}^{-1} \text{ Oe}^{-1}$ in the monoclinic ac phase, where the polarization is inclined to the surfaces of BaTiO_3 nanolayers. This sensitivity corresponds to the coefficient $\alpha_{E31} \approx 300 \text{ V cm}^{-1} \text{ Oe}^{-1}$ significantly exceeding the ME voltage coefficients predicted previously by the thermodynamic theory for ferroelectric-ferromagnetic film-substrate hybrids.

Finally, we demonstrated that the output charge signal can be drastically enhanced by using conductive ferromagnetic slabs as interdigitated electrodes. In this electrical scheme, the magnetically induced charge increases linearly with the number of ferroelectric layers, which opens the way for detection of ultralow magnetic fields.

The conducted study and the obtained results show that multiferroic nanocomposite materials represent exceptional systems exhibiting rich physics and properties

which can be advantageous for practical applications. However, the methods developed within the course of the thesis need to be refined in order to allow for more reliable predictions of various finite-temperature properties of these complex compounds. For instance, it is essential to ameliorate the treatment of the magnetic and AFD degrees of freedom within the developed effective Hamiltonian model in order to account for the magnetic anisotropy at the interface. Further improvements would concern possible modifications of the antisymmetric exchange interaction, the propagation of the oxygen octahedra rotations across the interface, etc. Moreover, the investigation of the properties of the ferroelectric (Ba,Sr)TiO₃ fractal nanostructures indicates that in order to use the full potential of nanocomposite materials, a more thorough study of the effect of geometry on the properties of the system is needed.

Bibliography

- [1] L. D. Landau, E. M. Lifshitz, *Electrodynamics of Continuous Media*, Course of Theoretical Physics, 2nd edn., transl. from the Russian (Pergamon, Oxford, 1984), Vol. 8
- [2] D. N. Astrov, *Zh. Exp. Teor. Fiz.*, 38, 984 (1960) [*Soviet Phys. JETP* 11, 708 (1960)]
- [3] D. N. Astrov, *Zh. Exp. Teor. Fiz.*, 40, 1035 (1961) [*Soviet Phys. JETP* 13, 729 (1961)]
- [4] W. F. Brown Jr., R. M. Hornreich, and S. Shtrikman, *Phys. Rev.*, 168, 574–577 (1968)
- [5] E. A. Turov, *Physics–Uspekhi*, 37, 303–310 (1994)
- [6] W. Eerenstein, N. D. Mathur and J. F. Scott, *Nature*, 442, 759–765 (2006)
- [7] J. Shieh, J. H. Yeh, Y. C. Shu, and J. H. Yen, *Mat. Sc. Engineer. B*, 161, 50 (2009)
- [8] N. A. Hill, *J. Phys. Chem. B*, 104, 6694 (2000)
- [9] D. I. Khomskii, *Bull. Am. Phys. Soc. C*, 21.002 (2001)
- [10] D. I. Khomskii, *Physics*, 2, 20 (2009)
- [11] B. K. Ponomarev et al., *Ferroelectrics*, 161, 43 (1994)
- [12] T. Kimura, T. Goto, H. Shintani, K. Ishizaka, T. Arima, and Y. Tokura, *Nature*, 426, 55 (2003)
- [13] L. Wang, D. Wang, Q. Cao, Y. Zheng, H. Xuan, J. Gao, and Y. Du, *Nature*, 429, 392 (2004)
- [14] W. F. Brown Jr., R. M. Hornreich, and S. Shtrikman, *Phys. Rev.*, 168, 574 (1968)

-
- [15] G. T. Rado, Magnetoelectric interaction phenomena in crystals, p.3, ed. by A. J. Freeman, H. Schmidt, (Gordon and Breach science publishers, 1975)
- [16] H. Yatom, *Solid State Commun.*, 12, 1117 (1973.)
- [17] L. D. Landau, E. M. Lifshitz, Statistical Physics, Course of Theoretical Physics, 2nd edn., transl. from the Russian (Pergamon, Oxford,1969), Vol. 5
- [18] G. T. Rado, *Phys. Rev. Lett.*, 6, 609 (1961)
- [19] G. T. Rado, *Phys. Rev.*, 128, 2546 (1962)
- [20] R. Hornreich, and S. Shtrikman, *Phys. Rev.*, 161, 506 (1967)
- [21] M. Date, J. Kanamori, and M. Tachini, *J. Phys. Soc. Japan*, 16, 2589 (1961)
- [22] S. Alexander, and S. Shtrikman, *Solid State Commun.*, 4, 115 (1966)
- [23] E. F. Bertaut, *J. Phys. Radium*, 23, 460 (1962)
- [24] G. T. Rado, *Phys. Rev. Lett.*, 13, 335 (1964)
- [25] G. T. Rado, *J. Appl. Phys.*, 37, 1403 (1966)
- [26] J. van Suchtelen, *Philips Res. Rep.*, 27, 28 (1972)
- [27] C.-W. Nan, *Prog. Mater. Sci.*, 37, 1 (1993)
- [28] C.-W. Nan, *Phys. Rev. B*, 50, 6082 (1994)
- [29] R. E. Newnham, D. P. Skinner, L. E. Cross, *Vater. Res. Bull.*, 13, 525–536 (1978)
- [30] L. E. Cross, and R. F. Newnham, *Mater. Res. Bull.*, 1, 599 (1975)
- [31] J. F. Nye, Physical Properties of Crystals: Their Representation by Tensors and Matrices, Oxford University Press (1985)
- [32] C.-W. Nan, M. I. Bichurin, S. Dong, D. Viehland and G. Srinivasan, *J. Appl. Phys.*, 103, 031101 (2008)
- [33] M. Bichurin, D. Viehland, Magnetoelectricity in Composites, Pan Stanford Publishing (2011)
- [34] M. N. Barber, Phase Transitions and Critical Phenomena, edited by C. Domb and J.L. Lebowitz (Academic, New York, 1983), Vol. 8
- [35] S. Singh, R. K. Pathria, *Phys. Rev. Lett.*, 55, 347 (1985)

- [36] R. Diestel, Graph Theory, Electronic Edition, 2005 (<http://diestel-graph-theory.com>)
- [37] O. Riordan, Percolation, Cambridge University Press (2006)
- [38] S. P. Novikov, I. A. Taimanov, Modern Geometric Structures And Fields (Graduate Studies in Mathematics), American Mathematical Society (2006)
- [39] P. Ponte Castaneda, J. J. Telega, and B. Gambin, Nonlinear Homogenization and its Applications to Composites, Polycrystals and Smart Materials, Kluwer Academic Publishers, Springer (2004)
- [40] T. A. Witten Jr., L. M. Sander, *Phys. Rev. Lett.*, 47, 1400 (1981)
- [41] R. A. Neher, K. Mecke, H. Wagner, *J. Stat. Mech.*, 1, 01011 (2008)
- [42] M. F. Sykes, J. W. Essam, *J. Math. Phys.*, 5:1117 (1964)
- [43] O. D. Lavrentovich, *Liquid Cryst.*, 24, 117 (1998)
- [44] W. Zhong, D. Vanderbilt, and K. M. Rabe, *Phys. Rev. Lett.*, 73, 1861 (1994)
- [45] M. E. Lines, A. M. Glass, Principles and Applications of Ferroelectrics and Related Materials (Clarendon Press, Oxford, 1977)
- [46] T. Mitsui *et. al.*, Landolt-Bornstein Numerical Data and Functional Relationships in Science and Technology (Springer-Verlag, 1981), NS, III/16
- [47] T. Nishimatsu, U. V. Waghmare, Y. Kawazoe, and D. Vanderbilt, *Phys. Rev. B*, 78, 104104 (2008)
- [48] M. G. Harwood, P. Popper, D. F. Rushman, *Nature*, 160, 58 (1947)
- [49] B. A. Strukov, A. P. Levanyuk, Ferroelectric Phenomena in Crystals: Physical Foundations (Springer London, Limited edition, 2011)
- [50] A. Garcia, and D. Vanderbilt, *Appl. Phys. Lett.*, 72, 2981 (1998)
- [51] D. Berlincourt, and H. Jaffe, *Phys. Rev.*, 111, 143 (1958)
- [52] Z. Li, S.-K. Chan, M. H. Grimsditch, and E. S. Zouboulis, *J. Appl. Phys.*, 70, 7329, (1991)
- [53] T. Yamada, *J. Appl. Phys.*, 43, 328 (1972)
- [54] A. Schaefer, H. Schmitt, and A. Dor, *Ferroelectrics*, 69, 253 (1986)

- [55] C. A. Randall, R. E. Newnham, and L. E. Cross, *History of the First Ferroelectric Oxide, BaTiO₃*, The Electronics Division, <http://209.115.31.62/electronicdivision> (26 Spet. 2004)
- [56] S. V. Grabovsky, I. V. Shnidshtein, M. Takesada, A. Onodera, B. A. Strukov, *Journal of Advanced Dielectrics*, 3, 1350032 (2013)
- [57] X. Lu, H. Li, and W. Cao, *J. Appl. Phys.*, 114, 224106 (2013)
- [58] J. J. Wang, F. Y. Meng, X. Q. Ma, M. X. Xu, and L. Q. Chen, *J. Appl. Phys.*, 108, 0344107 (2010)
- [59] H. H. Wieder, *Phys. Rev.*, 99, 1161 (1955)
- [60] G. Catalan, J. F. Scott, *Adv. Matter.*, 21, 2463 (2009)
- [61] S. L. Shang, G. Sheng, Y. Wang, L. Q. Chen, and Z. K. Lui, *Phys. Rev. B*, 80, 05102 (2009)
- [62] C. Ederer, and N. A. Spaldin, *Phys. Rev. B*, 71, 060401(R) (2005)
- [63] C. Michel, J.-M. Moreau, G. D. Achenbach, R. Gerson, and W. J. James, *Solid State Commun.*, 7, 701 (1969)
- [64] F. Kubel, and H. Schmid, *Acta Crystallogr. B*, 46, 698 (1990)
- [65] J. R. Teague, R. Gerson, and W. J. James, *Solid State Commun.*, 8, 1073 (1970)
- [66] S. V. Kiselev, R. P. Ozerov, and G. S. Zhdanov, *Sov. Phys. Dokl.*, 7, 742 (1963)
- [67] I. Sosnowska, T. Peterlin-Neumaier, and E. Streichele, *J. Phys. C*, 15, 4835 (1982)
- [68] I. E. Dzyaloshinskii, *Sov. Phys. JETP*, 5, 1259 (1957)
- [69] T. Moriya, *Phys. Rev.*, 120, 91 (1960)
- [70] Y. F. Popov, A. K. Zvezdin, G. P. Vorob'ev, A. M. Kadomtseva, V. A. Murashev, and D. N. Rakov, *JETP Lett.*, 57, 69 (1993)
- [71] C. Tabarez-Munoz, J.-P. Rivera, A. Bezinges, A. Monnier, and H. Schmid, *Jap. J. Appl. Phys.*, 24, 1051 (1985)
- [72] I. A. Kornev, L. Bellaiche, *Phys. Rev. B*, 79, 100105(R) (2009)

- [73] D. Rahmedov, D. Wang, J. Íñiguez, and L. Bellaiche, *Phys. Rev. Lett.*, 109, 037207 (2012)
- [74] S. Prosandeev, D. Wang, W. Ren, J. Íñiguez, and L. Bellaiche, *Adv. Funct. Mater.*, 23, 234 (2012)
- [75] J. C. Wojdel, J. Íñiguez, *Phys. Rev. Lett.*, 103, 267205 (2009)
- [76] S. Lisenkov, I. A. Kornev, and L. Bellaiche, *Phys. Rev. B*, 79, 012101 (2009)
- [77] I. A. Kornev, S. Lisenkov, R. Haumont, B. Dkhil, and L. Bellaiche, *Phys. Rev. Lett.*, 99, 227602 (2007)
- [78] S. Lee, M. T. Fernandez-Diaz, H. Kimura, Y. Noda, D. T. Adroja, S. Lee, J. Park, V. Kiryukhin, S.-W. Cheong, M. Mostovoy, and J.-G. Park, *Phys. Rev. B*, 88, 060103(R)
- [79] J. X. Zhang, Y. L. Li, Y. Wang, Z. K. Liu, L. Q. Chen, Y. H. Chu, F. Zavaliche, and R. Ramesh, *J. Appl. Phys.*, 101, 114105 (2007)
- [80] A. Kumar, J. F. Scott, R. Martinez, G. Srinivasan, and R. S. Katiyar, *Phys. Status Solidi A*, 209, 1, (2012)
- [81] H. Toupet, V. V. Shvartzman, F. Lemerrec, P. Borisov, W. Kleeman, and M. Karkut, *Integr. Ferroelectr.*, 100, 165 (2008)
- [82] P. Yang, K. M. Kim, Y.-G. Joh, D. H. Kim, J.-Y. Lee, J. Zhu, and H. Y. Lee, *J. Appl. Phys.*, 105, 061618 (2009)
- [83] R. Ranjith, U. Luders, W. Prellier, *J. Phys. Chem. Sol.*, 71, 1140 (2010)
- [84] M. Lorenz, V. Lazenka, P. Schwinkendorf, F. Bern, M. Ziese, H. Modarresi, A. Volodin, M. J V. Bael, K. Temst, A. Vantomme, and M. Grundmann, *J. Phys. D: Appl. Phys.*, 47 135303 (2014)
- [85] Yu. N. Venevtsev, G. S. Zhdanov, Yu. E. Roginskaya, S. A. Fedulov, V. V. Ivanov, V. V. Chkalova, A. S. Viskov, A. G. Kapyshev, V. S. Kondratenko, and I. B. Ladyzhinskii, *Izv. Akad. Nauk SSSR Ser. fiz.*, 28, 683 (1964)
- [86] I. H. Ismailidze, R. M. Ismailov, A. I. Alekberov, and F. M. Salaev, *Phys. Stat. Sol.*, 68, K81 (1981)
- [87] M. Mahesh Kumar, A. Srinivas, G. S. Kumar, and S. V. Suryanarayana, *J. Phys.: Condens. Matter*, 11, 8131 (1999)

-
- [88] A. Singh, V. Pandey, R. K. Kotnala, and D. Pandey, *Phys. Rev. Lett.*, 101, 247602 (2008)
- [89] P. Hohenberg, W. Kohn, *Phys. Rev.*, 136 (1964) B864
- [90] W. Kohn and L. J. Sham, *Phys. Rev.*, 140 (1965) A1133
- [91] E. H. Lieb, *Int. J. Quantum Chem.*, 24 (1983) 243
- [92] D. M. Ceperley, B. J. Alder, *Phys. Rev. Lett.*, 45 (1980) 566
- [93] W. Zhong, D. Vanderbilt, K. M. Rabe, *Phys. Rev. B*, 52 (1995) 6301
- [94] P. Lacour-Gayet, and G. Toulouse, *J. Phys. (Paris)*, 35, 425 (1974)
- [95] Y. Imry, and S.-K. Ma, *Phys. Rev. Lett.*, 35, 1399 (1975)
- [96] D. Nicolaides, and A. A. Lisiansky, *J. Appl. Phys.*, 85, 6067 (1999)
- [97] K. Binder and A. P. Young, *Rev. Mod. Phys.*, 58, 801 (1986)
- [98] D. P. Belanger and A. P. Young, *J. Magn. Mater.*, 100, 272 (1991)
- [99] K. H. Fischer, J. A. Hertz, *Spin Glasses* (Cambridge University Press, 1993)
- [100] G. Parisi, N. Sourlas, *Phys. Rev. Lett.*, 43, 744 (1979)
- [101] L. F. Pontin, J. A. Baeta Segundo, J. Fernando Perez, *J. Stat. Phys.*, 75, 51 (1994)
- [102] J. Z. Imbrie, *Phys. Rev. Lett.*, 53, 1747 (1984)
- [103] J. Bircmont, and A. Kupiainen, *Comm. Math. Phys.*, 116, 539 (1988)
- [104] A. Aizenman, and J. Wehr, *Comm. Math. Phys.*, 130, 489 (1990)
- [105] T. C. Proctor, D. A. Garanin, and E. M. Chudnovsky, *Phys. Rev. Lett.*, 112, 097201 (2014)
- [106] Z.-G. Ye, A. A. Bokov, Y. Kim, Y. Xie, X. Long, S. Jesse, and S. V. Kalinin, Proceedings of the “Fundamental Physics of Ferroelectrics and Related Materials 2014” workshop, p.84 (2014)
- [107] D. S. Fisher, G. M. Grinsrein, and A. Khurana, *Physics Today*, 56 (1988)
- [108] R. Pirc, R. Blinc, *Phys. Rev. B*, 60, 13470 (1999)
- [109] J. C. Wojdel, P. Hermet, M. P. Ljungberg, P. Ghosez and J. Íñiguez, *J. Phys.: Condens. Matter*, 25, 305401 (2013)

- [110] I. A. Kornev, L. Bellaiche, P.-E. Janolin, B. Dkhil, and E. Suard, *Phys. Rev. Lett.*, **97**, 157601 (2006)
- [111] D. Albrecht, S. Lisenkov, W. Ren, D. Rahmediv, I. A. Kornev, and L. Bellaiche, *Phys. Rev. B*, **81**, 140401(R) (2010)
- [112] N. Metropolis, A. W. Rosenbluth, M. N. Rosenbluth, A. H. Teller, E. Teller, *Journal of Chemical Physics*, **21** (6): 1087–1092 (1953)
- [113] W. K. Hastings, *Biometrika*, **57** (1): 97–109 (1970)
- [114] D. P. Landau and K. Binder, *A guide to Monte Carlo Simulations in Statistical Physics*, Cambridge University Press (2000)
- [115] W. Krauth, *Statistical Mechanics: Algorithms and Computations*, Oxford University Press, Sep 14 (2006)
- [116] M. Mostovoy, A. Scaramucci, N. A. Spaldin, and K. T. Delaney, *Phys. Rev. Lett.*, **105**, 087202 (2010)
- [117] J.-M. Liu, Q. C. Li, X. S. Gao, Y. Yang, X. H. Zhou, X. Y. Chen, and Z. G. Liu, *Phys. Rev. B*, **66**, 054416 (2002)
- [118] C. J. C. Filho, and G. E. Barberis, *J. Phys.: Conf. Ser.*, **273**, 01213 (2011)
- [119] S.-W. Cheong, M. Mostovoy, *Nature Materials*, **6**, 13 (2007)
- [120] W. Eerenstein, N. D. Mathur and J. F. Scott, *Nature*, **442**, 759 (2006)
- [121] J. F. Scott, *NPG Asia Materials*, **5**, e72(2013)
- [122] A. Roy, R. Gupta, and A. Garg, *Adv. Cond. Mat. Phys.*, **2012**, 926290 (2012)
- [123] A. S. Tatarenko, M. I. Bichurin, *Adv. Cond. Mat. Phys.*, **2012**, 286562 (2012)
- [124] S. P. Crane, C. Bihler, M. S. Brandt, S. T. B. Goennenwein, M. Gajek, R. Ramesh, *Journal of Magnetism and Magnetic Materials*, **321**, 5, (2009)
- [125] L. Yan, Z. Wang, Z. Xing, J. Li and D. Viehland, *J. Appl. Phys.*, **107**, 064106 (2010)
- [126] Y. S. Oh, S. Crane, H. Zheng, Y. H. Chu, R. Ramesh and K. H. Kim, *Appl. Phys. Lett.*, **97**, 052902 (2010)
- [127] T.-J. Park, G. C. Papaefthymiou, A. J. Viescas, Y. Lee, H. Zhou, and S. S. Wong, *Phys. Rev. B*, **82**, 024431 (2010)

- [128] A. Singh, V. Pandey, R. K. Kotnala, and D. Pandey, *Phys. Rev. Lett.*, 101, 247602 (2008)
- [129] V. F. Freitas, G. S. Dias, O. A. Protzek, D. Z. Montanher, I. B. Catellani, D. M. Silva, L. F. Cotica, *Jour. Adv. Ceram.*, 2, 103, (2013)
- [130] A. M. Kadomtseva *et. al.*, *Phase Trans.*, 79, 11019 (2006)
- [131] D. Lebeugle *et. al.*, *Phys. Rev. B*, 76, 024116 (2007)
- [132] A. R. Makhdoom, M. J. Akhtar, M. A. Rafiq, M .M. Hassan, *Ceram. Int.*, 38, 3829 (2012)
- [133] X. Qi, J. Dho, R. Tomov, M. G. Blamire, and J. L. MacManus-Driscoll, *Appl. Phys. Lett.*, 86, 062903 (2005)
- [134] L. Luo, W. Luo, G. Yuan, W. Wei, X. Yuan, H. Zhang, K. Shen, M. Xu, Q. Xu, *J. Supercond. Nov. Magn.*, 26, 3309 (2013)
- [135] R. Das, K. Mandal, *J. Mag. Mag. Mat.*, 324,1913 (2012)
- [136] Y. Wang, C.-W. Nan, *Appl. Phys. Lett.*, 89, 052903 (2006)
- [137] L. Hongri, S. Yuxia, *J. Phys. D: Appl. Phys.*, 40, 7530 (2007)
- [138] M. M. Kumar, A. Srinivas and S. V. Suryanarayana, *J. Appl. Phys.*, 87, 855 (2000)
- [139] A. Singh, Ch. Moriyoshi, Y. Kuroiwa, and Dh. Pandey, *Phys. Rev. B*, 85, 064116 (2012)
- [140] A. Singh, Ch. Moriyoshi, Y. Kuroiwa, and Dh. Pandey, *Phys. Rev. B*, 88, 024113 (2013)
- [141] M. G. Harwood, P. Popper, D. F. Rushman, *Nature*, 160, 58-59 (1947)
- [142] R. A. M. Gotardo, D. S. F. Viana, M. Olzon-Dionysio, S. D. Souza, D. Garcia, J. A. Eiras, M. F. S. Alves, L. F. Cotica, I. A. Santos, and A. A. Coelho, *J. Appl. Phys.*, 112, 104112 (2012)
- [143] L. Bellaiche, A. García, D. Vanderbilt, *Phys. Rev. Lett.*, 84, 5427 (2000)
- [144] L. Walizer, S. Lisenkov, L. Bellaiche, *Phys. Rev. B*, 73, 144105 (2006)
- [145] A. R. Akbarzadeh , S. Prosandeev, E. J. Walter, A. Al-Barakaty, L. Bellaiche, *Phys. Rev. Lett.*, 108, 257601 (2012)

- [146] K. M. Rabe, U. V. Waghmare, *Phys. Rev. B*, 52, 13236 (1995)
- [147] W. Zhong, D. Vanderbilt, K. M. Rabe, *Phys Rev. Lett.*, 73, 1861 (1994)
- [148] W. Zhong, D. Vanderbilt, K. M. Rabe, *Phys. Rev. B*, 52, 6301 (1995)
- [149] I. A. Kornev, L. Bellaiche, *Phys. Rev. B*, 79, 100105(R) (2009)
- [150] R. H. T. Yeh, *Phys. Rev. B*, 1, 1186 (1970)
- [151] K. H. Rieder, M. Ishigame, and L. Genzel, *Phys. Rev. B*, 6, 3804 (1972).
- [152] P. Giannozzi, S. Baroni, N. Bonini, M. Calandra, R. Car, C. Cavazzoni, D. Ceresoli, G. L. Chiarotti, M. Cococcioni, I. Dabo, A. Dal Corso, S. Fabris, G. Fratesi, S. de Gironcoli, R. Gebauer, U. Gerstmann, C. Gougoussis, A. Kokalj, M. Lazzeri, L. Martin-Samos, N. Marzari, F. Mauri, R. Mazzarello, S. Paolini, A. Pasquarello, L. Paulatto, C. Sbraccia, S. Scandolo, G. Sclauzero, A. P. Seitsonen, A. Smogunov, P. Umari, R. M. Wentzcovitch, *J.Phys.: Condens.Matter*, 21, 395502 (2009)
- [153] D. Vanderbilt, *Phys. Rev. B*, 41, 7892 (1990)
- [154] J. H. Lee, U. V. Waghmare, J. Yu, *J. Appl. Phys.*, 103, 124106 (2008)
- [155] N. Sai, B. Meyer, D. Vanderbilt, *Phys. Rev. Lett.*, 84, 5636 (2000)
- [156] Y. Yang, M. Stengel, W. Ren, X. H. Yan, and L. Bellaiche, *Phys. Rev. B*, 86, 144114 (2012)
- [157] S. Tinte, B. P. Burton, E. Cockayne, and U. V. Waghmare, *Phys. Rev. Lett.*, 97, 137601 (2006)
- [158] J. Hoshen, and R. Kopelman, *Phys. Rev. B*, 14, 3438 (1976)
- [159] K. Binder, and A. P. Young, *Rev. Mod. Phys.*, 58, 801 (1986)
- [160] N. Ito, and M. Suzuki, *Prog. Theor. Phys.*, 77, 1391 (1987)
- [161] Y. Gefen, B. B. Mandelbrot, and A. Aharony, *Phys. Rev. Lett.*, 45, 855 (1980)
- [162] Y. Gefen, A. Aharony, B. B. Mandelbrot, and S. Kirkpatrick, *Phys. Rev. Lett.*, 47, 177L (1981)
- [163] R. Ramesh, and N. Spaldin, *Nature Materials*, 6, 21 (2007)
- [164] J. van Suchtelen, *Philips Res. Rep.*, 27, 28 (1972)

- [165] J. M. Rondinelli, M. Stengel, and N. A. Spaldin *Nature Nanotechnology*, 3, 46 (2008)
- [166] T. Cai, S. Ju, J. Lee, N. Sai, A. A. Demkov, Q. Niu, Z. Li, J. Shi, and E. Wang, *Phys. Rev. B*, 80, 140415(R) (2009).
- [167] C.-G. Duan, S. S. Jaswal, and E. Y. Tsybal, *Phys. Rev. Lett.*, 97, 047201 (006)
- [168] G. Srinivasan *Annu. Rev. Mater. Res.*, 40, 153 (2010)
- [169] M. Vopsaroiu, J. Blackburn, A. Muniz-Piniella, and M. G. Cain, *J. Appl. Phys.*, 103, 07F506 (2008)
- [170] J. Lou, M. Liu, D. Reed, Y. Ren, and N. X. Sun, *Adv. Mater.*, 21, 4711 (2009)
- [171] N. A. Pertsev, and H. Kohlstedt, *Appl. Phys. Lett.*, 95, 163503 (2009)
- [172] N. A. Pertsev, and H. Kohlstedt, *Nanotechnology*, 21, 475202 (2010)
- [173] T. -D. Onuta, Y. Wang, C. J. Long, and I. Takeuchi, *Appl. Phys. Lett.*, 99, 203506 (2011)
- [174] E. Lage, C. Kirchhof, V. Hrkac, L. Kienle, R. Jahns, R. Knöchel, E. Quandt, and D. Meyners, *Nature Materials*, 11, 523 (2012)
- [175] M. A. Zurbuchen, T. Wu, S. Saha, J. Mitchell, and S. K. Streiffer, *Appl. Phys. Lett.*, 87, 232908 (2005)
- [176] T. Wu, M. A. Zurbuchen, S. Saha, R.-V. Wang, S. K. Streiffer, and J. F. Mitchell, *Phys. Rev. B*, 73, 134416 (2006)
- [177] S.-K. Kim, J. W. Lee, S.-C. Shin, H. W. Song, C. H. Lee, and K. No, *J. Magn. Magn. Mater.*, 267, 127 (2003)
- [178] W. Eerenstein, M. Wiora, J. L. Prieto, J. F. Scott, and N. V. Mathur, *Nature Materials*, 6, 348 (2007)
- [179] C. Thiele, K. Dorr, O. Bilani, J. Rödel, and L. Schultz, *Phys. Rev. B*, 75, 054408 (2007)
- [180] N. A. Pertsev, H. Kohlstedt, and B. Dkhil, *Phys. Rev. B*, 80, 054102 (2009)
- [181] V. G. Kukhar, N. A. Pertsev, and A. L. Kholkin, *Nanotechnology*, 21, 265701 (2010)

- [182] J. Nair, and I. Lubomirsky, *Adv. Eng. Mater.*, 4, 604 (2002)
- [183] J. Mayer, L. A. Giannuzzi, T. Kamino, and J. Michael, *MRS Bulletin*, 32, 400 (2007)
- [184] L. W. Chang, M. McMillen, F. D. Morrison, J. F. Scott, and J. M. Gregg, *Appl. Phys. Lett.*, 93, 132904 (2008)
- [185] S. Ren, M. Laver, and M. Wuttig, *Appl. Phys. Lett.*, 95, 153504 (2009)
- [186] S. Prokhorenko, and N. A. Pertsev, *J. Appl. Phys.*, 110, 074116 (2011)
- [187] N. A. Pertsev, A. G. Zembilgotov, and A. K. Tagantsev, *Phys. Rev. Lett.*, 80, 1988 (1998)
- [188] N. A. Pertsev, V. G. Kukhar, H. Kohlstedt, and R. Waser, *Phys. Rev. B*, 67, 054107 (2003)
- [189] A. G. Zembilgotov, N. A. Pertsev, U. Böttger, and R. Waser, *Appl. Phys. Lett.*, 86, 052903 (2005)
- [190] W. Cao, and L. E. Cross, *Phys. Rev. B*, 44, 5 (1991)
- [191] J. Junquera, and Ph. Ghosez, *Nature (London)*, 422, 506 (2003)
- [192] I. Kornev, H. Fu, and L. Bellaiche, *J. Mater. Sci.*, 41, 137 (2006)
- [193] E. A. N. Love, *A Treatise on the Mathematical Theory of Elasticity* (New York: Dover, 1944)
- [194] J. P. Hirth, and J. Lothe, *Theory of Dislocations* (New York: McGraw-Hill, 1968)
- [195] Y. L. Li, L. E. Cross, and L. Q. Chen, *J. Appl. Phys.*, 98, 064101 (2005)
- [196] B. Wang, and C. H. Woo, *J. Appl. Phys.*, 103, 124107 (2008)
- [197] K. L. Livesey, *Phys. Rev. B*, 83, 224420 (2011)
- [198] M. J. Haun, E. Furman, S. J. Jang, and L. E. Cross, *Ferroelectrics*, 99, 13 (Secs. I–V) (1989)
- [199] A. E. Clark, J. B. Restorff, M. Wun-Fogle, T. A. Lograsso, and D. L. Schlagel, *IEEE Trans. Magn.*, 36, 3238 (2000)
- [200] J. Lou, R. E. Insignares, Z. Cai, K. S. Ziemer, M. Liu, and N. X. Sun, *Appl. Phys. Lett.*, 91, 182504 (2007)

-
- [201] J. S. Speck, and W. Pompe, *J. Appl. Phys.*, 76, 466 (1994)
- [202] H. M. Schurter, *Experimental investigation of the mechanical properties and auxetic behavior of iron-gallium alloys* (M.Sc. thesis, University of Maryland, 2009).
- [203] O. Diéguez, S. Tinte, A. Antons, C. Bungaro, J. B. Neaton, K. M. Rabe, and D. Vanderbilt, *Phys. Rev. B*, 69, 212101 (2004)
- [204] F. A. Urtiev, V. G. Kukhar, and N. A. Pertsev, *Appl. Phys. Lett.*, 90, 252910 (2007)
- [205] J. Ryu, S. Priya, K. Uchino, and H.-E. Kim, *J. Electroceram.*, 8, 107 (2002)
- [206] C. Israel, N. D. Mathur, and J. F. Scott, *Nature Materials*, 7, 93 (2008)
- [207] N. A. Pertsev, and H. Kohlstedt, *Phys. Rev. Lett.*, 98, 257603 (2007)